

# LONG-TERM MECHANICAL ANALYSIS OF NUCLEAR REACTOR CONTAINMENTS

REPORT 2024:1031



NUCLEAR POWER CONCRETE TECHNOLOGY



# **Long-term mechanical analysis of nuclear reactor containments**

FE-modelling of pressurization tests, thermal expansion,  
shrinkage, and creep

**MAGNUS ÅHS, RICHARD MALM, DANIEL RYDLE, CHRISTIAN BERNSTONE  
MANOUCHEHR HASSANZADEH, KIM CALONIUS**

ISBN 978-91-89919-31-0 | © Energiforsk July 2024

Energiforsk AB | Phone: 08-677 25 30 | E-mail: [kontakt@energiforsk.se](mailto:kontakt@energiforsk.se) | [www.energiforsk.se](http://www.energiforsk.se)

## Foreword

The Energiforsk Nuclear Power Concrete Program aims to increase the knowledge of aspects affecting safety, maintenance and development of concrete structures in the Nordic nuclear power plants. A part of this is to investigate possibilities to facilitate and simplify the work that is performed in the nuclear business.

The VERCORS project aims to investigate the ability to assess the remaining service life of concrete nuclear reactor containments. These assessments rely on complex models of the material's behaviour during ageing, which must be validated. To support this validation, EDF provided extensive monitoring data from a purpose-built containment mock-up in France. This dataset enabled international participants to compare and evaluate computer-based predictions of long-term mechanical behaviour with actual measurements.

Three workshops have taken place in 2015, 2018 and 2022 focusing on predicting mechanical behaviour during construction, aging of the concrete containment building, and behaviour during severe accident conditions. All workshops have been followed and studied by a Energiforsk financed project group, and this report is the last in a series that also includes "Verifiering av struktur- och fuktmekaniska beräkningsverktyg", Energiforsk rapport 2017:432 and "Reaktorinneslutningars mekaniska långtidsbeteende" Energiforsk rapport 2019:632.

The study was carried out by Magnus Åhs, LTH; Richard Malm, KTH Royal Institute of Technology; Daniel Rydle and Christian Bernstone, Vattenfall AB; Manouchehr Hassanzadeh, Sweco and Kim Calonius, VTT. The study was performed within the Energiforsk Nuclear Power Concrete Program, which is financed by Vattenfall, Uniper, Fortum, TVO, Skellefteå Kraft, Karlstads Energi, SSM and SKB.

These are the results and conclusions of a project, which is part of a research programme run by Energiforsk. The author/authors are responsible for the content.

These are the results and conclusions of a project, which is part of a research programme run by Energiforsk. The author/authors are responsible for the content.

## Summary

**Benchmark VERCORS is an international benchmark on numerical modelling of long-term structural behaviour of a nuclear reactor containment. The benchmark was initiated and organized by Electricité de France, EDF, in 2015. One purpose of this benchmark is to study the long-term mechanical behaviour of a nuclear reactor containment. A second purpose is to study leakage during pressurization tests. These pressurization tests are performed on a regular basis during the service life of a reactor containment.**

This project's main purpose is to develop a numerical FE-model that may be applied by consultants or researchers to study long-term structural response of a nuclear reactor containment. The model considers the mechanical response caused by external loads, temperature, relative humidity, and aging effects. These parameters affect volumetric changes such as thermal expansion and contraction, shrinkage, and creep.

The developed numerical model aims to describe the response of a physical scale model of a nuclear reactor containment, built in scale 1:3. The height of the reactor containment is 21 m, and the inner diameter is 14.6 m. It was completed in 2015 and a simplified digital twin was supplied to the participants in the benchmark VERCORS. The digital twin is a digital replica of the structure and consists of many important data. Among others it contains a description of materials used, important properties of the materials, a digital geometry of the structure, the tendon configuration, and positions of sensors in the structure. The sensors monitored ambient temperature, relative humidity and strains of the structure.

Three different subjects have been studied within this project. The main subject was to simulate the evolution of long-term deformations in a reactor containment. This study was performed on two different geometries, a cut out wedge, 45° angle of the geometry and the complete geometry. Another subject was to estimate the evolution of air leakage during reoccurring pressurization tests. In addition, this project investigated the scale effect of drying in the cylindrical wall.

The results of the study showed that the developed model deviates from long-term deformations of the RC by 25-30 %. The best results were achieved in the cylindrical wall of the reactor containment at mid height. The results from the simulations showed that the calculated strains agreed reasonably well with the measurements.

The developed leakage model describes the air flow through the porous uncracked concrete structure. The model is based on Darcy's law. It considers both the pressure dependency of the air density, which is significant, and the air permeability as a function of the moisture content in the concrete structure. The model was able to predict the porous air flow reasonably well compared with the measured porous air flow.

The scale effect study of the drying indicates that it is not sufficient to analyse drying of concrete based only on the theory of diffusion. Aspects such as the age dependency of material properties and self-desiccation also need to be included to achieve reasonable results of drying and its effects on predicted stresses in a nuclear containment.

## Keywords

Mechanical behaviour, long-term, leakage, concrete, nuclear reactor containment, numerical methods, FE-model, scale-effect of drying

## Author contribution

**Magnus Åhs:** Conceptualization, Methodology, Formal analysis, Writing - Original Draft, Project administration, Funding acquisition **Richard Malm:** Writing – Review & Editing **Daniel Rydle:** Writing – Review & Editing **Christian Bernstone:** Writing – Review & Editing **Manouchehr Hassanzadeh:** Writing – Review & Editing – **Kim Calonius:** Writing – Review & Editing

## Sammanfattning

Benchmark VERCORS är en internationell benchmark för numerisk modellering av strukturellt beteende hos en kärnreaktorinneslutning under lång tid. Benchmarken initierades och organiseras av Electricité de France, EDF, 2015. Ett syfte med denna benchmark är att studera det långsiktiga mekaniska beteendet hos en kärnreaktorinneslutning. Ett andra syfte är att studera läckage under trycktester. Dessa trycktester utförs regelbundet under en reaktorinneslutnings livslängd.

Det här projekts huvudsakliga syfte var att skapa en modell utifrån redan kända samband och sedan använda denna för att utveckla en numerisk FE-modell. En sådan modell kan användas av konsulter eller forskare för att studera det långsiktiga strukturella beteendet hos en kärnreaktorinneslutning. Den framtagna modellen tar hänsyn till den mekaniska responsen orsakad av externa belastningar, temperatur, relativ fuktighet och åldringseffekter. Dessa parametrar påverkar volymetriska ändringar som termisk expansion och kontraktion, krympning och svällning, samt krypning.

Modellen har tillämpats på en kärnreaktorinneslutning, byggd i skala 1:3. Höjden på reaktorinneslutningen är 21 m och innerdiametern är 14,6 m, vilken färdigställdes 2015. En digital tvilling för reaktorinneslutningen gavs till deltagarna i benchmark VERCORS. En digital tvilling är en digital kopia av reaktorinneslutningen och består av många viktiga data för beräkningarna. Den innehåller bland annat en beskrivning av använda material, materialens viktiga egenskaper, en digital geometri för den fasta strukturen, spännkablarnas geometriska data och positioner för sensorer i strukturen. Sensorerna mätte bland annat omgivningstemperatur, relativ luftfuktighet och töjningar.

Tre olika studier har genomförts i det här projektet. Huvudstudiens syfte var att beräkna utvecklingen av den långsiktiga deformationen i en reaktorinneslutning. Den studien genomfördes med två olika geometrier, en kilformad utklippt del av den totala geometrin, 45° vinkel och den kompletta geometrin. En mindre studie syftade till att beräkna luftläckage under återkommande trycksättningstester och hur det förändrades med tiden. Dessutom studerades skaleffekten av uttorkning av den cylindriska väggen.

Resultaten av studien visade att den framtagna modellen avviker från långtidsdeformationer med 25 till 30 %. De bästa resultaten uppnåddes i den cylindriska väggen av reaktorinneslutningen på medelhöjd. Resultaten från simuleringarna visade att de beräknade töjningarna överensstämde någorlunda med mätningarna.

Den framtagna läckagemodellen beskriver läckaget genom den ospruckna betongkonstruktionen, det porösa läckaget. Den är baserad på Darcys lag. I modellen beaktas både luftdensitetens tryckberoende, vilket är betydande, och luftpermeabiliteten som funktion av relativa fuktigheten och fuktinnehållet i betongkonstruktionen. Modellen kunde förutsäga det porösa läckaget med rimlig noggrannhet jämfört med mätningar.

Studien av skaleffekten av uttorkning tyder på att det, för exakta resultat, inte är tillräckligt att analysera uttorkning av betong baserat enbart på diffusionsteorin. Förändringen av den unga betongens materialegenskaper bör inkluderas för att erhålla rimliga resultat av uttorkningen och dess betydelse för spänningarna i en reaktorinneslutning.

## Nyckelord

Mekaniskt beteende, läckage, betong, reaktorinneslutning, FE-modell, skaleffekt av uttorkning

## List of content

<b>1</b>	<b>Introduction</b>	<b>4</b>
1.1	Benchmark VERCORS workshop	4
1.1.1	Benchmark VERCORS	6
1.1.2	International collaboration	6
1.1.3	Swedish project team	6
1.2	Aim and goals	7
1.3	Modelling assumptions	7
<b>2</b>	<b>Material and material properties</b>	<b>10</b>
2.1	Air properties	10
2.2	Concrete	11
2.3	Concrete properties	12
2.3.1	Mechanical properties	12
2.3.2	Heat properties	12
2.3.3	Moisture properties	13
2.3.4	Air permeability	16
2.4	Tendon properties	18
<b>3</b>	<b>Concrete mechanical material models</b>	<b>19</b>
3.1	Elastic strains	19
3.2	Thermal strains	19
3.3	Shrinkage strains	20
3.4	Basic creep and drying creep	20
<b>4</b>	<b>Tendons</b>	<b>21</b>
4.1	Tendon pre-stressing	21
4.2	Tendon model	24
<b>5</b>	<b>FE models</b>	<b>25</b>
5.1	Case studies	25
5.2	Geometry	25
5.2.1	Mechanical long-term	25
5.2.2	Air leakage	32
5.2.3	Scale effect of drying	33
5.3	Meshes	33
5.3.1	Wedge geometry	33
5.3.2	Complete RC geometry	35
5.3.3	Scale effect of drying	39

5.3.4	Air leakage mesh	40
5.4	Heat transfer model	42
5.5	Moisture transfer model	42
5.6	Air transport model	43
5.7	Boundary conditions	44
5.7.1	Mechanical long-term case study	44
5.7.2	Air leakage	47
5.7.3	Scale effect of drying	48
5.7.4	Ambient temperature and relative humidity	49
<b>6</b>	<b>Computation strategies</b>	<b>52</b>
6.1	Structural mechanics computation strategy of the RC (Study 1a and 1b)	52
6.2	Air leakage computation strategy (Study 2)	53
6.3	Strategy for computing the scale effect of drying (Study 3)	53
<b>7</b>	<b>Results</b>	<b>55</b>
7.1	The long-term mechanical behaviour of the RC (Study 1)	55
7.1.1	Temperature	57
7.1.2	Humidity	64
7.1.3	Radial and vertical displacement in wedge geometry	65
7.1.4	Radial and vertical displacement in complete RC geometry	67
7.1.5	Strain field before and after pre-stressing	69
7.1.6	Stress field before and after pre-stressing	72
7.1.7	Evolution of strains with time using the wedge geometry	75
7.1.8	Evolution of strains with time using the complete RC geometry	100
7.2	The air leakage through the RC (study 2)	121
7.3	The scale effect of drying (Study 3)	123
<b>8</b>	<b>Results from other participants</b>	<b>138</b>
8.1	Participants	138
8.2	Models	139
8.3	Results	140
8.3.1	Temperature	140
8.3.2	Moisture profiles	141
8.3.3	Displacement	142
8.3.4	Strain evolution	142

8.3.5	Leakage	144
<b>9</b>	<b>General discussion</b>	<b>146</b>
9.1	Long- and short-term overall behaviour	146
9.2	Geometry	147
9.3	Temperature effects	147
9.4	Relative humidity	147
9.5	Leakage	147
9.6	Scale effect of drying	148
9.7	Stresses/cracks	148
9.8	VERCORS measurements	149
<b>10</b>	<b>Conclusions</b>	<b>150</b>
<b>11</b>	<b>Future perspective</b>	<b>152</b>
11.1	Design of new reactor containments	152
11.2	Sensitivity analysis	152
11.3	Pressure test	153
11.4	Corrosion of steel liners	153
11.5	Creating a digital twin of a reactor containment	153
<b>12</b>	<b>Acknowledgements</b>	<b>155</b>
<b>13</b>	<b>References</b>	<b>156</b>

# 1 Introduction

Nuclear reactor containments, RCs, have been used all over the world for decades in nuclear power plants. The main objective of an RC is to be an external barrier for the reactor, and is thereby important to maintain, to ensure the safety of nuclear power plants throughout their service life.

Many of the nuclear power plants that are in operation were built in the 1970s and 1980s, and they are thus approaching the end of their originally planned service life. A large number of these power plants have been upgraded to extend their initial service life. However, it is important to be able to predict their remaining service life with a reasonable accuracy. In France, Electricité de France, EDF, has therefore started a research program aiming to investigate the ability to estimate the remaining service life.

Detailed assessment of the remaining service life of containment buildings is complex and involves aspects to determine the structural integrity as well as the leak tightness of the containment, and how these are influenced by aging (long-term effects). EDF has therefore invited researchers and experts from all over the world to participate in a series of benchmark workshops. Within the scope of these workshops, a mock-up of a reactor containment building was built in 2015 in scale 1:3. The aim was to compare advanced computer-based predictions made by international experts with data from extensive monitoring.

The studied reactor containment building in this test is designed with two separate concrete shells. The inner shell is a pre-stressed concrete structure, while the outer shell is a concrete structure without pre-stressed reinforcement. This type of containment does not include a steel liner, which means that the leak tightness depends on the concrete properties and how these develop over time. The two shells create a space in between, which is kept at a constant pressure below the ambient air pressure. In case of leakage of hazardous emissions from the containment, these emissions may be taken care of in the space between the two walls. This prevents the emissions from reaching the environment. Even though possible leakage may be taken care of, there is a limit for the allowed leakage through the pre-stressed inner wall. The leak tightness of the inner containment structure is carefully monitored by testing each nuclear powerplant every 10 years. This is done by performing regular pressure tests, where the pressure inside the pre-stressed containment is increased to an absolute pressure of 5.2 bar.

## 1.1 BENCHMARK VERCORS WORKSHOP

The mock-up containment building, see Figure 1.1, was completed in 2015 and is built to be a downscaled replica of the pre-stressed concrete containment building of Nogent sur Seine. This containment mock-up has a mechanical behaviour that represents an average P4-reactor (1300 MWe), which is common in nuclear power plants, NPP, of the French fleet. The construction work took about 15 months, from May 2014 until August 2015, and was performed at EDF's research facility near Fontainebleau, outside of Paris. The main part of the construction was poured in sequence with fresh concrete to the dome top. The dome itself was composed of a pre-cast concrete shell, approximately 45-50 mm thick, with fresh concrete poured on top to achieve the intended thickness. The research project is planned to be ongoing for over 10 years.

The VERCORS mock-up containment building consists of the following

- A double-wall containment ( $H=27\text{m}$ ,  $\varnothing=17\text{m}$ ),
- 5000 ton of concrete,
- 700 sensors, 2 km of fibre optic cables and over 1000 concrete test specimens,
- 4 penetrations: material hatch, personal hatch, and two penetrations of large pipes (steam generators main feedwater flow control system, ARE, and main steam system, vents valves and steam generator vents and valves, VVP),
- 1 auxiliary building (ventilation, heating, measurements).



**Figure 1.1 Photo of the construction of the VERCORS mock-up in scale 1/3., from [1]**

The mock-up scale 1:3 was chosen to accelerate the drying process of concrete. The drying of concrete influences both shrinkage and creep. These two factors are assumed to have the most significant influence on the leak-tightness of the concrete containment over time. Since the thickness is only one-third of a real containment, the drying process is faster. Theoretically, given the assumption that the drying process is governed by pure diffusion, this means that 1 year in the experiment corresponds to 9 years in a real reactor containment building. Therefore, the expected service life of 60 years may be reached already after about 7 years in the mock-up. In the mock-up test, regular pressure tests have been performed using a similar procedure as for a real containment building. However, the time interval between the tests is one-ninth of the interval used for real containment buildings.

The main objectives of the VERCORS project are to study:

- the behaviour of the structure at early age and during ageing,
- the evolution of the leak tightness during the aging process (drying effects are about 9 times faster in the mock-up because of scale effects),
- the behaviour of the structure under severe accidental conditions during which the thermo-mechanical loading is maintained for several days. The severe accidental condition is simulated by increasing the absolute pressure from 5.2 bar to 7.0 bar in steps of 0.5 bar up to 6.7 bar, and then in a final step to 7.0 bar. Regular pressure tests are performed at an absolute pressure of 5.2 bar.

The work carried out in the mock-up experiment is important for development and validation of numerical models. Therefore, a vast number of sensors (700), and 2 km of fibre optic sensors were installed, and 1000 material tests were conducted to determine the

material properties and the behaviour of the containment over time [2]. The measurements conducted on the containment building include measurements of displacements and strains, as well as ambient climate data such as relative humidity and temperature.

All participants have been provided with construction drawings, a 3D model of the geometry, material properties, pre-stressing tendon scheme, etc.

The VERCORS project is performed in three phases.

- Phase 1: Behaviour of the structure during early age.
- Phase 2: The influence of aging on the structural leak tightness.
- Phase 3: The behaviour during severe accidental conditions.

### 1.1.1 Benchmark VERCORS

Three VERCORS benchmark workshops have to this date been finalized, 2015, 2018 and 2022, and their outcome have been documented in three reports by EDF [1, 3, 4]. The first benchmark focused on predicting mechanical behaviour during construction, while the second benchmark focused on predicting the aging of the concrete containment building. The third benchmark focused on the behaviour during severe accident conditions. This third benchmark was concluded in a workshop held in January/February 2023.

A Swedish team, financially supported by Energiforsk, actively participated in all three benchmarks. This team included individuals from Lund University, KTH Royal Institute of Technology, Sweco, and Vattenfall [5, 6].

While there are plans for further activities within the VERCORS project, as of the completion of this report, there is no plan for further workshops.

### 1.1.2 International collaboration

Several teams of researchers have participated in the previous benchmark workshops, 2015 and 2018. In the first workshop, 46 teams from 19 countries in 3 continents were registered. The majority of the participating teams are from France and about 70 % of the participants are from Europe. Overall, the participation was 50 / 50 between participants from design offices and participants from universities and research centres. All teams applied for their own funding; hence their level of engagement varied, and unfortunately not all registered participants were able to finalize their contributions [3].

In the second benchmark, 37 teams from 14 countries across 3 continents were registered to participate [1]. Several of the teams that participated in the second workshop also participated in the first workshop. Similar to the first workshop, not all participants finalized their work. In total, 18 teams delivered a final report.

When the third benchmark was launched, 64 teams expressed interest, but in the end only 10 teams participated. An overview of their work is presented in section 8 of this report.

### 1.1.3 Swedish project team

The core of the Swedish project team has participated in all previous VERCORS workshops. Associate Professor Magnus Åhs from Lund university served as the project leader for workshops 2 and 3 and responsible for the contact with the VERCORS organizing team and has performed all numerical analyses.

The other project members listed below have contributed with experience of the integrity and behaviour of containment buildings at nuclear power plants, numerical simulations, etc.

- Assoc. Professor Richard Malm, KTH Royal Institute of Technology / Sweco.
- Dr. Daniel Rydle, Vattenfall.
- Dr. Manouchehr Hassanzadeh, Sweco.
- Dr. Christian Bernstone, Vattenfall.

In addition, M.Sc. Kim Calonijs, VTT, who is a member of the scientific committee of VERCORS and participated in phase 1 and 2, also followed this project and participated in the project meetings and reviewed the report.

## 1.2 AIM AND GOALS

The overall goal of this project is to increase the knowledge and gain further insights into the structural response of reactor containment building by taking the unique opportunity to participate in the benchmark VERCORS 2022. Thereby this project also contributes to increase the competence in Sweden regarding numerical analyses of nuclear facilities and how these are affected by aging and external loads.

This project is also closely related to the overall goal of the Nuclear Power Concrete Technology program at Energiforsk regarding assessment of service life while ensuring safe, reliable, and cost-effective operations.

The aim of this study is to model, by using commonly used modelling approaches, the RC's long-term mechanical behaviour for a time-period of about 7 years. These models are tools used by designers when designing large concrete structures. Another aim is to calculate the leakage through the inner pre-stressed concrete structure during the pressure tests and investigate its evolution with time. A third aim is to analyse the scale effect of drying and differences in obtained stresses between assuming constant and time dependent concrete properties.

## 1.3 MODELLING ASSUMPTIONS

The following modelling assumptions have guided the work:

1. The concrete material model used to simulate the reactor containment's structural behaviour is an isotropic linear elastic model. The material properties of the concrete, i.e. thermal conductivity, sorption isotherm, moisture transport coefficient, modulus of elasticity and, air permeability are assumed constant with time, as the concrete is about 6 months old when the simulations start. The assumption is based on the fact that the evolution of the material properties is moderate in concrete at the age at which these simulations are performed.
2. The tendons were modelled as an ideal elastoplastic material. The pre-stressing procedure was simplified, with all tendons being tensioned simultaneously. This pre-stressing was simulated by incrementally increasing the tendon stresses from an initial non-stressed state to a fully stressed condition. It's worth noting that in this study, a perfect bond between the tendons and the concrete is assumed. This assumption is

grounded in the fact that all tendons are grouted, establishing a physical bond with the concrete.

3. Based on the assumption in the first bullet point, the reinforcement is not included in this study, since the reinforcements contribution to the stiffness of the RC is insignificant compared to the concrete stiffness.
4. The boundary surfaces are subjected to fluctuating temperature and humidity conditions. The actual temperature and humidity data was supplied as mean values each 24 hours. This supplied data was used as input in the simulations with a few exceptions.
5. The relative humidity, RH, in the air surrounding the concrete structure is, according to the measurements, sometimes above 100% RH. Such readings are in reality not possible but may occur due to condensation on the sensors. Condensation may occur on the sensors at high humidity levels in the event of sudden temperature changes. The RH was set to 95% when the actual registered RH exceeded 95%. No modification of the temperature data was performed.
6. Residual stresses, originating from the construction of the structure are assumed to be zero.
7. The air leakage through the concrete's porous network in the reactor containment is assumed independent of its mechanical response.
8. The analysis of the scale effect of drying is performed as a parametric study. The thickness of the cylinder wall has an impact on the evolution of the temperature and moisture distribution. The evolution will cause stresses in the concrete as temperature and moisture related deformations will occur on a short-term and on a long-term basis. Two modelling cases are studied, one case with constant and one with time-dependent material properties. The case that assumes constant material properties does not include heat generated by the hydration of the cement. The initial moisture state of the concrete is assumed to correspond to 90 % RH as a result of drying caused by self-desiccation. The case that assumes time-dependent material properties also considers heat generation and self-desiccation. In these two cases both the moisture distribution and stresses caused by drying will be presented. Creep is not included in the scale effect analyses.



## 2 Material and material properties

The material properties in this study are equal to those in the two previous studies regarding air and tendons. Thermal and moisture properties of concrete are also equal to those used in the two previous studies. The air permeability and its moisture dependence in this study is based on results from studies performed on a real reactor containment, in Ringhals, Sweden. The tendon properties in this study are equal to the two previous studies.

### 2.1 AIR PROPERTIES

The saturation vapour content of air,  $v_s$ , ( $\text{kg}/\text{m}^3$ ) was estimated using equation (1)

$$v_s = 10^{-3} \cdot e^{\left(\frac{a-b}{T}\right)} \quad (1)$$

where,  $a$  and  $b$  are model parameters, and  $T$  represents the temperature (K). Above a temperature of 273.15 K,  $a$  and  $b$  are equal to 20.11 and 5061, respectively. Below 273.15 K,  $a$  and  $b$  are equal to 23.08 and 5872, respectively [7]. The vapour content in air at saturation ( $\text{kg}/\text{m}^3$ ) is shown in Figure 2.1.

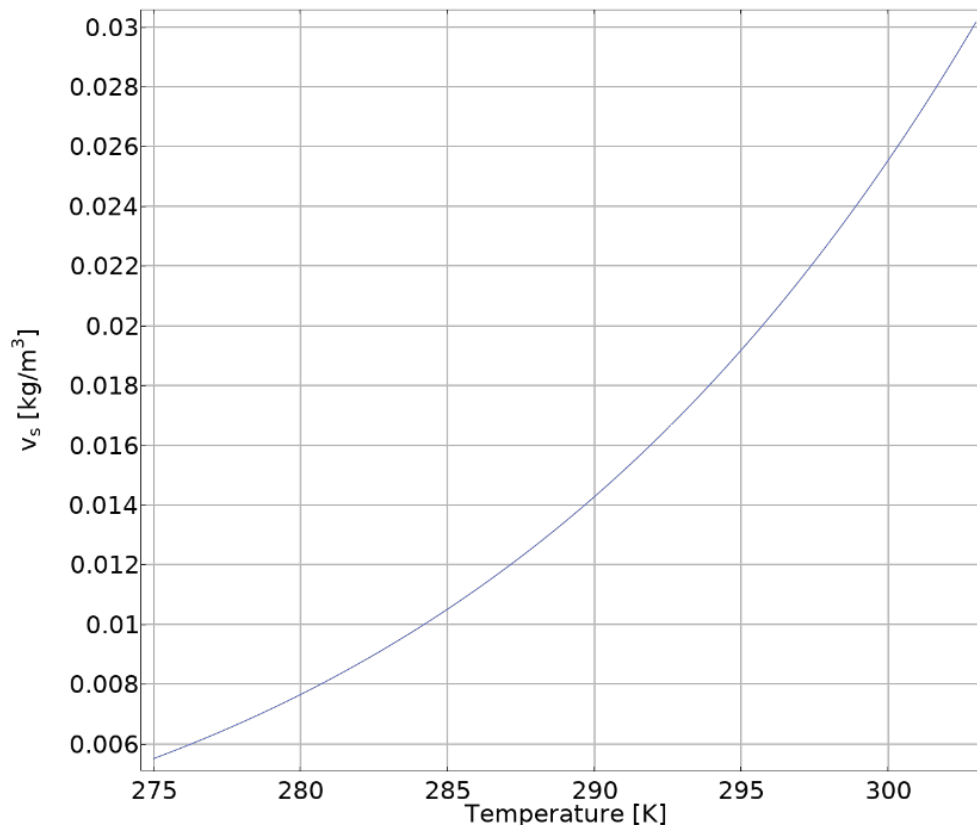


Figure 2.1 Diagram showing the saturation vapour content in air with respect to temperature in Kelvin.

The air density is pressure and temperature dependent. The air density was modelled using the ideal gas law according to equation (2)

$$\rho_{air} = \frac{M_{air} \cdot p_{abs}}{R \cdot T} \quad (2)$$

where,  $M_{air}$  represents the molar mass of air, 0.0289647 kg/mol,  $p_{abs}$  represents the absolute pressure (Pa),  $R$ , represents the universal gas constant, 8.314 J/(mol K).

The dynamic viscosity,  $\mu$ , is dependent on both temperature and pressure. However, the pressure dependency is negligible in the applied pressure range. The temperature dependency of the dynamic viscosity is modelled using equation (3) [8]

$$\mu = 1.458 \cdot 10^{-6} \frac{T^{\frac{3}{2}}}{T + 110.4} \quad (3)$$

## 2.2 CONCRETE

The concrete mixing proportions used in the mock-up containment building are outlined in Table 2.1, as specified by the benchmark VERCORS 2022.

**Table 2.1** Mixing recipe with material supplier and amount per 1 m<sup>3</sup> of concrete

Material	Supplier	Amount (kg/m <sup>3</sup> )
Cement CEM I 52.5 N CE CP2 NF	Gaurain	320
Sand 0/4 rec	GSM LGP1	830
Aggregate 4/11 R	GSM LGP1	445
Aggregate 8/16	Balloy	550
Admixture	Sikament Techno 80	2.6
Added water	-	195.5
Total water	-	197.6

The table shows that the mass ratio between water and cement is 197.6 kg/m<sup>3</sup>/ 320 kg/m<sup>3</sup>, which means that the W/C-ratio is 0.62. Data from this recipe has been used as a reference mixture when choosing representative material properties in this study.

The density was assumed equal to 2350 kg/m<sup>3</sup>.

## 2.3 CONCRETE PROPERTIES

### 2.3.1 Mechanical properties

The strength development with time was neglected in the simulations of the RC behaviour. This simplification is justified as the simulation starts at a concrete age of about 1 year, when most of the strength development is completed. The concrete compression strength was therefore considered constant and equal to the mean value of the measured strength, 50.8 MPa. The tensile strength was set equal to 4.5 MPa. The tensile strength was provided by Benchmark VERCORS 2022. This tensile strength was evaluated by Benchmark VERCORS as the mean value from destructive testing performed on separately cast samples from each concreting sequence in the VERCORS mock-up.

The modulus of elasticity was also treated as constant in the simulation of the RC's structural behaviour and was set to 33.8 GPa. This modulus of elasticity corresponds to the measured mean value of the concrete used in the VERCORS mock-up. The Poisson ratio was set to 0.2.

The scale effect of drying was studied by comparing the results achieved by using constant (with regard to time) material properties with results achieved by using time-dependent material properties. When time dependent material properties were used both the development of strength and modulus of elasticity were estimated according to Eurocode 2 [9].

The mean compressive strength,  $f_{cm}(t)$ , was modelled by using equation (4)

$$f_{cm}(t) = e^{\left(s \cdot \left(1 - \left(\frac{28}{t}\right)^{0.5}\right)\right)} \cdot f_{cm} \quad (4)$$

where,  $s$ , represents a coefficient that depends on the type of cement and was set to 0.2 (-),  $t$ , represents the time in maturity days, and,  $f_{cm}$ , is the mean compressive strength at 28 days, set to 50.8 MPa.

The time dependency of the modulus of elasticity,  $E_{cm}(t)$ , was estimated according to equation (5),

$$E_{cm}(t) = \left(\frac{f_{cm}(t)}{f_{cm}}\right)^{0.3} \cdot E_{cm} \quad (5)$$

where,  $f_{cm}(t)$ , represents the time dependent compressive strength,  $t$ , represents the time in maturity days,  $f_{cm}$ , represents the mean compressive strength at a maturity age of 28 days, and  $E_{cm}$ , represents the mean modulus of elasticity at a maturity age of 28 days.

### 2.3.2 Heat properties

The thermal conductivity of concrete typically ranges from 1.7 to 2.6 W/mK; however, for these simulations, it was set to 1.8 W/mK [10]. The specific heat capacity of concrete ranges from between 840 and 1170 J/kgK [10], for these simulations 880 J/kgK was used.

### 2.3.3 Moisture properties

The sorption isotherm depends on the degree of hydration and the pore structure development with time. A model for generating generic sorption isotherms was developed by Jonasson [11], and was further developed by Norling-Mjörnell [12]. The further developed model [12] was used in this project.

A number of sorption isotherms generated with the model at various degrees of hydration,  $\alpha_c$ , are shown in Figure 2.2, to illustrate the change of the sorption isotherm with the degree of hydration.

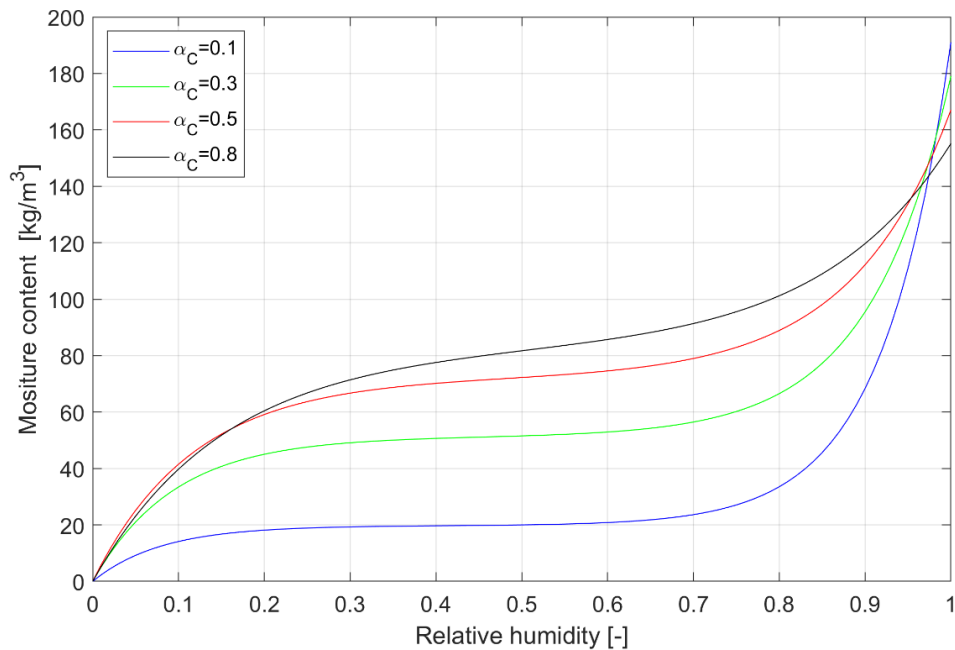


Figure 2.2 Sorption isotherms, at 20 °C, at various degrees of hydration.

The degree of saturation,  $S$ , in the concrete is evaluated by using equation (6)

$$S = \frac{W_e}{W_s} \quad (6)$$

where  $W_e$ , represents the moisture content ( $\text{kg/m}^3$ ) at the current relative humidity and  $W_s$ , represents the moisture content ( $\text{kg/m}^3$ ) at full saturation. Hence,  $S$ , is the ratio of the pore volume filled with moisture to the total pore volume, and varies between 0 and 1. In Figure 2.3,  $S$ , is shown as a function of the relative humidity when the degree of hydration is 0.8.

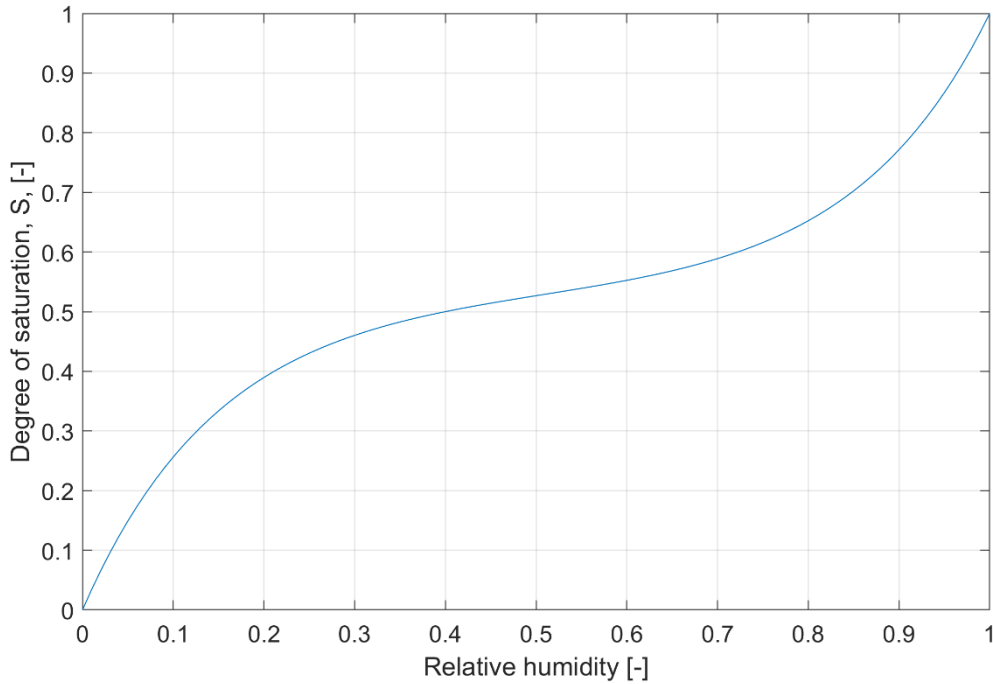


Figure 2.3 The degree of saturation in the concrete as a function of relative humidity

The moisture transport coefficient,  $\delta_\varphi$ , (kg/m·s) with relative humidity as the driving potential was estimated by using equation (7) [13]

$$\delta_\varphi = \delta_v \cdot v_s \quad (7)$$

where  $\delta_v$  is the moisture transport coefficient with the vapour content as the driving potential. The parameter  $v_s$  (kg/m<sup>3</sup>) represents the saturation vapour content of air and is temperature dependent.

When constant material properties with regard to time were used in the simulation the degree of hydration was set to 0.8. In the case with time dependent properties, the moisture transport coefficient,  $\delta_v$ , was modelled according to a theoretical expression proposed by Hedenblad [14] see equation (8)

$$\delta_v = \delta_{v\ 60\%} + (\delta_{v\ 100\%} - \delta_{v\ 60\%}) \cdot \left( \frac{\varphi - 0.6}{0.4} \right)^k \quad (8)$$

where  $\delta_{v\ 60\%}$  represents the moisture transport coefficient at 60% RH,  $\delta_{v\ 100\%}$  represents the moisture transport coefficient at 100% RH,  $\varphi$  represents the relative humidity and  $k$  is a constant which has a value of 10 when the W/C ratio is between 0.6 and 0.8 [7].

The moisture transport coefficient at 60% RH,  $\delta_{v\ 60\%}$ , is estimated using equation (9)

$$\delta_{v\ 60\%} = a_{\delta} + b_{\delta} \cdot P_{kap} \quad (9)$$

where  $P_{kap}$ , represents the capillary porosity of the cement paste.  $a_{\delta}$  is a constant  $1.0 \cdot 10^{-7}$  and  $b_{\delta}$  is a constant  $2.5 \cdot 10^{-7}$  when the W/C ratio is between 0.6 and 0.8 [7].

The moisture transport coefficient at 100% RH,  $\delta_{v\ 100\%}$ , is estimated using equation (10)

$$\delta_{v\ 100\%} = c_{\delta} + d_{\delta} \cdot P_{kap}^2 \quad (10)$$

where  $c_{\delta}$  is a constant  $-5.0 \cdot 10^{-6}$  and  $d_{\delta}$  is a constant  $4.2 \cdot 10^{-4}$  when the W/C ratio is between 0.6 and 0.8 [7].

And finally the  $P_{kap}$ , is estimated by using equation (11) [15]

$$P_{kap} = \frac{W - 0.39\alpha_c C}{\frac{C}{\rho_{cem}} + \frac{W}{\rho_{H_2O}}} \quad (11)$$

where  $W$ , represents the mixing water content in  $\text{kg}/\text{m}^3$ ,  $C$ , represents the cement content,  $\rho_{cem}$  in  $\text{kg}/\text{m}^3$ , represents the cement density in  $\text{kg}/\text{dm}^3$  and  $\rho_{H_2O}$  represents the water density in  $\text{kg}/\text{dm}^3$ .

The moisture transport coefficient,  $\delta_{v}$ , at various degrees of hydration,  $\alpha_c$ , at a temperature of 20 °C, are shown in Figure 2.4.

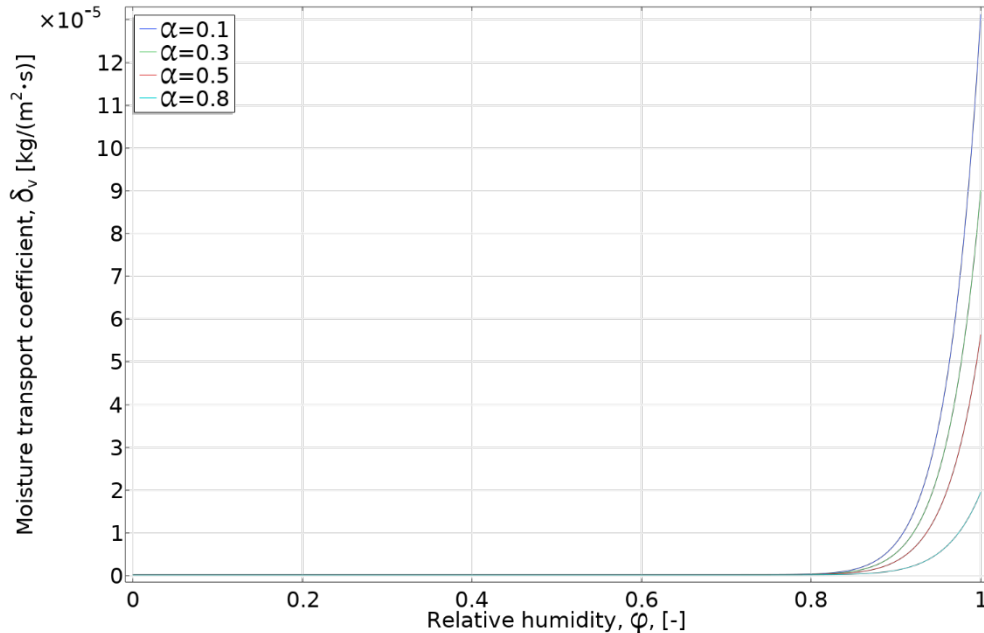


Figure 2.4 The moisture transport coefficient used in the simulations.

As the degree of hydration increases the moisture transport coefficient in the high relative humidity range decreases. Such a decrease in moisture transport is correlated to the decrease of capillary pore volume as the degree of hydration increases.

### 2.3.4 Air permeability

The air permeability in concrete is dependent on the current moisture condition. In a completely saturated concrete, the pore system is completely filled with water and therefore the air permeability is insignificant. Fredlund and Nilsson [16] determined the air permeability for a concrete used in a Swedish nuclear power plant, Ringhals, see Figure 2.5.

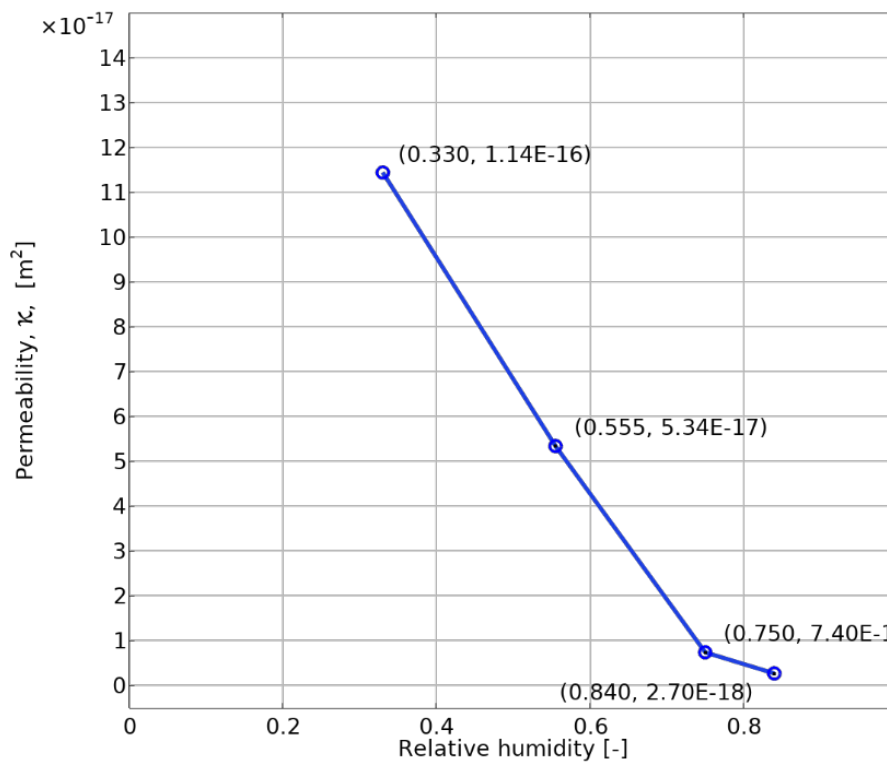


Figure 2.5 Effective air permeability for a concrete used in one of the reactor containment buildings at Ringhals, Sweden.

Figure 2.5 clearly shows that the permeability decreases with an increasing relative humidity.

An equation has been fitted to this data such that a representative effective air permeability,  $\kappa_p$ , is obtained in the relevant moisture range for the concrete, see equation (12)

$$\kappa_p = 45 \cdot 10^{-6} \cdot k_{rg} \quad (12)$$

where  $k_{rg}$  is a parameter that relates the permeability relative to the degree of saturation.

The equation used to describe the permeability relative to the degree of saturation was adopted from Mollouis- Bonnaire et al [17], see equation (13)

$$k_{rg} = (1 - S)^{5.5} \cdot (1 - S^2) \quad (13)$$

where  $S$ , represents the degree of moisture saturation.

The effective air permeability as a function of relative humidity used in this analysis is shown in Figure 2.6.

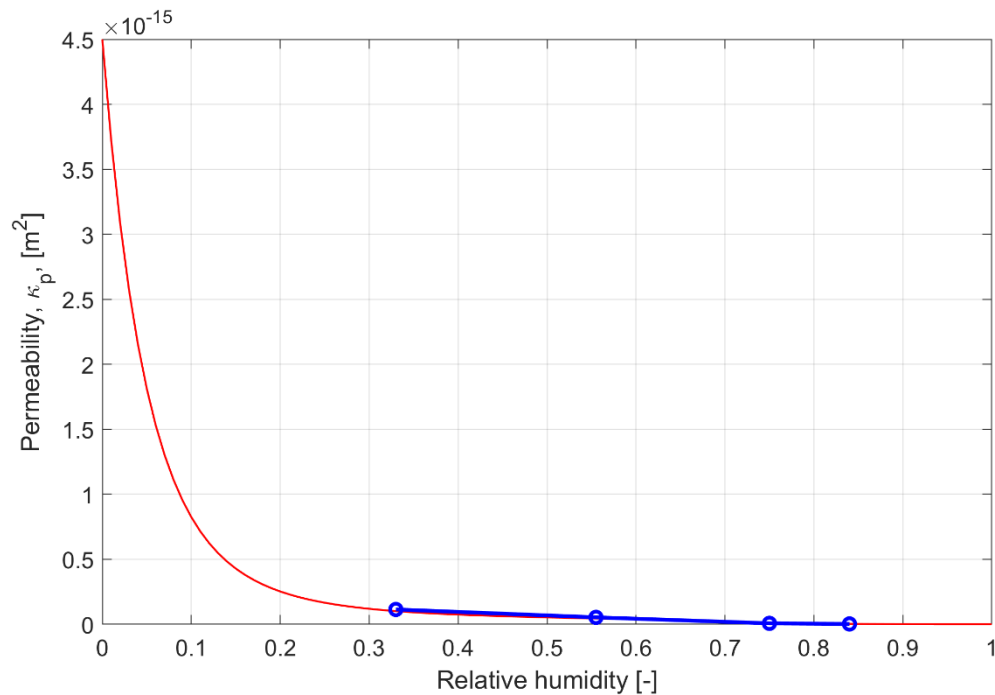


Figure 2.6 Effective air permeability for a concrete used in one of the reactor containment buildings at Ringhals, Sweden.

The blue line with circles shows the results from the measurements by Fredlund and Nilsson [16]. The red solid line shows the fitted curve of the air permeability used in the model. The fitted effective air permeability at  $RH < 0.35$  is considered of minor importance since such a low RH only occurs at the surfaces of the concrete structure.

Local air leakage that may occur in cracks is not considered in the model, since the mechanical part of the model is purely linear elastic.

## 2.4 TENDON PROPERTIES

Material properties of the used tendons are presented in Table 2.2. The tendons were modelled as linear elastic.

Table 2.2 Mechanical properties of the tendon cables in the simulation.

Pre-stressing system	
System C (4C15) (Freyssinet) ETA-06/0226	
Bonded pre-stressing (except 4 vertical and 2 horizontal tendons)	
Pull-In at wedgeblocking	8 mm
Strands	
Strand section (T15)	139 mm <sup>2</sup>
Tensile strength	1860 MPa
Yield strength	1620 MPa
Relaxation losses	$\rho_{1000}=2.5\%$
Tendons	
Tendon	4T15
Tendon maximal pre-stressing stress (at anchor, before wedge blocking)	1488 MPa
Tendon Young modulus	190 000 MPa
Friction	
Vertical tendons	
Friction coefficient	f=0.16
Wobble effect coefficient	$\Phi=k.f.=0.0008$
Horizontal tendons	
Friction coefficient	f=0.17
Wobble effect coefficient	$\Phi=k.f.=0.0015$
Gamma tendons	
(Vertical part) Friction coefficient	f=0.16
(Vertical part) Wobble effect coefficient	$\Phi=k.f.=0.0008$
(Dome part) Friction coefficient	f=0.16
(Dome part) Wobble effect coefficient	$\Phi=k.f.=0.0015$
Dome tendons	
Friction coefficient	f=0.16
Wobble effect coefficient	$\Phi=k.f.=0.0015$

### 3 Concrete mechanical material models

#### 3.1 ELASTIC STRAINS

The concrete is assumed to behave as an isotropic linear elastic material with the strains remaining small. Hence, the mechanical behaviour, in terms of the stress tensor  $\boldsymbol{\sigma}$ , can be expressed using Hooke's law on the following form, see equation (14)

$$\boldsymbol{\sigma} = \mathbb{C}_e : (\boldsymbol{\varepsilon} - \boldsymbol{\varepsilon}_{in}) \quad (14)$$

where  $\mathbb{C}_e$  is a fourth-order elasticity tensor defined by Young's modulus  $E = 33.8$  GPa and Poisson's ratio  $\nu = 0.2$ . Since small strains are assumed, the total strain tensor  $\boldsymbol{\varepsilon}$  is defined according to equation (15)

$$\boldsymbol{\varepsilon} = \frac{1}{2} [\nabla \mathbf{d} + (\nabla \mathbf{d})^T] \quad (15)$$

where  $\mathbf{d}$  is the displacement vector. The model also considers thermal strains as well as strains caused by varying moisture conditions and long-term stress levels, also known as creep. These inelastic strains enter equation (14) through the inelastic strain tensor  $\boldsymbol{\varepsilon}_{in}$  defined according to equation (16)

$$\boldsymbol{\varepsilon}_{in} = \boldsymbol{\varepsilon}_{th} + \boldsymbol{\varepsilon}_{sh} + \boldsymbol{\varepsilon}_{cr} \quad (16)$$

where  $\boldsymbol{\varepsilon}_{th}$ ,  $\boldsymbol{\varepsilon}_{sh}$  and  $\boldsymbol{\varepsilon}_{cr}$  denote strain tensors for thermal, shrinkage and creep strains, respectively.

#### 3.2 THERMAL STRAINS

Thermal strains occur when a concrete structure is subjected to a temperature change. The thermal strain tensor,  $\boldsymbol{\varepsilon}_{th}$ , is given in equation (17)

$$\boldsymbol{\varepsilon}_{th} = \alpha_T \mathbf{I} (T(t) - T_{ref}) \quad (17)$$

where,  $\alpha_T$  is the coefficient of thermal expansion for concrete, assumed to be  $1.1 \cdot 10^{-5}$  (1/K),  $\mathbf{I}$  is a unity tensor,  $T(t)$ , is the actual temperature (K), and  $T_{ref}$  is a reference temperature where the thermal stresses are assumed to be zero. The reference temperature was set to 9 °C which was the actual ambient temperature at the start of the simulation. This value was chosen in order to start the simulations with no thermal strains in the structure.

### 3.3 SHRINKAGE STRAINS

Shrinkage strains,  $\boldsymbol{\varepsilon}_{sh}(t)$ , are caused by differences in the concrete structure's moisture content, which changes with time. In this study,  $\boldsymbol{\varepsilon}_{sh}(t)$  is proportional to the current moisture content  $W$  (kg/m<sup>3</sup>), see equation (18)

$$\boldsymbol{\varepsilon}_{sh} = \left( \frac{W_i - W(t)}{W_i - W_\infty} \right) \mathbf{I} \boldsymbol{\varepsilon}_{sh,\infty} \quad (18)$$

where  $W_i$  represents the initial moisture content at 90% RH,  $W(t)$  represents the current moisture content (kg/m<sup>3</sup>) at time  $t$  (h),  $W_\infty$  represents the moisture content (kg/m<sup>3</sup>) at 50% RH,  $\mathbf{I}$  represents a unity tensor,  $\boldsymbol{\varepsilon}_{sh,\infty}$  represents the shrinkage strain at a reference moisture content of 50 % RH, which was estimated to 0.05% [18].

### 3.4 BASIC CREEP AND DRYING CREEP

Creep is modelled according to Eurocode 2 [9] using the creep coefficient  $\varphi_c(t, t_{0cr})$ , see equation (19)

$$\varphi_c(t, t_{0cr}) = \varphi_0 \cdot \beta_c(t, t_{0cr}) \quad (19)$$

where  $\varphi_0$  represents the notional creep coefficient, and  $\beta_c(t, t_{0cr})$  represents a coefficient that includes the evolution of creep with time after loading  $t_{0cr}$ .

The creep strain tensor,  $\boldsymbol{\varepsilon}_{cr}$ , is defined according to equation (20)

$$\boldsymbol{\varepsilon}_{cr} = \frac{\varphi_c(t, t_{0cr})}{E} \begin{bmatrix} \sigma_{11} - \nu(\sigma_{22} + \sigma_{33}) & 0 & 0 \\ 0 & \sigma_{22} - \nu(\sigma_{11} + \sigma_{33}) & 0 \\ 0 & 0 & \sigma_{33} - \nu(\sigma_{11} + \sigma_{22}) \end{bmatrix} \quad (20)$$

where  $\sigma_{xx}$  represents the current stresses in the material,  $E$  represents the elastic modulus, and  $\nu$  represents the Poisson ratio, set to 0.2, as mentioned previously. The elastic modulus was considered constant with time when simulating the mechanical behaviour of the RC. When simulating the scale effect of drying, the elastic modulus was time dependent when time dependent material properties were applied. Basic creep and drying creep was not modelled separately.

When evaluating the factor to allow for the effect of the relative humidity,  $\varphi_{RH}$ , according to Annex B in Eurocode 2 [9], it is suggested to use ambient RH as input data. However, ambient RH is not consistent between the exterior and interior of the RC; furthermore, it changes continuously. The factor,  $\varphi_{RH}$ , is suggested to change with the actual RH variations at the exterior and interior sides of the RC. Additionally, RH varies within the cross-sections of different concrete structures, which also likely affects the creep coefficient. In this study, the RH at each node point in the mesh was utilized as input data for the evaluation of  $\varphi_{RH}$ . This resulted in a creep coefficient that varies from the surface to the centre of the material, in correspondence with the internal variations of RH. This is a deviation from the suggestion in Eurocode 2. The notional size,  $h_0$ , was set to 400 mm, which corresponds to the thickness of the cylinder wall.

## 4 Tendons

### 4.1 TENDON PRE-STRESSING

The tendons (cement grouted) are pre-stressed in a carefully designed order. The pre-stressing is considered completed 106 days after the completion of the RC, which is 384 days after beginning the casting of the raft. Pre-stressing of all tendons takes about 3 months to complete.

The tendons are oriented in different directions and spans over different parts of the RC and are not equally distributed around the RC. This means that the magnitude of the resulting stresses is not uniformly distributed. The number of horizontal tendons, spanning the circumference of the RC, is larger. The vertical distance between the horizontal tendons is on average smaller (around 0.15 m) compared to the average distance between the vertical tendons (around 0.3 m), see Figure 4.1 and Figure 4.2. This means that the horizontal stresses are larger than the vertical stresses.



Figure 4.1 An overview of the tendon arrangement used in the RC.

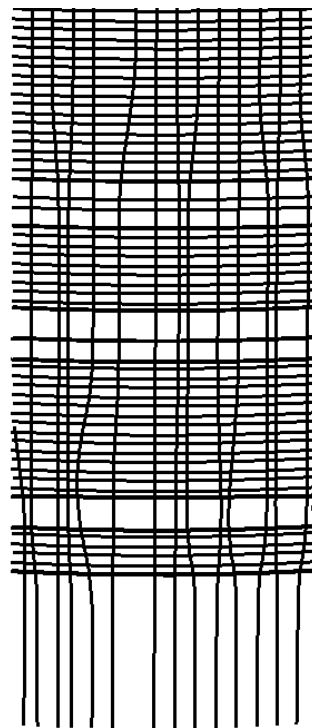


Figure 4.2 A detail of the tendons near the lower part of the RC.

The tendon configuration was provided from benchmark VERCORS 2022.

Apart from the differences in distribution of tendons, the resulting stresses in the tendons are also affected by other parameters, e.g. friction and wobbling effects. Friction has a smaller effect on straight tendons. However, since a large part of the

tendons are slightly curved, friction has a significant effect on the stresses. According to EC2, the curvature does not affect the wobbling effect. This means that the stress becomes higher in the straight vertical tendons compared with the curved tendons in the dome, vertical tendons that extends through the dome and the horizontal tendons in the cylindrical wall.

The strains are assumed to be zero at day 278, which represents the day of completing the RC. The exact response of each tendon during pre-stressing is not relevant in this simulation. The concrete in the RC is modelled with a linear elastic material model, while the tendons are modelled with a perfectly elastoplastic material model. As a simplification of the modelling approach, the principal of superposition is applied. This means that the final result is not affected by the exact pre-stressing sequence. This technique has been applied in a number of different projects with adequate results [19, 20].

The stress in the tendons has been evaluated according to a method that accounts for the stress distribution along the tendon and includes stress losses due to friction, end slip (8 mm), creep, relaxation (2.5%) and shrinkage [19].

The tensile force in the horizontal tendons decreases significantly with the distance from the anchorage. However, since these tendons are placed with an overlap, a relatively uniform constant tensile force is still obtained in the cylindrical wall [19]. An example of an evaluated tensile force according to Eriksson et al. [19] and how it is assumed to vary in a horizontal tendon in the cylindrical wall is shown in Figure 4.3. An average force of 611 kN in each tendon is used in the simulation.

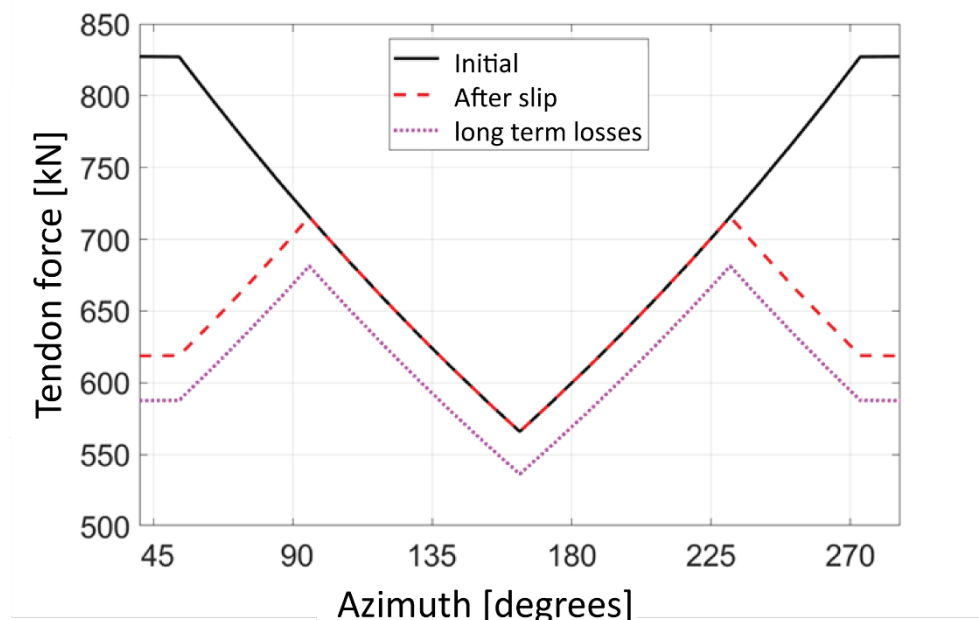


Figure 4.3 Tendon forces along the cylindrical wall after losses

Since the horizontal tensile force is assumed to be evenly distributed around the circumference of the RC, the stresses also become evenly distributed. The assumption of an average tendon force along the tendons does not affect the

accuracy in a global model if the stresses in the tendons are below the yield stress [20]. If concrete failure and cracking is considered, it may be important to consider the real stress distribution. Concrete failure and cracking are not considered in this study, and therefore the tensile force along all tendons has been assumed to be constant.

In this study, the pre-stressing procedure has been simplified and all tendons are simultaneously tensioned. This is not the case in reality, where tendons are pre-stressed in a special order. The pre-stressing has been modelled by gradually increasing the tendon stresses from a non-stressed condition up to a fully stressed condition, see Figure 4.4.

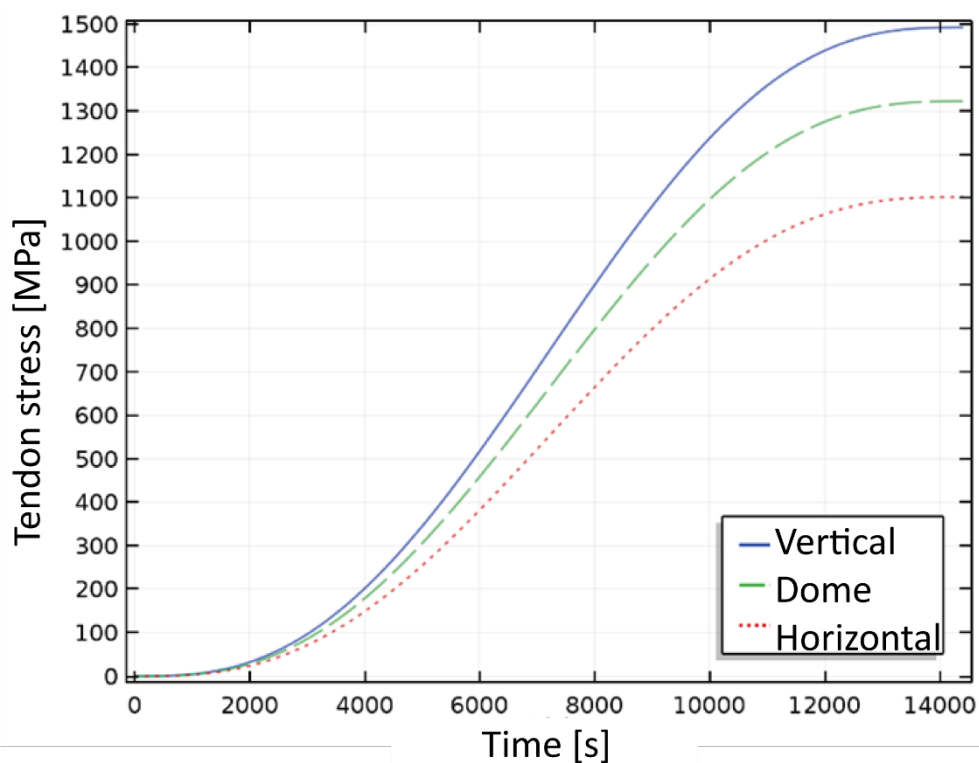


Figure 4.4 Tendon pre-stressing as a function of time

The pre-stressing magnitude in MPa as a function of time, is shown for the three different tendon types, vertical, dome and horizontal tendons. The pre-stressing of the cables increases gradually in order to prevent convergency problems. The duration of pre-stressing is assumed to be 14400 seconds, which is equal to 4 hours, see Figure 4.4. The pre-stressing in the vertical tendons is about 1500 MPa, (corresponds to 834 kN), dome tendons 1350 MPa (corresponds to 750 kN) and 1100 MPa (corresponds to 611 kN) in the horizontal tendons.

## 4.2 TENDON MODEL

In this study a perfect bond was assumed between the tendons and the concrete. This assumption is based on the fact that all tendons are grouted and therefore are physically bonded to the concrete.

The tendons were modelled as an ideal elastoplastic material, see Figure 4.5, with a yield strength,  $\sigma_Y$ , equal to 1620 MPa see Table 2.2.

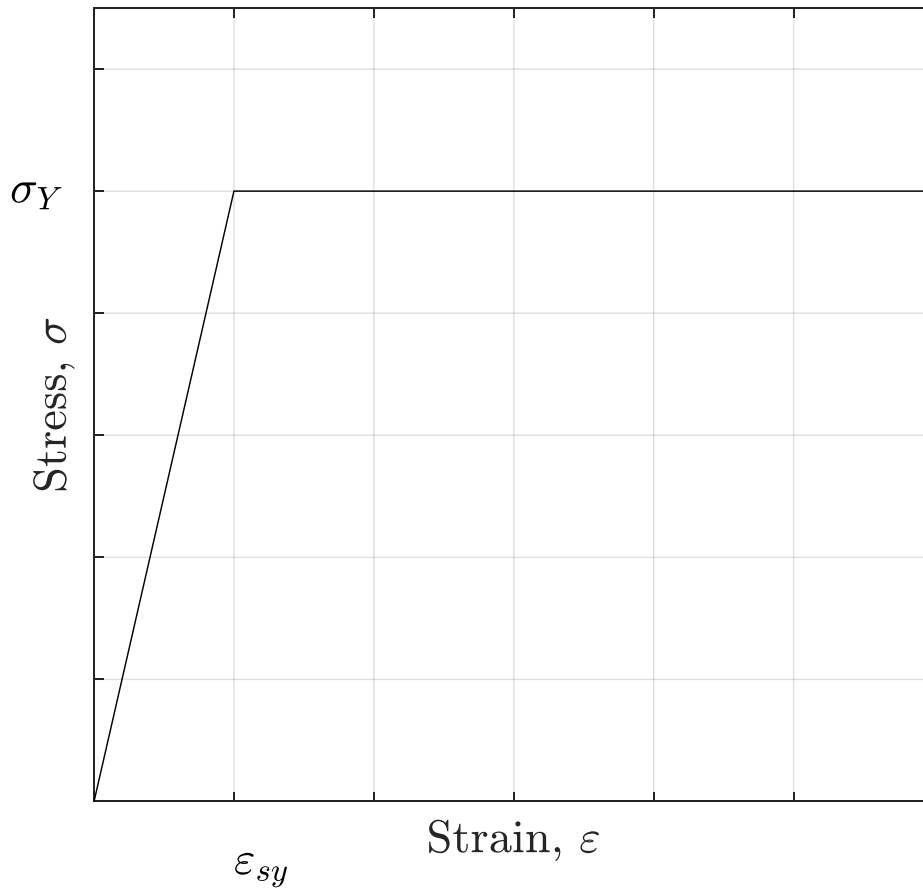


Figure 4.5 Illustration of the stress-strain diagram used for the tendons

## 5 FE models

### 5.1 CASE STUDIES

Four different case studies were performed in this project:

- 1) Analysis of the long-term mechanical behaviour of the RC in 1:3 scale (constant concrete properties).
  - a) On a cut out wedge, 45° angle, of the RC geometry.
  - b) On the complete RC geometry.
- 2) Air leakage through the RC (constant concrete properties).
- 3) Analysis of the influence of the scale effect of drying (both using constant mechanical and moisture properties and using time dependent properties including heat generation and self-desiccation).

### 5.2 GEOMETRY

The complete geometry was provided by benchmark VERCORS 2022. It was provided as a collection of Initial Graphics Exchange Specification files, IGES files. IGES files is a common file format used for the exchange of 2D and 3D computer aided design, CAD, data between different CAD software applications. COMSOL is able to import such files. Unfortunately, these files are not accessible from an internet source. The used geometries were adopted to the different studies outlined in section 5.1. The geometries were extracted from the complete 3D geometry to fit the important aspects of the study.

#### 5.2.1 Mechanical long-term

Two 3D geometries were used in the mechanical analysis. The two geometries corresponded to 1a) a cut out wedge, 45° angle, of the actual RC structure and 1b) the complete RC structure. Both these only included the inner concrete shell with pre-stressed tendons. The outer concrete shell was not included in the simulation. The outer shell has no significant impact on the structural behaviour of the inner shell.

The wedge geometry consisted of a solid 3D structure and did not include any penetrations, such as equipment hatches or other large openings. This wedge geometry was chosen in order to reduce the complexity of the FE-modelling and to reduce calculation time.

The complete RC geometry included every part of the RC including large penetrations and other local irregularities. An example of an irregularity is the extra thick wall around the equipment hatch. This geometry was used to investigate if the wedge geometry used in the earlier studies was an appropriate simplification of the total geometry.

The main reason for using a 3D geometry was to be able to describe the structural response to both the horizontal and vertical tendons in the RC wall and the dome. A 2D geometry could be used if the vertical or horizontal tendons were evenly distributed in the RC wall.

The total height of the geometry was about 21 m, the inner radius 7.3 m, and the cylinder wall thickness was 0.4 m. The thickness of the raft was about 4.5 m. The cut-out wedge geometry used in case study 1a, is shown in Figure 5.1.

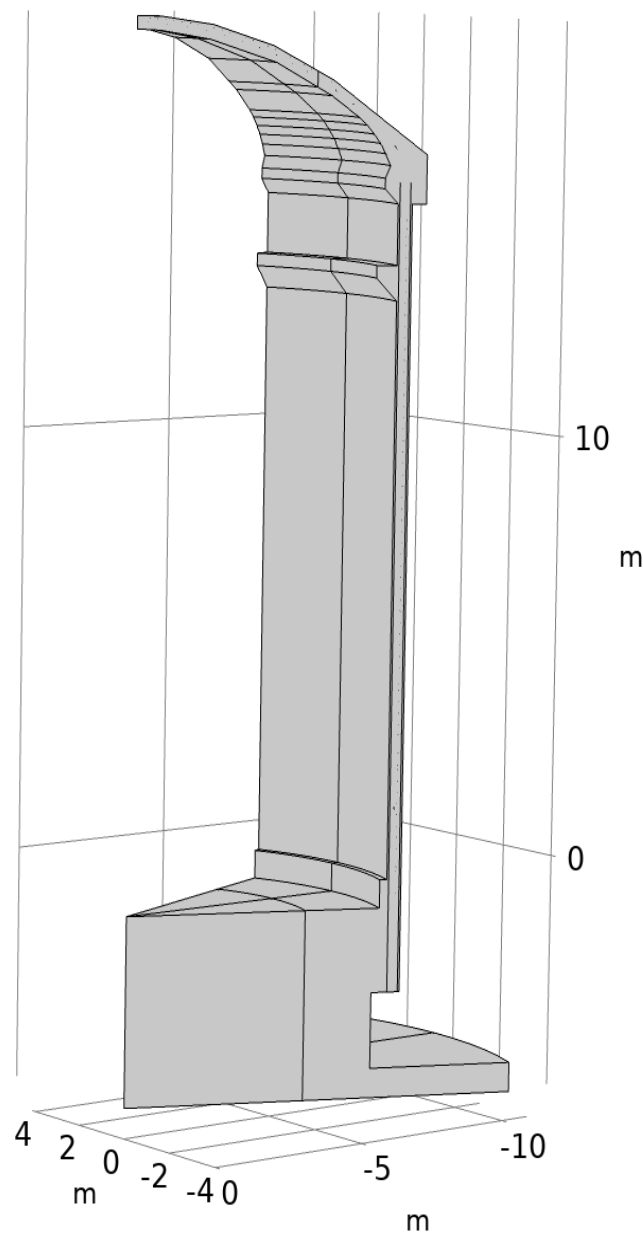


Figure 5.1 The 3D geometry used for the wedge simulation of the reactor containment.

All tendons of the wedge geometry were arranged and configured according to Figure 5.2.

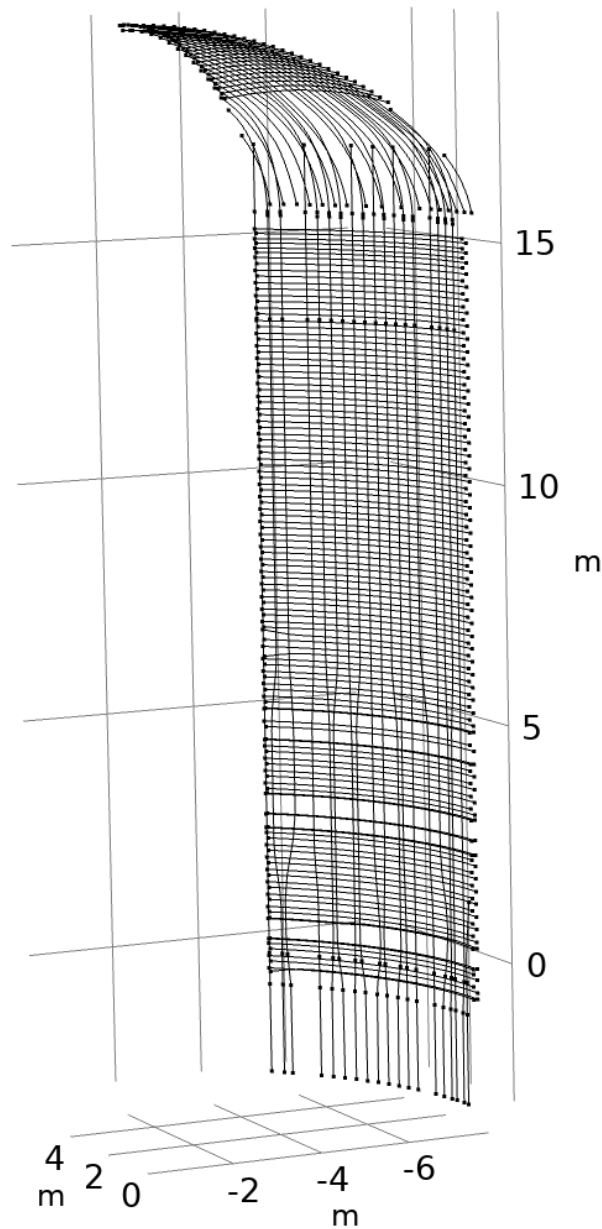


Figure 5.2 The arrangement of the tendons used in the wedge simulation.

Note that many of the tendons were cut at the boundaries of the solid geometry. The tendons needed to be cut because of the 3D wedge geometry used for the concrete. The tendon arrangement included in the model is from a part of the RC that does not contain any penetrations. Hence, the tendons are rather uniformly distributed through the geometry.

The frontside view of the complete geometry and the tendon configuration used for study case 1b are shown in Figure 5.3 and Figure 5.4.

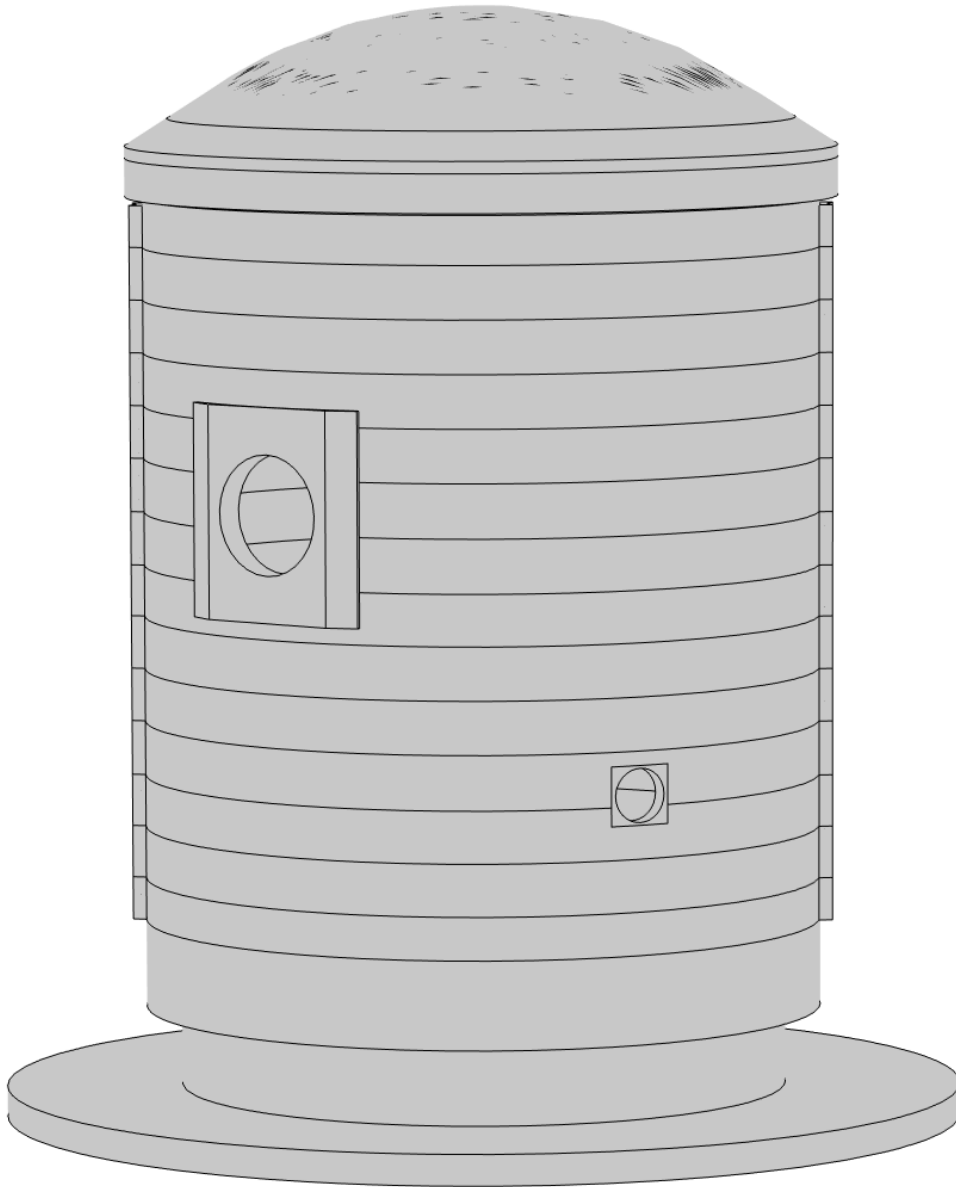


Figure 5.3 Front side view of the complete geometry

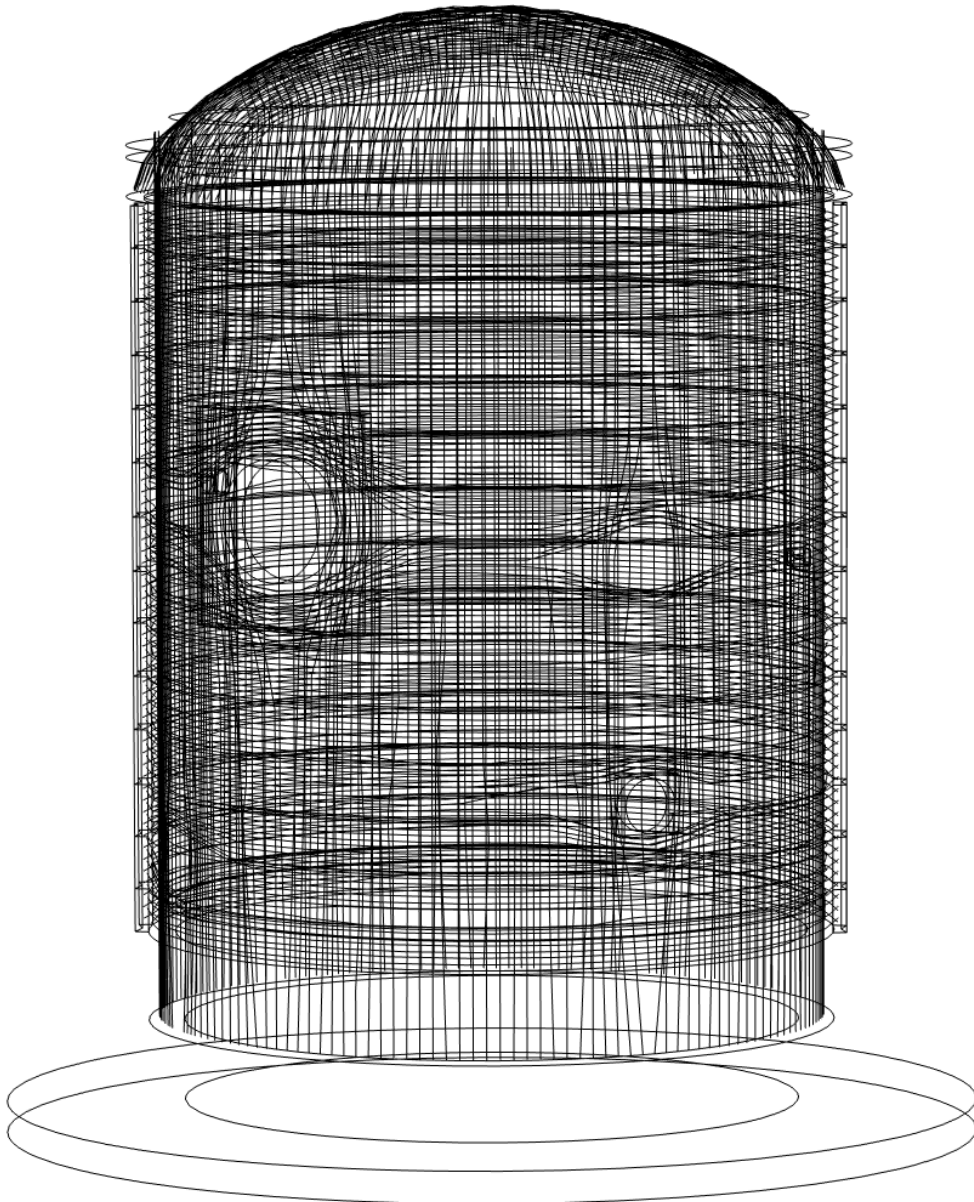


Figure 5.4 Front side view of the tendon configuration.

The back side view of the complete geometry and the tendon configuration used for study 1b are shown in Figure 5.5 and Figure 5.6.

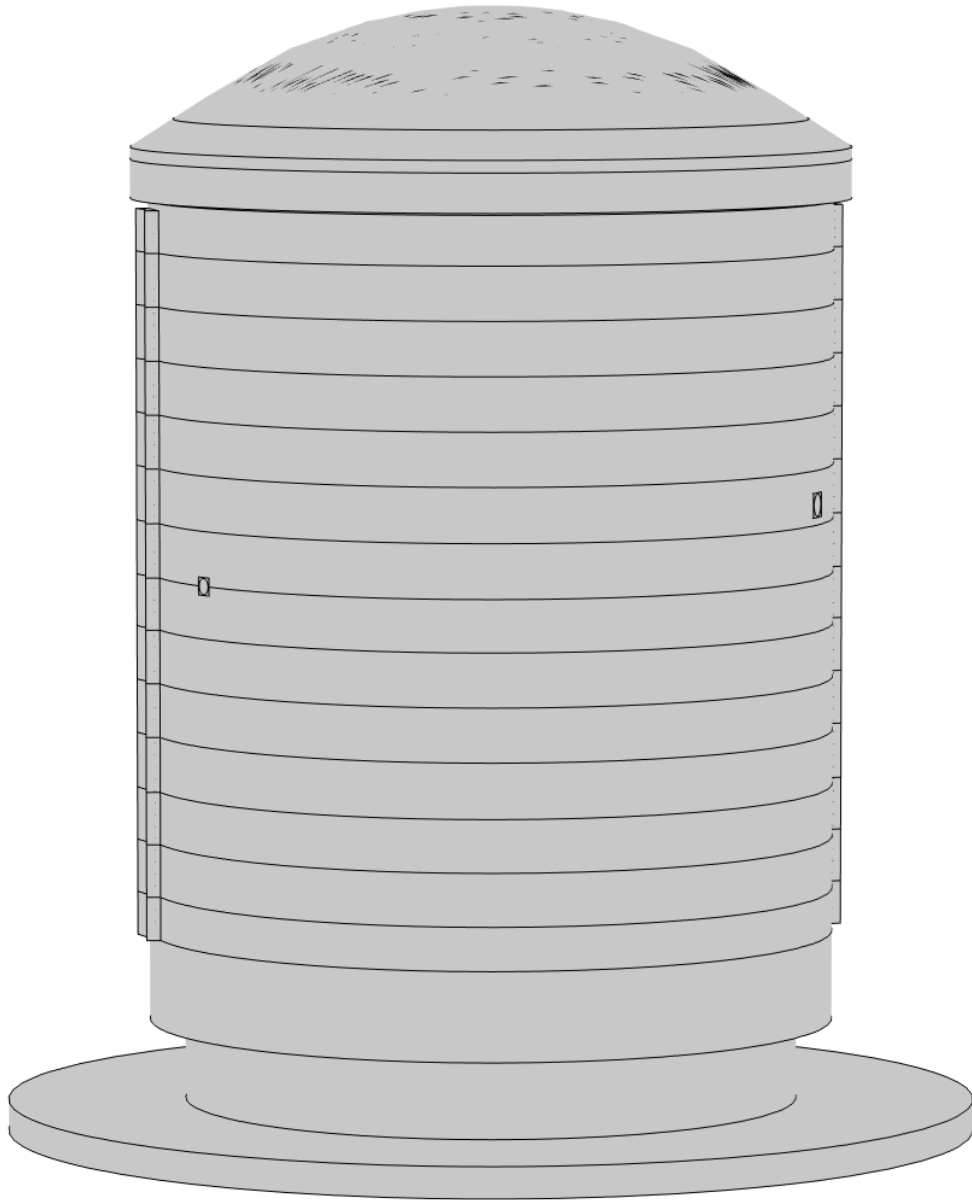


Figure 5.5 Back side view of the complete geometry

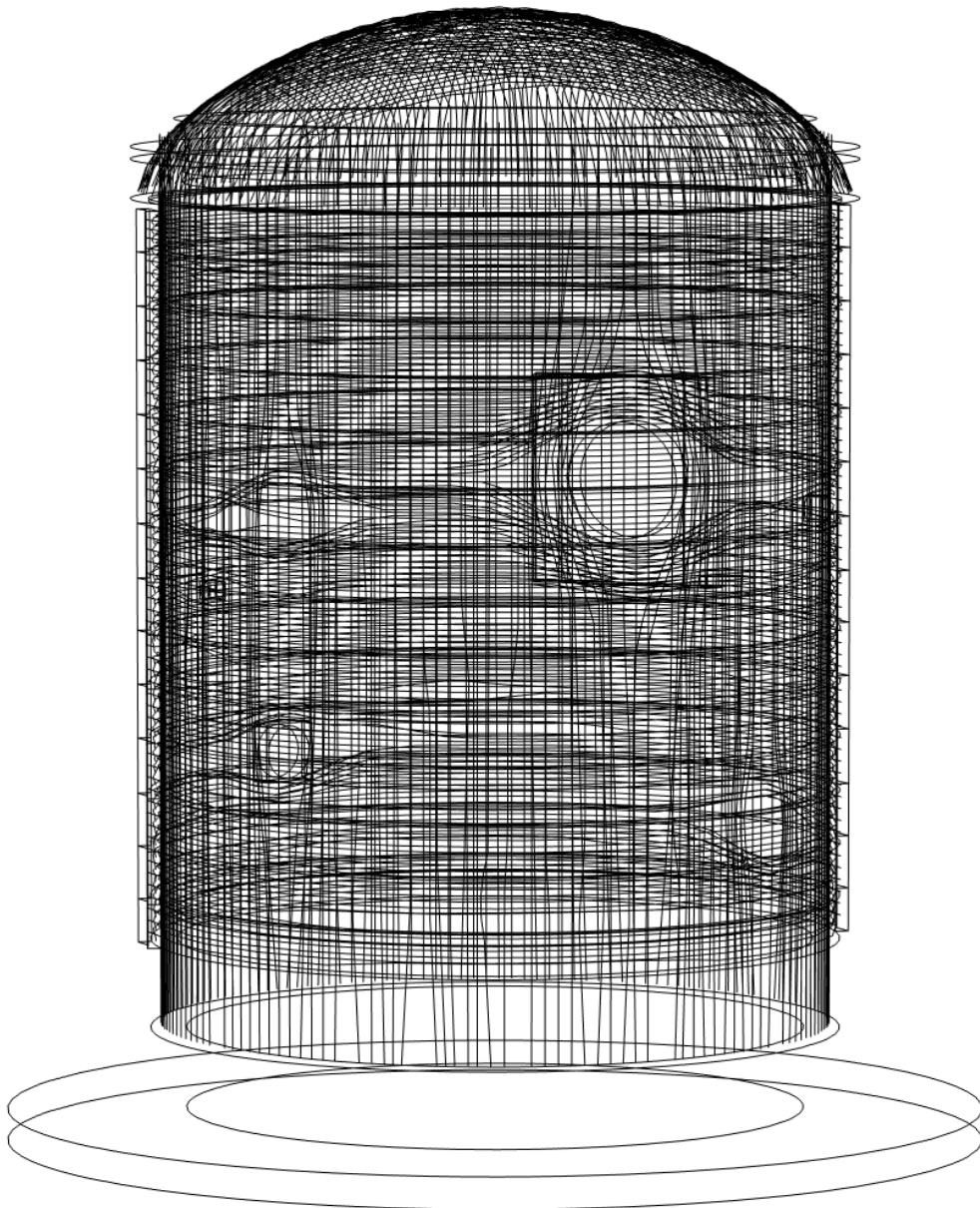


Figure 5.6 Back side view of the tendon configuration

### 5.2.2 Air leakage

The 2D geometry used for the air leakage simulation corresponded to a cross section of the 3D geometry, see Figure 5.7.

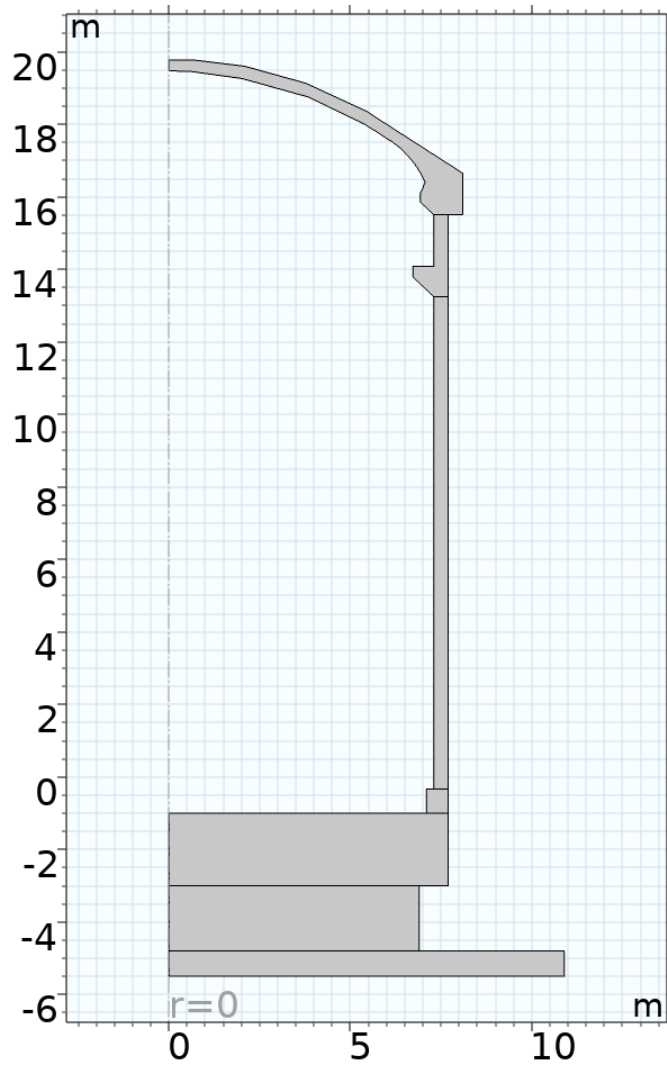


Figure 5.7 Geometry used to study air leakage through the RC.

Note that the cross section was chosen from a part that exhibited a uniform wall thickness, except from the gusset.

### 5.2.3 Scale effect of drying

The geometry used for analysing the influence of the scale effect of drying, was a cut-out of the cylindrical wall, Figure 5.7. A 3D geometry was used to investigate tangential stresses caused by shrinkage.

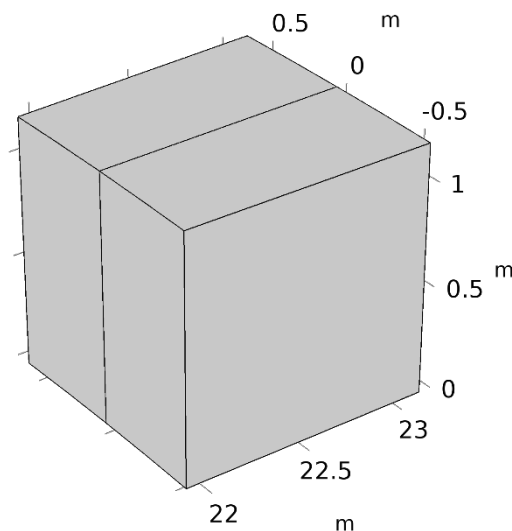


Figure 5.8 Geometry used for studying the influence of scale effect of drying.

Figure 5.8 shows the geometry when the scale was set to 3, which is equal to the size of a real RC. The purpose was to study possible differences between drying of a 1:3 scale containment compared with a real RC. Such a difference may have an impact of tensile stresses in the tangential direction. Note that the geometry was not shaped as a perfect cube, it was in fact shaped as part of a cylinder wall. The inner radius of the cut-out was about 22 m, and the outer radius was about 23.2 m, when the scale was set to 3. In the parametric study, the geometry was changed such that the radius, height, and width was dependent on the scale.

## 5.3 MESHES

The four meshes used in the studies are described in detail in sections 5.3.1 to 5.3.4. Other meshes were provided from the VERCORS organization; however, due to compatibility issues, importing them into COMSOL was not feasible. The provided meshes are available for download [21].

### 5.3.1 Wedge geometry

The solid 3D mesh used for the heat transfer, moisture transfer and the two solid mechanics simulations, see chapter 6, consisted of 47 k hexahedrons and 800 prisms. The number of degrees of freedom in the heat and moisture transfer model was 55 k, while the solid mechanics model resulted in 165 k degrees of freedom. The average length of the hexahedrons is approximately 0.5 m.

Linear solid elements with full integration were used, such elements are proper to use when analysing long-term deformations in concrete structures. The mesh was created by applying an unstructured quadrilateral mesh on the boundaries of the 3D geometry built in COMSOL [22]. This mesh was swept in a tangential direction across the geometry, hence dividing the wedge geometry in 10 smaller wedges. A boundary mesh was applied on the surfaces subjected to varying temperature and humidity.

The dome mesh is shown in Figure 5.9.

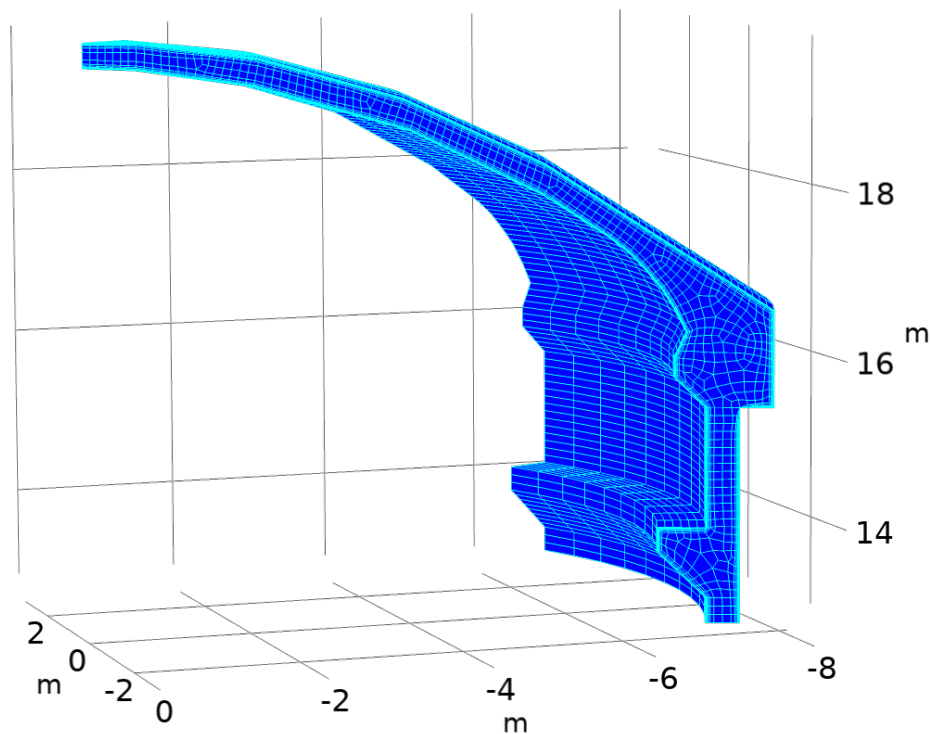


Figure 5.9 Illustration of the mesh of the dome.

The mesh close to the surface is denser than in the central parts of the geometry. This distribution was applied since sharp gradients in terms of relative humidity are expected close to the surfaces. The mesh of the cylinder wall and raft is shown in Figure 5.10.

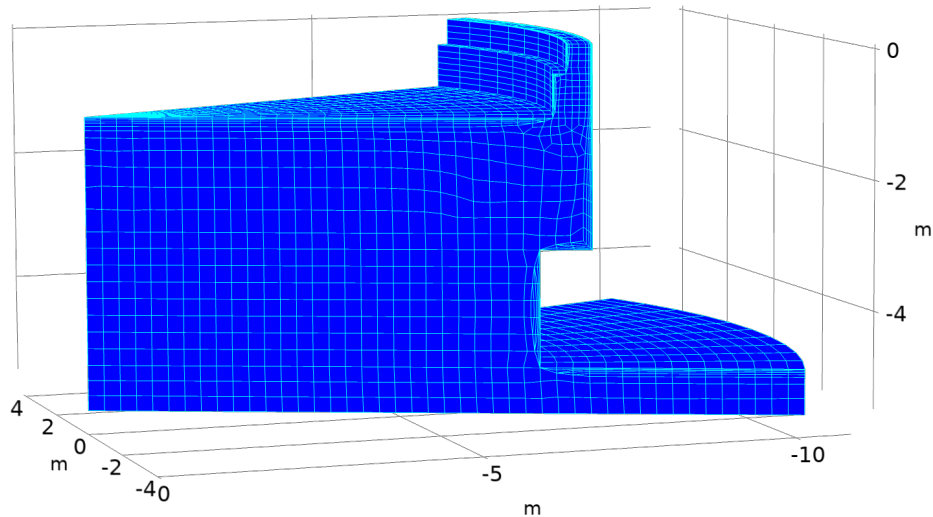
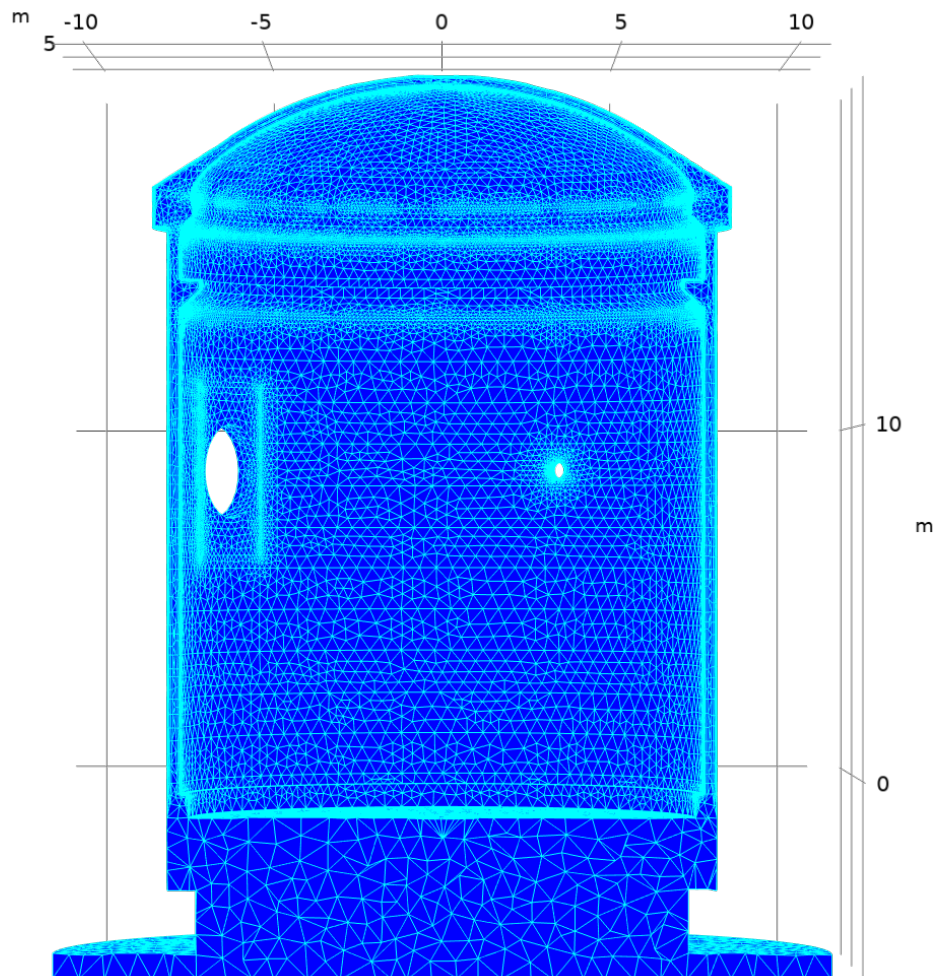


Figure 5.10 Illustration of the mesh at raft and the lower part of the cylinder wall.

The tendons were modelled with linear truss elements with a mean length of approximately 0.5 m. The truss element length was chosen to approximately follow the curvature of the dome without introducing sharp corners between each element.

### 5.3.2 Complete RC geometry

Two different meshes were used for the complete RC geometry. These two meshes were used to reduce the total calculation time. One mesh was used to calculate temperature, relative humidity, and the first solid mechanics part of the simulation, see section 6.1. This mesh is shown in Figure 5.11 and a detail of that mesh is shown in Figure 5.12. The other mesh used to calculate the creep is shown in Figure 5.13 and a detail of that mesh is shown in Figure 5.14.



**Figure 5.11** Illustration depicting the mesh employed for temperature, relative humidity, and the initial solid mechanics component calculations.

The mesh consisted of around 400 k tetrahedrons, 340 k prisms and 750 k elements in total. Linear solid elements with full integration were used and the mesh was created by using COMSOL Multiphysics option “Free tetrahedral”, which is an unstructured tetrahedral mesh. The configuration is not important when analysing linear elastic structural behaviour. The initial part of solid mechanics involved 805 k degrees of freedom and is described in section 6.1.

A maximum element size of 0.5 meters was used for the cylindrical wall and dome. The maximum element mesh size in the raft, was set to around 0.9 m. Additionally, five boundary layers were applied to both the interior and exterior surfaces of the cylinder wall and the dome. The decision regarding the number of boundary layers was influenced by the anticipated sharp gradients in relative humidity near these surfaces. Using smaller elements improves precision but increases computation times, while choosing larger elements may decrease computation time but could potentially compromise the accuracy of the solution.

A detail of the mesh at the dome is shown in Figure 5.12.

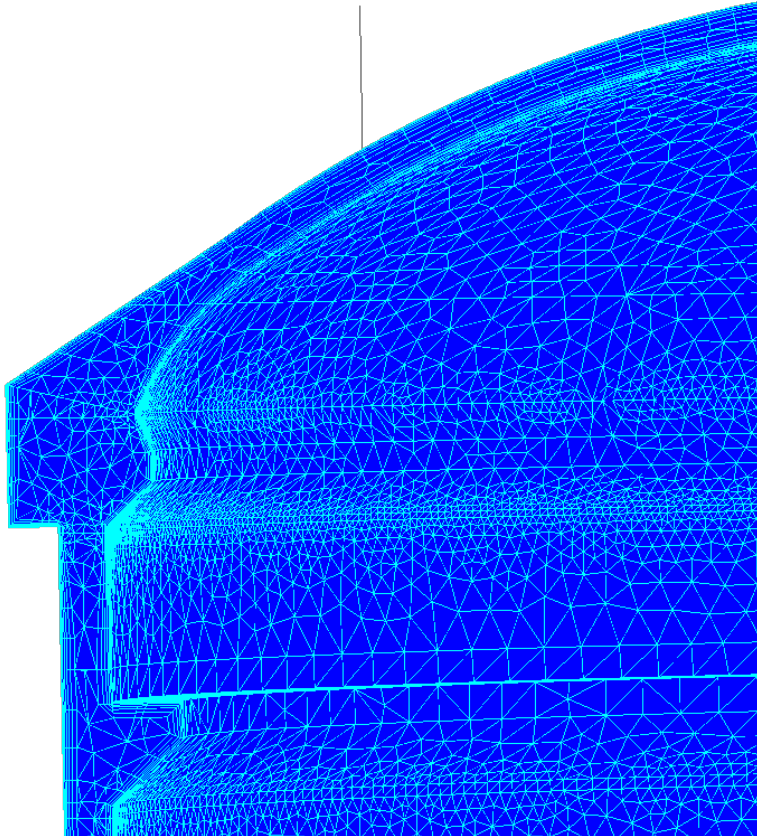


**Figure 5.12** Detail of the mesh employed at the dome for the first solid mechanics calculation.

The detail of the mesh at the dome shows solid elements and the five boundary layers at the boundary surfaces.

The mesh for the second solid mechanics part of the simulation, creep, is shown in Figure 5.13. It is reduced compared with the first solid mechanics' part. The mesh was reduced to decrease the degrees of freedom from 12.4 M down (same mesh as employed in the first solid mechanics part) to 2.3 M (reduced mesh compared with the first solid mechanics part).

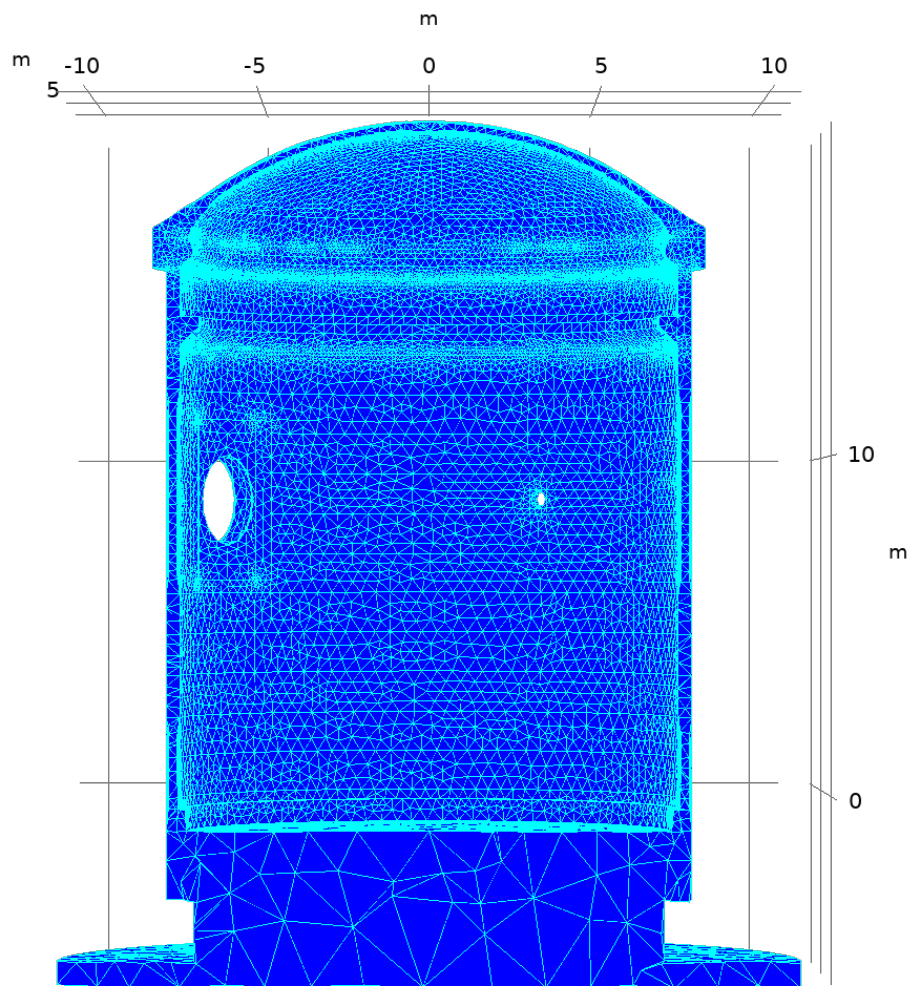


**Figure 5.13** Illustration depicting the mesh employed for the second solid mechanics component calculations.

The mesh consisted of around 310 k tetrahedrons, 55 k prisms and 371 k elements in total. Linear solid elements with full integration were used and the mesh was created by using COMSOL Multiphysics option “Free tetrahedral”, which is an unstructured tetrahedral mesh. The configuration is not important when analysing linear elastic structural behaviour. The second part of solid mechanics involved 2.3 M degrees of freedom; this part is further discussed in section 6.1.

A maximum element size of 0.9 meters was used for the cylindrical wall and dome. The maximum element mesh size in the raft, was set to around 2.7 m. Around the penetrations the maximum mesh element size was 0.2 m.

A detail of the employed mesh for the second solid mechanics part, creep, is shown in Figure 5.14.

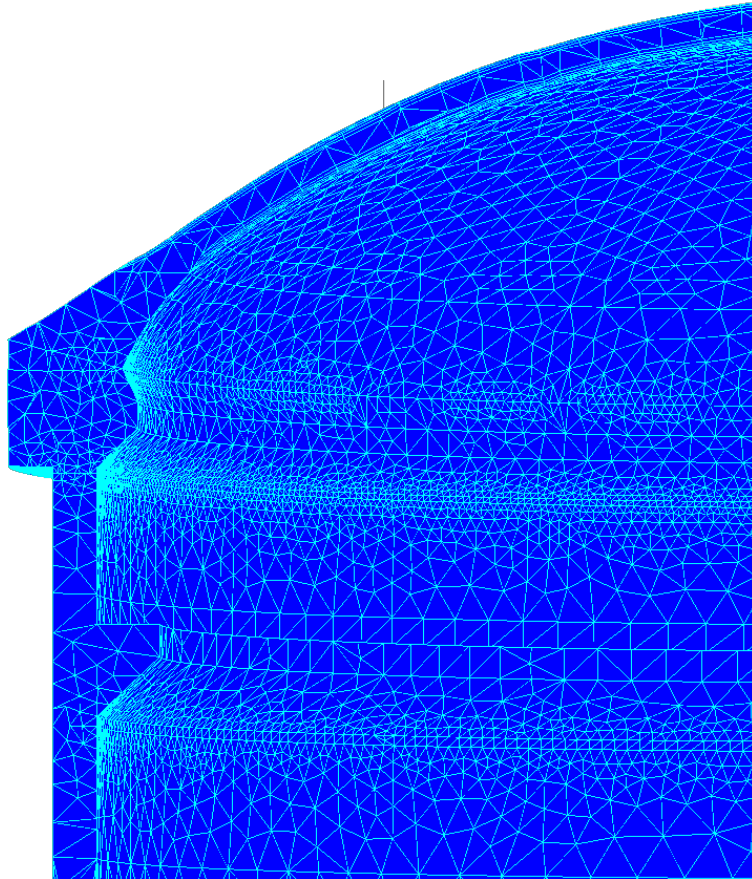


**Figure 5.14** Detail of the mesh employed at the dome for the second solid mechanics calculation.

The detail shows areas (dome) where an additional three boundary layers were added to the mesh. These boundary layers were also added to some parts of the cylindrical wall.

The tendons were modelled with linear truss elements with a mean element length of approximately 0.5 m in both of these solid mechanics parts.

### 5.3.3 Scale effect of drying

The mesh used in the study of the scale effect of drying and temperature variations is shown in Figure 5.15.

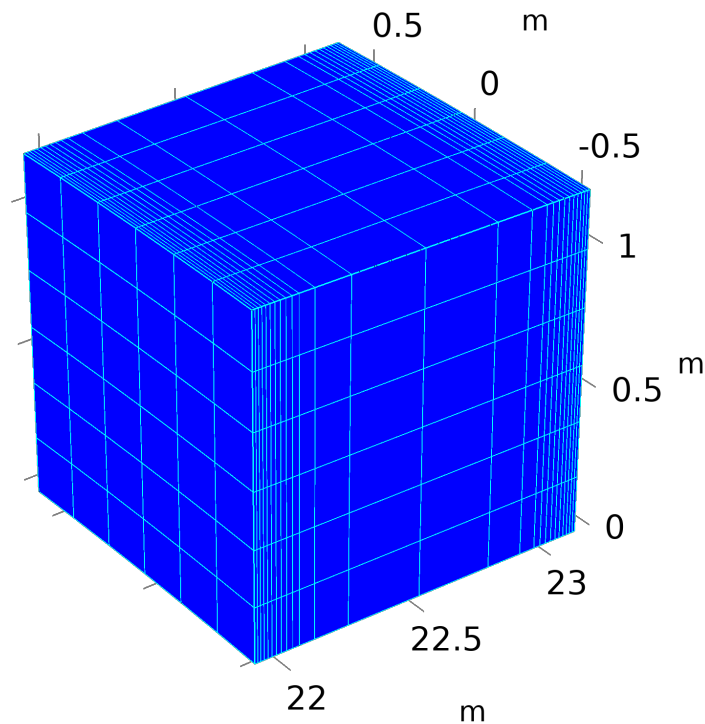


Figure 5.15 Illustration of the mesh used for the simulation of the scale effect of drying.

The mesh was generated as a structured hexahedral. The mesh close to the boundary surfaces was denser compared with the central parts. This high density at the surface was selected because a sharp moisture gradient was expected at the surface of the concrete wall. The boundary surface of the geometry was divided into 6 by 6 equally sized squares. There were ten boundary layers at each boundary surface subjected to the interior and exterior climate.

#### 5.3.4 Air leakage mesh

A 2D geometry was used to evaluate the air leakage. Such an approach was selected in order to reduce the computation time.

The mesh was created by applying an unstructured quadrilateral mesh on the 2D geometry built in COMSOL. A boundary layer was applied at the surface of the cylinder wall to be able to capture sharp gradients close to the boundaries. Illustrations of the 2D mesh used for the leakage simulation are shown in Figure 5.16 and Figure 5.17.

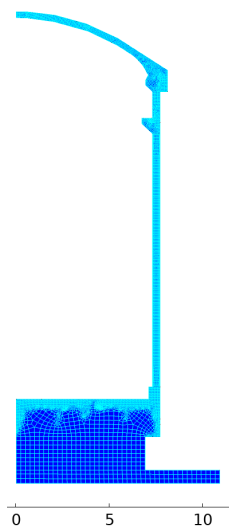


Figure 5.16 Illustration of the 2D mesh used for the leakage simulation.

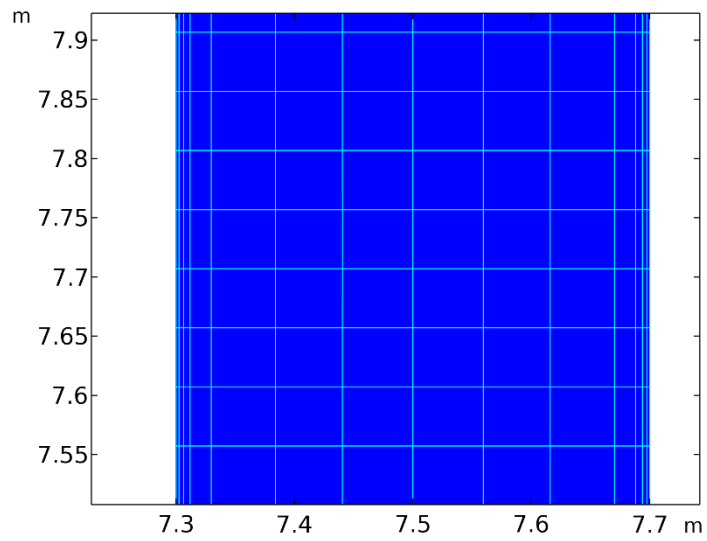


Figure 5.17 Detail of mesh at the cylinder wall.

The 2D mesh consisted of 9000 quadrilateral elements with a maximum element size of 0.05 m.

#### 5.4 HEAT TRANSFER MODEL

The heat transfer in the concrete was modelled using the ordinary heat equation, see equation (21)

$$\rho C_p \frac{\partial T}{\partial t} = \nabla \cdot (\lambda \mathbf{I} \nabla T) + Q_h \quad (21)$$

where  $\lambda$ , represents the heat conductivity in W/mK,  $\mathbf{I}$ , is a unity tensor,  $Q_h$  is a source term that represents the heat generated by the exothermic chemical reaction when the cement is reacting with the mixing water. The source term,  $Q_h$ , was used when analysing the scale effect of drying, see section 6.3.  $Q_h$  was described by using equation (22) [23]

$$Q_h = Q_\infty \cdot \alpha_c \cdot C \quad (22)$$

where  $Q_\infty$  is the total heat of hydration of the cement, assumed to 500 kJ/kg,  $\alpha_c$  is the degree of hydration, and  $C$  is the cement content (kg/m<sup>3</sup>) in the concrete. The other studies started when concrete was over 6 months old. At that age the heat generation is insignificant.

#### 5.5 MOISTURE TRANSFER MODEL

The moisture flow,  $\mathbf{q}_m$  (kg/m<sup>2</sup>s), is modelled as a diffusion process of moisture described by Fick's first law as in equation (23)

$$\mathbf{q}_m = -\delta_\varphi \mathbf{I} \nabla \varphi \quad (23)$$

where  $\delta_\varphi$  (m<sup>2</sup>kg/sm<sup>3</sup>) represents the moisture transport coefficient, and  $\varphi$  (-) represents the relative humidity, RH.

The change of moisture content with time,  $\frac{\partial W}{\partial t}$ , in kg/(s·m<sup>3</sup>) is obtained from the conservation of mass according to equation (24).

$$\frac{\partial W}{\partial t} = \frac{\partial W_e}{\partial \varphi} \frac{\partial \varphi}{\partial t} = \nabla \cdot (\delta_\varphi \mathbf{I} \nabla \varphi) + Q_m \quad (24)$$

where  $\frac{\partial W}{\partial \varphi}$  represents the moisture capacity of the concrete. The moisture capacity is equal to the ratio between change of moisture content to the change of RH (kg/m<sup>3</sup>).  $Q_m$  is a source term that represents the self-desiccation. The source term,  $Q_m$ , was not considered in the mechanical long-term study and the air leakage study since the concrete was considered as mature and more than six months old at the start of the simulation. Self-desiccation is a form of drying that takes place when the cement reacts with the mixing water. The moisture then becomes chemically bound to the cement paste structure and is thereby no longer affected by diffusion caused by changes in air humidity.

The initial moisture condition in the RC was assumed to be 90% RH as a consequence of the cement's chemical binding of moisture in the concrete, which had a water cement ratio of 0.62.

The source term,  $Q_m$ , was used when analysing the scale effect of drying, i.e., outlined in section 6.3. The scale effect of drying was only applied on a cut out part of the cylinder wall not the complete RC. The self-desiccation was described as stated in equation (25)

$$Q_m = 0.25 \cdot \alpha_c \cdot C \quad (25)$$

where, 0.25 represents the assumed mass ratio of water chemically bound to the cement, and  $C$  is the mass of cement in each  $m^3$  of concrete [15]. The other studies started when concrete was over 6 months old. At that age the heat generation is insignificant.

Sorption hysteresis exhibited by concrete in wetting-drying cycles was not considered in the analysis (not relevant).

## 5.6 AIR TRANSPORT MODEL

The leakage rate through the concrete is modelled using a generalized form of Darcy's law, where the air flux,  $\mathbf{q}_{air}$ , is modelled with Darcy's law see equation (26)

$$\mathbf{q}_{air} = -\frac{\kappa_p}{\mu} \mathbf{I} \nabla p \quad (26)$$

where,  $\kappa_p$ , represents the effective air permeability,  $\mu$ , represents the dynamic viscosity in Pa·s, and  $p$  represents the air pressure in Pa. Diffusive air transport is not included.

An important prerequisite for equation (25) to be applicable is that the density of the air is close to constant i.e., the air density does not change significantly with the pressure. If the pressure is significant and a large pressure gradient exists equation (25) is no longer applicable.

The mass balance of air in the concrete is expressed according to equation (27)

$$\frac{\partial}{\partial t} (\epsilon_p \rho_{air}) + \nabla \cdot (\rho \mathbf{q}_{air}) = 0 \quad (27)$$

where,  $\rho_{air}$ , represents the density of the air in  $kg/m^3$  that varies with the actual pressure and  $\mathbf{q}_{air}$  represents the flow density for the air in  $m/s$ . This is a simplification since all terms related to the degree of air saturation in the pore network are not included.

Equation (26) is applicable if no part of the air is physically bound to or released from the inner surfaces of the material or to the pore solution. In pressure tests with a short duration -and at moderate pressures below the design limits when the structure behaves elastically - this binding or release was assumed insignificant.

The benchmark VERCORS pressure tests were performed at a maximum over pressure of 4.2 bar, and in such a case the air density, see equation (2), changes from  $1.2 kg/m^3$  to about  $5 kg/m^3$  (it is thus not nearly constant) which is considered in the model.

In short, equation (26) states that the flow of a substance into a porous material is equal to the outflow from the porous material, which usually is called the equation of continuity or the mass balance equation.

The continuity equation for the air with consideration of the air density and equation (26) inserted can be rewritten into equation (28)

$$\frac{\partial}{\partial t}(\epsilon_p \rho_{air}) + \nabla \cdot \left( \rho \left[ -\frac{\kappa}{\mu} \mathbf{I} \nabla p \right] \right) = 0 \quad (28)$$

Since the concrete is more than 6 months old at the start of the simulation, the porosity was considered constant during the simulation. This simplification was considered to have an insignificant impact on the air transport.

## 5.7 BOUNDARY CONDITIONS

### 5.7.1 Mechanical long-term case study

The applied mechanical boundary conditions regarding the wedge study are shown in Figure 5.18.

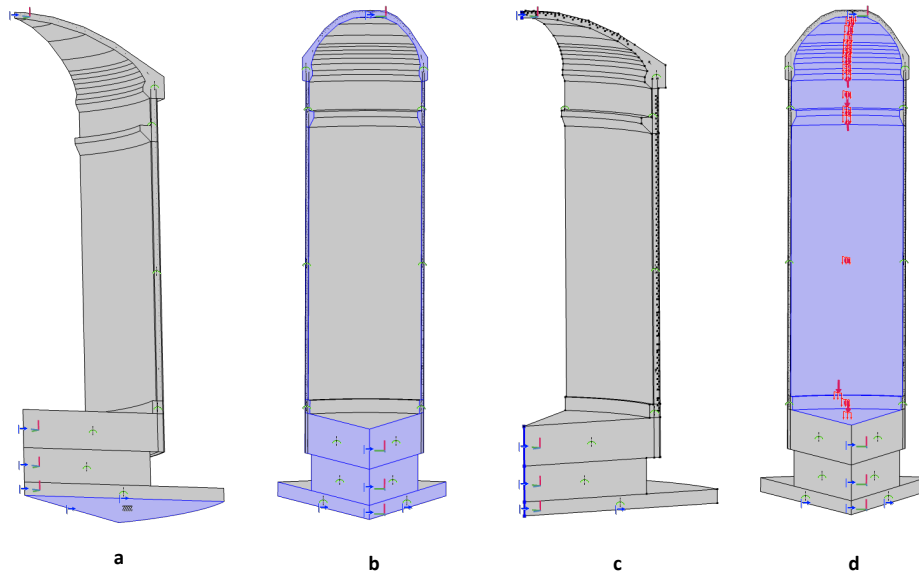


Figure 5.18 Mechanical constraints used in the analysis

A fixed constraint was applied on the bottom surface of the raft, see blue surface in Figure 5.18a. The two vertical sides of the geometry had a symmetry condition, see blue surfaces in Figure 5.18b. A prescribed displacement condition set to zero in the x- and y-direction was applied on the vertical axis at the centre of the geometry, see blue vertical line to the left in Figure 5.18c. Finally, a pressure load with a magnitude corresponding to the pressure test was applied on the inner surface, see blue surface in Figure 5.18d.

The mechanical boundary conditions for the complete RC study were analogue to those applied on the wedge study, see Figure 5.18a and Figure 5.18d, except for those not applicable, Figure 5.18b and Figure 5.18c.

The regular pressure tests were performed according to the pressure sequence shown in Figure 5.19.

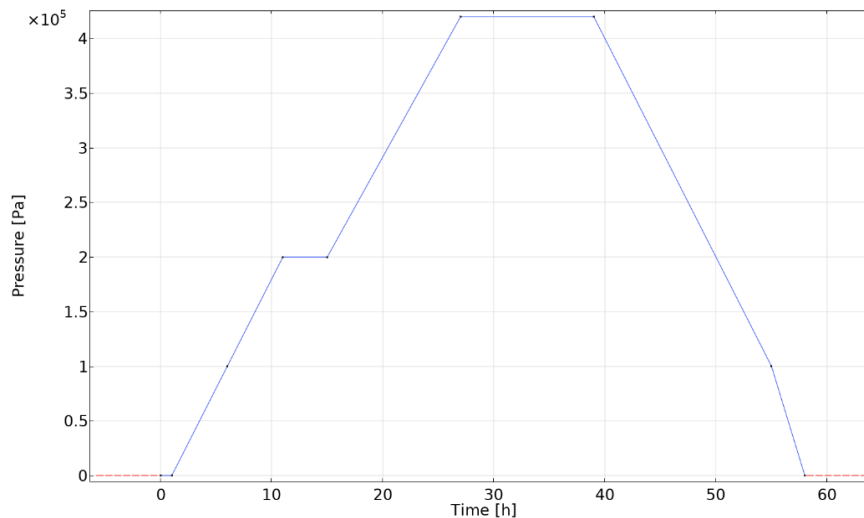


Figure 5.19 Regular pressure test.

The pressure is shown as the relative pressure on the y-axis and the time is shown on the x-axis. These regular pressure tests were to be performed according to the time schedule shown in Table 5.1. Note that pressure test VD 4 was cancelled due to Covid.

Table 5.1 Time plan for pressure tests

Pressure test	Date	Days after beginning of raft casting	Time in years and month after raft casting
Pré op	2015-11-05	469	1 year 3 months
VC1	2016-01-26	551	1 year 6 months
VD1	2017-03-14	964	2 years 8 months
VD1 bis	2017-03-21	971	2 years 8 months
VD2	2018-03-29	1344	3 years 8 months
VD3	2019-03-19	1699	4 years 8 months
VD4 (Cancelled)	2020-03-20	2066	5 years 8 months
VD5	2021-02-20	2403	6 years 8 months
VD6UP	2022-03-30	2806	7 years 8 months

The boundary condition corresponding to the ultimate pressure test, VD6UP, was defined according to the pressure sequence shown in Figure 5.20. This ultimate pressure test was performed on day 2806 (7 years and 8 months), with reference to date 2014-07-24.

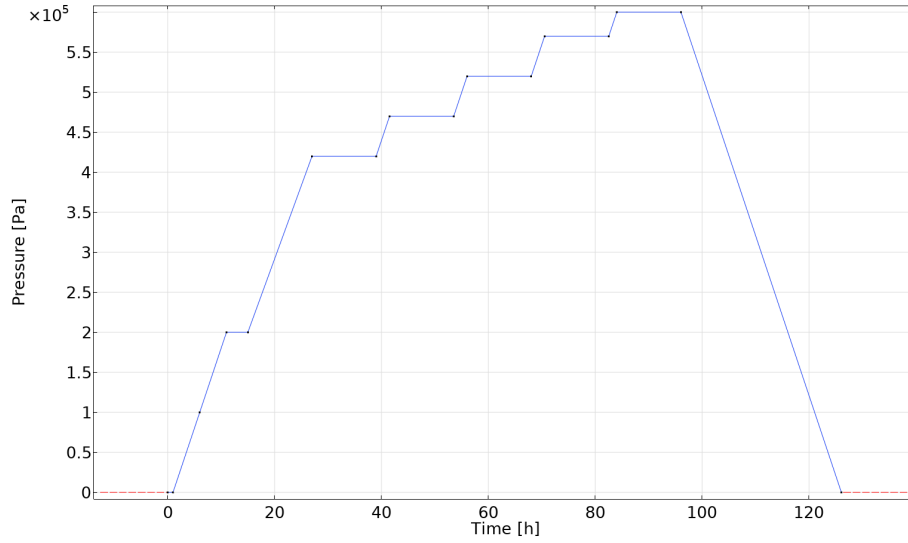


Figure 5.20 Ultimate pressure test.

The applied boundary condition for the heat transfer was described as a heat flux,  $\mathbf{q}$ , with a constant heat transfer coefficient,  $h_T$ , of 20 W/(m<sup>2</sup>K), see equation (29)

$$\mathbf{q} \cdot \mathbf{n} = h_T(T_{ext} - T) \quad (29)$$

where,  $T_{ext}$ , represents ambient temperature,  $T$  represents the surface temperature of the RC, and  $\mathbf{n}$  is the normal vector of the boundary surface.

The boundary condition for the moisture transfer was defined on the same form as for the heat transfer, viz a moisture flux condition see equation (30)

$$\mathbf{q} \cdot \mathbf{n} = h_{RH}(\varphi_{ext} - \varphi) \quad (30)$$

where,  $\varphi_{ext}$ , represents ambient relative humidity and,  $\varphi$ , represents the surface relative humidity of the RC.

The moisture transfer coefficient,  $h_{RH}$ , is dependent on the saturation vapour content, which is temperature dependent. This relationship was modelled according to Lewis relation [24] see equation (31)

$$h_{RH} = \frac{h_T \cdot v_s}{\rho_{air} \cdot C_{p(air)}} \quad (31)$$

where,  $h_T$ , represents the heat transfer coefficient,  $v_s$ , represents the saturation vapour content of air, and,  $C_{p(air)}$ , represents the specific heat capacity of air 1000 J/(kg K).

The exterior and interior boundaries are shown in Figure 5.21 and Figure 5.22.

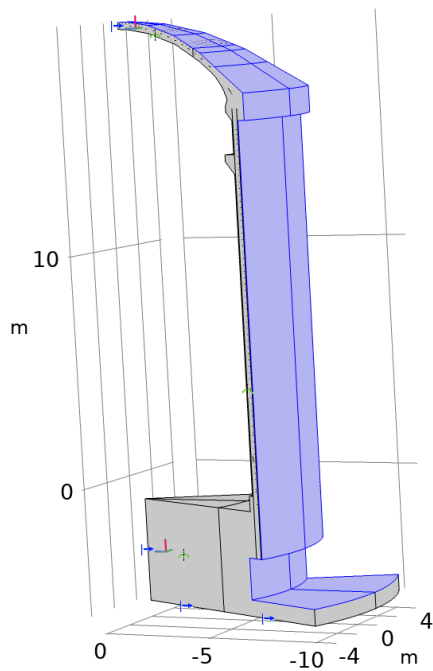


Figure 5.21 Exterior boundaries on the wedge geometry.

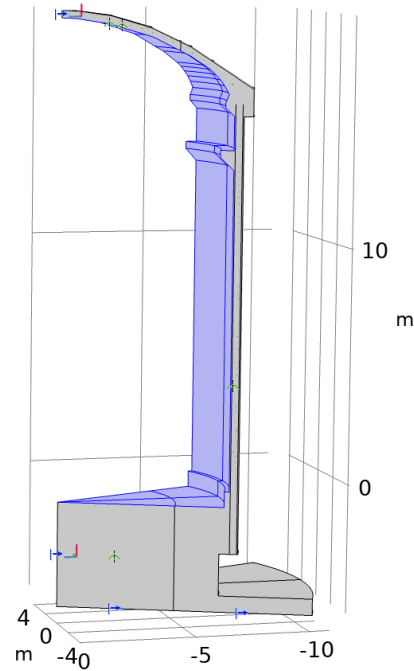


Figure 5.22 Interior boundaries on the wedge geometry.

On these boundaries the ambient temperature and moisture conditions were applied.

### 5.7.2 Air leakage

The air leakage was evaluated by using a 2D geometry. Therefore, the interior and exterior boundary conditions were applied on a line instead of a surface. The pressure condition according to the pressure test sequence, see Figure 5.19 and Figure 5.20 was applied in the interior boundary see Figure 5.23. On the exterior boundary the atmospheric pressure was applied see Figure 5.24.

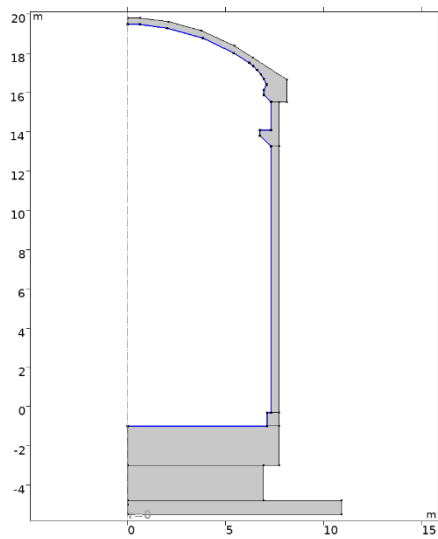


Figure 5.23 Interior boundary where the temporary pressure test sequence was applied.

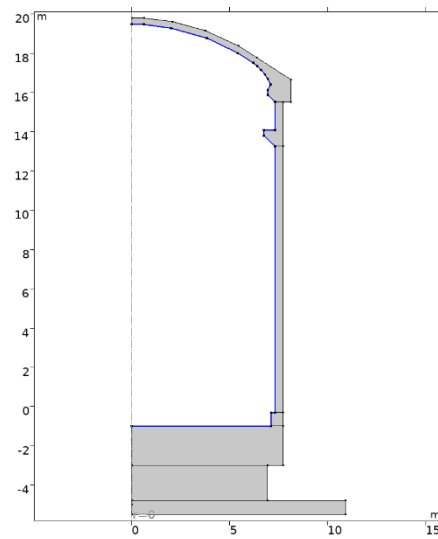


Figure 5.24 Exterior boundary where the atmospheric pressure was applied.

### 5.7.3 Scale effect of drying

The interior and exterior boundaries used in the scale effect study are shown in Figure 5.25 and Figure 5.26. The ambient temperature and moisture conditions were applied on these surfaces.

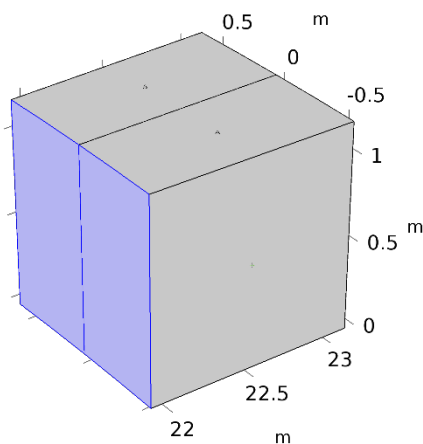


Figure 5.25 Interior boundary

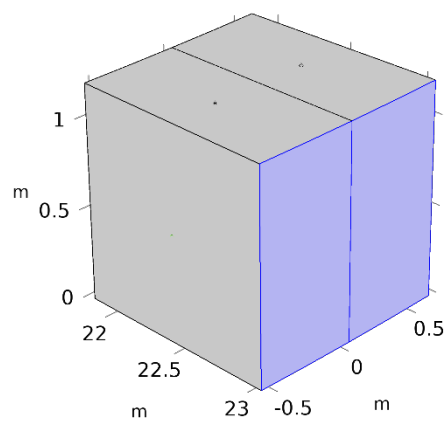


Figure 5.26 Exterior boundary

Note that the geometry is rotated about  $90^\circ$  around the vertical z-axis in Figure 5.26 compared with the geometry in Figure 5.25.

The applied boundary conditions in the mechanical analysis are shown in Figure 5.27 and Figure 5.28.

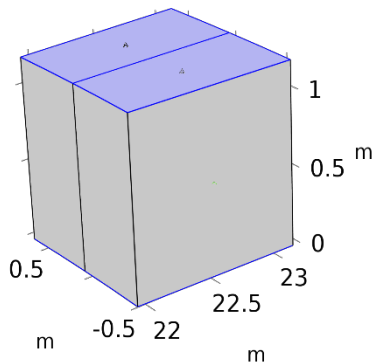


Figure 5.27 Horizontal surface roller constraint.

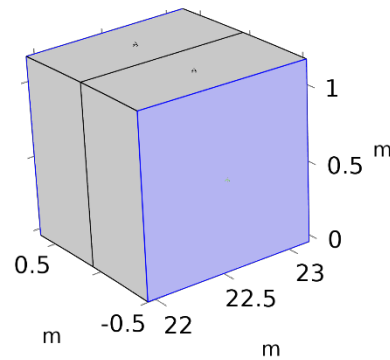


Figure 5.28 Vertical surface symmetry boundary constraint.

A roller constraint was applied to the horizontal surface, indicated in blue, restricting movement in the z-direction while allowing freedom of movement in the x- and y-directions (top), shown in Figure 5.27. This constraint was also applied to the opposite horizontal surface (bottom). A symmetry constraint was applied to the vertical surface, indicated in blue, shown in Figure 5.28. The same type of constraint was also applied on the opposite vertical surface. These constraints ensure that this cut out geometry behaves in a similar way as the complete RC geometry.

In addition to these constraints the displacement was restricted to the radial direction. The tangential displacement and displacement along the z-axis were set to zero.

#### 5.7.4 Ambient temperature and relative humidity

Benchmark VERCORS recorded hourly ambient temperature and relative humidity data using four sensors, with two each for exterior and interior measurements. These sensors were positioned near a hatch at an elevation of +10 meters. Mean temperature and relative humidity values at these locations were calculated from pairs of sensors.

These datasets formed the foundation for calculating daily mean temperature and relative humidity values by summing the 24-hour measurements and dividing each sum by 24. These results were used as boundary conditions for both the exterior and interior of the structure in this study.

Linear interpolation was employed to estimate values between data points for temperature and relative humidity. When the simulation extended beyond the last recorded data point, a constant temperature and humidity, equal to the last recorded value, was assumed.

The ambient temperatures acting on the exterior and interior surfaces of the RC are assumed equal to the results from temperature measurements provided by the benchmark, see Figure 5.29.

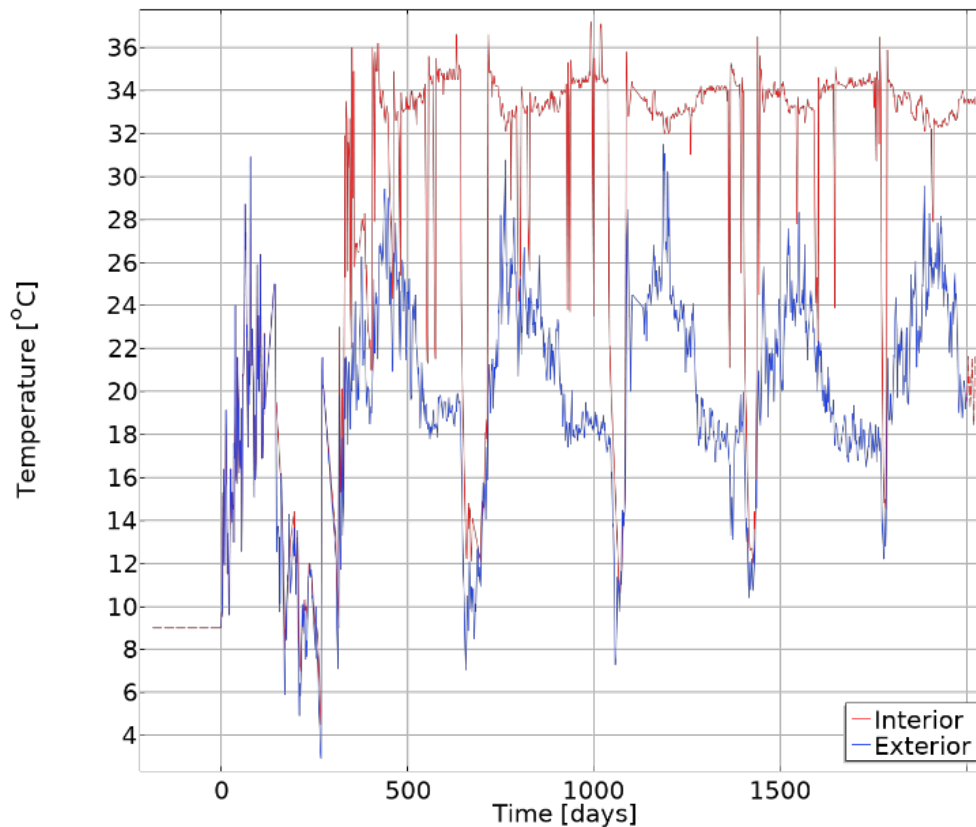


Figure 5.29 The registered exterior and interior temperatures (°C) used in the simulation.

Note that day 0 (zero) represents day 278 in the simulation results.

The relative humidity was expressed as the ratio between actual air vapour content and saturation air vapour content at the current temperature. The exterior and interior boundaries were assumed to be equal to the registered relative humidity, except that readings were – as previously explained - cropped to not exceed 0.95 (95% RH) as seen in Figure 5.30.

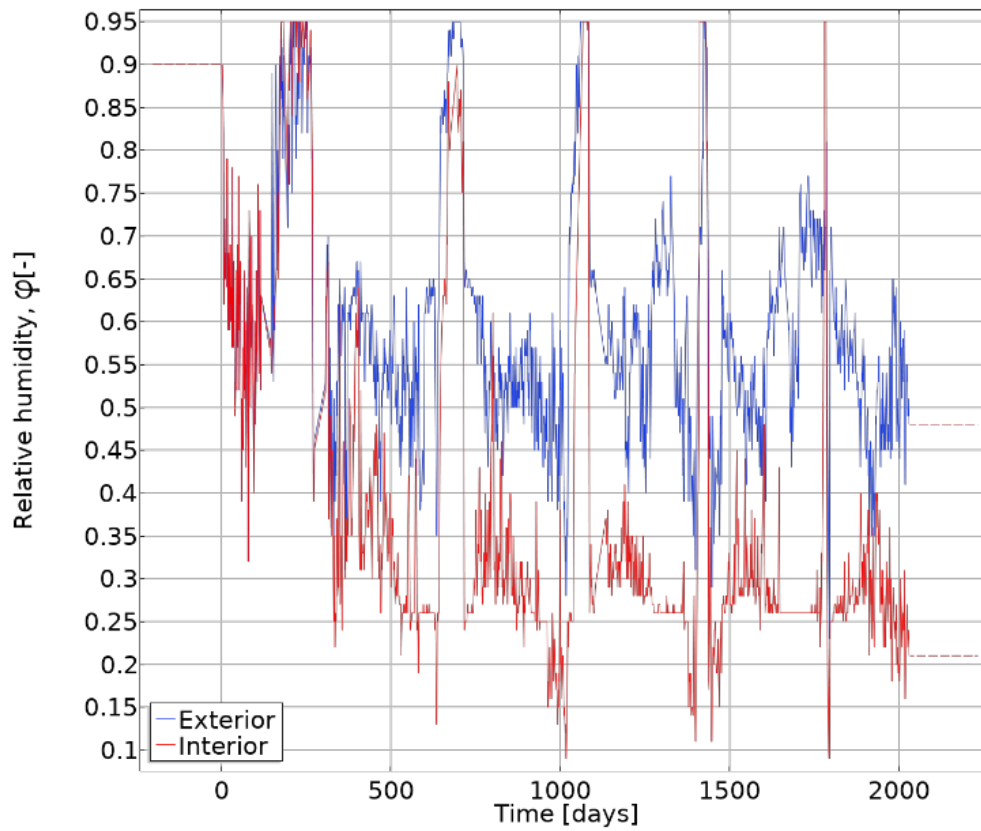


Figure 5.30 The registered exterior and interior relative humidity used in the simulation.

## 6 Computation strategies

### 6.1 STRUCTURAL MECHANICS COMPUTATION STRATEGY OF THE RC (STUDY 1A AND 1B)

The analysis of the mechanical behaviour of the RC was computed in four steps. The analysis started with solving the heat transfer simulation and thereby obtaining the temperature distribution in the structure and its evolution with time, see Figure 6.1. The results of the temperature calculation were used as input to the next step of the simulation sequence, the moisture transfer simulation.



Figure 6.1 Computational simulation sequence, structural mechanics

In the moisture transfer simulation, the surrounding humidity was taken into account and the evolution of the moisture state with time inside the structure was calculated.

In the next step, Solid mechanics 1, the first part of the solid mechanics simulation was performed. In this step, the structural deformations originating from temperature, humidity and the pressure tests were computed. In this step the tendons were not active. The structural transient behaviour was set to quasistatic, meaning that the dynamic effects were not included in the governing partial differential equation, PDE.

In the last step, Solid mechanics 2, the tendons were activated and creep according to Eurocode 2 [2] was considered. The result from the Heat and Moisture transfer step was used as an input to the Solid mechanics 2 to be able to evaluate the notional creep coefficient and creep strains. Temperature and moisture gradient-induced stresses were assumed to have no influence on creep. Furthermore, the stresses resulting from pressure tests were also considered non-contributory to creep.

Finally, the principle of superposition was applied to evaluate the total deformation from the two solid mechanics simulations to obtain the total deformation of the structure.

The simulation of the wedge 3D model was performed on a computer cluster, HPC2N, which is a part of the Swedish National Infrastructure for Computing (SNIC). The CPU was an Intel® Xeon® Processor E5-2690 v4, with a processor base frequency of 2.6 GHz, with 28 cores. The physical memory on the used node was 128 GB. It was not required to use a cluster with a fast CPU, but the time of calculation and number crunching decreased substantially by using such hardware. It is possible to solve this model on an ordinary PC, but the time for solving and extracting data increases substantially.

The computation time (including saving time) for the 4 different steps using the cluster was 40 minutes (Heat transfer), 50 minutes (Moisture transfer), 120 minutes (Solid mechanics 1), and 100 minutes (Solid mechanics 2).

Lund university computer cluster COSMOS at Lunarc, was used when calculating the complete RC model. Lunarc is a part of the Swedish National Infrastructure for Computing (SNIC). The CPU was 2 AMD® EPYC™ 7413, with a processor base frequency of 2.65 GHz, with 24 cores each. The physical memory on the used node was 256 GB.

The computation time (including saving time) for the 4 different steps using the cluster was 45 minutes (Heat transfer), 156 minutes (Moisture transfer), 82 minutes (Solid mechanics 1), and 176 minutes (Solid mechanics 2).

## 6.2 AIR LEAKAGE COMPUTATION STRATEGY (STUDY 2)

Air leakage through the reactor containment was calculated using a multiphysics approach. This approach involved a simultaneous analysis that resolved heat transfer, moisture transfer, and the evolution of leakage over time in a single step, see Figure 6.2.



Figure 6.2 Simultaneous multiphysics analysis for computing the air leakage

This simulation was performed on a PC. The CPU was an Intel® Xeon® Processor E5-1650 v4 with 6 cores with a processor base frequency of 3.6 GHz, with 6 cores. The physical memory (RAM) on the PC was 32 GB. The computation time, except saving time, was 14 minutes.

## 6.3 STRATEGY FOR COMPUTING THE SCALE EFFECT OF DRYING (STUDY 3)

The scale effect was analysed as a parametric study where the wall thickness varied from 0.4 to 1.2 m in steps of 0.2 m. The complete computation was performed as a simultaneous analysis where the heat transfer, moisture transfer and the solid mechanics were solved in one step, see Figure 6.3.



Figure 6.3 Simultaneous multiphysics analysis for computing the scale effect of drying

The simulation of the 3D model was performed on the same computer cluster, HPC2N, which was used for structural mechanics computation of the wedge geometry, see section 6.1. It was not required to use a cluster with a fast CPU, but the calculation and number crunching decreases substantially by using such hardware. The total computation time, including data saving, for the two different analyses was 20 hours when considering time-dependent material properties and 9 hours with constant material properties. This long calculation time was needed because of the short interval between each time step in the simulation.

## 7 Results

The results of the three studies are presented in this chapter, i.e., the long-term mechanical behaviour of the RC (section 7.1), the air leakage through the RC (section 7.2) and the influence of the scale effect of drying (section 7.3).

The calculations of all parameters were conducted based on data on different materials properties, prestressing data, and ambient conditions in terms of relative humidity and temperature.

The calculations in this study, as well as the previous [5, 6], were all performed using these parameters, independently of the results obtained from the measurements.

At the first workshop, measurements of strains, stresses, temperature, relative humidity, and leakage from the first month of experiments were distributed to participants after they had submitted their calculation results. During the second benchmark workshop, data from approximately three years of measurements was shared. In the third benchmark workshop, data from five years of measurements became available after participants had submitted their calculation results.

### 7.1 THE LONG-TERM MECHANICAL BEHAVIOUR OF THE RC (STUDY 1)

The temperature evolution with time is presented in different points of the structure in section 7.1.1. In the next section, section 7.1.2, the evolution of humidity is presented as the degree of saturation through the cross-section of the cylindrical wall. In section 7.1.3, the radial and vertical displacements from the wedge study are presented. The radial and vertical displacements from the complete RC study are presented in section 7.1.4. In section 7.1.5, different contour plots of strains from the wedge study are presented. In section 7.1.6, different contour plots of stresses are presented. The evolution of strains with time in tangential, vertical and radial directions in several points from the wedge study are presented in section 7.1.7. Finally, in section 7.1.8, the evolution of tangential, vertical, radial and meridian strains with time, are presented without temperature induced strains.

The results at specified points of the wedge study were evaluated at a vertical cross section of the 3D model, see Figure 7.1. This means that potential boundary effects because of the modelled geometry were minimized.

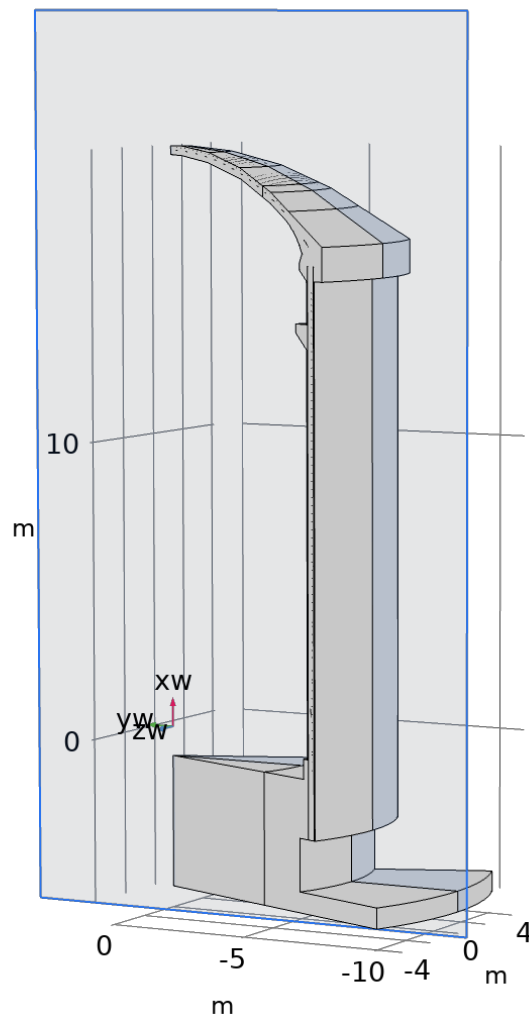


Figure 7.1 Illustration of the geometry and the vertical cross section on which the results are evaluated.

In reality, measurements were performed over the whole RC and not at a single cross section. The results from the simulations are compared with the actual measurements at the specified radius and height. The simplified wedge geometry does not include the equipment hatch, where the wall thickness is slightly thicker. Therefore, one point at the equipment hatch, M3E, was not included in the results as the measurements were performed at a radius of 7.75 m, whereas the maximum radius of the modelled wedge geometry was 7.7 m.

Please note the following timeline. Day 0 (zero) marks the start of the raft casting, which occurred on 2014-07-24. After 278 days, on 2015-04-28, the construction of the dome was completed. Pre-stressing was finished 384 days after start of the raft casting, on 2015-08-12.

The pressure test sequence initiated on days 469, 551, 964, 971, 1344, 1699, 2403, and 2806. These days are all referenced to day 0 (zero). All strain gauges were set to zero at day 384. The time scale in all figures is presented in days with reference to day 0 (zero), except in figures showing the scale effect of drying.

### 7.1.1 Temperature

The zones, names, and positions and angle of the 17 points selected by benchmark VERCORS 2022 are shown in Table 7.1.

**Table 7.1** Position of each temperature sensor.

Zone	PT100 sensors	Radius (m)	Height (m)	Angle (gr)
Raft	TETA_C2	4.13	-1.74	172.02
	TETA_C7	6.38	-1.77	235.02
	TETA_E2	4.12	-1.14	171.89
	TETA_E8	4.00	-1.17	20.81
Gusset	TETA_F1	7.24	-0.88	172.01
	TETA_F12	7.59	-0.88	19.99
	TETA_G11	7.40	-0.25	20.18
	TETA_G12	7.60	-0.26	20.21
Cylindrical part (mid-height)	TETA_H10	7.38	2.15	171.70
	TETA_H16	7.39	7.46	333.20
	TETA_H7	7.58	8.49	294.90
	TETA_P12	7.39	7.47	378.30
Torique belt	TETA_T102	7.77	16.21	172.20
	TETA_T2	7.35	16.06	172.20
	TETA_T304	7.48	16.12	97.00
	TETA_T5	8.02	16.10	367.40
DOME	TETA_I2	0.04	19.60	0.00

The results are extracted from points on the vertical cross-section in the centre of the model, see red dots in Figure 7.2.

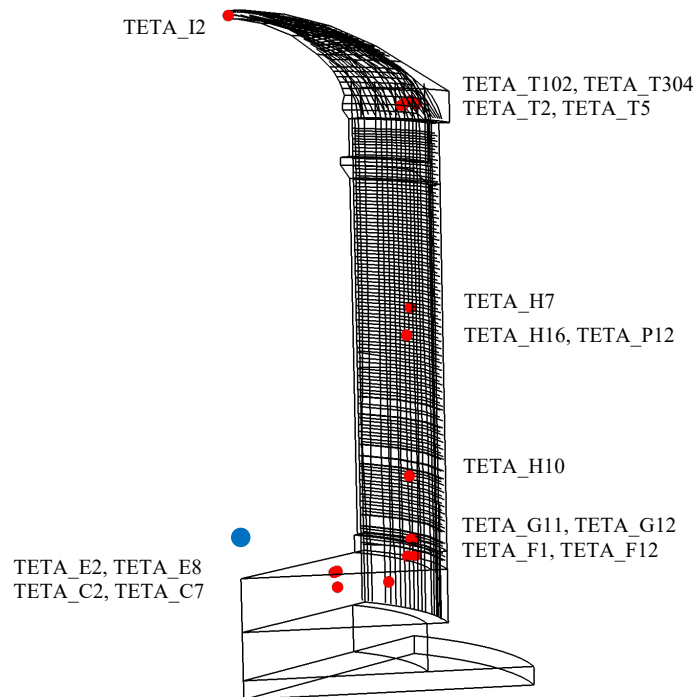
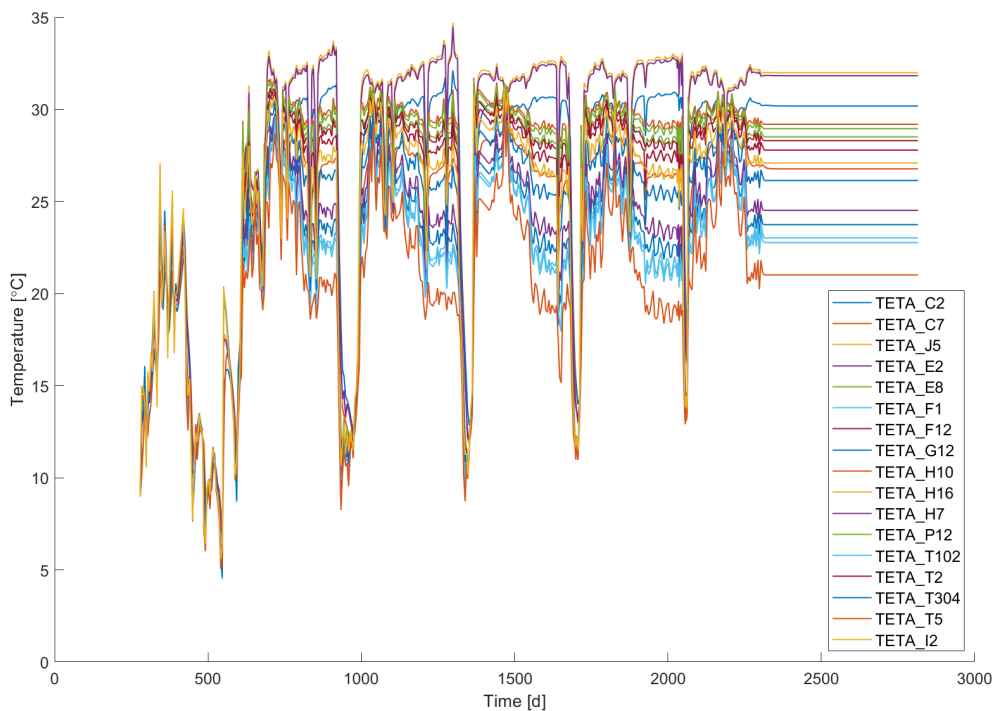


Figure 7.2 Overview of the temperature sensor positions in the RC, marked with a red dot. Origo of the coordinate system is marked with a blue dot.

The obtained temperature evolution with time in all sensor positions are shown in Figure 7.3. Note that ambient conditions (air temperature) were measured at a level of +10 m, at a position close to TETA\_H7 which is close to the equipment hatch. The measured temperature at +10 m was used as input as a boundary condition in the analysis. This means that the temperature was assumed to be independent of the elevation.



**Figure 7.3 The evolution of the temperature at all the positions from the simulations**

The simulation shows that the temperature changes significantly with time. During the first time period before the first pressure test between approximately 300 to 500 days, the climate control system was not running. This means that the temperature in the RC was governed by the outdoor temperature. As a consequence, all sensors show a similar temperature. After around 500 days the climate control system started, and the interior of the RC was heated to about 35 °C. Therefore, the temperature sensors that are closer to the inner surface reach a temperature of approximately 32 °C, while the sensors that are closer to the exterior surface show a temperature equal to roughly 20 °C.

There are seven time periods, at 469, 551, 964, 971, 1344, 1699, 2403, and 2806 days, where the temperature is significantly lower compared with the overall mean temperature. During these time periods, pressure tests were conducted, leading to the temporary shutdown of the climate control system. It is evident that the duration of these periods without the climate control system running has progressively decreased with each pressure test.

The last part of the graph shows constant temperatures in each position, and this is because a constant temperature was assumed during the last time period.

The measured and calculated temperature in four points, TETA\_C2, TETA\_F1, TETA\_H7 and TETA\_I2 are shown in Figure 7.4-Figure 7.7, respectively. The points where the measurements are shown together with the calculations are selected to represent four different locations: the raft, the gusset, the cylindrical wall, and the dome.

The calculated and measured temperatures at point TETA\_C2, in the raft, are shown in Figure 7.4.

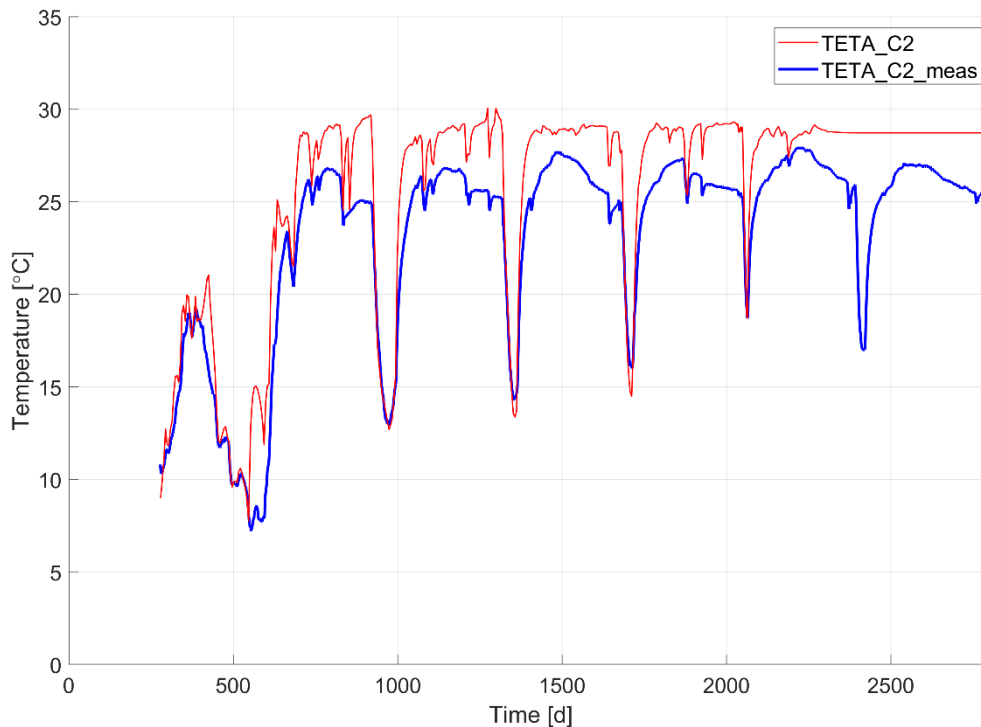


Figure 7.4 Evolution of calculated and measured temperature at TETA\_C2 in the raft

At the start of the period, the calculated temperature closely aligns with the measured temperature, with the lines nearly overlapping. During this period the climate system is turned off. Later, when the climate system control is turned on, the measured temperature is on average 2°C lower than the calculated. One reason for this may be that the ambient conditions near the raft at a level of -1.7 m and 4.12 m from the centre, is not equal to the conditions at a level of +10 m close to the hatch. Cooler temperatures near the raft are plausible, due to natural convective air movements, such as warm air rising when the climate system is in operation. The temperature difference is larger when the climate control is active at the raft.

The calculated and measured temperatures at point TETA\_F1, in the gusset, are shown in Figure 7.5.

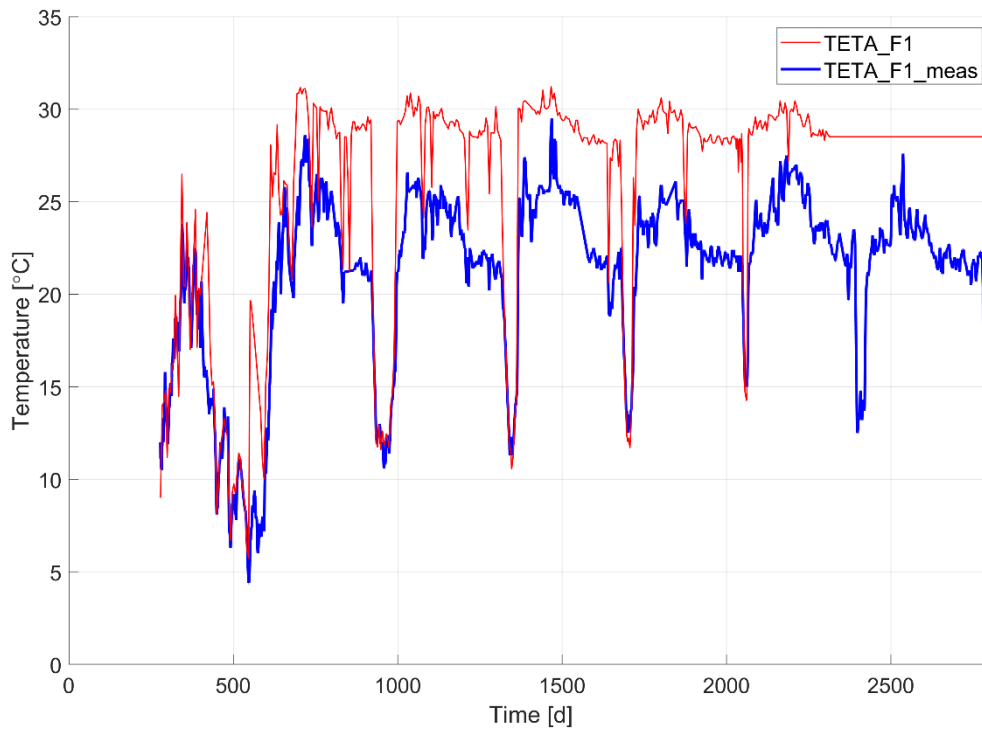


Figure 7.5 Evolution of calculated and measured temperature at TETA\_F1 in the gusset

The measured and calculated temperatures at point TETA\_F1, interior side of the gusset, are also almost overlapping each other at the beginning of the period. As earlier mentioned, the climate system is turned off during this period. Later, when the climate system control is turned on, the measured temperature is on average about 5°C lower than the calculated. One potential explanation for this difference could be that the ambient conditions at a level of -0.88 m and 7.24 m from the center are colder than those at a level of +10 m. This is where ambient temperatures are evaluated. There could be even cooler temperatures near the gusset due to larger natural convective air movements close to the cylinder wall, such as warm air rising when the climate system is in operation. The temperature difference is larger when the climate control is active at the gusset.

The calculated and measured temperatures at point TETA\_H7, in the cylindrical wall, are shown in Figure 7.6.

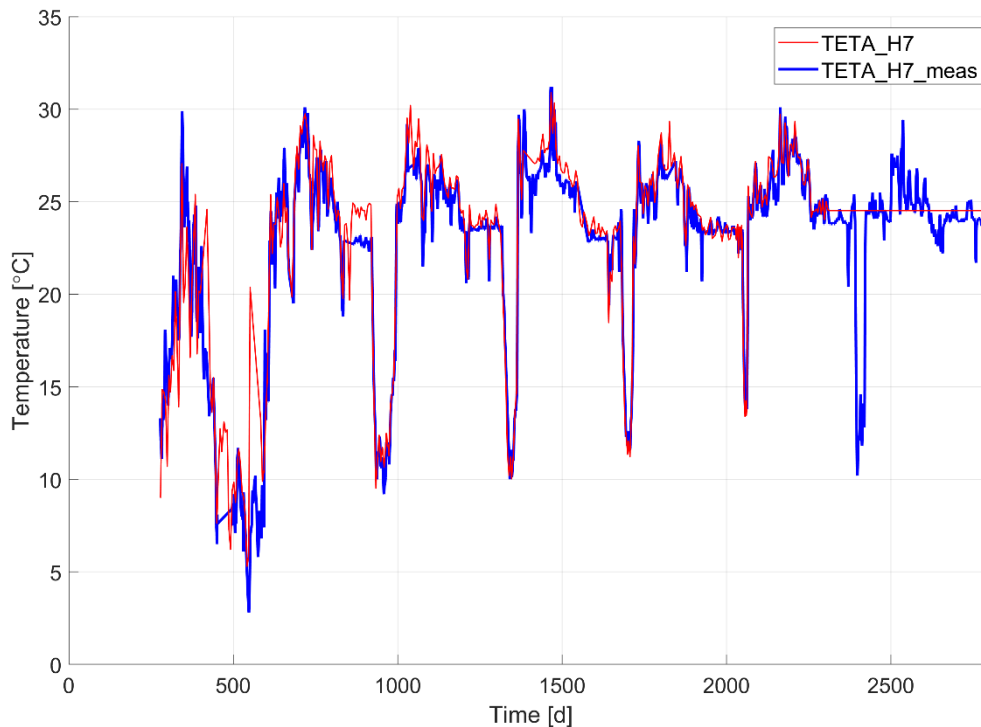


Figure 7.6 Evolution of calculated and measured temperature at TETA\_H7 in the cylinder wall

The measured and calculated temperatures at point TETA\_H7, exterior side of the gusset, are almost overlapping each other during the complete period. The deviation from the measured temperatures is small. One potential explanation for this small difference is that the ambient conditions at a level of +8.49 m and at 7.58 m from the centre is almost equal to those at a level of +10 m. This is close to the hatch, where ambient temperatures are evaluated. There is no significant difference between the calculated and the measured temperatures with and without a running climate system. Note that a constant temperature was used as a boundary condition during the last period of time.

The calculated and measured temperatures at point TETA\_I2, in the dome, are shown in Figure 7.7.

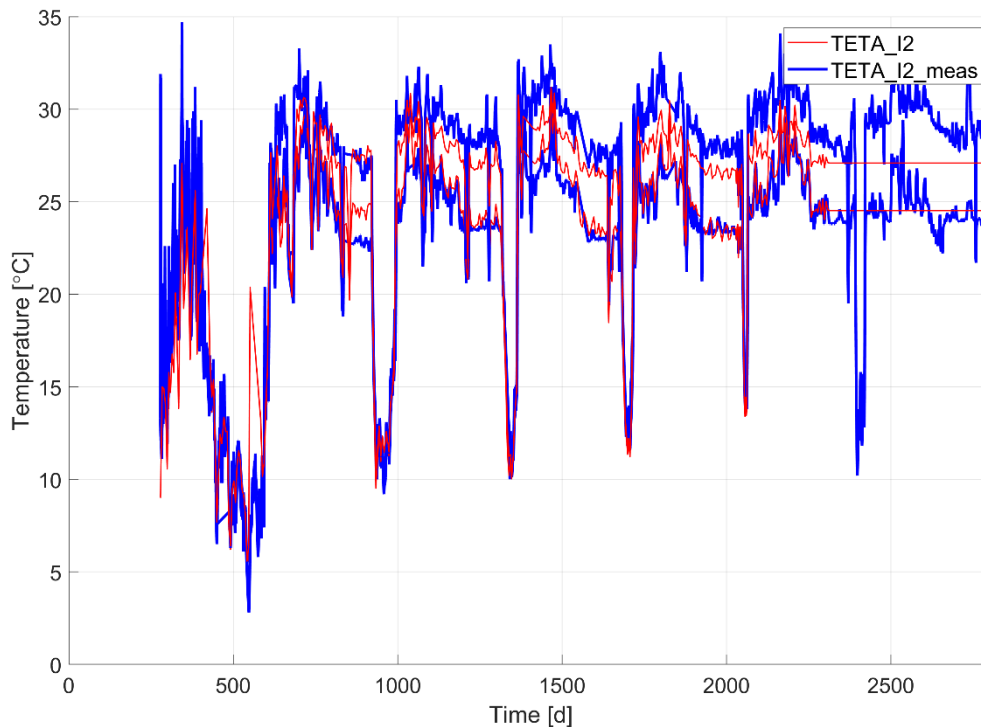


Figure 7.7 Evolution of calculated and measured temperature at TETA\_I2 in the dome

The measured and calculated temperatures at point TETA\_I2, interior side of the gusset, are almost overlapping each other except for the beginning where the difference is larger. The deviation from the measured temperatures is small after the initial period, and approximately 2°C. One potential explanation for this difference is that the ambient conditions at a level of +19.6 m and at 0.04 m from the centre is a little warmer compared with those at a level of +10 m.

The differences between the calculated and measured temperatures in the other points were of similar magnitude as the results presented in this section.

### 7.1.2 Humidity

The calculated moisture content in the cylindrical wall is presented in terms of degree of saturation in Figure 7.8. This parameter is evaluated by dividing the actual moisture content with the moisture content at saturation.

The evolution of the degree of saturation is shown along a cross section of the cylindrical wall at an altitude of +10 m, see Figure 7.8. The interior surface, at wall thickness 0 m, is exposed to a drier climate, resulting in a lower moisture content compared with the exterior surface at 0.4 m. The distribution of the degree of saturation distribution was evaluated at the start of each pressure test as stated in the legend.

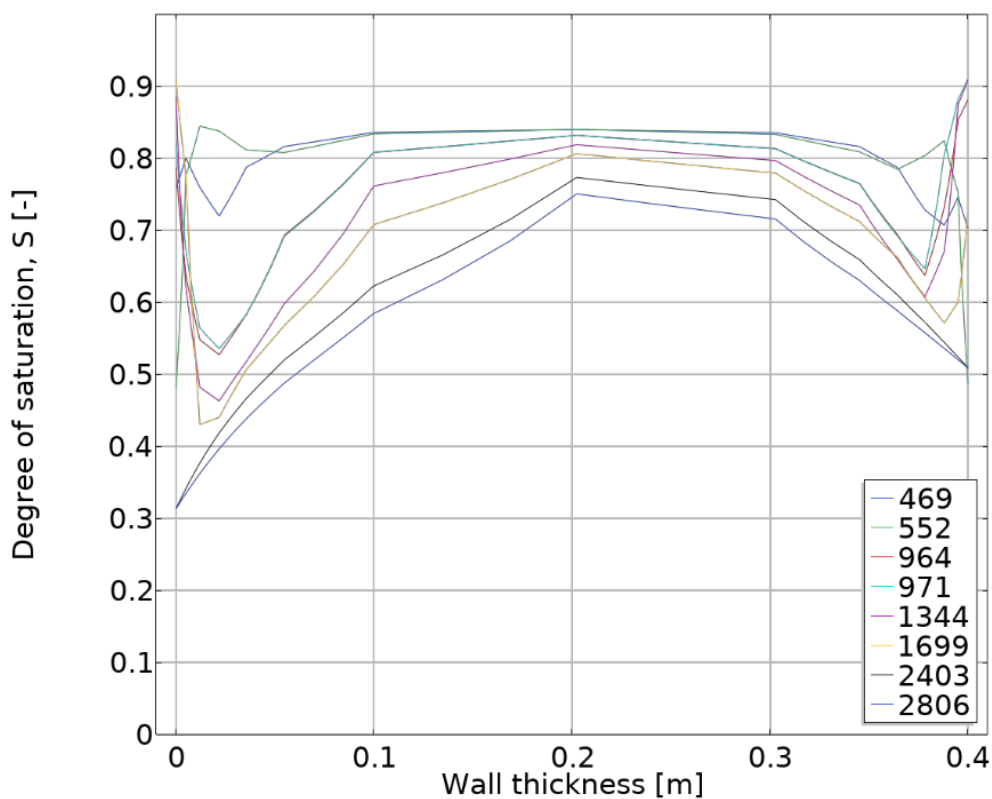


Figure 7.8 The evolution of the humidity with time from the simulations, at a cross section of the cylindrical wall

The saturation profiles clearly show that significant drying occurs with time. The early saturation profile, at day 469, reaches a maximum value of about 0.82 in the centre of the wall. About six years later, at day 2806, the degree of saturation in the centre of the wall is about 0.74. The degree of saturation near the surface varies, due to fluctuations in air humidity. Unfortunately, the Benchmark VERCORS did not include any measurements of how moisture content was distributed through the cylinder wall.

The moisture content was measured in certain points of the RC cylinder wall by the use of time domain reflectometry, TDR. The results from these measurements are shown and discussed in section 8.3.2.

### 7.1.3 Radial and vertical displacement in wedge geometry

The radial and vertical displacements were evaluated at three different altitudes -1 m, +4 m, and +9 m. Both the radial and vertical displacements were set to zero at the start of the simulation (day 278).

The evaluated total radial displacements (including thermal effects) of the cylindrical wall using results from the wedge study are shown in Figure 7.9.

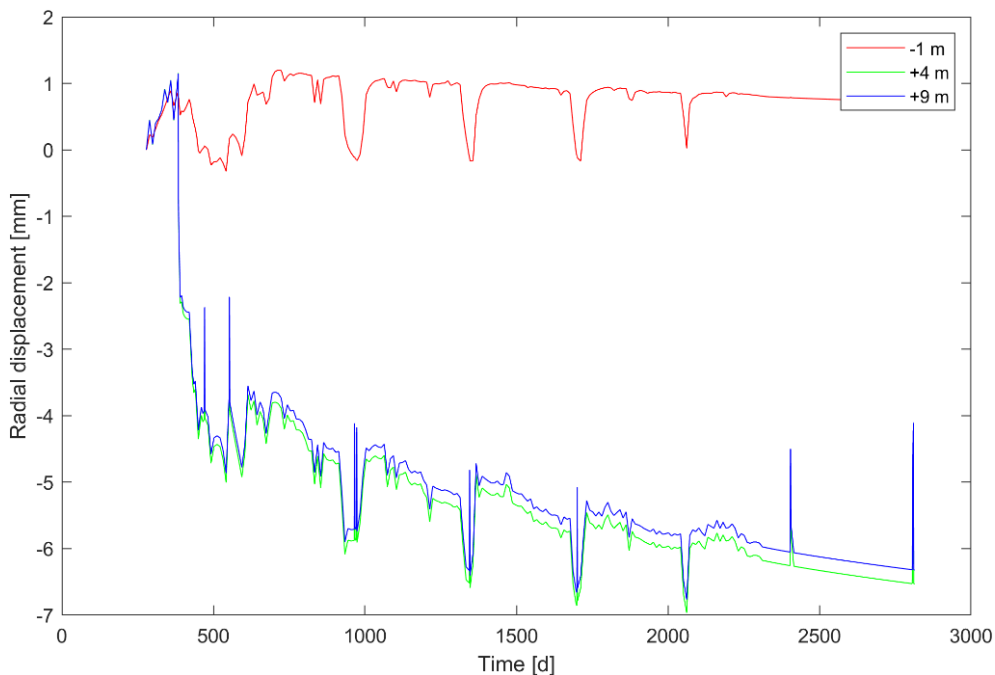


Figure 7.9 Radial displacement of the cylindrical wall at three different altitudes: -1 m, +4 m, and +9 m.

About 100 days after the simulation start, see Figure 7.9 day 384, there is a large radial displacement of approximately -3.5 mm at the +4 m and +9 m level. This is a result of the pre-stressing of the tendons that occurs 384 days after the completion of the dome. Both these levels are at the level of the cylinder wall. The other evaluated point, at -1 m, is at the same level as the raft, hence, resulting in small radial displacements. The negative number means that the radius of the RC is 3.5 mm smaller compared with the unloaded state when no pre-stressing is applied. The radius continues to decrease over time as a result of creep and at day 2800 the total radius decrease is about 6.5 mm.

Each time a pressure test is performed there is a short-term change in the radial displacement, see for example day 2400 and day 2800. This means that when the pressure inside the pre-stressed structure increases, the radius of the structure also increases.

The radial displacement changes significantly with changes in temperature. This is clearly shown at each pressure test when the temperature drops by about 10-15 °C. This temperature drop results in a contraction of the structure, hence, the radius decreases, see for example day 900-1000.

The evaluated total vertical displacements (including thermal effects) of the cylindrical wall using results from the wedge study are shown in Figure 7.10.

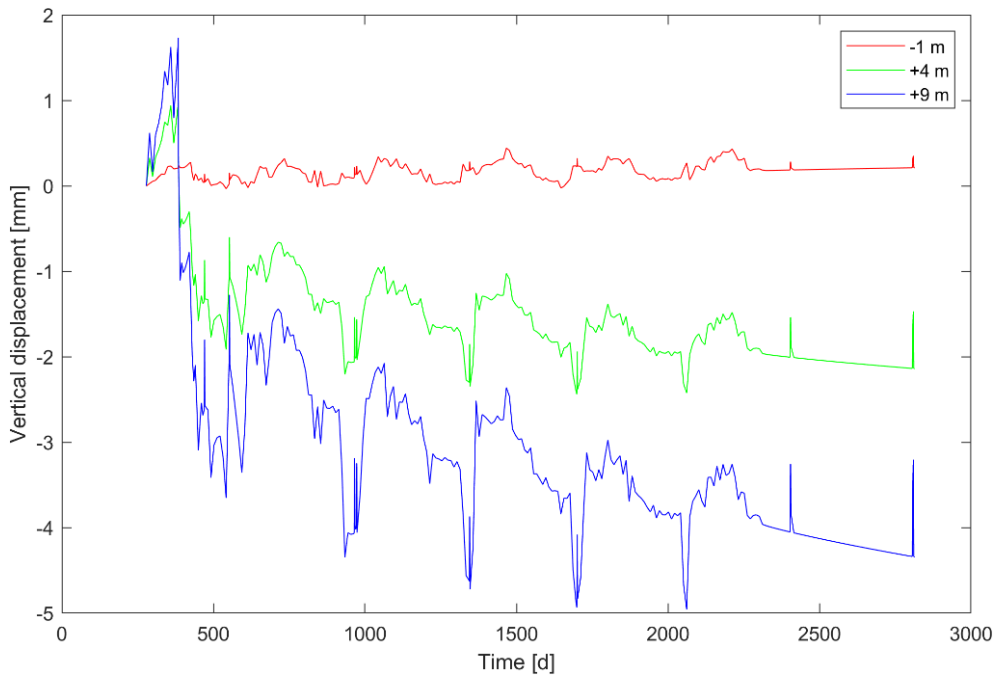


Figure 7.10 Vertical displacement of the cylindrical wall at three different positions: -1 m, +4 m, and +9 m.

The evolution of the vertical displacement at an altitude of -1 m show a small response to the pressure tests. This response is expected because of the large stiffness of the raft. A major part of vertical displacement is caused by temperature changes. There is a small but notable decrease of the RC's height over time which is a result of creep and shrinkage.

The vertical displacement of the RC wall at +4 m and +9 m show large variations during the simulation period because of the temperature changes, for example day 900-1000 when the temperature decreases. In addition, the vertical displacement at +4 m is approximately 50% of the displacement at +9 m, 2.1 mm compared with 4.2 mm. This is logical since vertical displacement is proportional to the distance between the stiff raft and the point in the cylinder wall. The vertical distance between -1 m to +4 m is 5 m and the distance between -1 m and +9 m is 10 meters. The vertical displacement during the pressure tests is larger in the RC wall compared with the raft due to the large difference in stiffness, as mentioned earlier.

#### 7.1.4 Radial and vertical displacement in complete RC geometry

The radial and vertical displacements were evaluated at three different altitudes -1 m, +4 m, and +9 m. Both the radial and vertical displacements were set to zero at the start of the simulation (day 278).

The evaluated total (including thermal effects) vertical displacements of the cylindrical wall using results from the complete geometry study are shown in Figure 7.11.

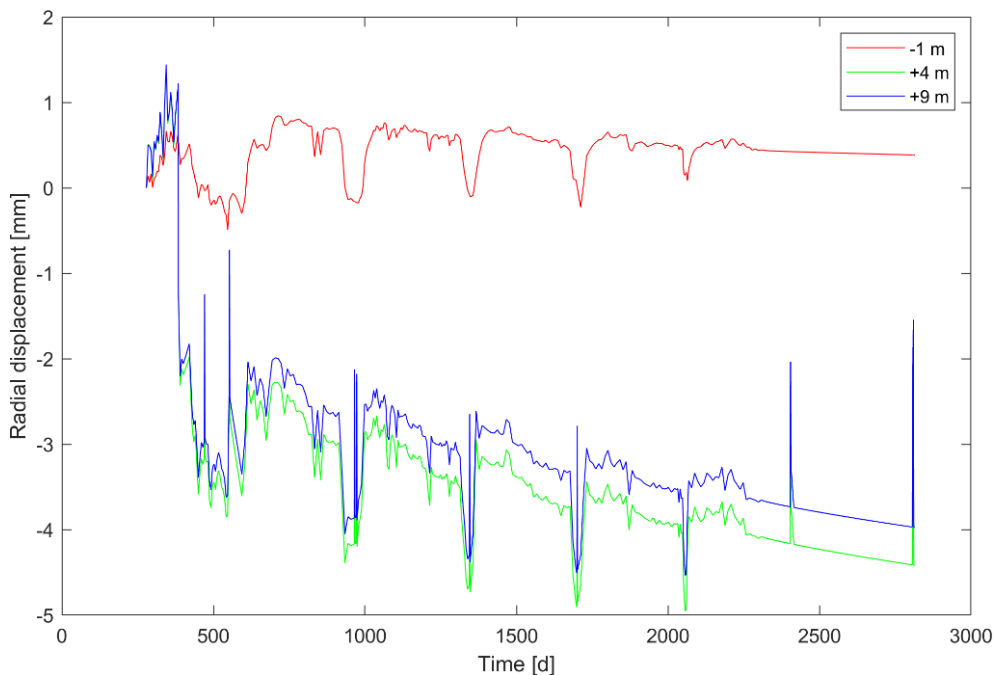


**Figure 7.11 Total radial displacement of the cylindrical wall at three different altitudes: -1 m, +4 m, and +9 m.**

There is a large radial displacement at day 384 of approximately -3 mm at the +4 m and +9 m level. This is a result of the pre-stressing of the tendons that occurs 384 days after the completion of the dome. Both these levels are at the level of the cylinder wall. The radial displacement at day 2800 is approximately -4 mm at the +4 m and +9 m level. The negative number means that the radius of the RC is 4 mm smaller compared with the unloaded state when no pre-stressing is applied. The radius continues to decrease over time as a result of creep. The other evaluated point, at -1 m, is at the same level as the raft, hence, resulting in small radial displacements at a magnitude of approximately 0.5 mm.

Each time a pressure test is performed there is a short-term change, a narrow peak, in the radial displacement, see for example day 2400 and day 2800. This means that when the pressure inside the pre-stressed structure increases, the radius of the structure also increases. These increases in radius also take place at the other pressure test but are more difficult to observe, see Figure 7.11, at day 950.

The radial displacement changes significantly with changes in temperature. This is clearly shown at each pressure test when the temperature drops by about 10-15 °C. This temperature drop results in a contraction of the structure, hence, the radius decreases, see for example day 900-1000.

The evaluated total vertical displacements (including thermal effects) of the cylindrical wall using results from the complete geometry study are shown in Figure 7.12.

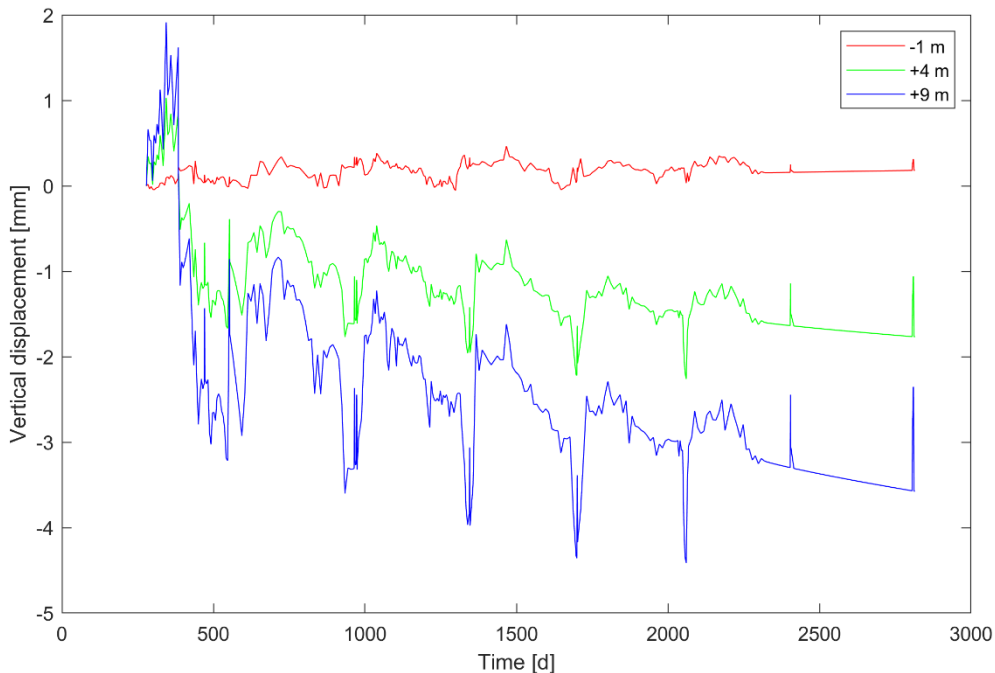


**Figure 7.12** Vertical displacement of the cylindrical wall at three different altitudes: -1 m, +4 m, and +9 m.

The evolution of the vertical displacement at an altitude of -1 m show a small response to the pressure tests. This response is expected because of the large stiffness of the raft. A major part of vertical displacement is caused by temperature changes. There is a small but notable decrease of the RC's height over time which is a result of creep and shrinkage.

The vertical displacement of the RC wall at +4 m and +9 m show large variations during the simulation period because of the temperature changes, for example day 900-1000 when the temperature decreases. In addition, the vertical displacement at +4 m is approximately 50% of the displacement at +9 m, 1.7 mm compared with 3.6 mm. This is logical since vertical displacement is proportional to the distance between the stiff raft and the point in the cylinder wall. The vertical distance between -1 m to +4 m is 5 m, which is 50% of 10 meter which is the vertical distance between -1 m and +9 m. The vertical displacement during the pressure tests is larger in the RC wall compared with the raft due to the large difference in stiffness, as mentioned earlier.

The largest difference between the two simulations is evident in the radial displacement at heights +4 and +9 m. The mechanical boundary conditions of the wedge geometry strongly influence the radial displacement at these specific heights. The likely explanation for this difference is that the mechanical boundary conditions of the wedge geometry do not adequately account for the non-included geometry of the complete RC.

### 7.1.5 Strain field before and after pre-stressing

The results in the following subsections are shown before and after pre-stressing of the tendons. Note that the contour plots of the strains and stresses show the cross-section of the geometry, see Figure 7.13.

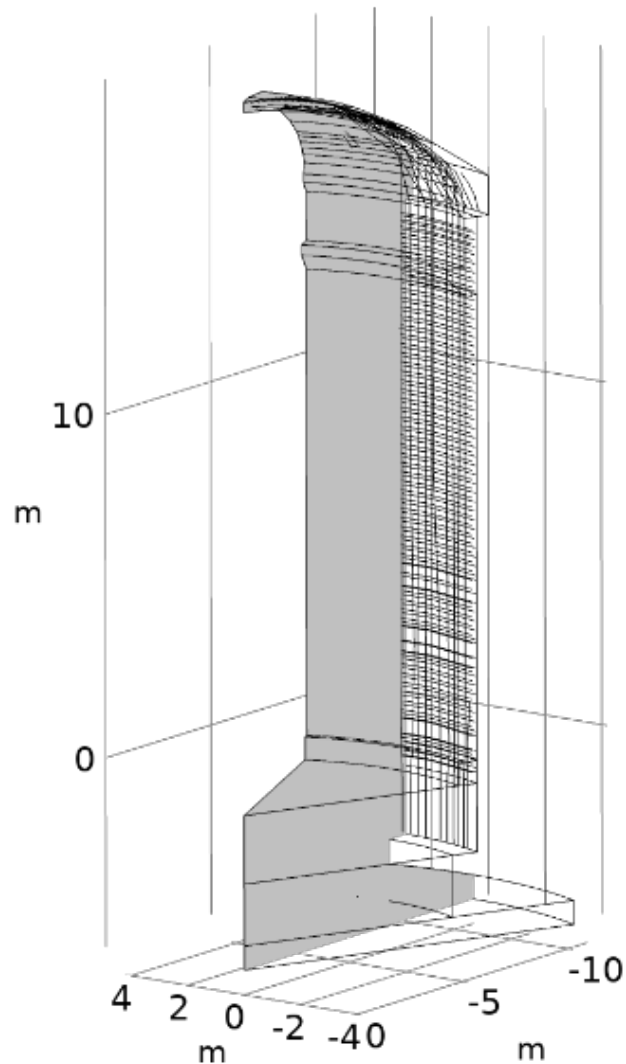


Figure 7.13 The shaded volume (grey), shows the part of the geometry which is displayed in the contour plots.

When half of the geometry is not shown it is possible to see the cross section at the mid part of the geometry, where the edge effects are small.

In the presented result plots, the time is given in days with reference to the actual date of completion of the dome casting, which took place 2015-04-28.

### Vertical strains

The vertical strains of the RC before (a) and after (b) pre-stressing at day 384 and 384.17 are shown in Figure 7.14. The colour bar shows the magnitude of the strains in  $\mu\text{m}/\text{m}$ .

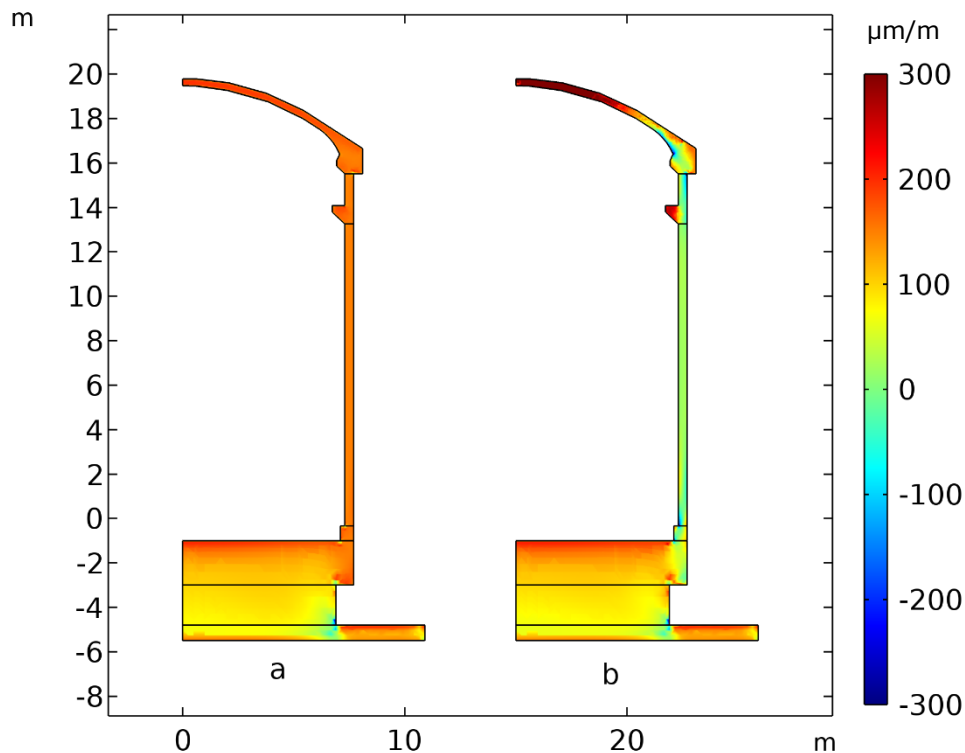


Figure 7.14 Vertical strains before (a) and after (b) pre-stressing of the tendons, day 384 and 384.17, respectively.

The vertical strains in the raft before and after pre-stressing are almost equal, which is expected since this part of the structure does not contain any tendons. The largest change in vertical strains occurs in the cylindrical wall. The strains in the vertical wall changes from about  $+200 \mu\text{m}/\text{m}$  to  $-50 \mu\text{m}/\text{m}$  as the pre-stressing is applied. Temperature changes occurring at day 384 and 384.17 may also have an impact on the vertical strains. A temperature increase will increase the vertical strain, and this may increase the stresses in the tendons.

### Tangential strains

The tangential strains before (a) and after (b) pre-stressing of the tendons are shown in Figure 7.15. The colour bar shows the magnitude of the strains in  $\mu\text{m}/\text{m}$ .

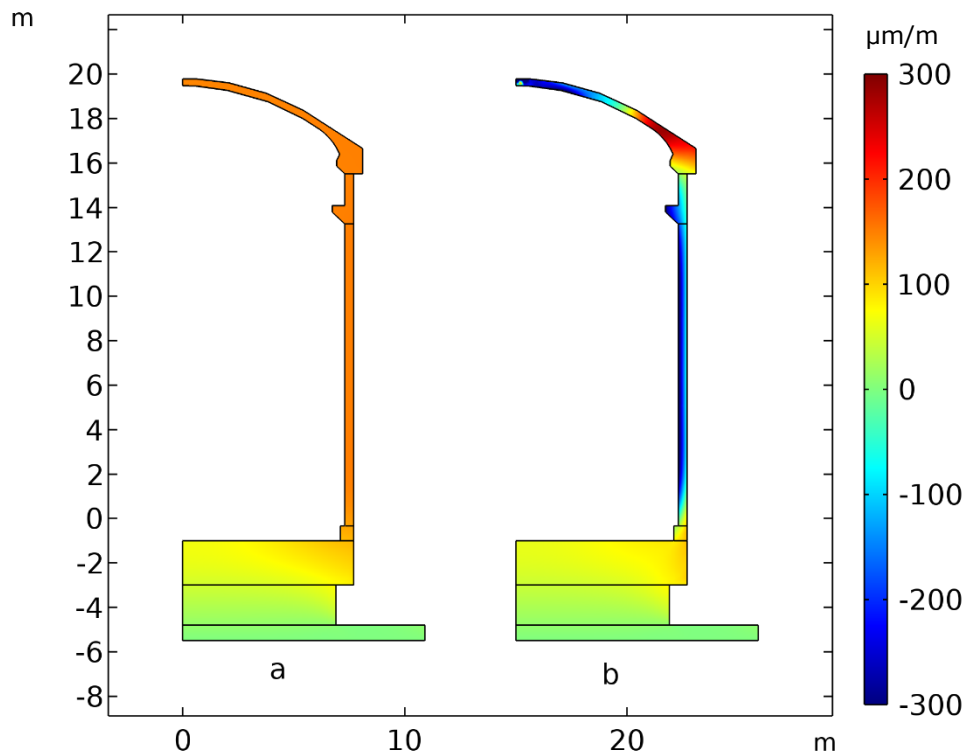


Figure 7.15 Tangential strains before (a) and after (b) pre-stressing of the tendons, day 384 and 384.17 respectively.

The tangential strains in the raft are small, close to  $0 \mu\text{m}/\text{m}$ , which is expected since this part of the structure does not contain any tendons.

The largest change in tangential strains occurs in the cylinder wall from about  $+100 \mu\text{m}/\text{m}$ , see Figure 7.15a to  $-300 \mu\text{m}/\text{m}$ , see Figure 7.15b. This result is expected as this part of the structure contains a significant number of tendons. Changes in tangential strains also appear in the dome, especially at a radius of zero. The horizontal tendons are about four times as many as the vertical tendons and the vertical section of the hoop tendons. This means that vertical forces acting on the structure are about four times the horizontal forces. Temperature changes also affects the tangential strains, but the effect of the pre-stressing is more significant.

### 7.1.6 Stress field before and after pre-stressing

#### *Vertical stresses*

The stresses in the vertical direction before (a) and after (b) pre-stressing at day 384 and 384.17 are shown in Figure 7.16. The colour bar ranges from 4.5 MPa (red) in tension to -10 MPa (blue) in compression.

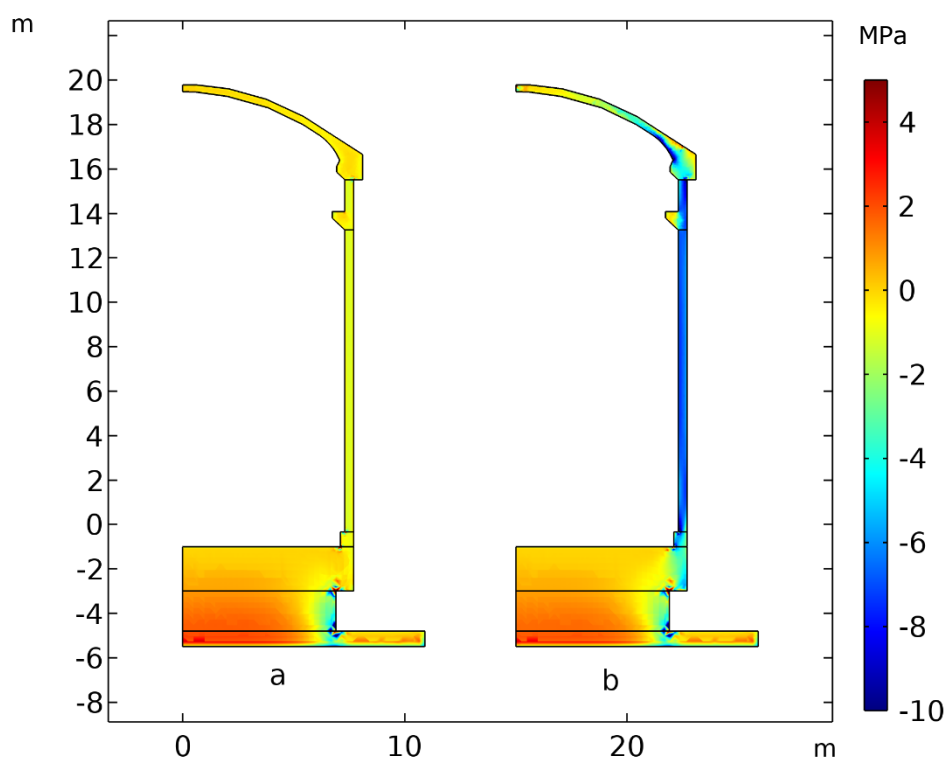


Figure 7.16 Vertical stresses before (a) and after (b) pre-stressing of the tendons, day 384 and 384.17, respectively

The vertical stresses in the inner parts of the raft before pre-stressing is almost identical to the vertical stresses after pre-stressing. This is expected since there are no tendons in the raft.

The vertical stresses in the central parts of the cylindrical wall are compressive with a magnitude of about 1 MPa before pre-stressing. These stresses are significantly lower than the compressive strength. The compressive stresses in the cylindrical wall are about -7 MPa, after pre-stressing of the tendons is performed.

The simulated vertical stresses are shown at a cross section through the cylindrical wall at an elevation of +9 m at day 384 and 384.17, see Figure 7.17.

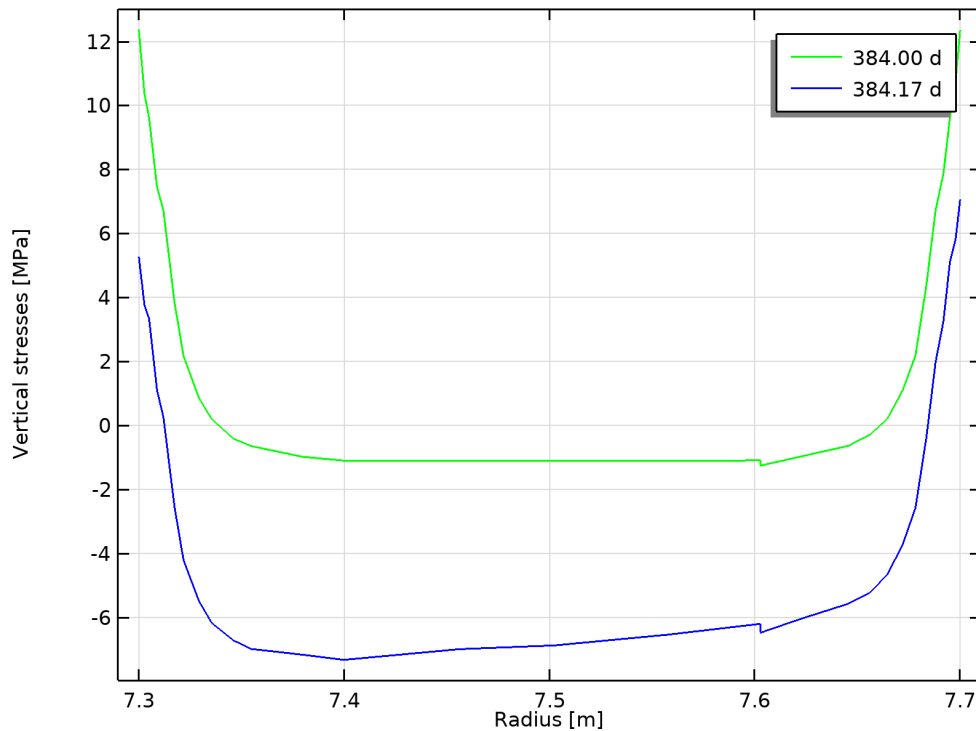


Figure 7.17 Vertical stresses at a cross section of the cylindrical wall at an elevation of +9 m

The stresses are 12 MPa at the surfaces and -1 MPa at the centre of the cylindrical wall. The tensile stresses at the surface are higher than the tensile strength (4.5 MPa) of the concrete. Therefore, surface cracks are likely to form. These stresses are caused by shrinkage as an effect of drying. After pre-stressing is performed, the stresses in the cylindrical wall range from about 5 MPa to about -7 MPa.

### Tangential stresses

Tangential stresses before (a) and after (b) pre-stressing at day 384 and 384.17 are shown in Figure 7.18. The colour bar ranges from 4.5 MPa (red) in tension to -10 MPa (blue) in compression.

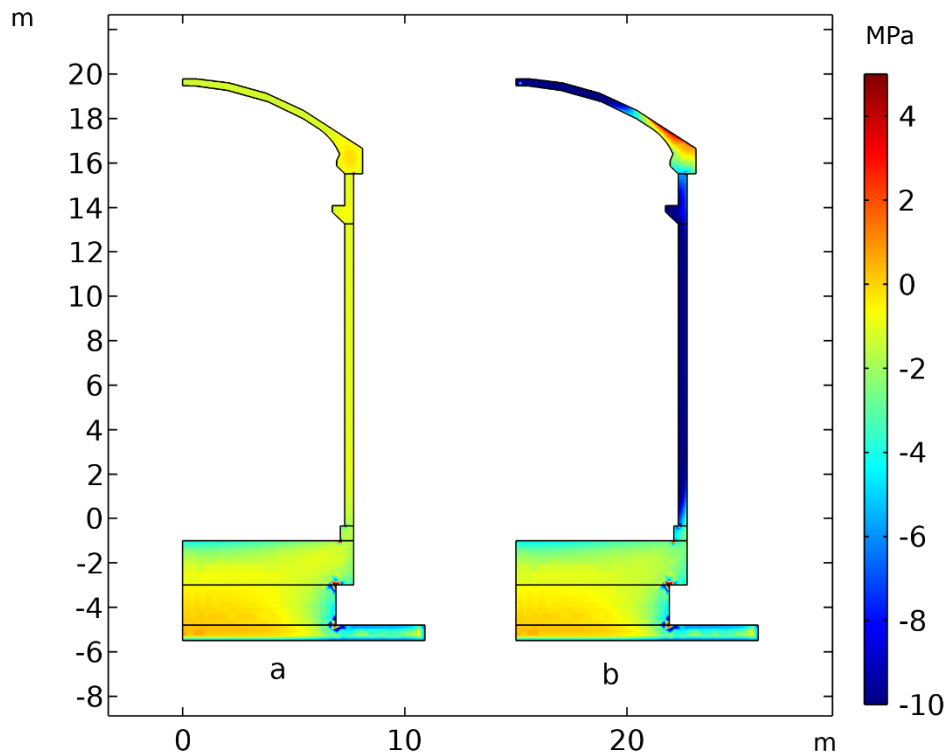


Figure 7.18 Tangential stresses before (a) and after (b) pre-stressing of the tendons, day 384 and 384.17, respectively

The tangential stresses in the central parts of the raft do not change because of pre-stressing since there are no tendons in this part of the structure. The tangential stresses are about -1 MPa before pre-stressing and below -10 MPa after pre-stressing. This also means that surface cracks are more likely to form before pre-stressing and some cracks may partly close when pre-stressing is applied.

The simulated tangential stresses are shown at a cross section through the cylindrical wall at an elevation of +9 m at day 384 and 384.17, see Figure 7.19.

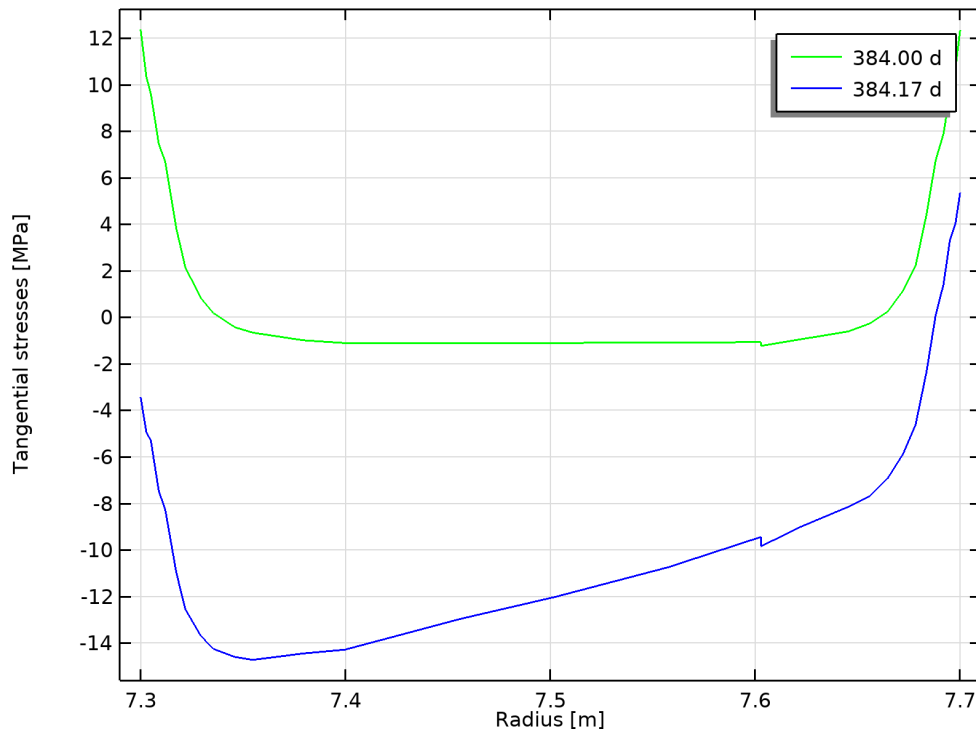


Figure 7.19 Tangential stresses at a cross section of the cylindrical wall at an elevation of +9 m

The tangential stresses that the boundary surfaces of the structure are in tension at a magnitude of 12 MPa before pre-stressing, which is above the tensile strength (4.5 MPa). These stresses are caused by shrinkage as an effect of drying. In the centre, tangential stresses are in compression of about 1 MPa. After pre-stressing of the tendons, the surface stresses are reduced. The stresses at the interior surface are in compression of about 3.5 MPa and the exterior surface is still in tension but at a reduced magnitude 5 MPa, slightly above the tensile strength.

In the central parts of the cylindrical wall, there are compressive stresses both before, about -1 MPa, and after pre-stressing of the tendons, about -12 MPa. The compressive tangential stresses after pre-stressing are significantly larger than the vertical compressive stresses, see Figure 7.19. As explained above this is because of the larger number of horizontal tendons, about 4 times the number of vertical tendons. The RC is designed like this because the interior pressure creates higher tensile stresses in the horizontal (tangential) direction.

#### 7.1.7 Evolution of strains with time using the wedge geometry

In this section the strain evolution with time is shown at several points in the RC evaluated by using the wedge geometry. All points are presented in Table 7.2 and Table 7.3. In these tables, the zone, strain gauge name, radius, height, angle, and direction of the strain gauges are specified. The third letter of the strain gauge name, I and E, indicates if the gauge is placed near the interior or the exterior

surface of the concrete structure. The last letter in each name indicates the direction of the gauge; radial, R, vertical, V, tangential, T, or, meridian, M. The meridian and the tangential directions are illustrated in Figure 7.20.

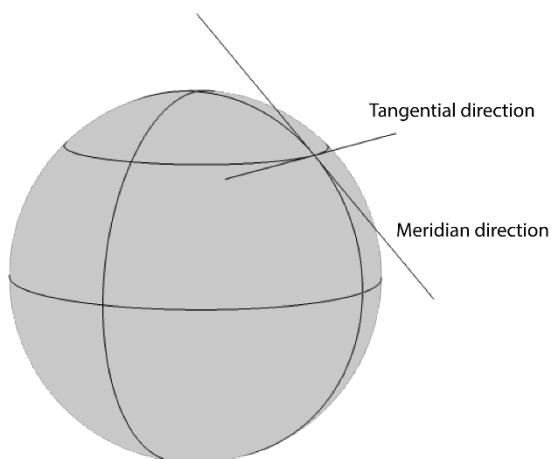


Figure 7.20 Illustration of the tangential and the meridian direction on a sphere, which has a similar shape as the dome.

The results are presented in the order of the zone in which the gauges are placed in the RC.

Table 7.2 Specification of the zone, name and position of the strain gauges selected by benchmark VERCORS 2022.

Zone	Strain gauge	Radius	Height	Angle	Direction
Raft	C1_CENTRE_95_R	0	-1.73	95.0	Radial
	C1_CENTRE_195_R			195.0	Radial
	E1_CENTRE_95_R	0	-1.15	95.0	Radial
	E1_CENTRE_195_R			195.0	Radial
Gusset	F1IV	7.24	-0.88	172.0	Vertical
	F1IT				Tangential
	F2EV	7.58	-0.90	172.3	Vertical
	F2ET				Tangential
	G1IV	7.40	-0.25	172.2	Vertical
	G1IT				Tangential
	G2EV	7.61	-0.25	172.3	Vertical
	G2ET				Tangential
Cylindrical part (mid height)	P1EV	7.65	8.01	389.3	Vertical
	P1ET				Tangential
	P2IV	7.31	8.01	387.8	Vertical
	P2IT				Tangential
	H1EV	7.58	8.43	172.0	Vertical
	H1ET				Tangential
	H2IV	7.42	8.43	172.0	Vertical
	H2IT				Tangential
	H5EV	7.65	8.00	369.0	Vertical
	H5ET				Tangential
	H6IV	7.40	7.99	367.7	Vertical
	H6IT				Tangential

**Table 7.3 Specification of the zone, name and position of the strain gauges selected by benchmark VERCORS 2022.**

Zone	Strain gauge	Radius	Height	Angle	Direction
Equipment hatch	M3EV	7.75	8.7	222.0	Vertical
	M3ET				Tangential
	M4IV	7.39	8.69	222.2	Vertical
	M4IT				Tangential
	M7EV	7.63	10.40	232.1	Vertical
	M7ET				Tangential
	M8IV	7.38	10.40	232.1	Vertical
	M8IT				Tangential
Dome	I1_194_EM	0	19.75	194	Radial
	I1_94_EM				Radial
	I2_194_IM	0	19.60	194	Radial
	I2_94_IM				Radial
	J1EM	5.93	17.80	344	Meridian
	J1ET				Tangential
	J2IM	6.00	17.73	344	Meridian
	J2IT				Tangential

Note that two of the gauges at the equipment hatch, M3EV and M3ET, are located at a radius of 7.75 m. The simplified geometry of the cylinder wall used in this study has an inner radius of 7.3 m and an outer radius of 7.7 m. Consequently, these two gauge points fall outside the scope of the simplified model, making it impossible to evaluate their results. It is worth mentioning that none of the gauges are placed precisely at the surface.

Additionally, it is important to observe that four gauges in the raft and four gauges in the dome are placed in the centre of the structure at a radius of 0 m and at different heights. Four of these eight gauges show the radial strains at an angle of 94 or 95 gradians and the other four at an angle of 194 or 195 gradians. Note that an angle of 100 gradians corresponds to a right angle. Each strain gauge position is shown in Figure 7.21.

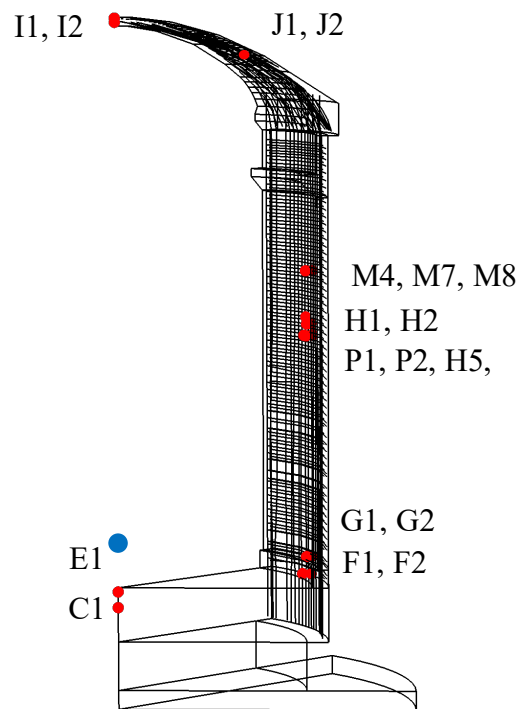


Figure 7.21 Overview of the wedge geometry, tendon configuration, and positions, red dots, at which the strains are evaluated. Origo of the coordinate system is marked with a blue dot.

Seven significant variations in strain occur in all gauges, at day 469, 551, 964, 971, 1344, 1699, 2403, and 2806. These changes correlate to the periods at which the climate control system was switched off before and during the pressure tests. The temperature strains are not included in the measurements from VERCORS. Therefore, the impact of temperature is not included in the results of this study to make measurements and calculations comparable. The presented model includes temperature effects to make it complete.

The effect of temperature induced strains is illustrated with an example from point P2 where the total tangential strains are shown in the same graph as the measured strains with deducted temperature strains. In Figure 7.22 and Figure 7.23 the total calculated strains, P2IT, and the measured strains, P2IT meas, without temperature induced strains in P2 are shown.

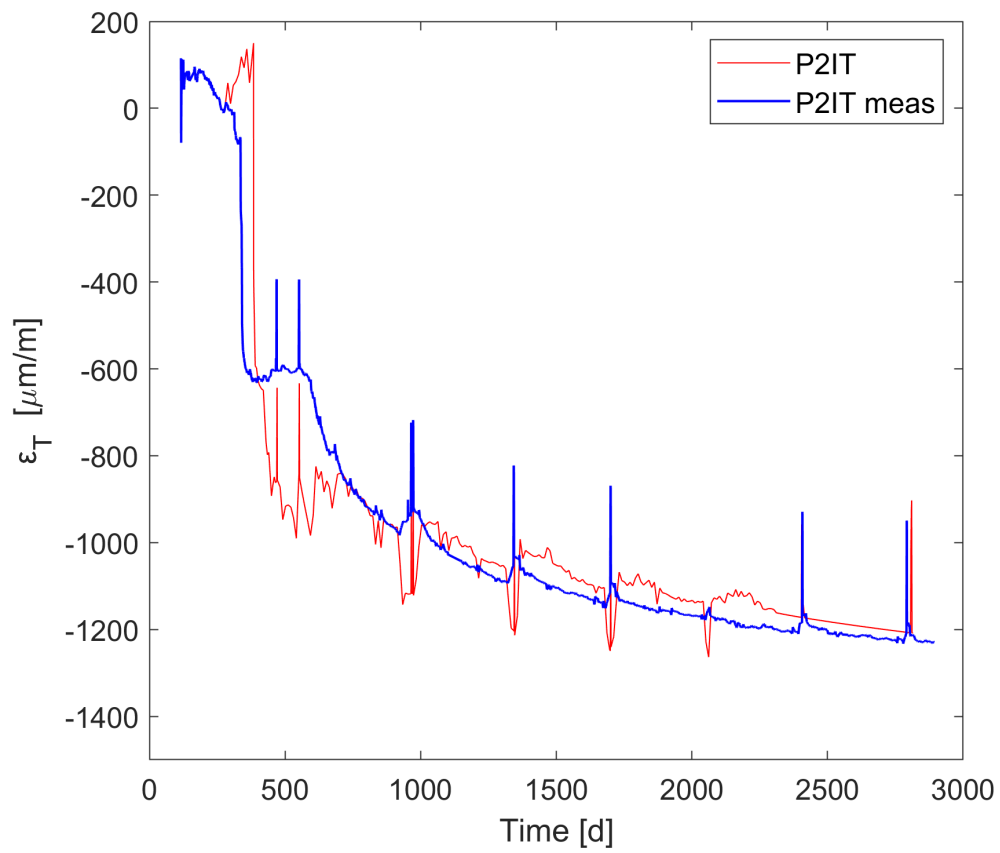


Figure 7.22 Overview of total tangential strains in point P2.

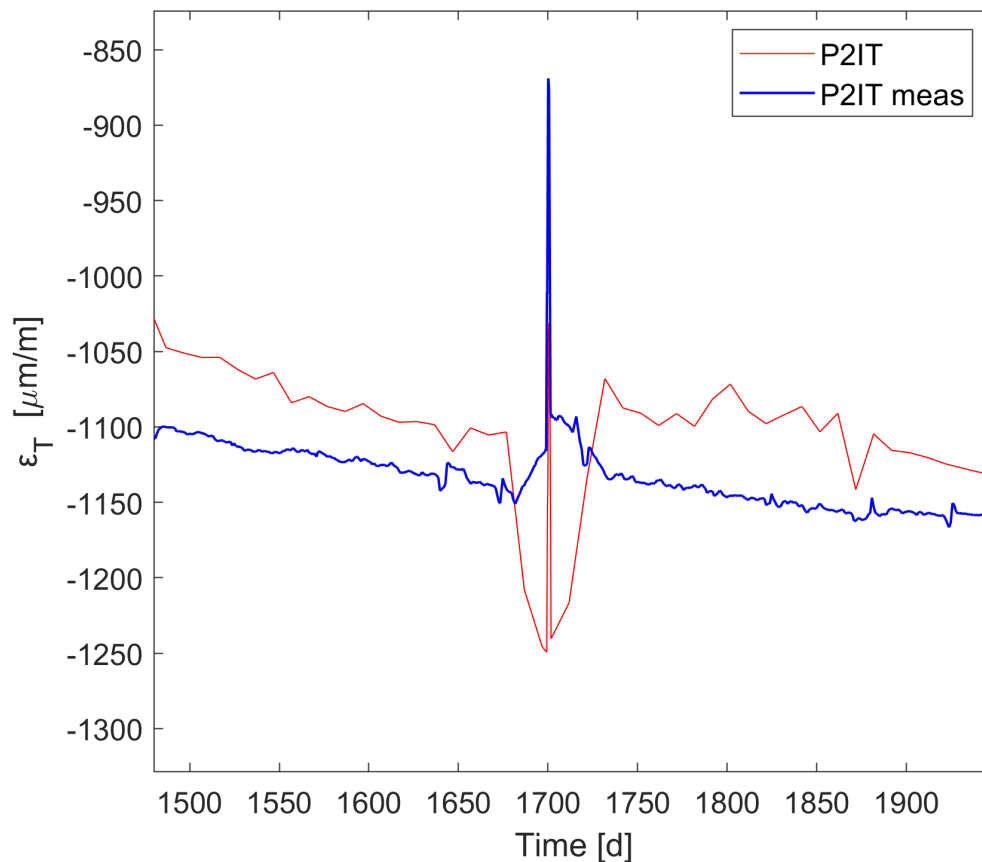


Figure 7.23 Detail of tangential strains in point P2

Temperature fluctuations exert a significant impact on the overall tangential strains, as shown by the pronounced variations in the thin red line in Figure 7.22. Particularly noteworthy is the considerable decrease, from  $-1100 \mu\text{m/m}$  to  $-1250 \mu\text{m/m}$ , in the calculated *total tangential strain*, P2IT, especially in the periods before and during each pressure test, see Figure 7.23, at day 1675 to 1725. This decrease in radius is caused by the temperature decrease that occurs when the climate control system is turned off before and after the pressure test. Simultaneously, humidity increases, which makes the radius to expand, tangential strains increase from  $-1125 \mu\text{m/m}$  to  $-1075 \mu\text{m/m}$  as a result of the swelling of the RC, P2IT meas, hump at day 1675 to 1725, see Figure 7.23. These two volumetric changes act in opposite directions one increases (increase in humidity) and the other decreases (decrease in temperature) the radius. To distinguish the impacts of humidity-induced volumetric effects, the temperature induced strains were excluded from the measurements.

To ensure a meaningful comparison between calculations and measurements, it is essential that the model accounts for temperature-induced strains. If the temperature strains are deducted, which is the case with the provided strains from the benchmark VERCORS 2022, the model should not include temperature strains to enable a direct comparison between measurements and simulation results.

Figure 7.24 and Figure 7.25 show both the calculated, narrow blue and red solid lines, and measured, wide blue and red solid lines, strains at a randomly selected example point. The behaviour of all investigated points in the RC exhibits a consistent pattern.

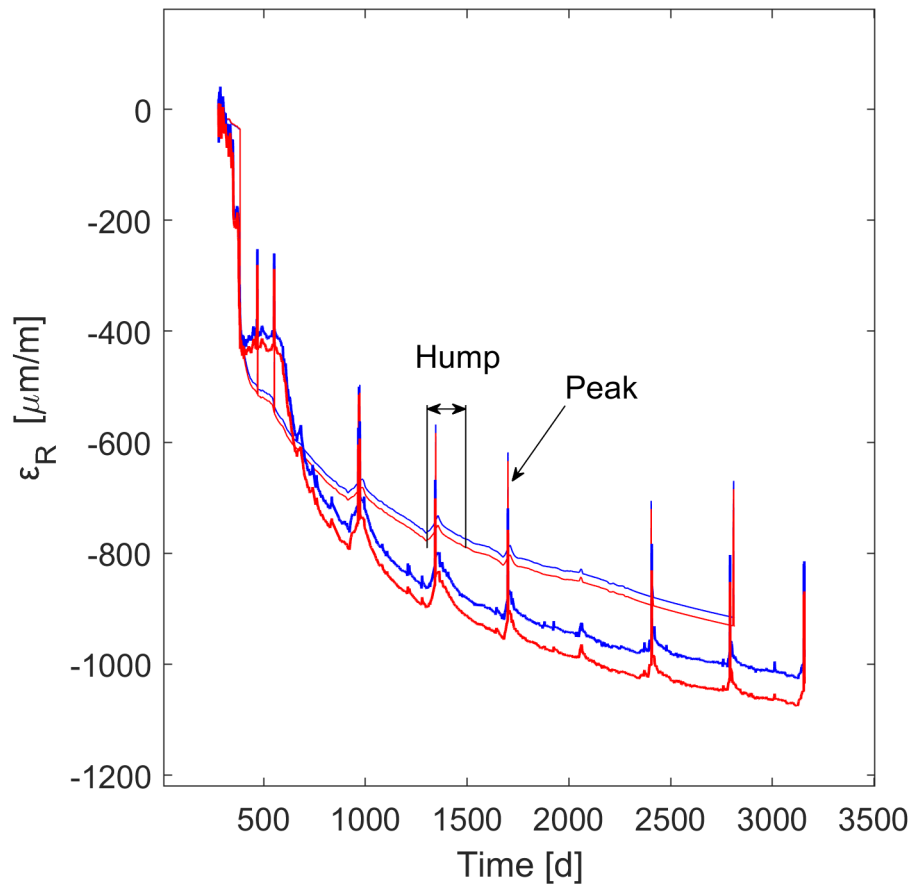


Figure 7.24 Overview of radial strains at a randomly selected example point.

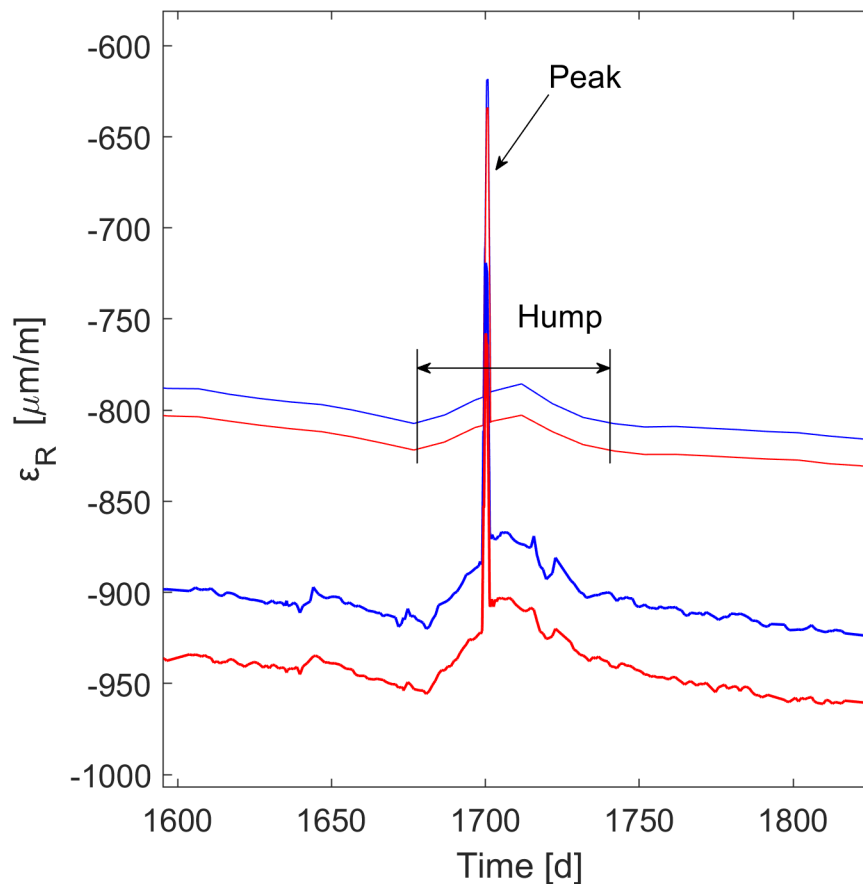


Figure 7.25 Detail of radial strains at a randomly selected example point.

Several effects are observed in this study. Firstly, a long-term creep effect resulting from tendon pre-stressing is apparent, see Figure 7.24. Secondly, semi short-term effects occur due to an increase in relative humidity between 40 and 100 days before and during each pressure test, referred to as “humps”, see Figure 7.25. Thirdly, short-term effects are evident during the actual pressure test, referred to as “peaks”. The influence of temperature on the strains is not included.

The calculated and the measured radial strains,  $\epsilon_R$ , at two positions in the raft, C1 CENTRE\_95\_R and E1 CENTRE\_95\_R, are shown in Figure 7.26.

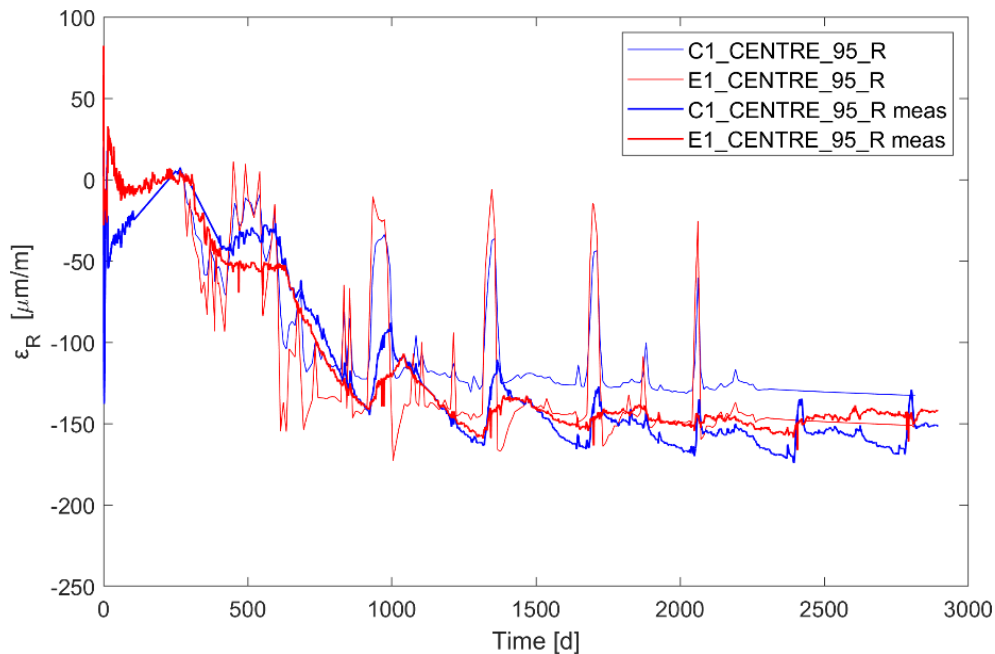


Figure 7.26 Radial strains, calculated and measured at points E1 and C1 (angle 95 gradians).

The calculated radial strains in the raft, gauge C1 95 and E1 95, exhibit a small magnitude during the simulation,  $150 \mu\text{m/m}$ . This is expected because of the raft's very stiff design. Creep is showing but the magnitude is small compared to other parts of the RC, for example the cylinder wall, see Figure 7.30. In addition, there is no response in radial strain from the pressure tests because of the large stiffness of the raft. The increasing relative humidity before and during the pressure test induces an expansion of the material, this is showing as a hump in the radial direction, see day 950 until day 1000 and 1350 to 1400 in Figure 7.26. The calculated strain humps have a larger magnitude, about  $125 \mu\text{m/m}$ , than the measured humps, about  $50 \mu\text{m/m}$ .

The calculated and measured radial strains,  $\varepsilon_R$ , in the other gauges near the centre of the raft, C1 CENTRE\_195\_R and E1 CENTRE\_195\_R, are shown in Figure 7.27. These gauges are perpendicular to gauge C1 CENTRE\_95\_R and E1 CENTRE\_95\_R.

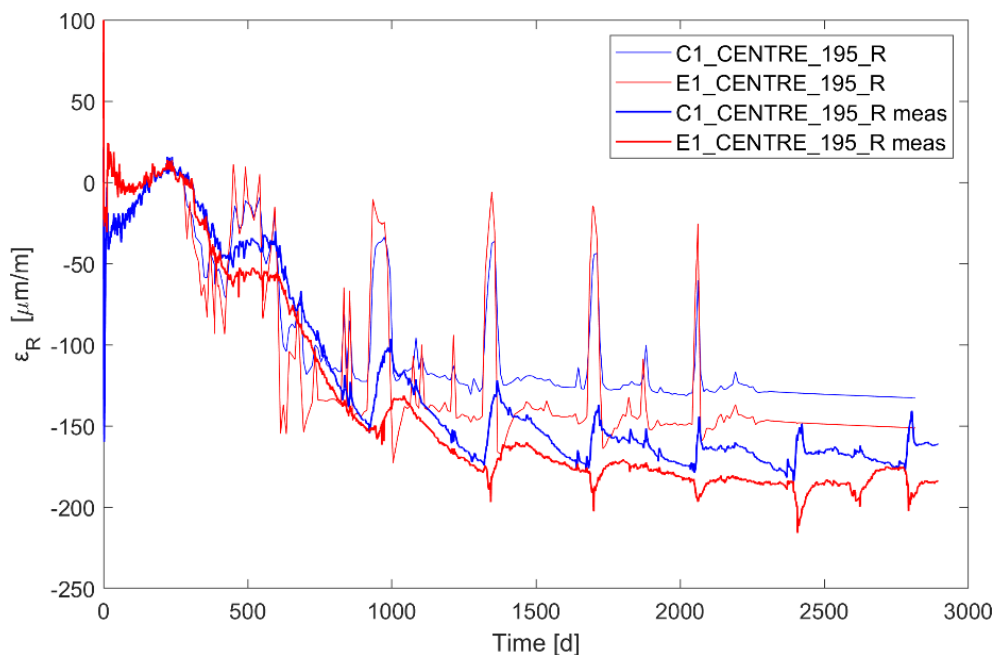


Figure 7.27 Radial strains, calculated and measured, at C1 and E1 (angle 195 gradians).

The radial strains in the points in the raft, C1 CENTRE\_195\_R and E1 CENTRE\_195\_R, show a similar magnitude, around 150  $\mu\text{m}/\text{m}$ , as the two gauges that are perpendicular to these gauges, C1 CENTRE\_95 and E1 CENTRE\_95. The strains also show a similar behaviour in response to the relative humidity variations.

The calculated and measured tangential strains,  $\varepsilon_T$ , in the gusset in F1 and F2 (0.12 m vertical distance from raft top), and G1 and G2 (0.75 m vertical distance from raft top), are shown in Figure 7.28 and Figure 7.29, respectively.

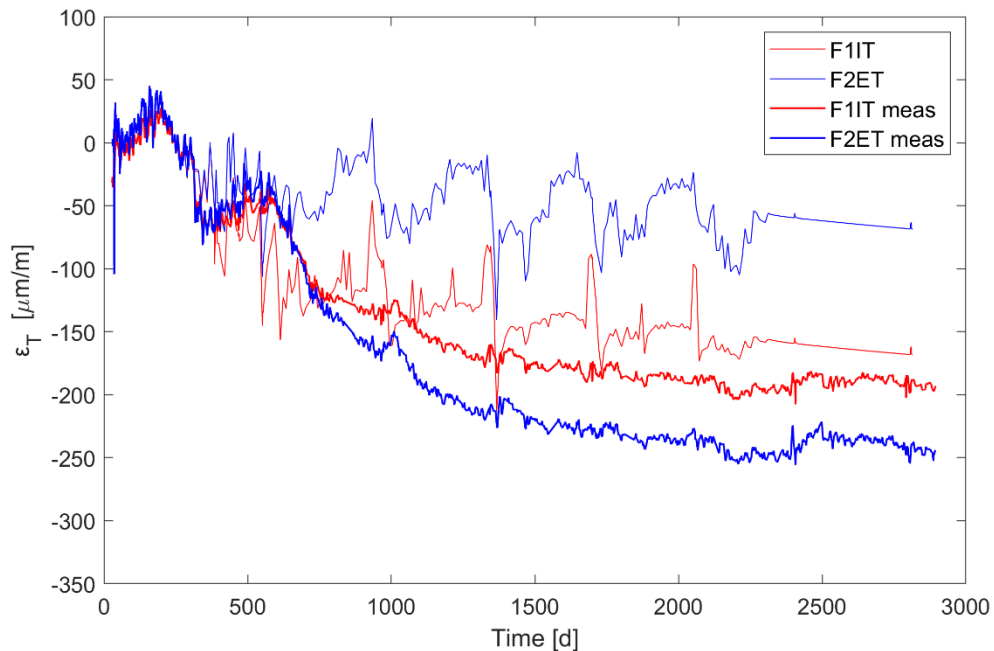


Figure 7.28 Tangential strains, calculated and measured, at F1 and F2.

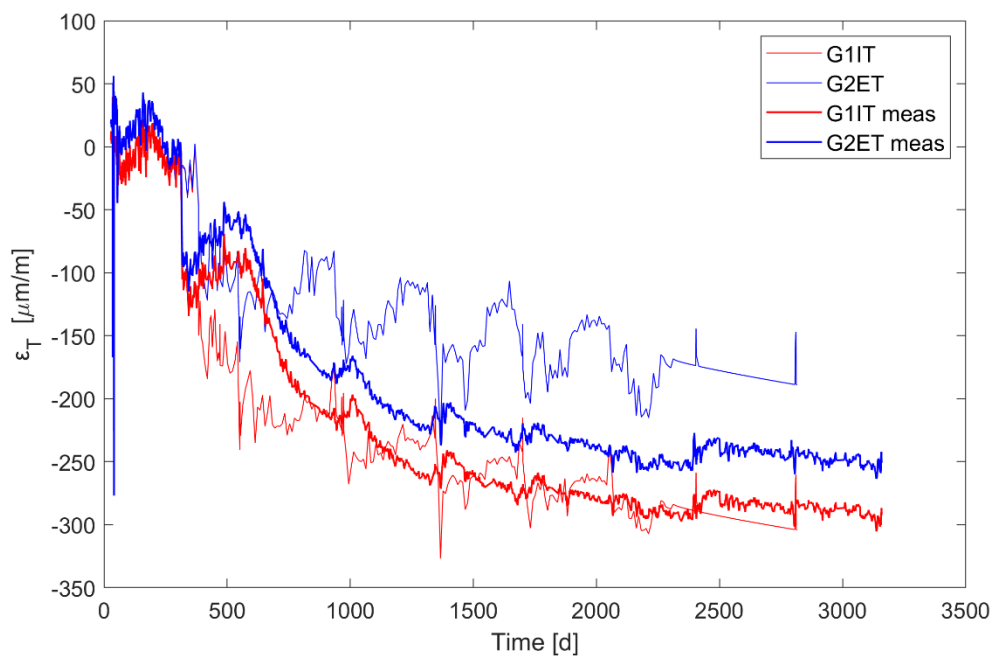


Figure 7.29 Tangential strains, calculated and measured, at G1 and G2.

The evolution of tangential strains in the four positions clearly show an impact of creep, the gradual change of strains with time, see Figure 7.28 and Figure 7.29. The

shrinkage is less clear but is evident as a hump in measurements at day 950 to 1050, see Figure 7.28 and Figure 7.29. The calculated strains in F1 differ from the measured, around 20%. In F2 the calculated strains are  $50\mu\text{m}/\text{m}$ , which is an underestimation by about  $200\mu\text{m}/\text{m}$ , compared with the measured strains  $250\mu\text{m}/\text{m}$ . F1 and F2 show a smaller impact of creep,  $50\text{-}150\mu\text{m}/\text{m}$  compared with G1 and G2,  $150\text{-}300\mu\text{m}/\text{m}$ . The two points, F1 and F2, show smaller strains during the simulations compared to G1 and G2. This is expected since the F1 and F2 gauges are placed closer to the stiff raft. The performed pressure tests have a larger impact on the calculated strains in G1 and G2, which are located at a larger distance from the raft, see Figure 7.29 day 2400 and 2800. The small peaks due to the pressure tests are hardly noticeable in the calculations of F1 and F2, see Figure 7.28 day 2400 and day 2800. There are no clearly distinguishable peaks in the measured strains that corresponds to the pressure test, neither in F1 and F2 nor in G1 and G2. The magnitude of the strains increases gradually, and this is an effect of the continuous decrease of the RC's radius due to creep. The reason for the larger difference between measurements and calculations on the outside compared with the inside, may be that the Eurocode creep model has a lower accuracy at a higher relative humidity range above 80% RH.

The calculated and measured tangential strains,  $\varepsilon_T$ , in the cylindrical wall, at points P1 and P2, H1 and H2, and H5 and H6, are shown in Figure 7.30, Figure 7.31 and Figure 7.32. Note that the measurements in H2 did not work between day 200 and day 1200.

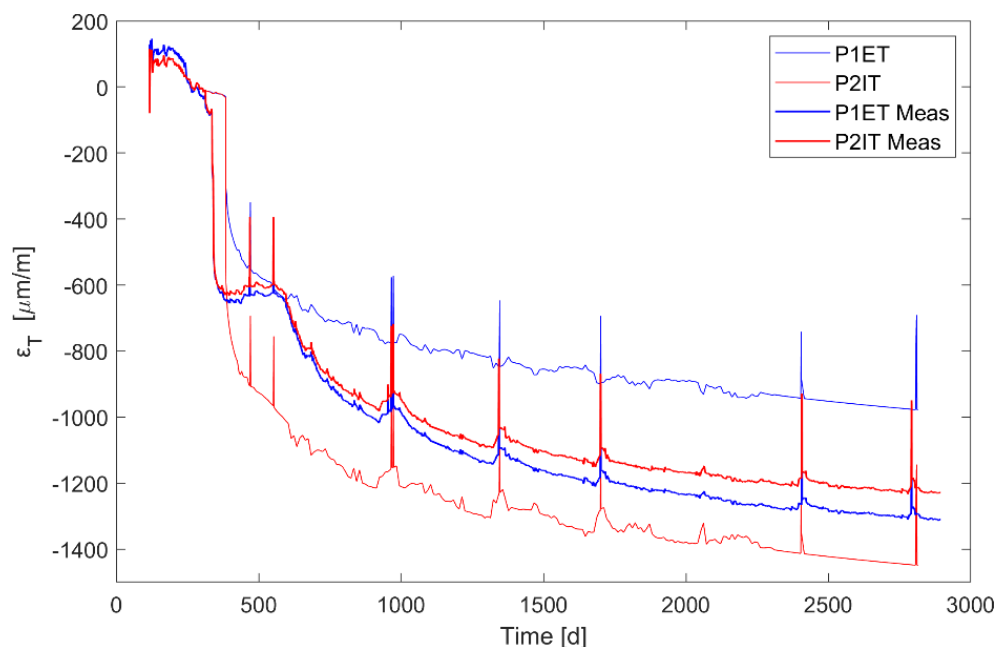


Figure 7.30 Tangential strains, calculated and measured, at P1 and P2.

The calculated tangential strains in P2 are larger than the measured strains. After day 1200 the simulated tangential strains are about  $200\mu\text{m}/\text{m}$  larger than the measured strains, and the difference is rather constant through time. This means

that the used model overestimates the total tangential strains, excluding thermal strains, about 20%. This is caused by the overestimated tangential strains because of pre-stressing.

The calculated tangential strains in P1 are smaller than the measured strains. After day 1200, the simulated vertical strains are about  $300 \mu\text{m/m}$  smaller than the measured strains and the difference is rather constant until the end. This means that the used model underestimates the total tangential strains, excluding thermal strains, about 25%. This is caused by the underestimation of tangential strains because of pre-stressing.

The calculated strains caused by both shrinkage and creep are of an equal rate as the measurements in both P1 and P2.

The points responses to pre-stressing are in some cases underestimated and in other overestimated by the applied model compared with the measurements.

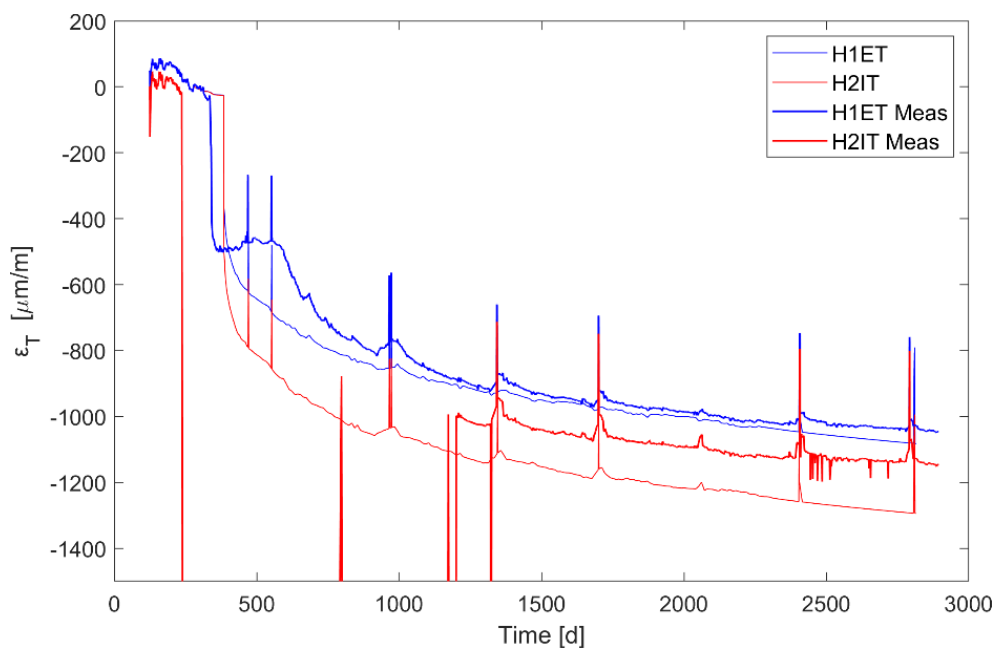


Figure 7.31 Tangential strains, calculated and measured, at H1 and H2.

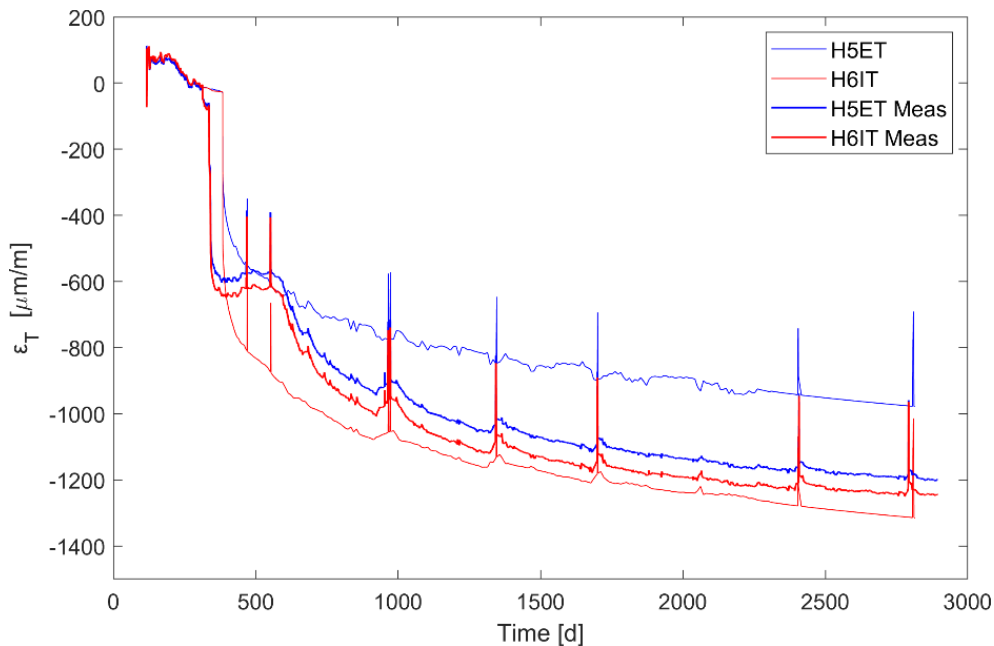


Figure 7.32 Tangential strains, calculated and measured, at H5 and H6.

The tangential strains in points P1ET, P2IT, H1ET, H2IT, H5ET, and H6IT all show a similar behaviour, and the response resulting from creep, relative humidity and pressure tests are more or less equal. This is expected since these points are exposed to similar loads. In addition, these points are not located near any geometrical discontinuities or irregularities, like sharp corners or holes. Furthermore, they are located at mid height of the RC, where the raft and the dome have a minor impact on the stiffness. The strains at the end of the simulation reach a magnitude between 900  $\mu\text{m/m}$  to 1300  $\mu\text{m/m}$ .

All points that are located near the interior of the RC, P2, H2 and H6, show larger calculated tangential strains than measured. This may suggest that the applied model overestimate the strains during pre-stressing. The exterior points P1, H1 and, H5, the calculated strains caused by pre-stressing are of an equal magnitude as the measured.

The strain humps that occur in the measurements are of a larger magnitude compared to the calculated. This suggests that the model underestimates the shrinkage and swelling caused by drying and wetting. The large hump in the measurements between day 400 and day 600 is also found in the calculations, but the hump is not as prominent because of the creep that occurs simultaneously. At later pressure tests, the humps in the calculations are easier to find.

The peaks in tangential strain are caused by the actual pressure test. These peaks clearly show in all points. In the tangential direction the predicted and the measured strains are of equal magnitude, about 200-250  $\mu\text{m/m}$ .

The calculated and measured tangential strains,  $\epsilon_T$ , in M3 and M4, and M7 and M8, are shown in Figure 7.33 and Figure 7.34. M3 and M4 are beside the equipment hatch and M7 and M8 are above the hatch. Note that this hatch is not included in

the geometry in the wedge study. Another missing geometric entity is the concrete wall thickness increase around the equipment hatch. A third difference is the simplification of the irregular tendon configuration around the equipment hatch. M3 is located outside of the wedge geometry and therefore, it is not possible to evaluate strains at this point.

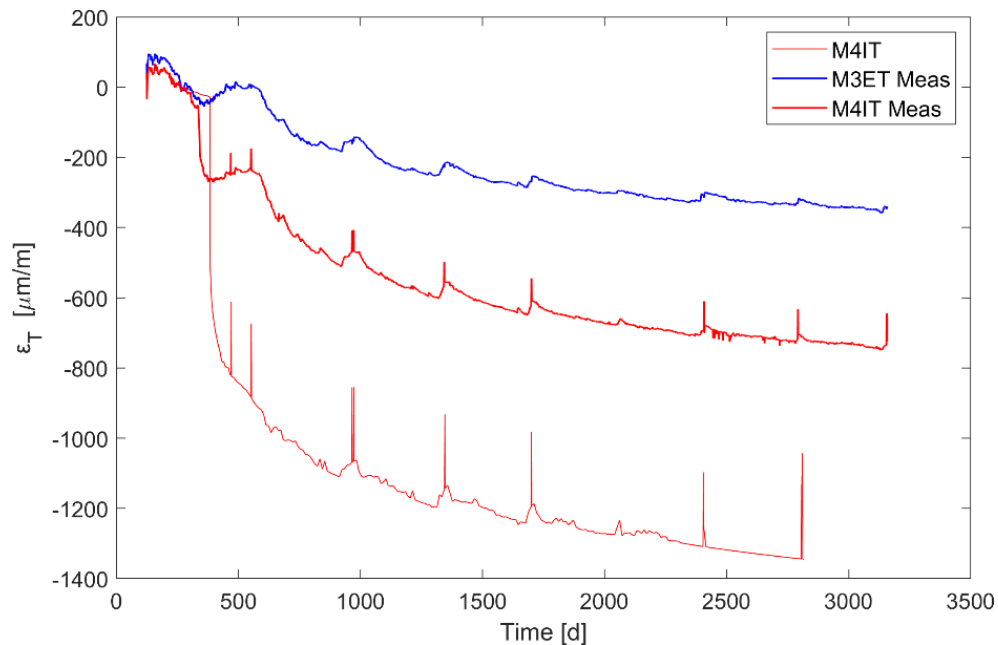


Figure 7.33 Tangential strains, calculated and measured, at M3 and M4

The measured strains in M3 lack the response to pre-stressing that M4 show, around day 300, see Figure 7.33.

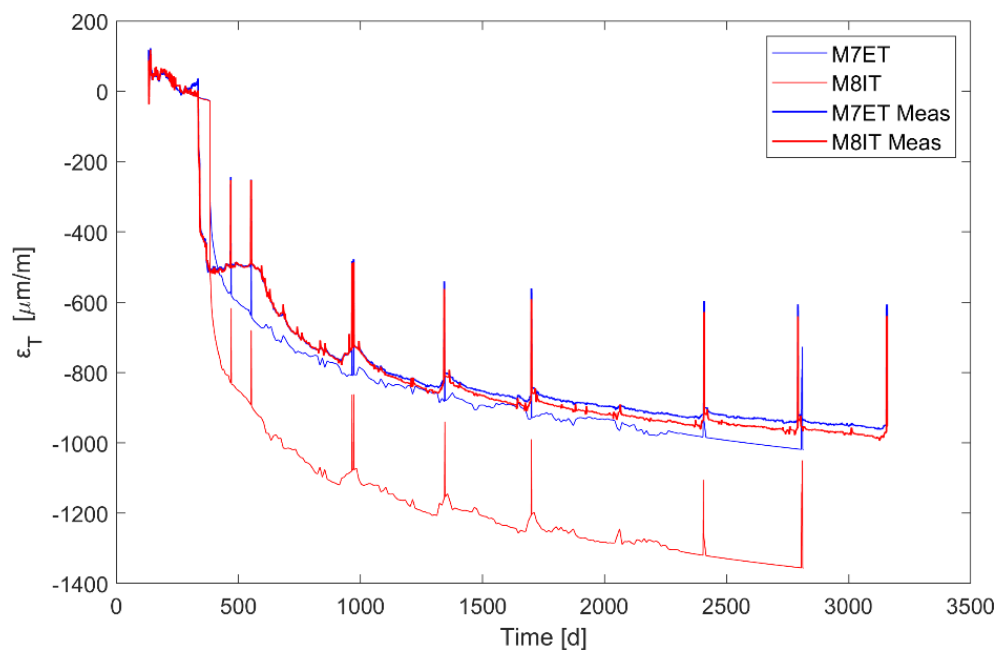


Figure 7.34 Tangential strains, calculated and measured, at M7 and M8.

The calculated tangential strains in the interior points M4 and M8 are larger than the measured strains, around 1200  $\mu\text{m}/\text{m}$  compared to 900  $\mu\text{m}/\text{m}$ .

The measured tangential strains in M3 and M4 are much lower than in M7 and M8 and this may be an effect caused by the equipment hatch. The door that covers the equipment hatch affects the stiffness in that location. This changes the stress distribution in the tangential direction at M3 as it is located beside the hatch. Tangential strains in point M7 and M8 are not that much affected by the equipment hatch since they are located above the hatch.

Regular strain humps occur both in the measurements and the calculations before and during each pressure test. These humps are a result of the increase of relative humidity inside the RC. When the humidity inside the RC wall radius increases. The magnitude of these humps in the calculations and measurements are equal, except for the first large hump at day 300 to 600 which is considerably larger than the calculations.

The peaks that are a direct structural response to the pressure tests are clearly shown by the measurements in points M4, M7 and M8 but not in point M3. The calculations overestimate the magnitude of the structural response in M4 by a factor of 3. The magnitude of calculated tangential peaks M7 and M8 are equal to the measured.

The calculations show that the early rate of creep is overestimated in the interior points M4 and M8. The creep rate in the calculations, at day 700 and onward, is almost identical to the measured, see Figure 7.34.

The calculated and the measured radial strains,  $\varepsilon_R$ , at two points in the dome, I1 94 EM and I2 94 IM, are shown in Figure 7.35.

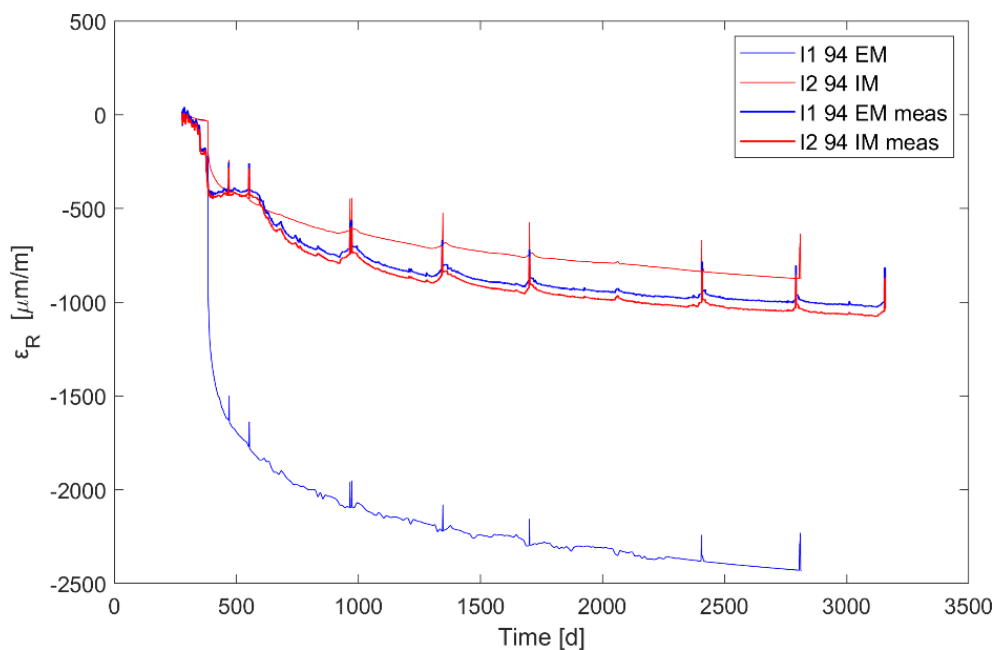


Figure 7.35 Radial strains, calculated and measured at points I1 and I2 in the dome, (angle 94 gradians).

The calculated radial strains at I2 decreases gradually with time from 0 (zero)  $\mu\text{m}/\text{m}$  to about  $700 \mu\text{m}/\text{m}$ , see Figure 7.35. The measurements show larger radial strains than what the model predicts. The increase of radial strains in point I1 is much higher than the measurements. This point is most likely affected by a mesh singularity at the top of the dome which did not affect I2\_94 IM.

The gradual strain increase is an effect of the creep that the concrete exhibits because of tendon pre-stressing. Additionally, the radial strains in both I1 and I2 are affected by the increasing relative humidity before and during the pressure tests, visible as humps. During the pressure tests, the dome diameter temporarily increases, and this is clearly shown as peaks, see e.g. day 2400 (roughly).

The calculated and measured radial strains,  $\varepsilon_R$ , in I1 194 EM and I2 194 IM are shown in Figure 7.36. These two sensors are perpendicular to I1\_94 EM and I2\_94 IM.

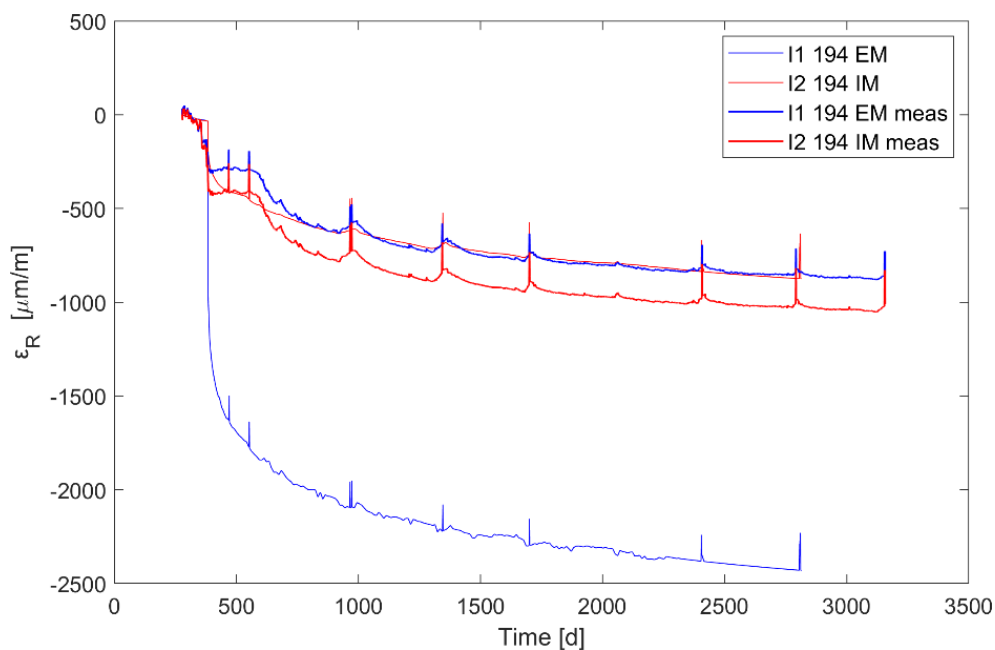


Figure 7.36 Radial strains, calculated and measured, at I1 and I21 (angle 194 gradians).

The magnitude in dome gauge I2\_194 IM shows that the radial strains of the RC decreases continuously. The calculated radial strains gradually decrease to a magnitude of about  $700 \mu\text{m}/\text{m}$ . The measurements show that the radial strains are about  $900 \mu\text{m}/\text{m}$ . This means that the model underestimates the radial strains in the dome centre. In this evaluation, point I1\_194 EM also shows that the radius decreases significantly which is most likely affected by a possible mesh singularity at the top of the dome.

Calculated and measured tangential strains in J1 and J2 are shown in Figure 7.37.

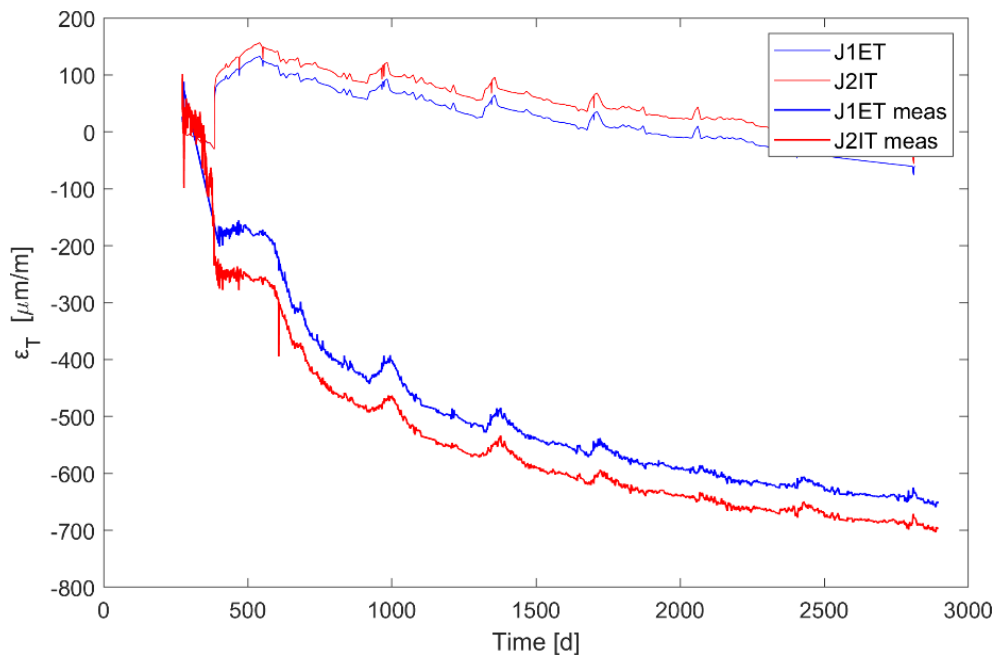


Figure 7.37 Tangential strains, calculated and measured, at J1 and J2.

The calculated tangential strains increase as a response to the pre-stressing of the tendons. This means that the radius increases but it should really decrease when the tendons are tensioned. This erroneous behaviour suggests that the simplified geometry used in the wedge study is not able to describe the structural behaviour of the pre-stressing in these points. One reason for this behaviour is that the mechanical boundary conditions are not feasible. To further enhance this, additional investigations are needed, or a comprehensive geometric approach can be employed. Conversely, the calculated creep rate shares the same magnitude and affects the structure in a manner consistent with the measured data. This behaviour can also be attributed to the fact that the tendon arrangement in the wedge model differs from that of the actual structure.

The measured strains clearly show that the radius decreases as the pre-stressing is applied. Regular strain humps in tangential strains occur because of the relative humidity increase before and during each pressure test. The measurements in J1 and J2 do not show any peaks as a response to the actual pressure tests.

The calculated and measured vertical strains,  $\epsilon_V$ , in the gusset in F1 and F2 (0.12 m vertical distance from raft top), and G1 and G2 (0.75 m vertical distance from raft top), are shown in Figure 7.38 and Figure 7.39, respectively.

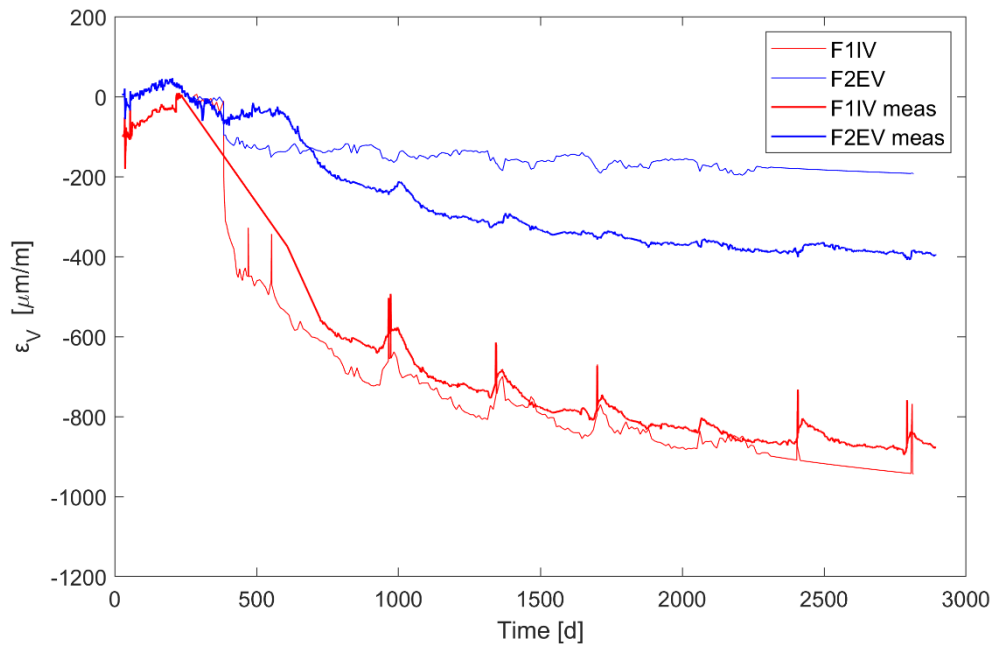


Figure 7.38 Vertical strains, calculated and measured, at F1 and F2.

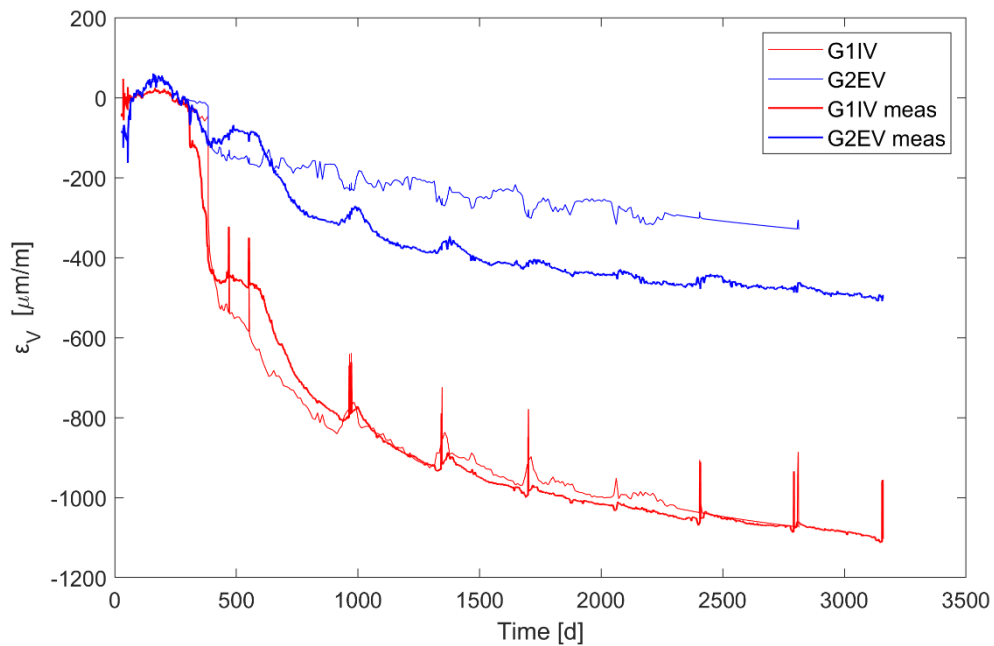


Figure 7.39 Vertical strains, calculated and measured, at G1 and G2.

The evolution of the vertical strains in the gusset show that the impact of creep is largest at F1 and G1, which are close to the interior surface. This may be an effect of the differences in stresses that has a large impact on creep. The magnitudes of the

calculated and the measured vertical strains in these two points are equal. However, the calculated and the measurement humps differ in size. In point F2 and G2 the calculated vertical strains underestimate the strain measurements.

The regular strain humps that occur in the measured strains are also visible in the calculated strains in the interior points, F1 and G1, see for example at day 1000 and day 1400. These humps correlates to the increase in relative humidity in the interior that take place before and during the pressure test. The measured and the calculated humps are of an equal magnitude. Note that the calculation at day 2400 and day 2800 do not show any humps. This is because the relative humidity was kept constant during the final part of the calculation.

The response of the pressure tests, peaks in vertical strain, is largest in point G1  $\sim 200 \mu\text{m/m}$  and smallest in point F2, not visible. G1 is located close to the interior of the RC, and also far from the stiff raft. F2 is located in the exterior of the gusset closer to the stiff raft. The difference in distance from the point to the raft, may be an explanation to the differences in response shown by the G1 and F2 during pressure tests.

Vertical strains,  $\varepsilon_V$ , calculated and measured, in point P1 and P2, H1 and H2, and H5 and H6, are shown in Figure 7.40, Figure 7.41, and Figure 7.42, respectively. These six points are in the cylindrical part at mid height,  $\sim 9 \text{ m}$  above the raft top surface. The altitude of P1, P2, H5, and H6 is 8 m, and H1 and H2 is 8.43 m.

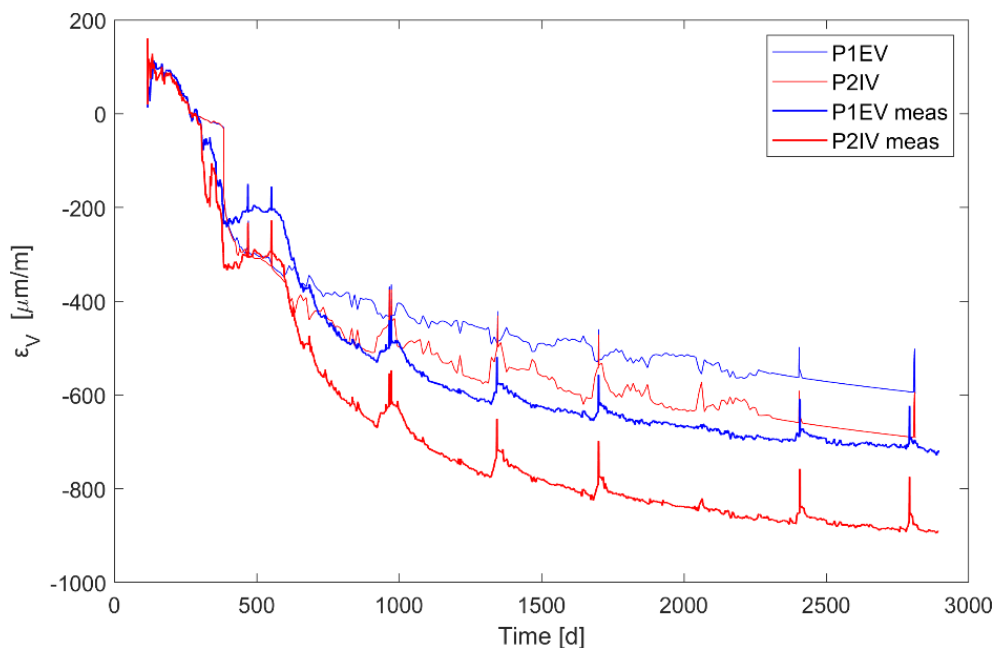


Figure 7.40 Vertical strains, calculated and measured, at P1 and P2.

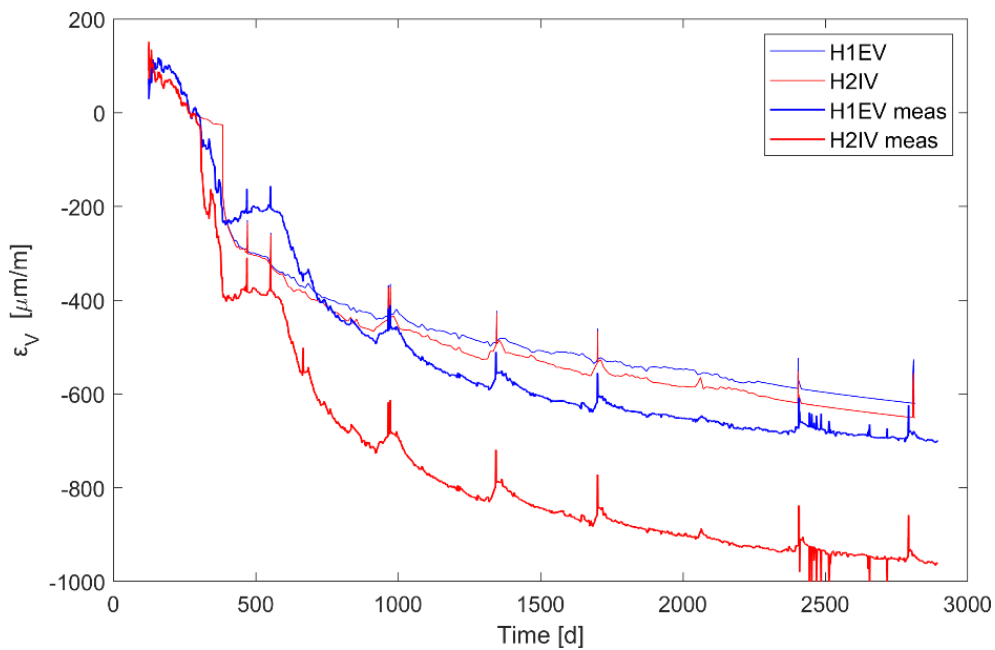


Figure 7.41 Vertical strains, calculated and measured, at H1 and H2.

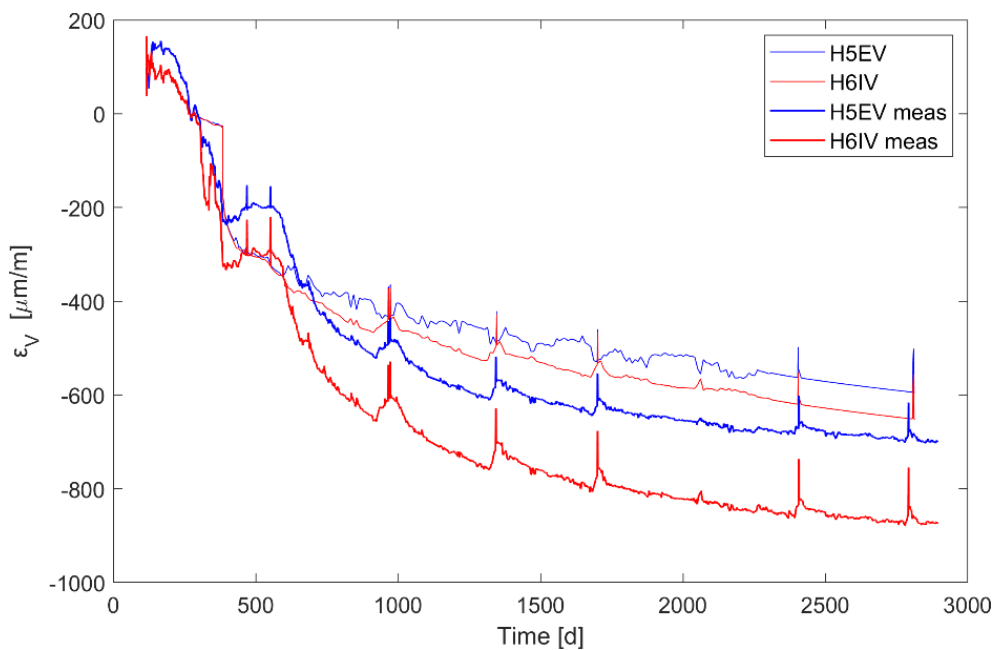


Figure 7.42 Vertical strains, calculated and measured, at H5 and H6.

The sharp change in the vertical strains at day 384 occurs because of the applied pre-stressing of the tendons. This sharp change is not as easily identified in the measured vertical strains due to the gradual application of the pre-stress.

After day 1200 the simulated vertical strains are about 150  $\mu\text{m/m}$  smaller at P1, H1 and H5, and about 300  $\mu\text{m/m}$  smaller at P2, H2 and H6 than the measured strains and the difference is rather constant. This means that the used model is able to

capture the long-term deformations caused by creep and shrinkage. However, the model underestimates the total vertical strains about 20%.

The predicted vertical and measured vertical strains caused by the pressure tests are almost identical in magnitude, about  $100 \mu\text{m/m}$ .

The strain humps at the interior side P2, H2, and H6, that occurs before and during the pressure tests are of an equal magnitude as the measured humps. These are caused by the increase of relative humidity, from 30% RH to 95% RH, inside the RC before and during the pressure test. The exterior points seem to underestimate the humps. The exterior is also subjected to an increase in relative humidity however not as large as the interior increase, from 50% RH up to 95% RH.

The calculated and measured vertical strains,  $\varepsilon_V$ , in point M3 and M4, are shown in Figure 7.43. Note that these points are located beside the equipment hatch, where the wall thickness is 0.66 m, compared with the surrounding cylindrical wall which is 0.4 m thick. The location of the points means that the equipment hatch may have a minor effect on the structural integrity and stiffness, as the strains are evaluated in the vertical direction.

As the wedge geometry excluded the wall thickness increase, it was not possible to evaluate vertical strains at point M3.

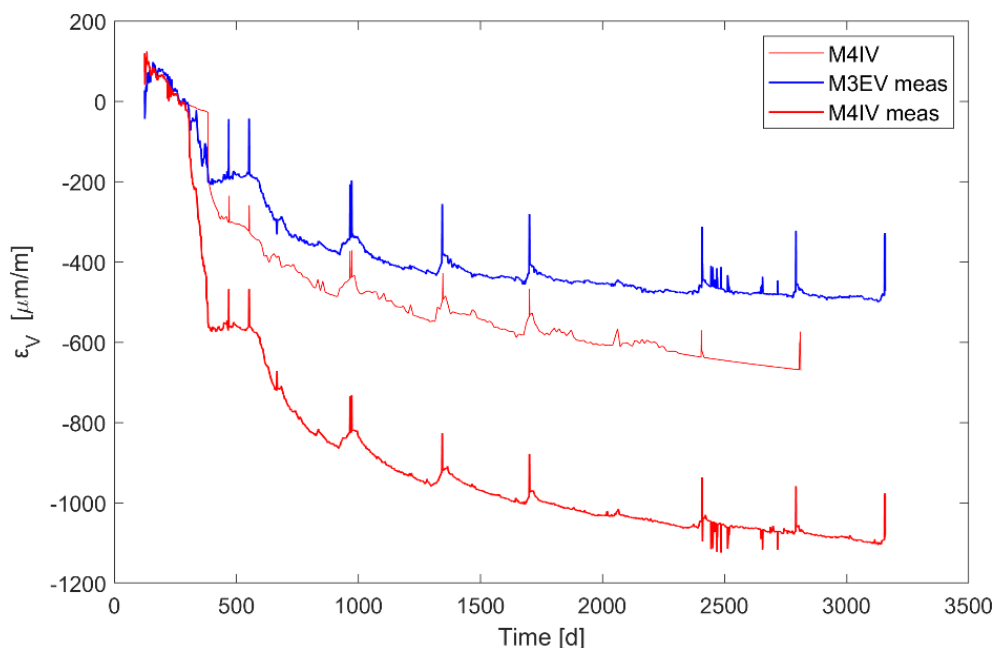


Figure 7.43 Vertical strains, calculated and measured, at M3 and M4.

The measurements in point M3 show a minor response to the pre-stressing of the tendons. This response may be explained because of the increased thickness of the cylinder wall around the equipment hatch which increases the stiffness. In point M4 the measurements clearly show a response of the pre-stressing as expected.

The evaluated vertical strains in M4 shows that the applied model underestimate the measurements by approximately 50%.

The calculated and measured vertical strains,  $\varepsilon_V$ , in point M7 and M8, are shown in Figure 7.44. Note that these points are located above the equipment hatch, where the wall thickness is 0.66 m, compared with the surrounding cylindrical wall which is 0.4 m thick. The equipment hatch influences the stiffness of the structure. Given that points M7 and M8 are positioned above the hatch, the strains in the vertical direction could be affected.

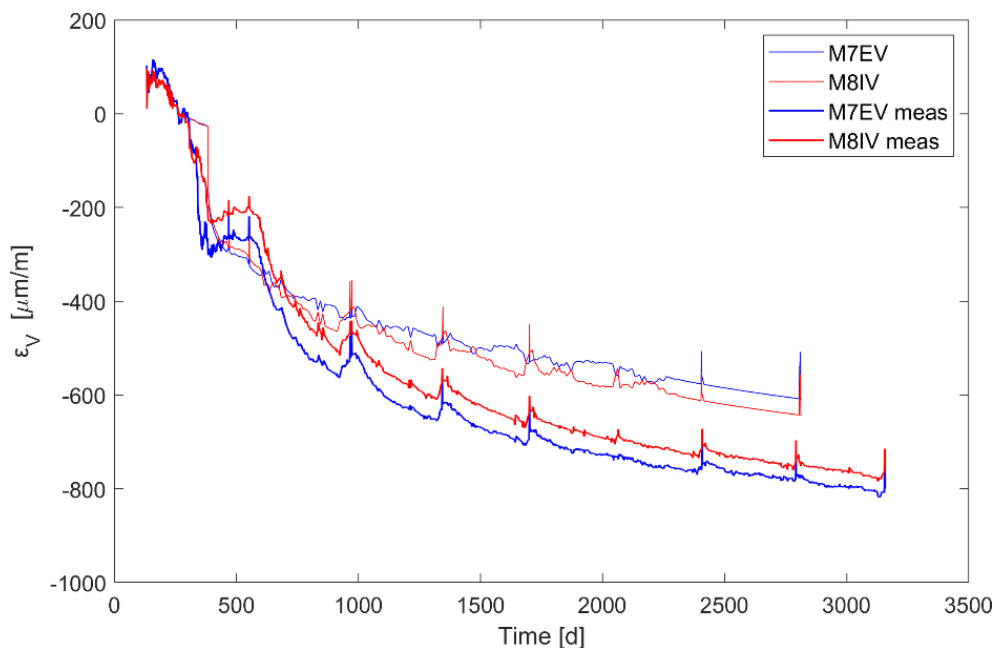


Figure 7.44 Vertical strains, calculated and measured, at M7 and M8.

The measurements in point M7 and M8 show a clear response to the pre-stressing of the tendons. The evaluated long-term vertical strains in these points underestimate the measurements by approximately 20%.

Despite the excluded equipment hatch the evaluated vertical strains show a similar response to the performed pressure tests. The interior point, M8, shows regular humps of that exhibit a similar magnitude as the measurements.

The strain rate, in M7 and M8, caused by shrinkage and creep are of an equal magnitude after day 750.

The measured and evaluated meridian strains,  $\varepsilon_M$ , in J1 and J2 are shown in Figure 7.45. These points are located in the dome at a radius of approximately 6 m.

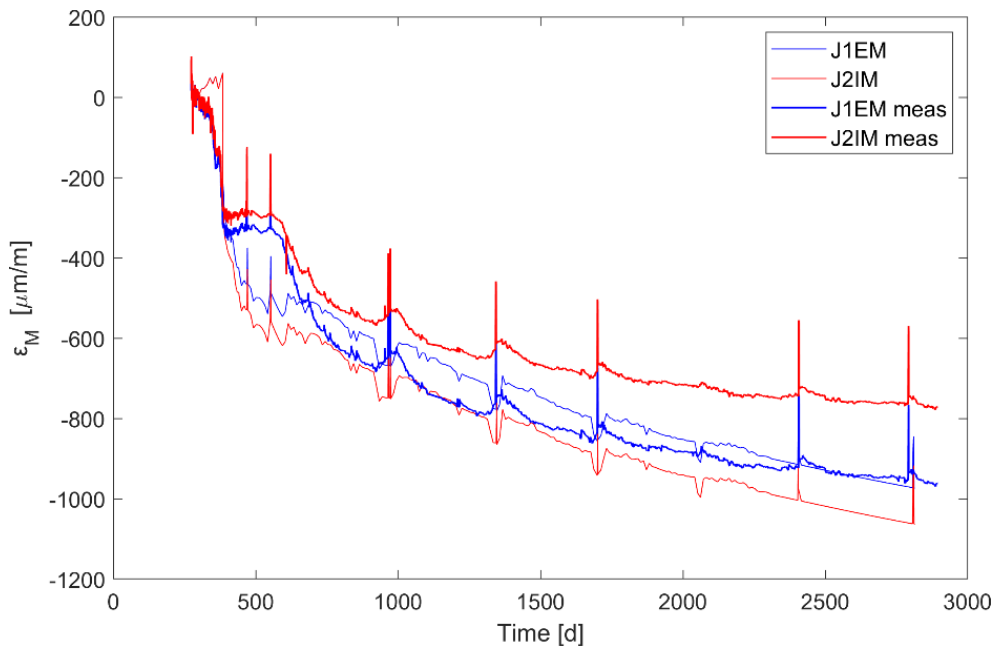


Figure 7.45 Meridian strains, calculated and measured, at J1 and J2.

The applied model overestimates the meridian strains in J2 by roughly 20%. The evaluated and measured meridian strains in exterior the point, J1, are of an equal magnitude.

The humps show that the dome radius decreases when the relative humidity increases. This is the opposite behaviour to what could be expected. It is also an opposite result compared to the measurements which show an increase of the dome radius. This erroneous behaviour suggests that the simplified geometry used in the wedge study is not able to describe the structural behaviour because of shrinkage at the dome.

The meridian strains increase when the pressure tests are performed. This is clearly shown by both the measurements and the evaluation. The magnitude of the evaluated strains is equal to the measurements. In this case, the limited geometry is not affecting the result.

The evaluated overall behaviour in the meridian direction of the dome matches the magnitude of the measured behaviour. The creep rate of meridian strains is somewhat higher in the evaluation compared to the measurement.

The absolute difference,  $D_\varepsilon$ , between the calculated strain,  $\varepsilon_{calc}$ , and the measured strain,  $\varepsilon_{meas}$ , at day 2811, was evaluated by using equation (32)

$$D_\varepsilon = \frac{|\varepsilon_{calc} - \varepsilon_{meas}|}{\varepsilon_{meas}} \quad (32)$$

The mean difference,  $\overline{D_\varepsilon}$ , was evaluated by using equation (32)

$$\overline{D_\varepsilon} = \frac{\sum_{i=1}^n D_{\varepsilon,i}}{n} \quad (33)$$

The difference between the calculated and measured strains at day 2811, along with the standard deviation of this difference when using wedge geometry are shown in Table 7.4.

**Table 7.4 Results from evaluation of the absolute difference, expressed as percentages, in relation to the measured value and the standard deviation.**

Points included	$\overline{D_\varepsilon}$	STD
All points	26.5%	25.1%
All points (excluding dome, hatch and raft)	20.1%	16.4%

### 7.1.8 Evolution of strains with time using the complete RC geometry

The evolutions of strains with time evaluated by using the complete RC geometry, are shown in this section. They were evaluated in several points where measurements also were performed.

The positions of the points are presented in Table 7.5.

**Table 7.5** Specification of the zone, name and position of the strain gauges selected by benchmark VERCORS 2022.

Zone	Position	x [m]	y [m]	z [m]
Raft	E1	0.040	0.000	-1.150
	C1	0.030	0.000	1.730
Gusset	F1	-6.550	-3.081	-0.880
	F2	-6.873	-3.196	-0.900
	G1	-6.707	-3.128	-0.250
	G2	-6.904	-3.202	-0.250
Cylindrical part (mid height)	P1	7.542	1.280	8.010
	P2	7.176	1.392	8.010
	H1	-6.859	-3.227	8.430
	H2	-6.714	-3.159	8.430
	H5	6.761	3.580	8.000
	H6	6.471	3.590	7.990
Equipment hatch	M3	-7.292	2.625	8.700
	M4	-6.983	2.539	8.690
	M7	-6.680	3.686	10.430
	M8	-6.462	3.566	10.380
Dome	I1	0.040	0.000	19.750
	I2	0.040	0.000	19.600
	J1	3.780	4.569	17.800
	J2	3.824	4.623	17.730

The position of each of these points is indicated in Figure 7.46.

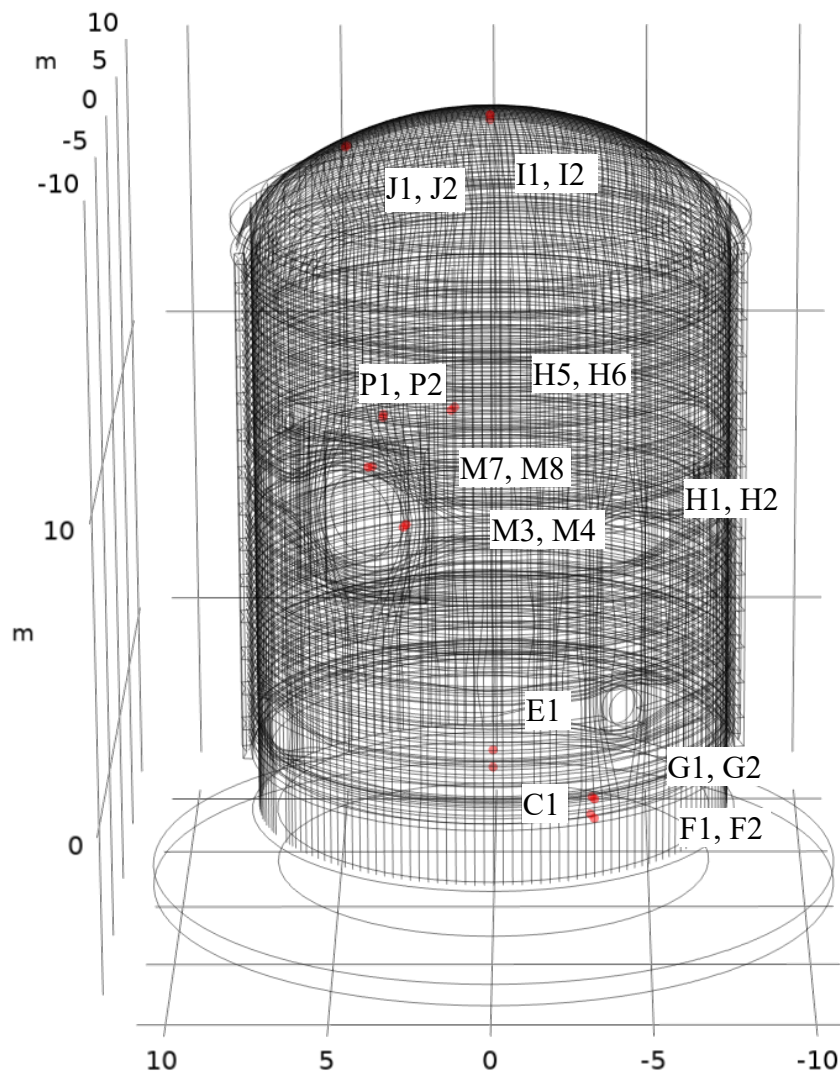


Figure 7.46 Illustration of each strain gauge position in the complete RC geometry (marked with a red dot).

All points are presented in Table 7.2 and Table 7.3. In these tables, the zone, strain gauge name, radius, height, angle, and direction of the strain gauges are specified. The third letter of the strain gauge name, I and E, indicates if the gauge is placed near the interior or the exterior surface of the concrete structure. The last letter indicates the direction of the gauge; radial, R, vertical, V, tangential, T, or, meridian M.

As the measured strains supplied from the VERCORS organisation are shown without temperature strains so are the evaluated strains.

The terms “hump” and “peak” are defined in section 7.1.7 see Figure 7.24 and Figure 7.25.

Calculated and measured radial strains,  $\epsilon_R$ , from gauges placed in the centre of the raft, C1 CENTRE\_95\_R and C1 CENTRE\_195, and E1 CENTRE\_95\_R and E1 CENTRE\_195, are shown in Figure 7.47 and Figure 7.48 respectively. These gauges are placed in the raft centre at an elevation of -1.73 m (C1) and -1.15 m (E1).

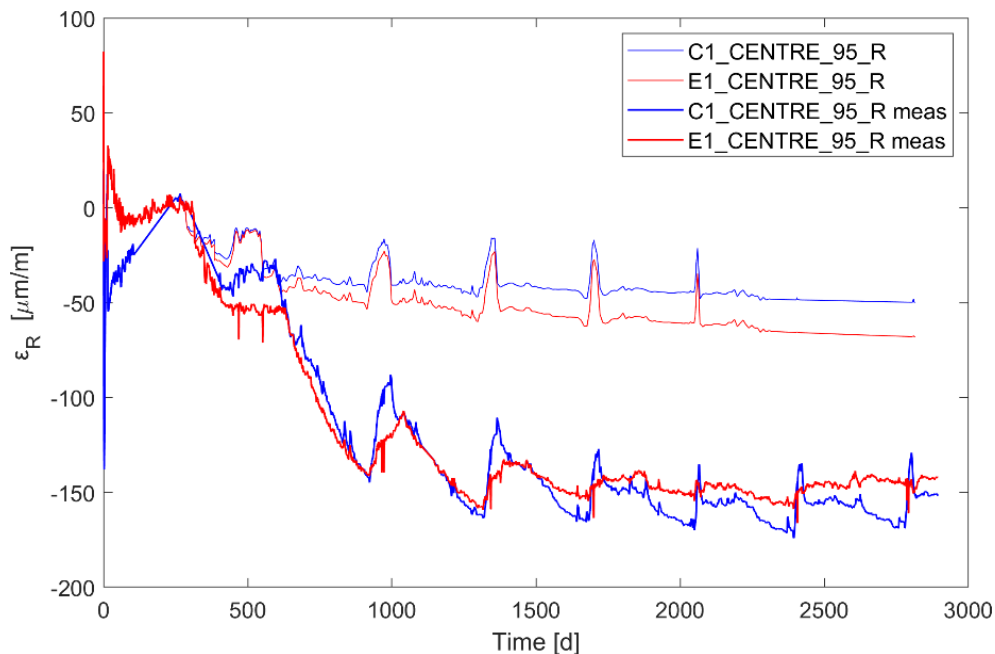


Figure 7.47 Radial strains in the two gauges placed in the raft of the RC (angle of 95 gradians).

The magnitude of calculated strains in both C1 and E1 increases with time. However, the magnitude of the calculated strains after 2800 days is around two thirds smaller,  $\sim 50 \mu\text{m/m}$ , compared with the actual measured strains,  $\sim 150 \mu\text{m/m}$ . This indicates that the applied used creep model underestimates the actual strain evolution. Note that the measurements in the raft approximately started at day 0 (zero) and the calculated strains are shown from day 278 and onward.

Calculated radial strains in C1 are around  $10 \mu\text{m/m}$  smaller compared with the E1. This is as expected since a point at a larger distance from the boundary surface is less affected by changes of the surrounding climate compared with a point at a smaller distance from the surface.

There are humps which lasts for about 50-100 days, which appear on a regular basis. These humps coincide with a certain time before and during the pressure tests. During these events the relative humidity increases, because of a temporary shut-down of the climate control system. When the relative humidity increases the RC structure expands in the radial direction because of swelling. This expansion is clearly shown in both the measurements and the evaluated strains. These humps exhibit similar magnitudes, including the duration, see point C1 in Figure 7.47. This implies that the model used for shrinkage and swelling corresponds well to the actual behaviour. The increase of strains originating from pressure test is less than  $5 \mu\text{m/m}$  because of the stiffness of the raft, see days 2400 and 2800 in Figure 7.47.

Calculated and measured radial strains,  $\varepsilon_R$ , in the raft centre at C1 and E1, 195 gradians direction, see Figure 7.48, exhibits an almost identical magnitude and evolution as in the orthogonal direction.

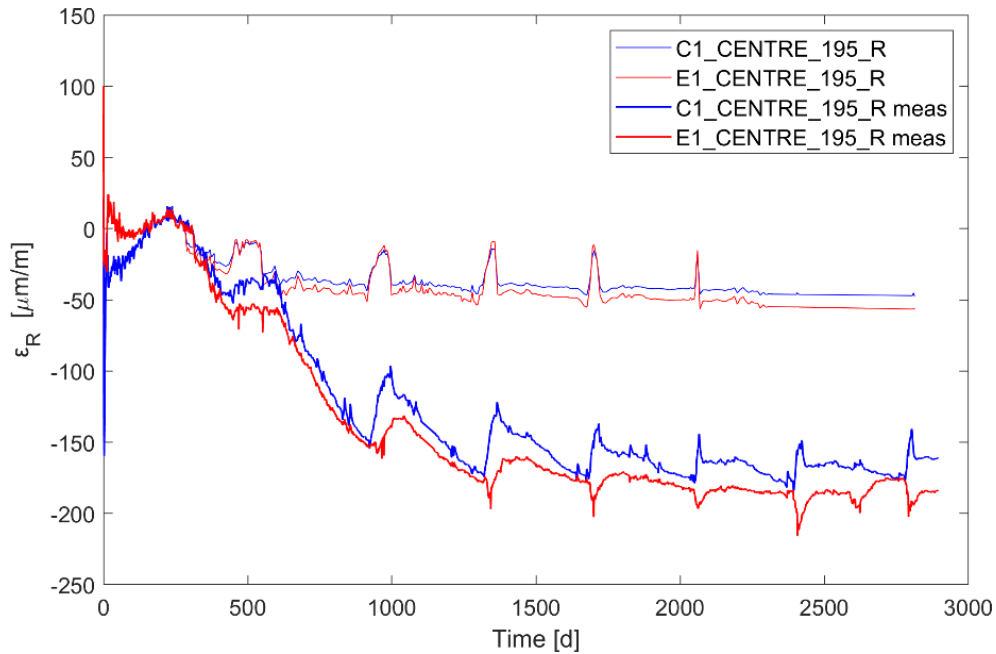


Figure 7.48 Radial strains in the two gauges placed in the raft of the RC, (angle of 195 gradians).

Tangential strain,  $\varepsilon_T$ , evolution with time in the gusset, at gauges F1 and F2, and gauges G1 and G2, are shown in Figure 7.49 and Figure 7.50.

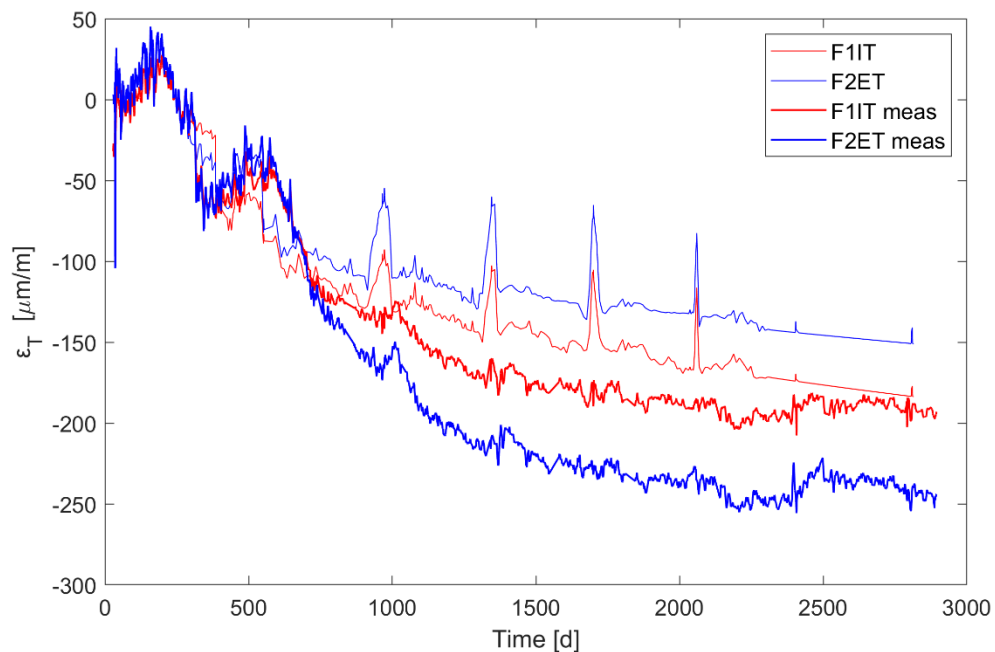


Figure 7.49 Tangential strains, calculated and measured, at F1 and F2.

The calculated strains in F1 and F2 are smaller ( $\sim 150 \mu\text{m/m}$ ) than actual strains ( $\sim 225 \mu\text{m/m}$ ) measured by the gauges, but the underestimation is much smaller than in the raft points. The regular strain peaks shown in the raft also appear in the points of the gusset. The magnitude of the calculated humps, occurring at before and during the pressure tests, is larger than the measured peaks, see Figure 7.49 day 1000. These humps correspond to an expansion (swelling) of the RC structure because of the increase in air humidity of the surroundings at the pressure tests. The effect of the pressure test itself, which is visible as a small peak, has a magnitude of  $\sim 20 \mu\text{m/m}$  see days 2400 and 2800 Figure 7.49. Its duration is about 2.5 days. Note that these measurements started around 50 days after the raft casting. Before that day the sensors were not in operation.

Tangential strains,  $\varepsilon_T$ , of gauges G1 and G2 are shown in Figure 7.50.

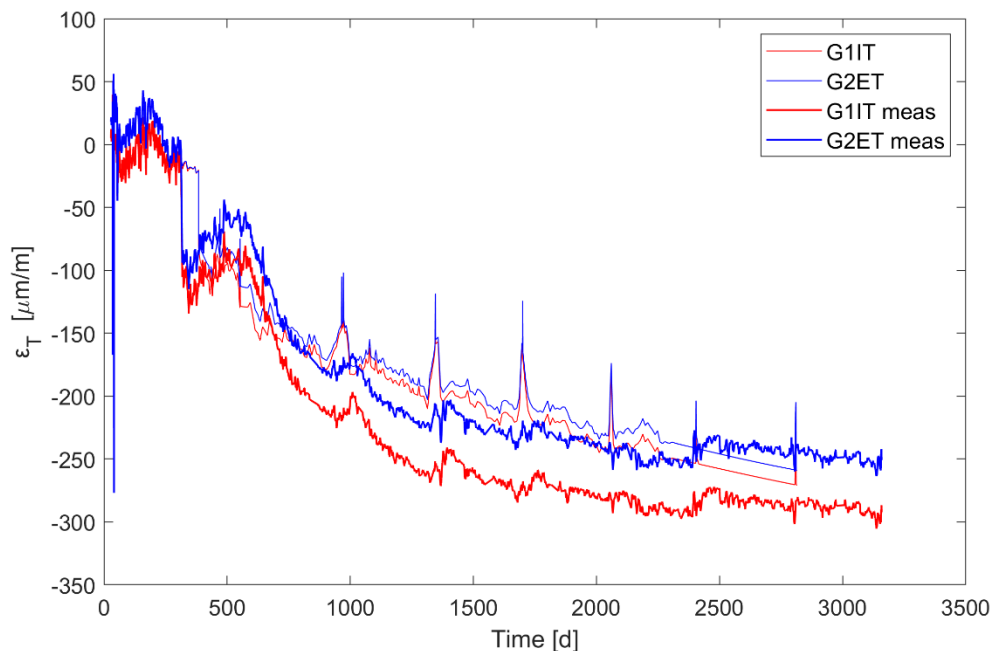


Figure 7.50 Tangential strains, calculated and measured, at G1 and G2.

The calculated strains at point G1 and G2 are of the same order of magnitude as the measured strains,  $\sim 270 \mu\text{m/m}$  at the end. In addition, the calculated strain evolution with time is also equal to the measurements. The calculated evolution of strains in both these points almost overlap the measured tangential strains. However, the measured tangential strains in G1, are  $\sim 40 \mu\text{m/m}$  lower than the calculated strains. The calculated humps about 50-100 days at each pressure test corresponds to the expansion due to swelling as the relative humidity increases. These calculated peaks are easier to distinguish compared with the measured peaks. During the actual pressure test there is a strain peak with a very small duration,  $\sim 2.5$  days. These strain peaks are significant and show the response in the tangential direction to the actual pressure test,  $\sim 40 \mu\text{m/m}$ . The measurement at these points is not able not capture these strains peaks.

The tangential strains in points G1 and G2 are located at a larger distance from the raft, and therefore the tangential strains become larger than in points F1 and F2. This difference may be attributed to the stiffness of the raft that have a stronger affect in points that are closer to it.

Tangential strains,  $\varepsilon_T$ , calculated and measured, in point P1 and P2, H1 and H2, and H5 and H6, are shown in Figure 7.51, Figure 7.52, and Figure 7.53 respectively. These results are presented and discussed as a group of sensors, since they are all placed in the RC cylinder wall, on a similar altitude of  $\sim 8.0$  m. Therefore, they are expected to have a similar behaviour and response to the simulated pressure tests. Note that sensor H2IT did not work well during the first 1200 days of monitoring, see Figure 7.52.

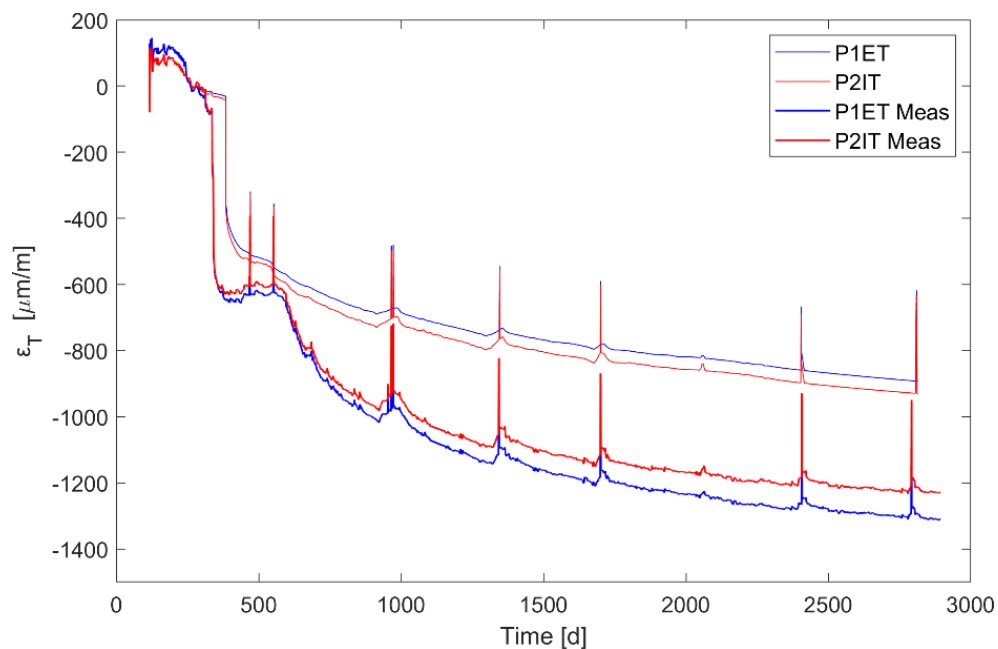


Figure 7.51 Tangential strains, calculated and measured, at P1 and P2.

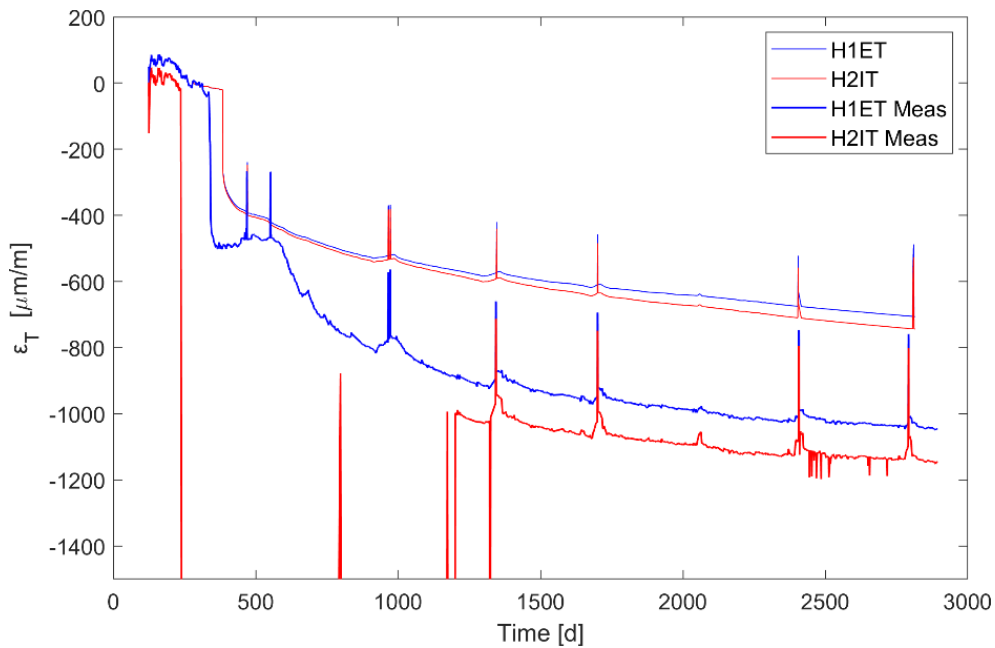


Figure 7.52 Tangential strains, calculated and measured, at H1 and H2.

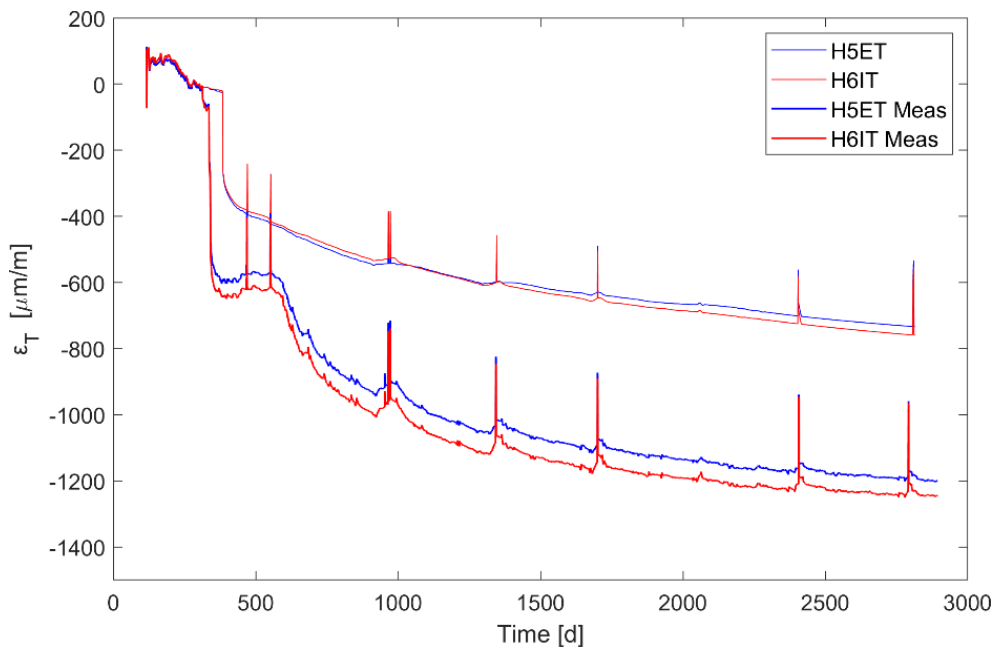


Figure 7.53 Tangential strains, calculated and measured, at H5 and H6.

The calculated results show that both the tangential strain at the exterior (E) and interior (I) points underestimate the actual strain. However, the calculated strain evolution with time is more or less equal to the measured evolution with time. The time gap between the measured and calculated strains observed around day 320 of the test is due to the discrepancy in the application of tendon prestressing compared with the simulation.

The humps before and during each pressure test corresponds to the period of a high relative humidity which causes the RC to swell and expand. The calculated humps, caused by the relative humidity increase, are less significant and smaller than the measured strains.

The rather large hump, measured at the beginning of the time-period at around day 380-600, is also present in the results from the calculations, see Figure 7.51. However, the magnitude of this peak is less distinguishable, as a large creep effect occur simultaneously. As a result, the peak's prominence is mitigated and making it more challenging to identify.

The strain peaks correspond to the elastic strains caused by the actual pressure test. The calculated strains are of an equal magnitude as the measured strains.

Points M3 and M4, M7 and M8, are located close to the equipment hatch, where the cylinder wall thickness is 0.66 m instead of 0.4 m. see Figure 7.54.

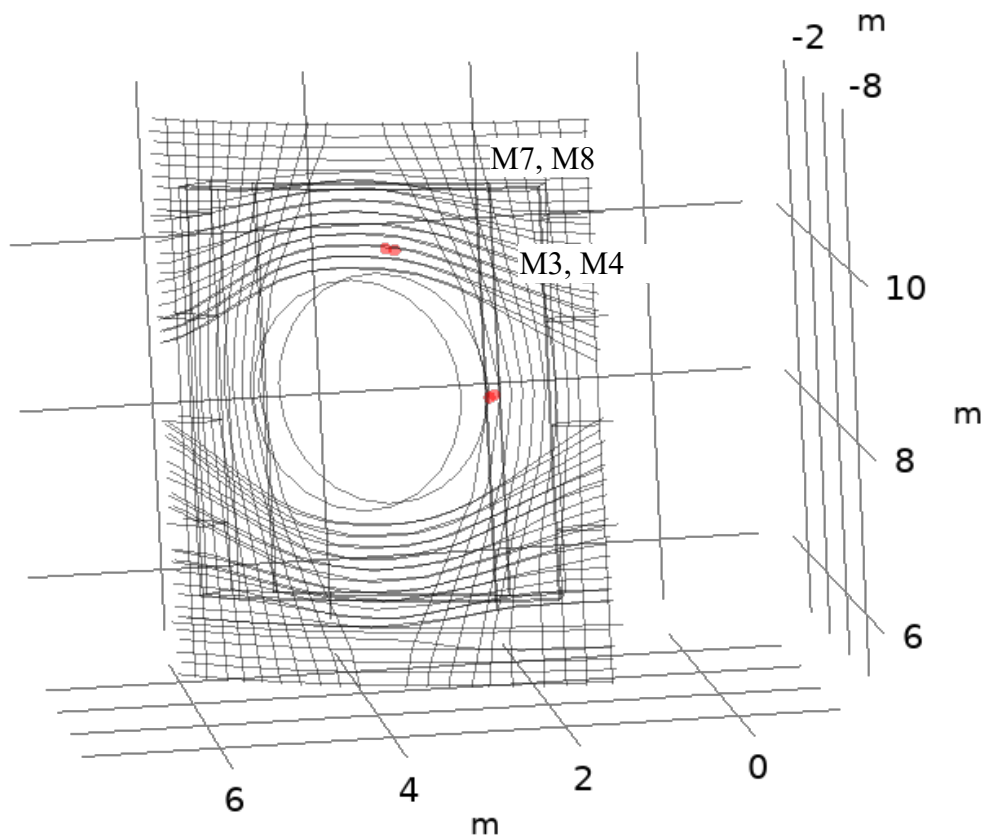


**Figure 7.54 Tendon configuration at the equipment hatch and location of points M3 and M4, and M7 and M8**  
 M3 and M4 are located at an altitude of 8.7 m (beside the equipment hatch) and, M7 and M8 are located at an altitude of 10.4 m (above the hatch). The door frame and the door covering the equipment hatch is not included in the geometry. This door frame may distribute stresses in both the tangential, radial, and vertical directions. This stress distribution is not included in the calculations and will therefore affect the evaluated strains.

Measured and calculated tangential strains,  $\varepsilon_T$ , at gauges M3 and M4, and M7 and M8, are shown in Figure 7.55 and Figure 7.56, respectively.

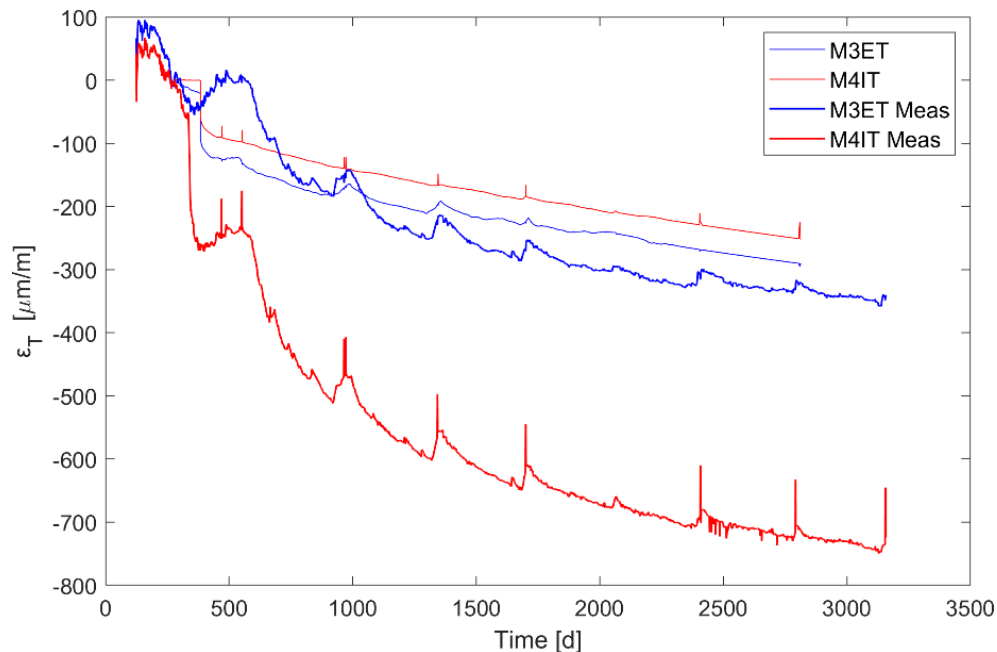


Figure 7.55 Tangential strains, calculated and measured, at M3 and M4.

The calculated tangential strains in M3 are of an equal order of magnitude,  $-250 \mu\text{m/m}$ , compared with the measured strains,  $-300 \mu\text{m/m}$ . In M4 the calculated strains are around  $-200 \mu\text{m/m}$  compared with  $-750 \mu\text{m/m}$ . The geometry does not include a representation of the door frame that surrounds equipment hatch. This means that there is no possibility to redistribute tangential forces horizontally around the equipment hatch. This affects the calculations and may possibly reduce the tangential strains. The measurements in point M3 do not show any response to the pre-stressing of the tendons. Such a result is not expected. In point M4, the measurements show a significant response of the pre-stressing as expected. In point M4, the calculated tangential strains underestimate the actual strains by a factor of  $\sim 3$ ,  $250 \mu\text{m/m}$  compared with  $700 \mu\text{m/m}$  at day 2800.

The calculated strain rate in M3 matches the measurements. In M4 the measured strain rate is higher in the early stage but decreases to an equal level in the later stage.

The calculated humps in M3 underestimate the measured tangential strain in the RC wall near the equipment hatch. The tangential strain peaks, due of the pressure test, are not visible in neither calculated results nor measurements in M3. In M4 these peaks are visible in both measurements,  $60 \mu\text{m/m}$ , and calculations, but the calculated strains are of a smaller magnitude,  $20 \mu\text{m/m}$ .

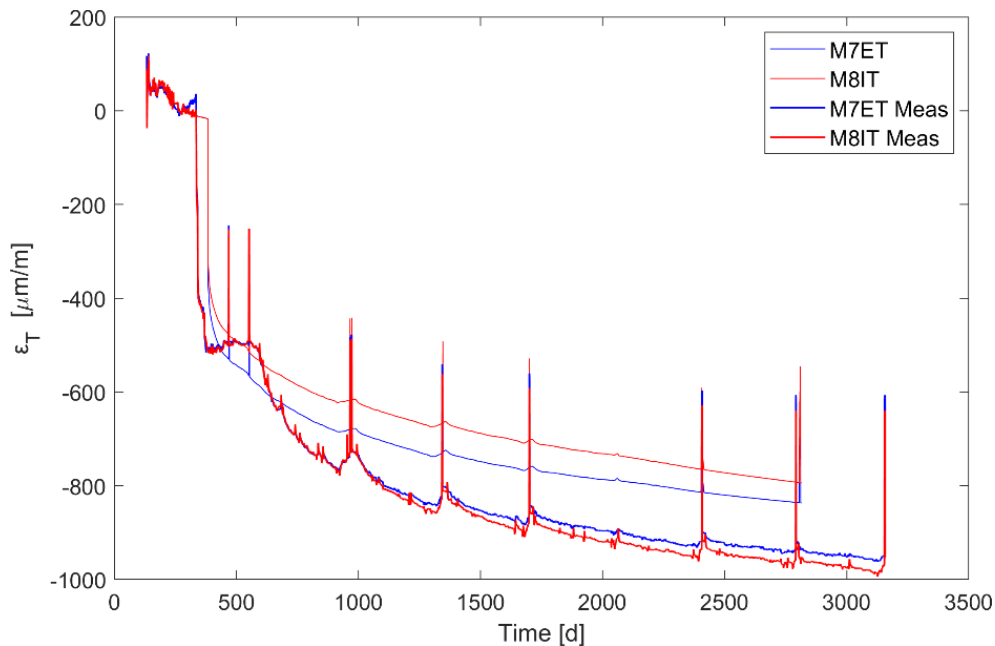


Figure 7.56 Tangential strains, calculated and measured, at M7 and M8.

The calculated tangential strains,  $\varepsilon_T$ , in both M7 and M8 are around 20% smaller compared with the measured strains. In these two points the underestimation is lower than in most of the other points. There is a good match between the calculated and measured response to pre-stressing of the tendons. The difference in time is because all tendons are tensioned at the same time in the calculations, but in reality, all tendons are tensioned individually in a predefined order. The magnitudes of the calculated humps are around 50% smaller than the measured.

Peaks that occur directly as a consequence of the pressure tests are underestimated by a factor of 2. Calculations give an increase in tangential strain of  $170 \mu\text{m/m}$  and measurements show an increase  $300 \mu\text{m/m}$ , from 0 bars over pressure up to the highest pressure, 4.20 bars over pressure.

The calculated and measured tangential strains,  $\varepsilon_T$ , in J1 and J2, are shown in Figure 7.57.

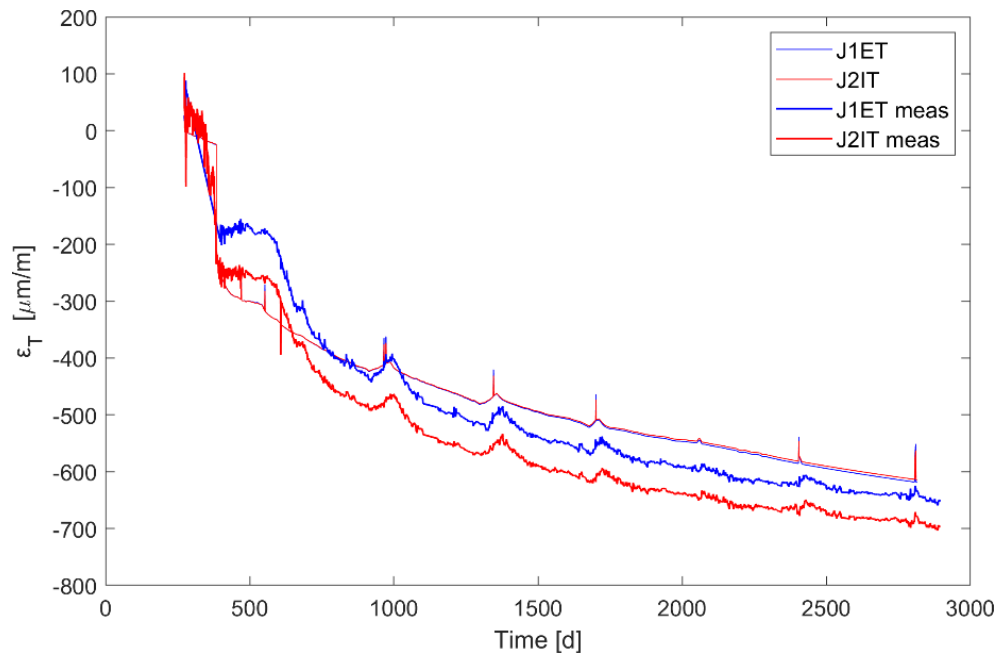


Figure 7.57 Tangential strains, calculated and measured, at J1 and J2.

The calculated tangential strains in both J1 and J2 are of equal magnitudes as the measurements. The expected humps due to an increase of relative humidity are clearly shown in both the measurements and the calculation results. However, a closer examination reveals that the peaks caused by the actual pressure tests show in the calculations, but do not show in the measurements.

Calculated and measured radial strains,  $\epsilon_R$ , in I1 and I2 are shown in Figure 7.58. These points are located at the centre of the dome, where point I1 is close to the exterior and I2 is close to the interior side of the RC.

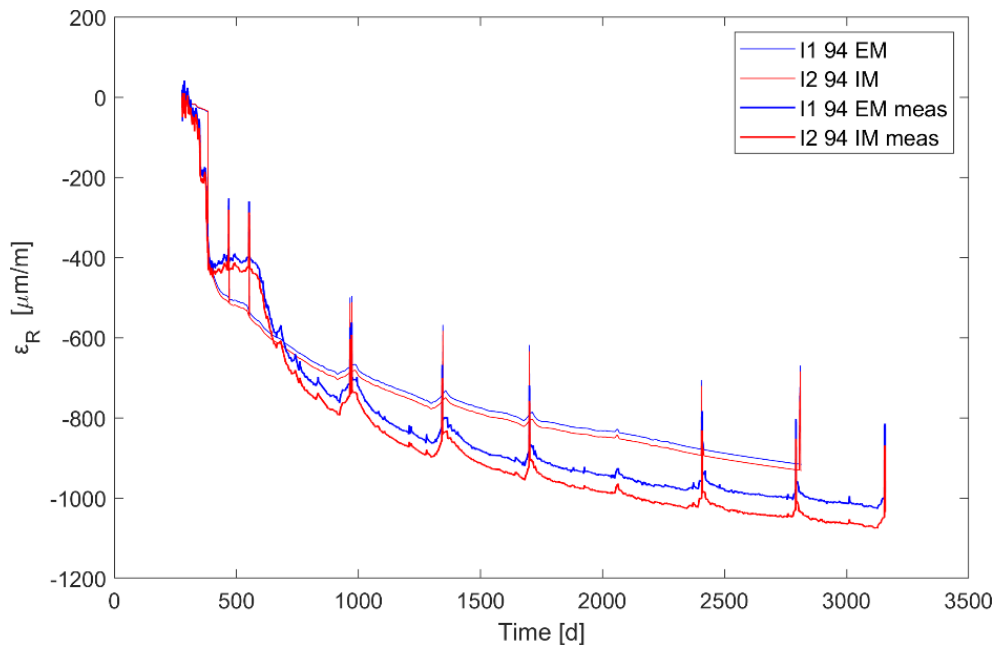


Figure 7.58 Radial strains, calculated and measured, at I1 and I2.

In these two points the calculated strains are of an equal magnitude as the measured strains. The calculated creep rate is a little bit higher in the beginning of the evaluated period but decreases with time. At the end of the evaluated period, it is equal to the measured creep rate.

The regularly occurring humps show that the model underestimate the influence on the strains due to the surrounding relative humidity. The strain peaks that occur as a result of the pressure test are of an equal magnitude as the measurements.

Vertical strains,  $\varepsilon_V$ , calculated and measured, in point F1 and F2, are shown in Figure 7.59. These two points are located 0.12 m above the raft top surface, at an altitude of -0.88 m. Note that the F1IV sensor did not work well between day 250 and 700.

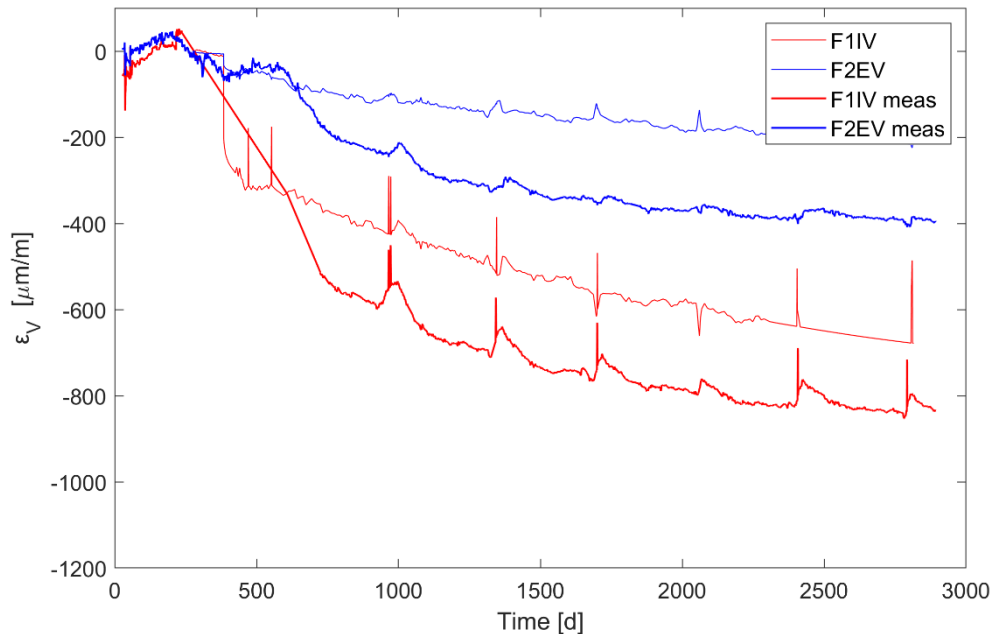
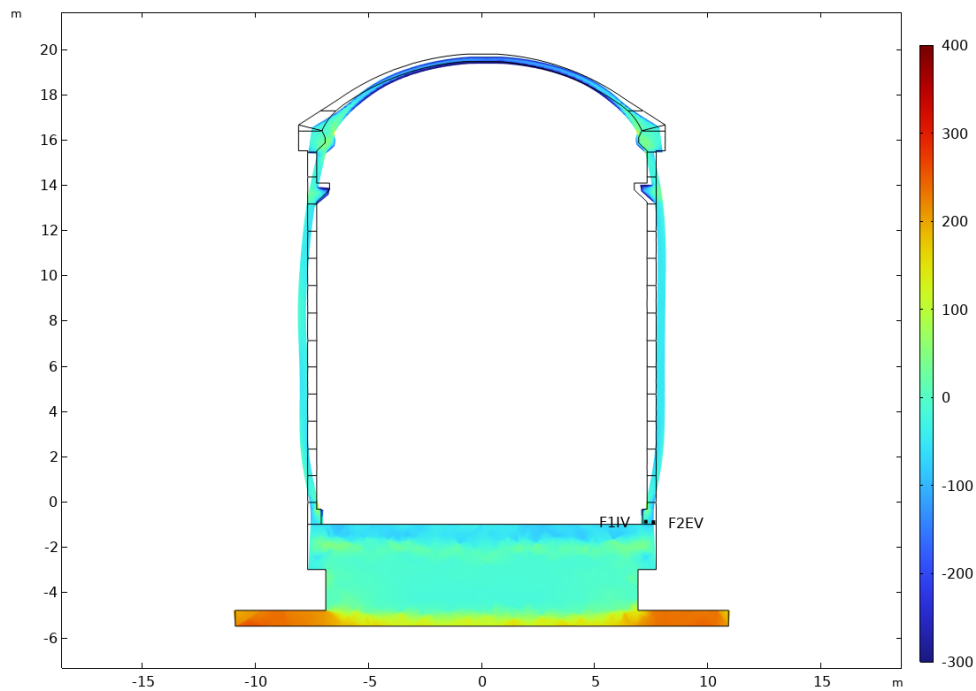


Figure 7.59 Vertical strains, calculated and measured, at F1 and F2.

The measured vertical strain evolution with time is larger in F1 compared with F2. This is also shown in the results from the calculations. This difference in behaviour corresponds to the lower relative humidity inside the RC, as both creep strains and shrinkage increases at a lower relative humidity. The calculated vertical strains underestimate the actual strains in both points. The regular humps occur because of the increase of the relative humidity inside the RC when the climate control system is shut down before each pressure test.

The measured vertical strain peaks in F1, caused by the pressure test, are of an equal magnitude as the calculated strains peaks,  $\sim 80\text{-}100 \mu\text{m/m}$ . However, peaks attributed to the pressure tests are not distinguishable in F2, neither in the measurements nor in the calculations. One possible explanation to this different behaviour may be that the interior point F1 is located in a section subjected to tensile stresses during the pressure test and F2 is subjected to compressive stresses, see Figure 7.60.



**Figure 7.60** Position of F1IV and F2EV and a contour plot of vertical strains in  $\mu\text{m}/\text{m}$  in the RC. The contour plot represent a deformed state of the structure (scale factor of 500) during a pressure test at day 1067.7.

The tensile stresses results in a clear strain peak in point F1 resulting in an extension of the concrete. The stiffness of the raft has little impact on the strains originating from the tensile stresses in point F1. Point F2 is subjected to vertical compressive stresses caused by the pressure test, which results in insignificant strain peaks, because of the stiffness of the raft.

Vertical strains,  $\varepsilon_V$ , calculated and measured, in point G1 and G2, are shown in Figure 7.61. These two points are located 0.75 m above the raft top surface, at an altitude of - 0.25 m.

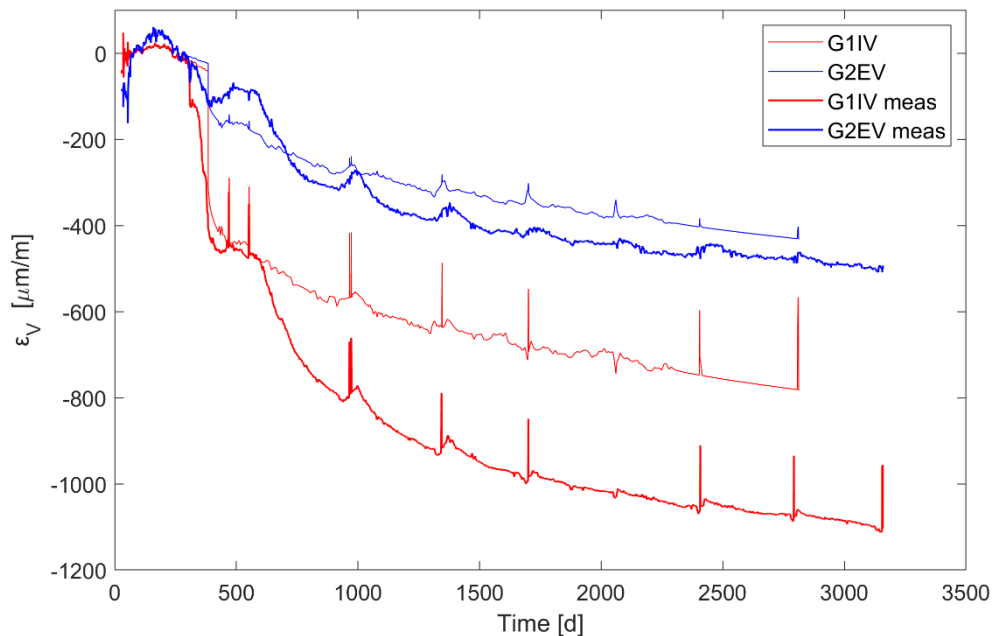


Figure 7.61 Vertical strains, calculated and measured, at G1 and G2.

The exterior point, G2, shows a smaller vertical strain compared with G1. This may be explained by the more humid exterior climate which decrease the impact of both shrinkage and creep. However, in both points the calculations underestimate the early effect of creep and shrinkage especially in the interior point G1. The calculated creep rate is however of the same order of magnitude after the day 750.

Strain humps caused by the increase of humidity before and during the pressure tests are distinguishable in both G1 and G2. These peaks correspond to the increase of relative humidity before and during the pressure tests. These climate changes cause swelling and expansion as the RC absorbs moisture from the air.

The measured and calculated strain peaks at the pressure tests are significant in G1, but hardly distinguishable in G2. In addition, the magnitude of the calculated and measured vertical strain is equal in both these points. Point G1 exhibits the same structural behaviour as F1, and this similarity extends to both G2 and F2.

Vertical strains,  $\varepsilon_V$ , calculated and measured, in point P1 and P2, H1 and H2, and H5 and H6, are shown in Figure 7.62, Figure 7.63, and Figure 7.64, respectively. These six points are in the cylindrical part at mid height,  $\sim 9$  m above the raft top surface, at an altitude of 8 m.

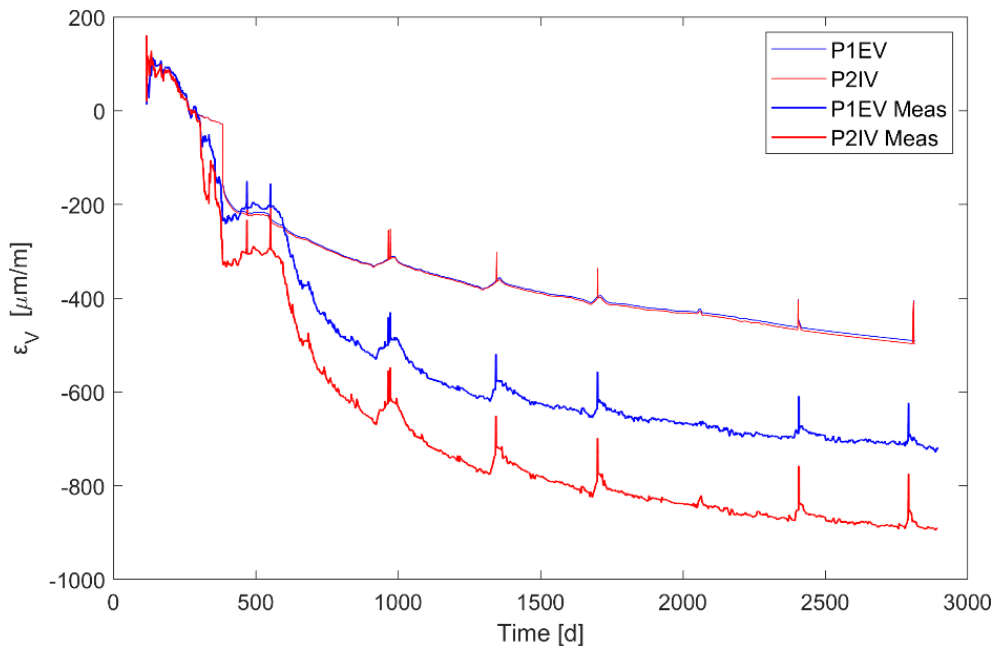


Figure 7.62 Vertical strains, calculated and measured, at P1 and P2.

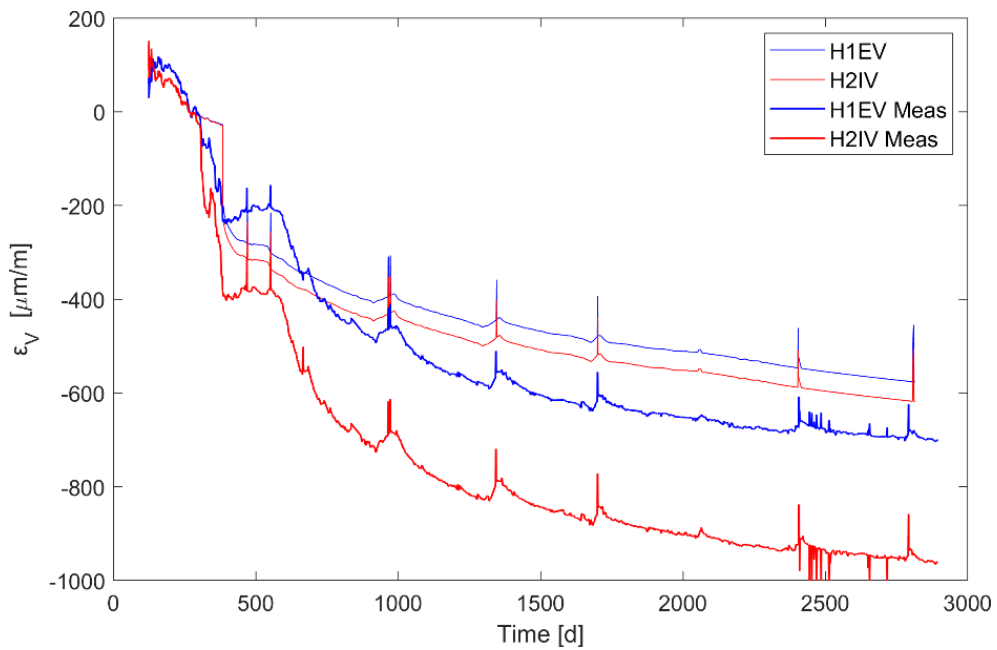


Figure 7.63 Vertical strains, calculated and measured, at H1 and H2.

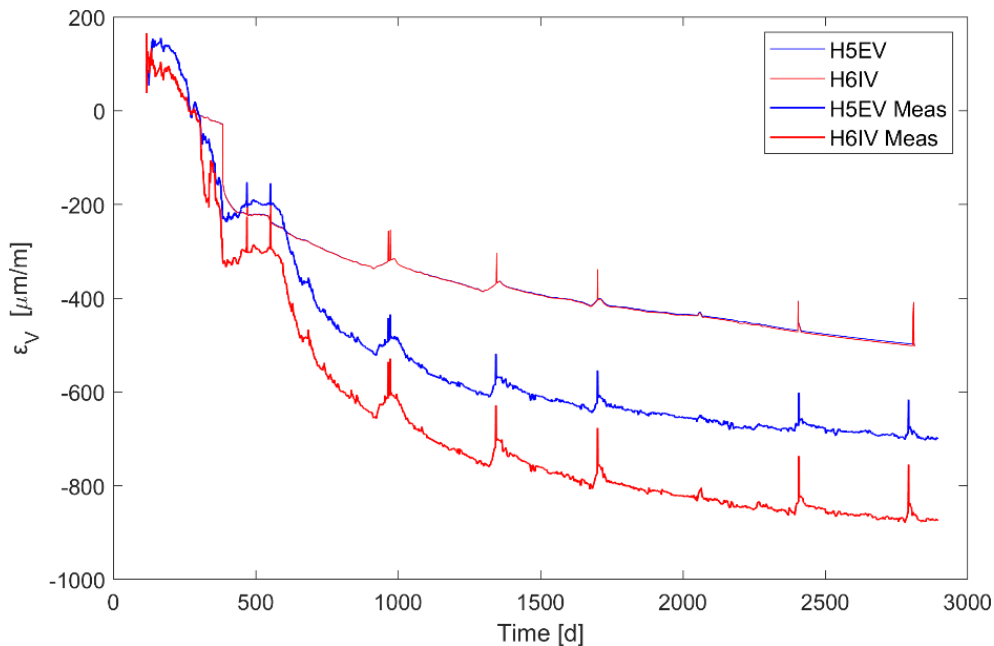


Figure 7.64 Vertical strains, calculated and measured, at H5 and H6.

The calculated vertical strains in all these six points underestimate the measured strains. The behaviour pattern of all the strain sensors is similar. However, there is a larger difference between the exterior and the interior and sensors at points H1 and H2 compared with points P1 and P2, and H5 and H6. There is no logical physical explanation in this behaviour.

Strain humps are found in both the calculations and the measurements but there is a small difference in magnitude. This could be interpreted as that the model is underestimating the shrinkage because of drying. But this underestimation becomes smaller as the concrete dries. In the last 1500 days, the calculated and the measured vertical strains evolution is similar.

The calculated strain peaks in the vertical direction, originating from the actual pressure-test, are of the same magnitude as the measured strains,  $\sim 80\text{-}100 \mu\text{m/m}$ . These peaks are clearly distinguishable in all six points.

The calculated and measured vertical strains,  $\varepsilon_V$ , in point M3 and M4, are shown in Figure 7.65. Note that these points are located at the equipment hatch, where the wall thickness is 0.66 m, compared with the cylindrical wall that is 0.4 m.

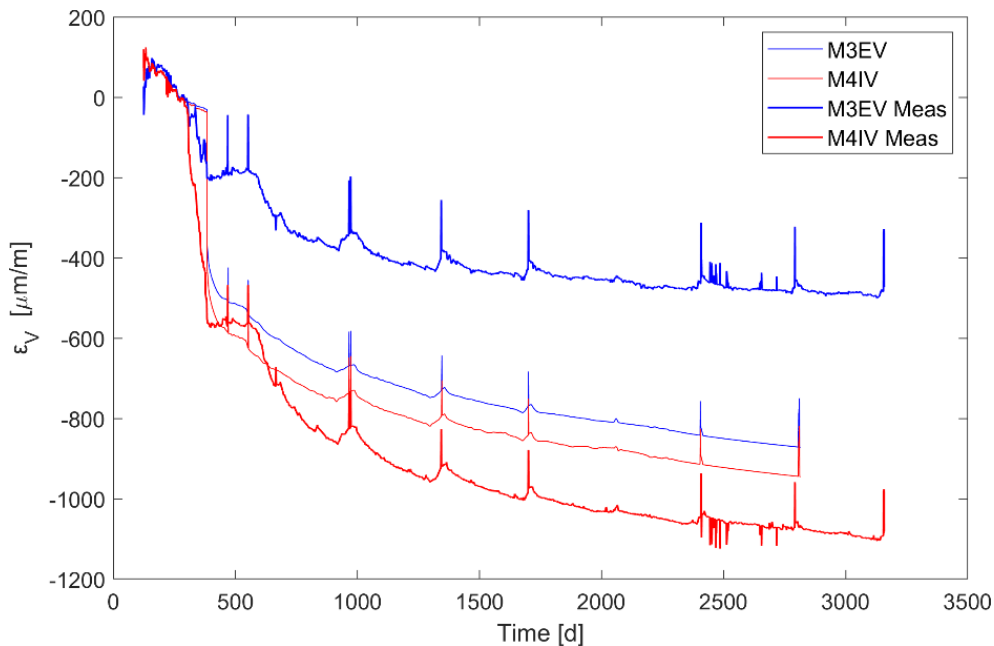


Figure 7.65 Vertical strains, calculated and measured, at M3 and M4.

There is a large difference between the measured vertical strains in M3 and M4. The measured strains in M3 (exterior), 450  $\mu\text{m/m}$  are less than half of the magnitude in M4 (interior), 1100  $\mu\text{m/m}$ .

The initial impacts of pre-stressing on the measurements of vertical strains at M3 are relatively small. However, at M4, they become significant and align in magnitude with the calculated values. This behaviour of M3 is not as expected, but it corresponds to what happened with the tangential measurements in M3 and M4, see Figure 7.55. In that direction, the measurements in M3 seem to have failed to capture the pre-stressing event and the large creep effect at an early stage.

Strain humps, caused by the increase in relative humidity, are clearly demonstrated in both the measurements and the calculations in both M3 and M4. The magnitude of the humps from the calculations is slightly smaller than the measured humps.

The peaks that correspond to the actual pressure test clearly show in both points and in both the measurements and the calculations. The calculated strains are of the same magnitude as the measurements.

The calculated and measured vertical strains,  $\varepsilon_v$ , in point M7 and M8, are shown in Figure 7.66. These points are also located close to the equipment hatch where the wall thickness is larger than in other parts of the cylinder wall.

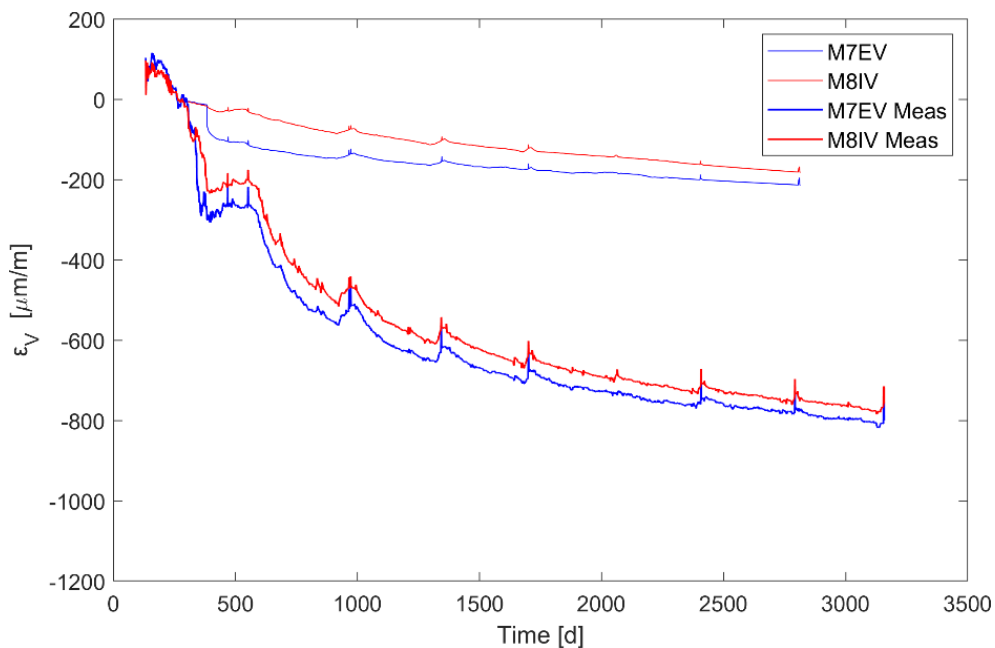


Figure 7.66 Vertical strains, calculated and measured, at M7 and M8.

The calculations significantly underestimate the vertical strains by a factor of 6-7. According to the calculations the effect of pre-stressing the tendons is insignificant in M8 and small in M7. This is not expected. One possible explanation for this result could be the positioning of these points directly above the equipment hatch. Vertical forces must be redistributed around the equipment hatch because there is no concrete or any other solid material in the global model at the hatch. In reality, this equipment hatch is locked with a steel frame and a steel door. That steel frame may redistribute the forces that act in the vertical direction.

Such a large difference between the calculations and the measurements is not shown in the tangential direction at the same points, see Figure 7.56. But in that case, the influence of the equipment hatch penetration is probably smaller.

Calculated and measured meridian strains,  $\varepsilon_M$ , in point J1 and J2 are shown in Figure 7.67. These points are located in the dome at a radius of  $\sim 6$  m.

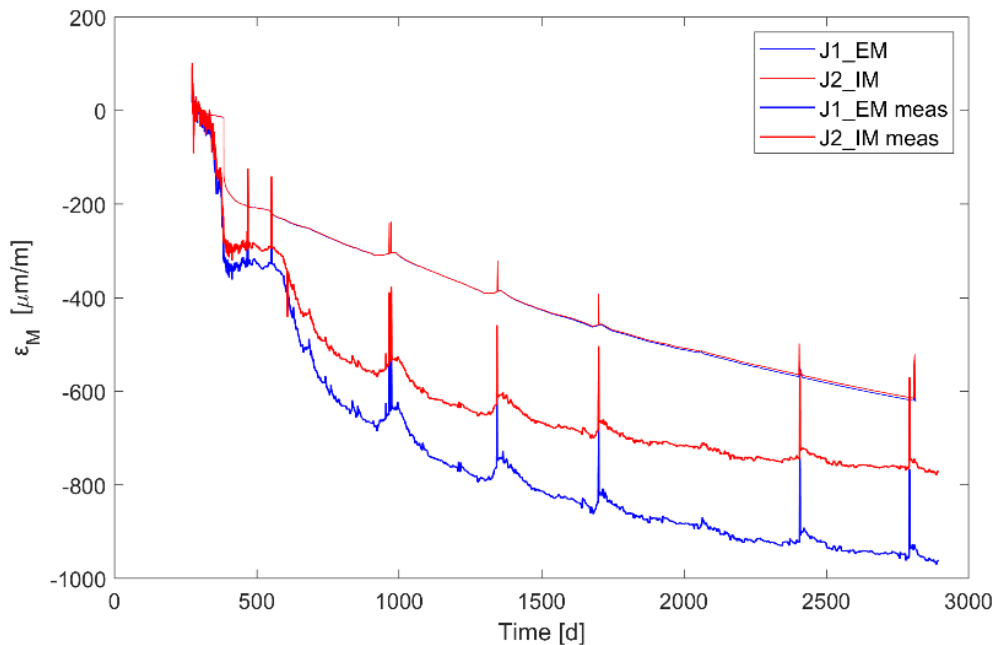


Figure 7.67 Meridian strains, calculated and measured, at J1 and J2

In these two points, the calculations underestimate the measured total meridian strains and reaches a magnitude around 60% (J1) and 80 % (J2) of the measured strains.

The pre-stressing of the tendons clearly increases the strains which is shown in both the calculations and the measurements. The calculated rate of creep is higher than the measured in the beginning.

Strain humps are visible in both the calculations and the measurements. The volumetric deformation due to relative humidity changes, like shrinkage and swelling, is underestimated by the applied model.

When the pressure tests are performed, peaks in the strains show. This is captured in both the calculations and the measurements. However, the calculations underestimate the magnitude of the peaks by about 50%, if compared with the measurements.

The difference between the calculated and measured strains at day 2811, along with the standard deviation of this difference when using the complete geometry, see section 7.1.7, are shown in Table 7.6.

**Table 7.6 Results from evaluation of the absolute difference, expressed as percentages, in relation to the measured value and the standard deviation.**

Points included	$\overline{D_\varepsilon}$	STD
All points	30.9%	23.5%
All point (excluding dome, raft and hatch)	26.5%	13.3%

Figure 7.68 shows the contribution of tangential strains in P1 attributed to shrinkage, P1ET shrink, and creep, P1ET Creep. Additionally, the mean coefficient of variation for creep, specified as +/- 20% in Eurocode 2 [9] are represented by dashed black lines. The total tangential strain, P1ET, obtained by super position of shrinkage and creep contributions, is shown as a bold solid blue line. The measured total strain, P1ET Meas, is shown as a narrow solid blue line.

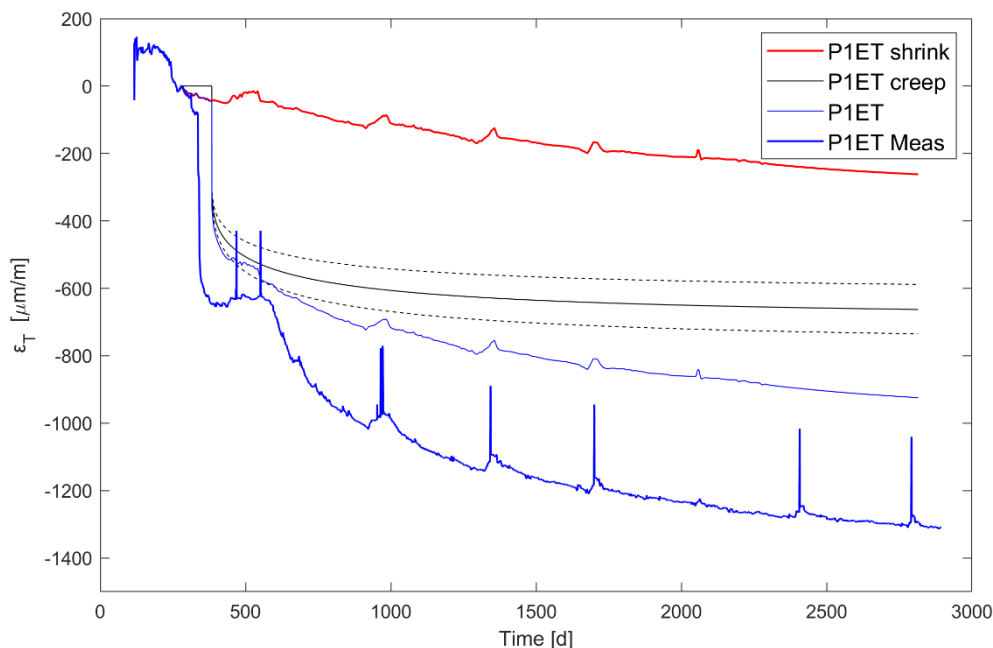


**Figure 7.68 Contribution of tangential strains due to shrinkage and creep at P1. The total tangential strains caused by shrinkage and creep and the measured strains at P1.**

It is evident that both shrinkage and creep phenomena significantly influence the long-term tangential strains. Creep (P1ET creep), in particular, exerts a substantial impact until day 1000, surpassing the contribution from shrinkage (P1ET Shrink), which amounts to around 100  $\mu\text{m}/\text{m}$  at day 1000. After day 1000 shrinkage has a larger impact on the total strain. The rate of shrinkage strain demonstrates relative stability over time. The rate of calculated total tangential strain is similar to the measured after day 1000. However, calculated strain magnitude at day 2800 is around 900  $\mu\text{m}/\text{m}$  and the measured is larger, around 1300  $\mu\text{m}/\text{m}$ . Moreover, it becomes apparent that the humps in tangential strains correlate with instances of swelling, notably influenced by fluctuations in humidity levels preceding and

during the pressure test. In contrast, the creep strain rate has its most significant impact from the moment of pre-stressing until around 100 days afterward. Subsequently, it gradually decreases and eventually falls below the shrinkage rate. The mean coefficient of variation for creep leads to a variation in tangential strains of approximately  $\pm 70 \mu\text{m/m}$ .

## 7.2 THE AIR LEAKAGE THROUGH THE RC (STUDY 2)

The calculated evolution of porous air leakage rate through the RC with time is shown in Figure 7.69. Note that the y-axis shows the porous leakage rate in normal cubic meters per hour,  $\text{Nm}^3/\text{h}$ , which is the air volume at atmospheric pressure and a temperature of 273.15 K.

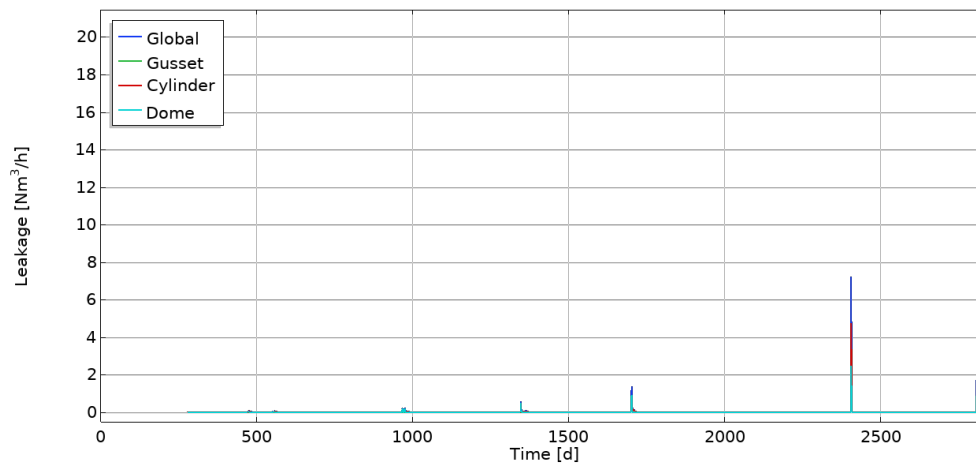


Figure 7.69 Evolution of the porous air leakage rate through the RC during the simulation.

The leakage rate increases with each performed pressure test, which is a consequence of the drying of the concrete. When concrete dries, the physically bound water is gradually emptied from the porous system. This increases the permeability, and thus also the leakage rate through the RC. At this time scale, it is not possible to distinguish the contributions of different parts of the RC to the total leakage. Note that no cracks are included in this simulation.

The global porous leakage was calculated by integrating the leakage rate over time during the duration of the pressure test, see shaded area in Figure 7.70.

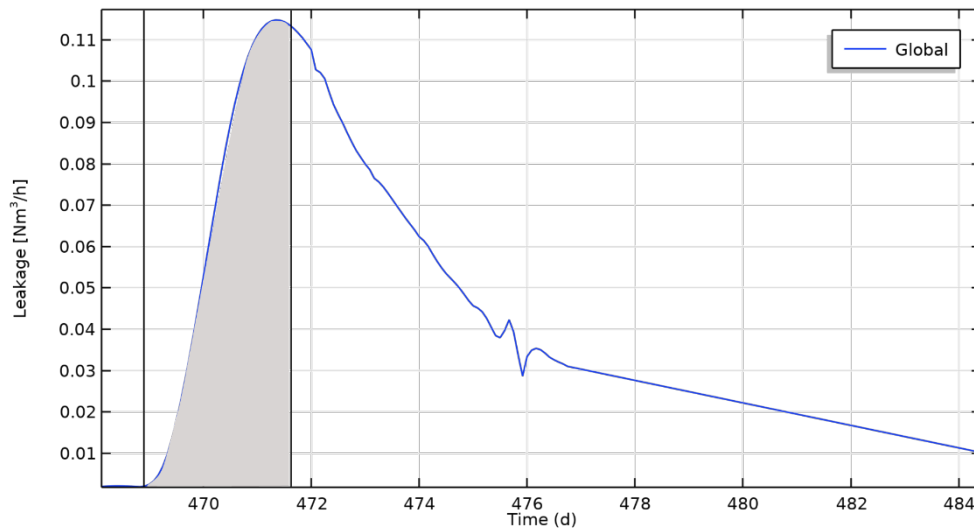


Figure 7.70 First pressure test at day 469, the Pré-op pressure test.

The prediction of the first pressure test, at day 469, shows that there is a significant air leakage after the pressure test is completed from day 471,67 until day 484. This extra leakage is not included in the measured air leakage since the measurements stopped at the end of the pressure test.

Results from measurements of the global, local, and porous leakage were supplied to the participants from the benchmark VERCORS 2022 after the leakage calculations had been performed. The porous leakage was assessed by the benchmark VERCORS 2022 as the difference between the global leakage and the local leakage (crack leakage). The local leakage was determined by measurements performed at all cracks by the benchmark VERCORS 2022. The measurement results of both global and local leakage, in Nm<sup>3</sup>/h, are presented in Table 7.7 together with the assessed porous leakage and the calculated porous leakage results.

Table 7.7 Leakage at each measured pressure test and the calculated global porous leakage, Nm<sup>3</sup>.

Pressure test	Day	Global	Local	Porous (assessed)	Porous (calc)
Pré-op	469	7.7	4.3	3.4	3.7
VC1	551	9.5	7.1	2.4	3.5
VD1	964	29.6	28.5	1.1	6.4
VD1bis	971	30.3	24.8	5.5	9.5
VD2	1344	46.2	31.7	14.4	18.5
VD3	1699	57.1	38.9	18.2	44.8

The calculated porous leakage is in the same order of magnitude as the assessed porous leakage except during the pressure test at day 964 and 1699. During these tests, the calculated value is six times larger and more than twice the size of the assessed porous leakage, respectively. The large difference at the last pressure test may be caused by an overestimation of the decrease in calculated moisture content compared with the actual conditions of the structure. This difference may also be

caused by the assumed relationship between the air permeability and relative humidity. In addition, challenges of conducting precise measurements of local leakage also affects the resulting porous leakage.

In Figure 7.71, the results show the calculated porous leakage rate, which was based on the project team's suggested testing conditions for an ultimate pressure test (see Figure 5.20). It is worth noting that the pressure itself was not conducted, preventing a comparison between the calculations and actual measurements. The figure shows the total leakage, and the contribution from the different major parts of the RC: the gusset, the cylinder wall, and the dome.

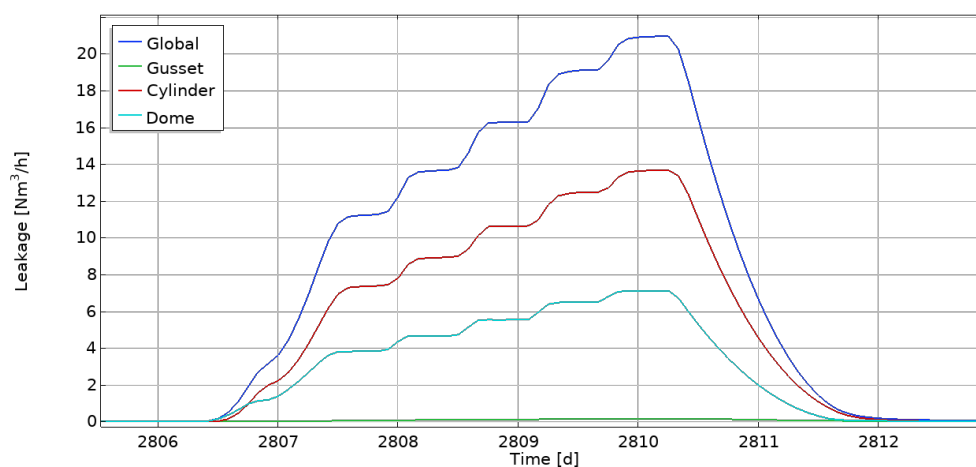


Figure 7.71 The leakage rate through the RC at the time of the ultimate pressure test reaching 6 bar, performed day 2806.

The porous leakage rate through the gusset, is low compared with the cylindrical wall and the dome. This is not surprising since the area of the gusset is much smaller than the two other parts. Another parameter that may explain this low leakage rate is that the gusset has a larger thickness, and therefore dries slower than the other two parts. Hence, the air permeability is lower in the gusset compared with the other parts.

The largest porous leakage occurs through the cylindrical wall, and this is expected since the area is significantly larger compared with the gusset and dome. In addition, the cylindrical wall's cross-section is the thinnest, resulting in faster response in drying/wetting and higher/lower moisture content, consequently leading to either lower or higher air permeability.

Furthermore, cracks may be expected in a real RC in the gusset area and near penetrations. These cracks may affect the air leakage especially if they are through cracks.

### 7.3 THE SCALE EFFECT OF DRYING (STUDY 3)

The moisture distribution, in terms of RH (-), has been evaluated at a cross section of the cylinder wall of an RC with different wall thicknesses. The thickness of the cylinder wall is divided by its own thickness, this means that the thickness

becomes dimensionless and ranges from 0 to 1. By performing this normalization, the distribution at a cross section in a thin wall may be compared with the distribution in a thick wall. The time at which these moisture distributions are displayed is multiplied with the scale of the wall thickness-squared. The drying time is proportional to the wall thickness-squared [25, 26] if the theory of diffusion is applicable to drying in concrete. This should mean that a 1.2 m thick wall that has dried for 9 years may be compared to a 0.4 m thick wall (one third of 1.2 m) that has dried for 1 year ( $9/3^2$  year). All times referred to below are multiplied by the scale of thickness squared.

Figure 7.72 and Figure 7.73 show the obtained RH distribution at a cross section of the wall with constant and time-dependent material properties, respectively, after one year of drying. The five lines show the evaluated RH distributions for different wall thicknesses ranging from 0.4 to 1.2 m.

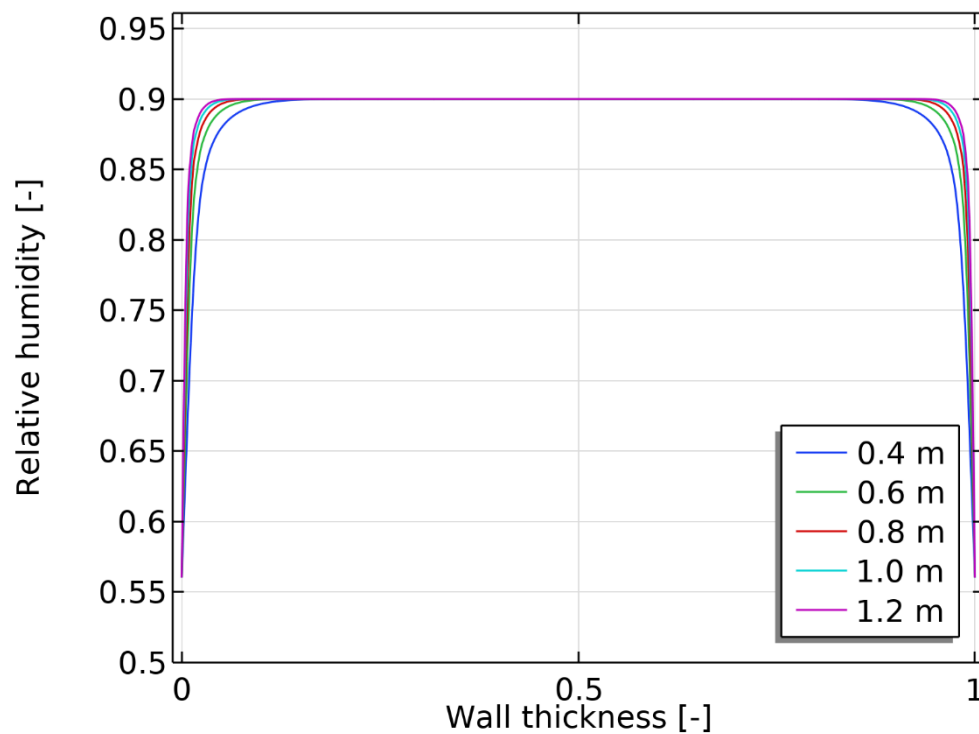


Figure 7.72 RH distribution after one year with constant material properties

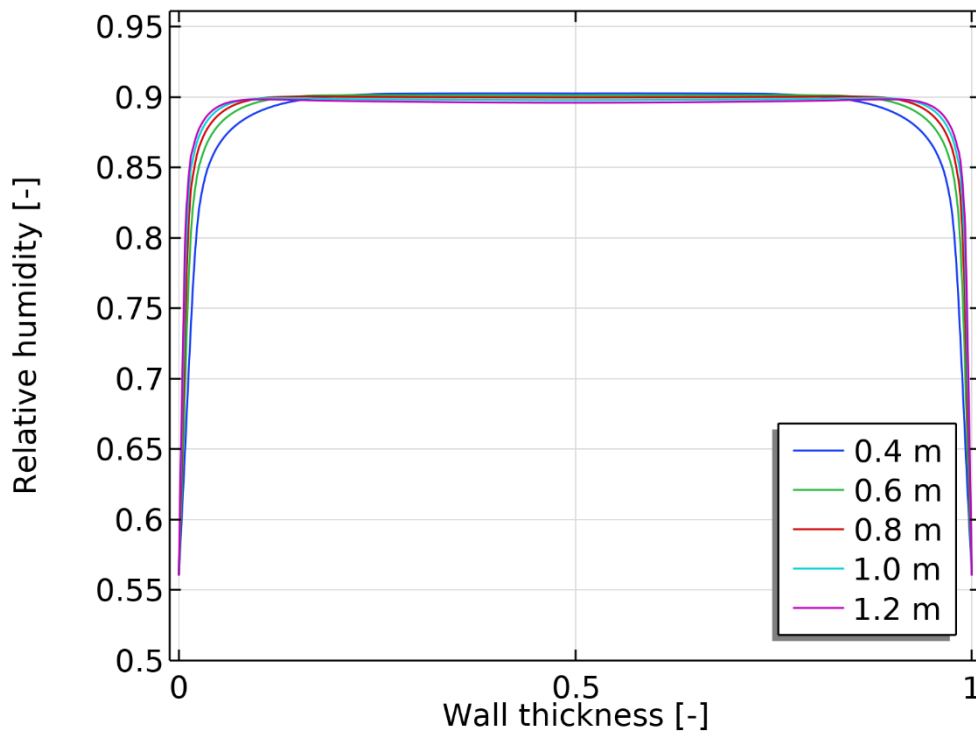


Figure 7.73 RH distribution after one year with time-dependent material properties

When constant material properties are assumed the RH distribution of the different wall thicknesses almost overlap each other, this is clearly shown in Figure 7.72. However, close to the surfaces there is a small but distinguishable difference in RH between the different wall thicknesses. The depth at which the RH is unaffected by drying is smaller in the case with constant material properties, see Figure 7.72, compared with time-dependent properties, see Figure 7.73. A substantial part of the concrete wall has not dried at all during this first year of drying.

When time-dependent material properties are assumed, the RH distribution in the different wall thicknesses are also almost overlapping each other, see Figure 7.73. However, since the simulations with time-dependent properties also include self-desiccation, there is a small but notable decrease in relative humidity also in the central parts of the wall. This small difference may be regarded as insignificant at a one-year time frame. It is not a coincidence that the relative humidity in the centre of the wall is 0.9 in both cases. The self-desiccation was evaluated in a separate one-year simulation of drying, when time dependent material properties were assumed. The relative humidity was found to be 0.9 after one year of self-desiccation.

The results suggest that it is possible to use the theory of diffusion to estimate drying at a time frame of about one year. Therefore, these results, also suggests that the drying time may be considered to be proportional to the wall thickness-squared.

In Figure 7.74 and Figure 7.75, the moisture content distribution evaluated after one year with constant and time dependent material properties for the different studied wall thicknesses are shown.

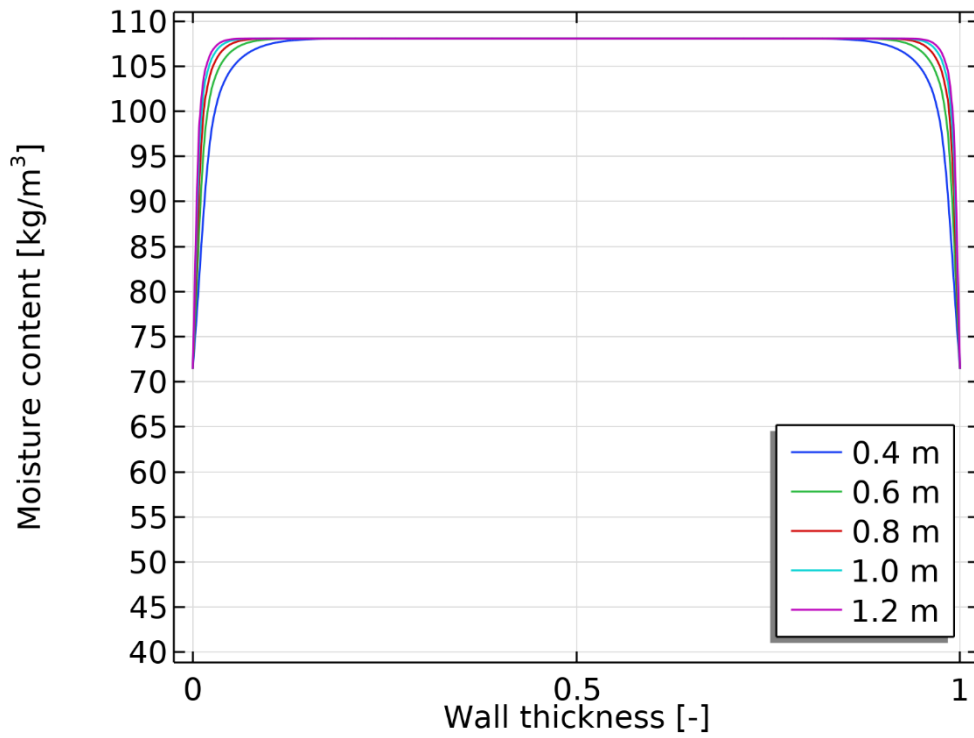


Figure 7.74 Moisture content distribution after one year of drying with constant material properties

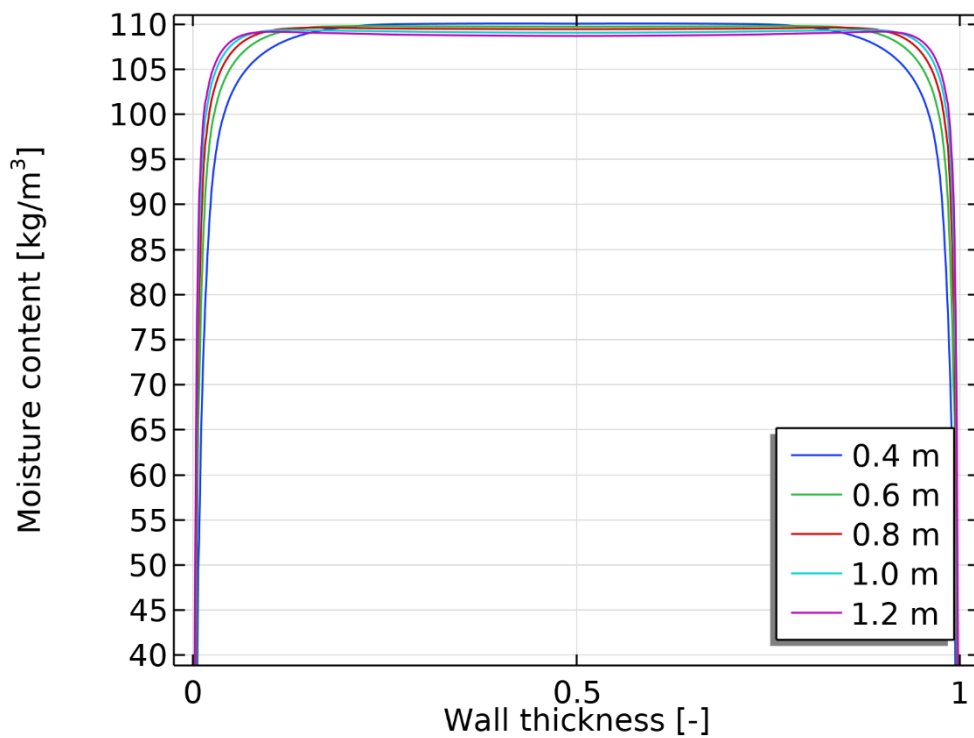


Figure 7.75 Moisture content distribution after one year of drying with time-dependent material properties

These results clearly show that the absolute value of the moisture content is affected by the assumption of constant or time dependent material properties. The surface moisture content is about  $70 \text{ kg/m}^3$  when constant material properties are used, see Figure 7.74. This result should be compared to  $40 \text{ kg/m}^3$  when time dependent properties are used, see Figure 7.75.

Figure 7.76 and Figure 7.77 show the RH distribution at a cross section of the wall for each wall thickness with constant and time dependent material properties respectively, after 7 years of drying.

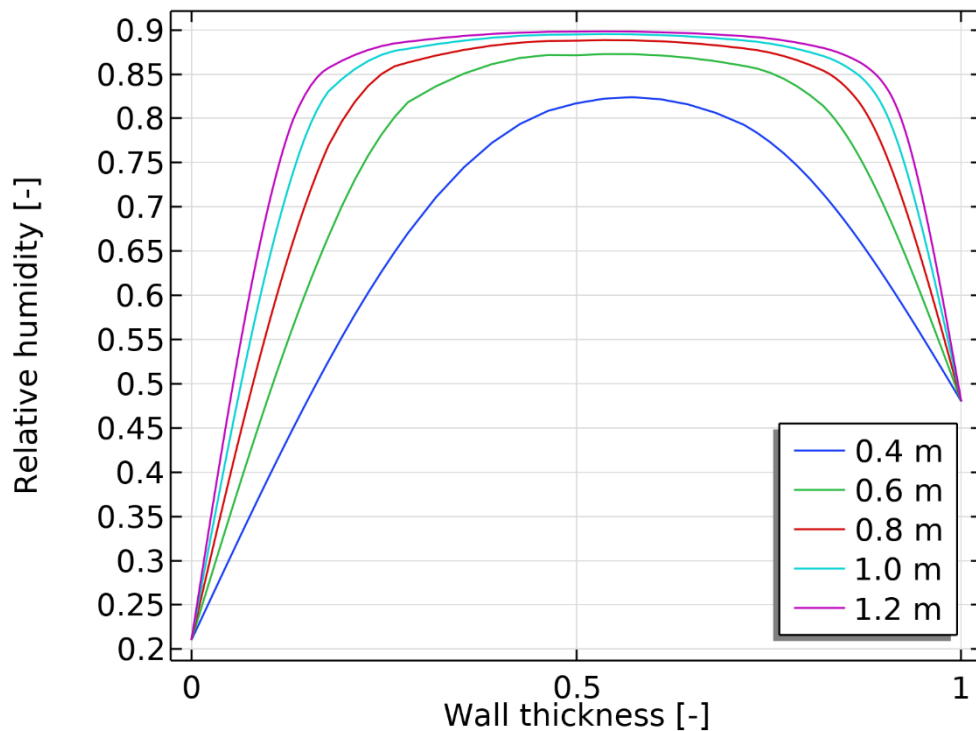


Figure 7.76 RH distribution after 7 years with constant material properties

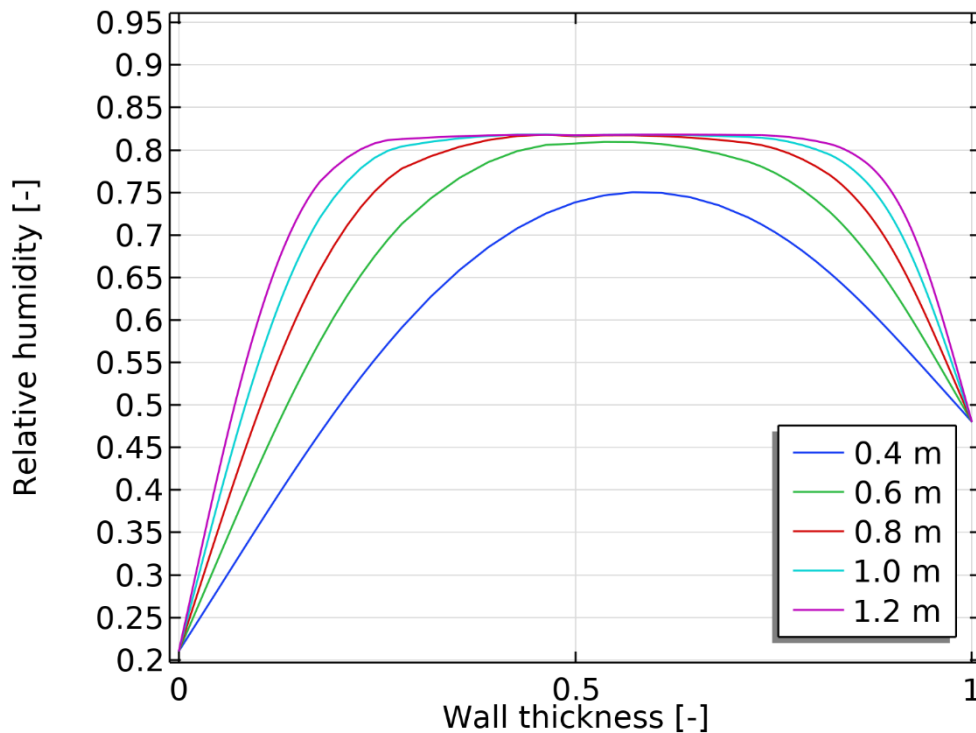


Figure 7.77 RH distribution after 7 years with time dependent material properties

The simulation shows that the RH distributions for the different thicknesses are clearly not proportional to the scale factor thickness-squared. This applies regardless of constant or time-dependent material properties are used.

The gradient of the RH distribution close to the surfaces is larger at a wall thickness of 1.2 m compared with a wall thickness of 0.4 m, see Figure 7.76 and Figure 7.77. The RH increase is roughly 0.7, from 0.2 to 0.9 between 0 (-) and 0.25 (-) of the wall thickness at a thickness of 1.2 m, see Figure 7.76. At the same distance from the surface, the increase of RH is roughly 0.4, from 0.2 to 0.6 at a thickness of 0.4 m. It is also clear that the RH in the centre of the wall (0.83) is lower in the 0.4 m thick wall compared with the 1.2 m thick wall (0.9), if constant materials are used in the analysis, see Figure 7.76.

Figure 7.77 shows that the RH is lower in every part of the wall when the material properties are assumed to be time-dependent than the RH when constant material properties are assumed, see Figure 7.76. This result was achieved even though the initial condition of the RH was set to 0.999 in the case of time-dependent material properties and 0.9 when material properties were set constant. The chemical drying of moisture in concrete may explain part of this difference, but not all of it. Another possible explanation to this difference might be the time dependency of the moisture diffusion coefficient and sorption isotherm exhibited by concrete.

These results suggest that drying in concrete is not only related to the thickness, but other factors also affect drying, such as age dependent material properties. In addition, the description of the environment and material properties in the simulation are treated as uniform through the structure. In a real structure the

material properties may vary, for instance as the concrete batches exhibit differences in composition. Furthermore, surface cracks in a real structure, may locally influence drying because humid or dry air may penetrate these cracks, impacting the drying. Such cracks are not included in the drying model.

The evaluated moisture content distribution in the two cases with constant and time dependent material properties, after 7 years, are shown in Figure 7.78 and Figure 7.79, respectively.

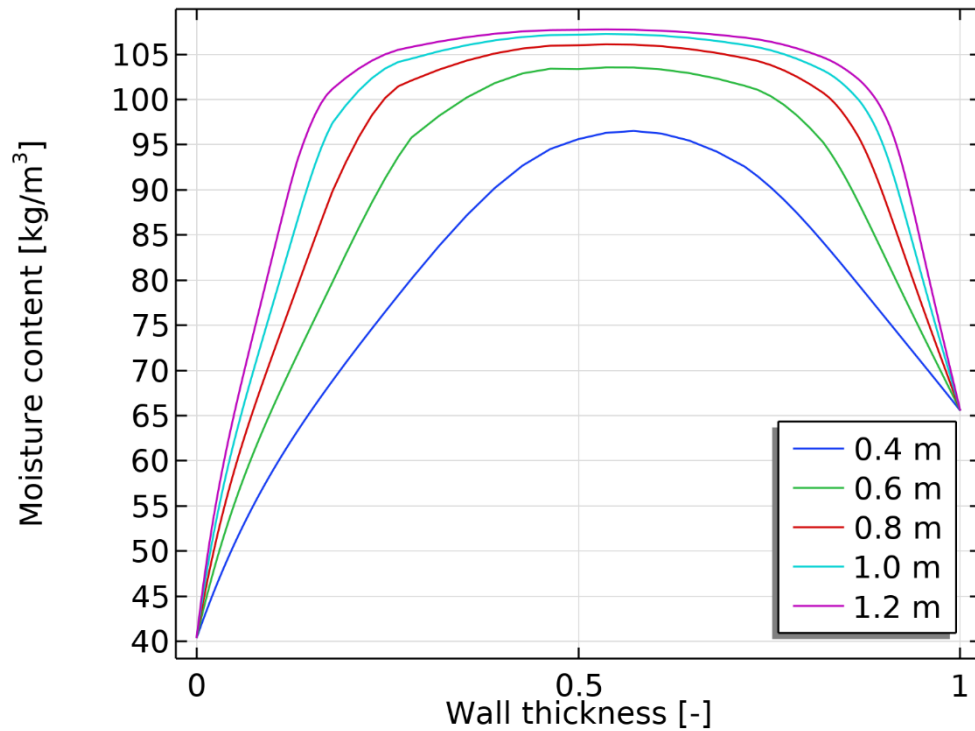


Figure 7.78 Moisture content after 7 years with constant material properties

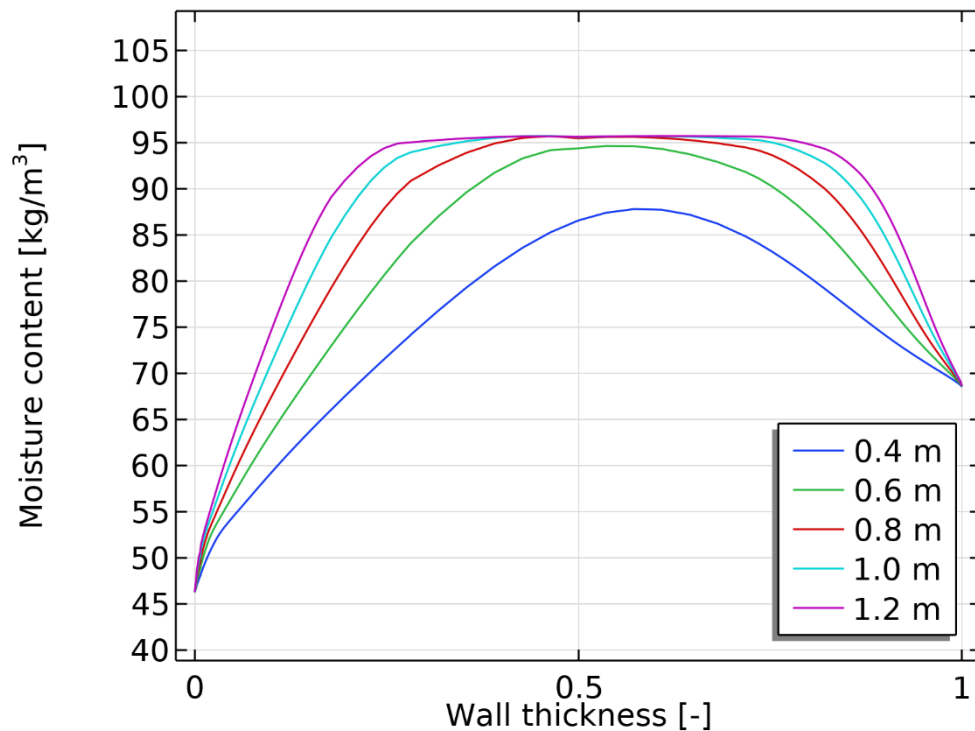


Figure 7.79 Moisture content after 7 years with time-dependent material properties

The results clearly show that the absolute value of the moisture content is affected by the assumption of constant or time-dependent material properties. The surface moisture content is about 40 kg/m<sup>3</sup> when constant material properties are used, see Figure 7.78. This result may be compared to 47 kg/m<sup>3</sup> when time-dependent properties are used, see Figure 7.79. The moisture content in the centre of the wall is roughly 107 kg/m<sup>3</sup> when constant properties are assumed and about 95 kg/m<sup>3</sup> when time-dependent properties are assumed. This difference is an effect of the assumed self-desiccation, which is included when time dependent properties are used. Measurements of the moisture content profile in a real RC after 30 years of operation show a similar distribution [27]. Experimental results on measurements of long-term shrinkage are in most cases limited to less than 3 years and these measurements are performed on rather small samples [28-30].

The predicted tangential stresses through the cross section of the wall with constant and time-dependent material properties, after 1 year, are shown in Figure 7.80 and Figure 7.81, respectively.

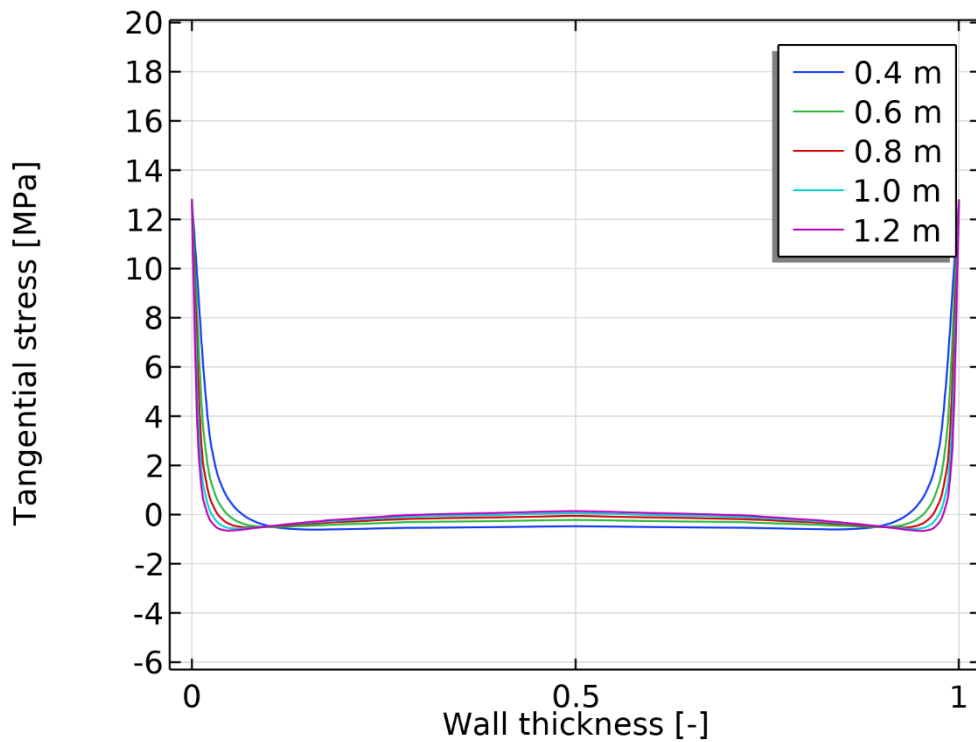


Figure 7.80 Tangential stress distribution after one year with constant material properties

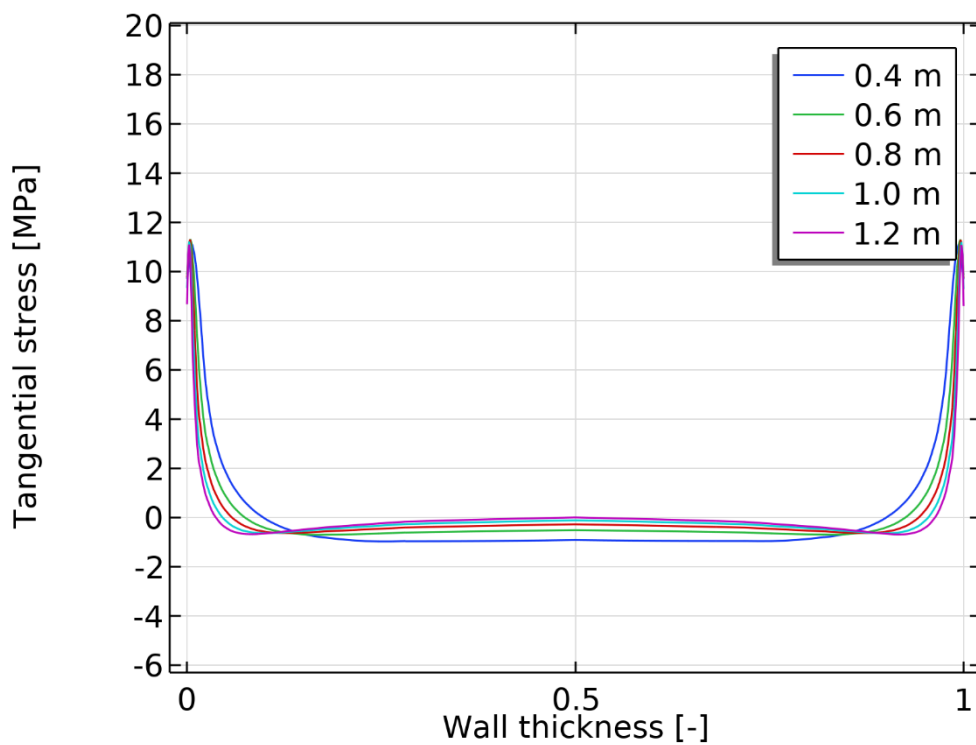


Figure 7.81 Tangential stress distribution after one year with time dependent material properties

The predicted stresses caused by shrinkage are large at the surfaces of the wall regardless of the use of constant or time-dependent material properties. The major cause of these stresses is drying. These large tensile stresses shift to compressive

stresses a short distance from the wall surfaces. The difference between the two assumptions of constant vs time-dependent material properties is of a small magnitude. The evaluated stresses are larger than the tensile strength of the concrete, 4.5 MPa, which means that surface cracks will develop. In addition, the stress distribution after one year shows that the stress distributions are almost equal, but they will happen at different time periods depending on the wall thickness.

Stresses caused by drying of concrete has been thoroughly investigated in the research community. Among these, a few projects have special relevance to this analysis. Drying concrete and the distribution of shrinkage stresses in concrete structures with impact of internal curing have been investigated by Jun et al. [31]. The estimated stress distributions in that research are similar to the distributions in this analysis, with large tensile stresses at the surface. Azenha et al. [32] have also investigated stresses caused by shrinkage during the service life of reinforced concrete structures. In that research paper thermal and moisture related stresses are modelled in a 250 mm thick concrete slab from an early age until about 50 years of drying. The evaluated stresses in that paper show a similar distribution to those shown in this analysis.

Evaluated tangential stress distributions at a cross section of the wall with constant and time-dependent material properties, after 7 years, are shown in Figure 7.82 and Figure 7.83, respectively.

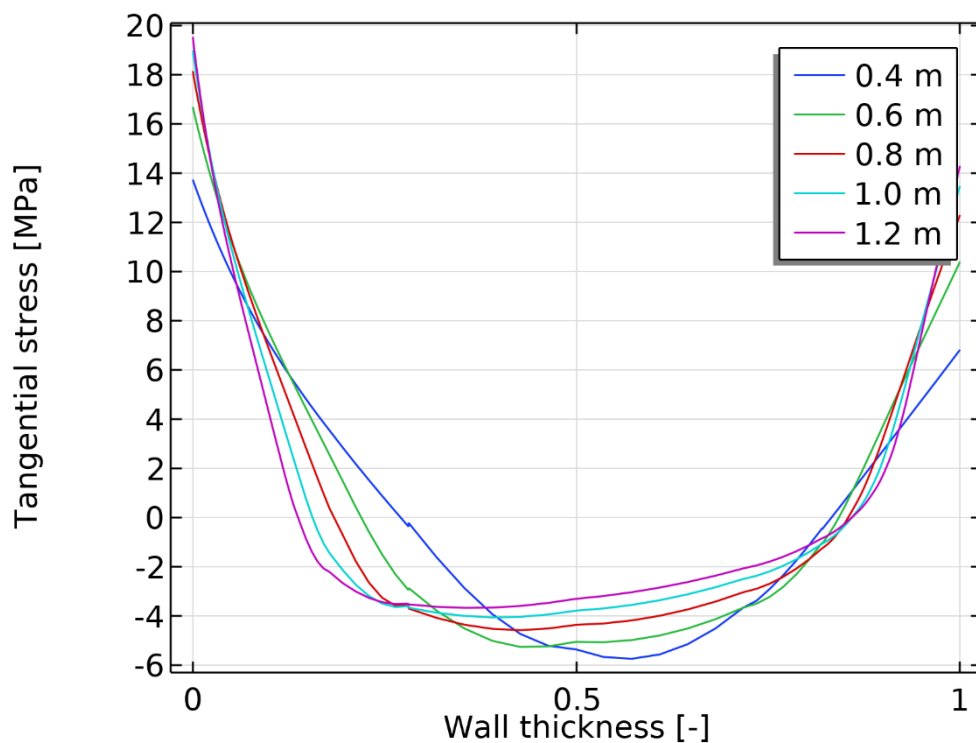


Figure 7.82 Tangential stress distribution with constant material properties after 7 years

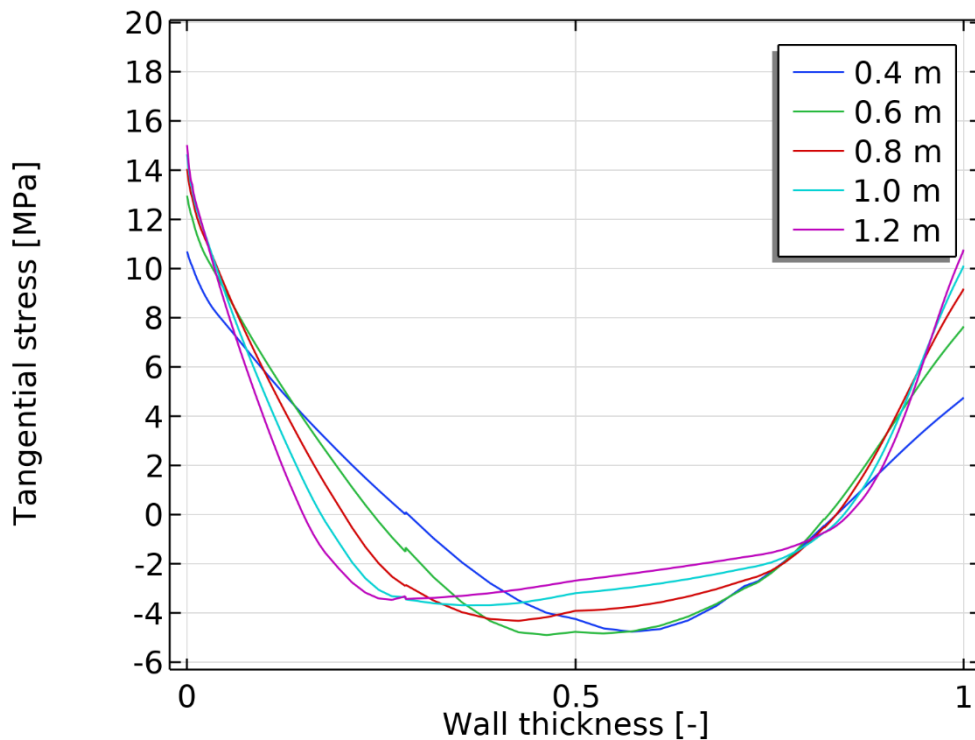


Figure 7.83 Tangential stress distribution with time dependent material properties after 7 years

The tangential stresses at the boundary surfaces are higher when constant material properties are assumed and lower when time dependent properties are used, see Figure 7.82 and Figure 7.83. In both cases, the obtained stresses are larger than the tensile strength, 4.5 MPa, which implies that the concrete surface will crack. In the centre of the wall there are compressive stresses of a magnitude of 5 MPa. Because of the compressive stresses in the centre, there is no reason to suspect cracks that propagate through the concrete wall from one surface to the other. Since the stresses tend to be higher when assuming constant material properties, the results will be on the safe side if such an assumption is selected. This means that constant material properties may be used in an early analysis to evaluate stresses. Note that this stress distribution is affected if/when cracks are introduced. If the evaluated stresses are lower than the tensile strength, when using constant material properties, there is little reason to perform a more advanced approach. The stresses obtained in this numerical analysis are of the same magnitude as previously shown by Granger [33]. A part of that study also analysed drying and stresses obtained in a nuclear containment element modelled as a 1.2 m thick ring [33].

Stresses in the tangential direction with constant and time-dependent material properties from 0 to 0.01 years are shown in Figure 7.84 and Figure 7.85, respectively. The stresses are evaluated at a point located at a normalized distance of 0.05 from the inner wall surface. This means that the point is 0.02 m and 0.06 m from the inner surface of the wall in the cases of a 0.4 m and 1.2 m thick wall, respectively.

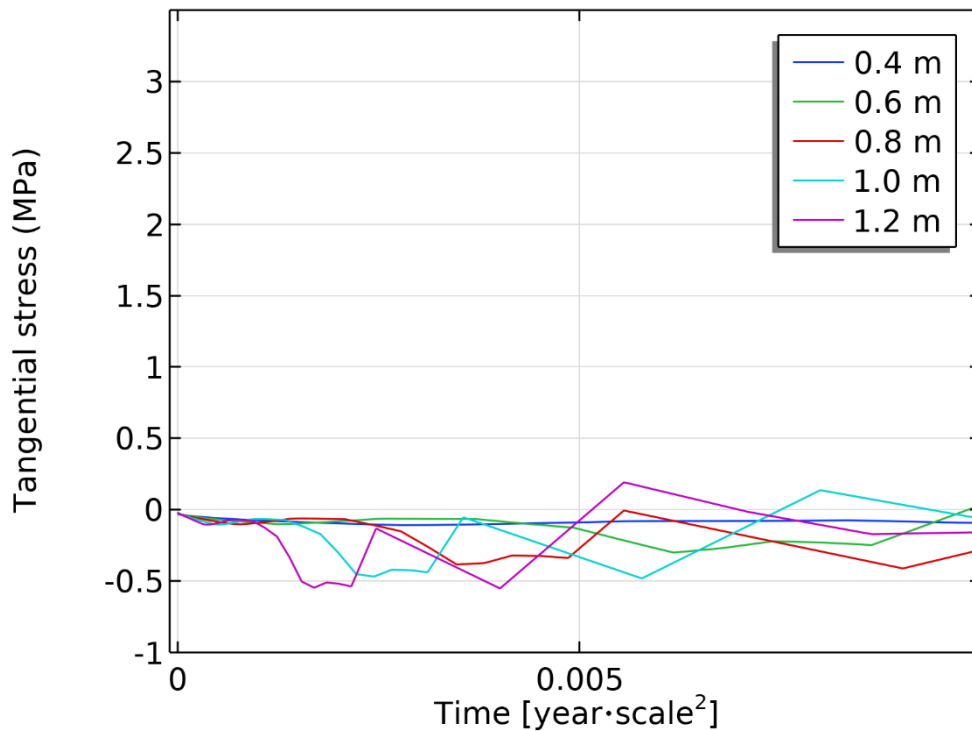


Figure 7.84 Tangential stresses close to the surface assuming constant properties

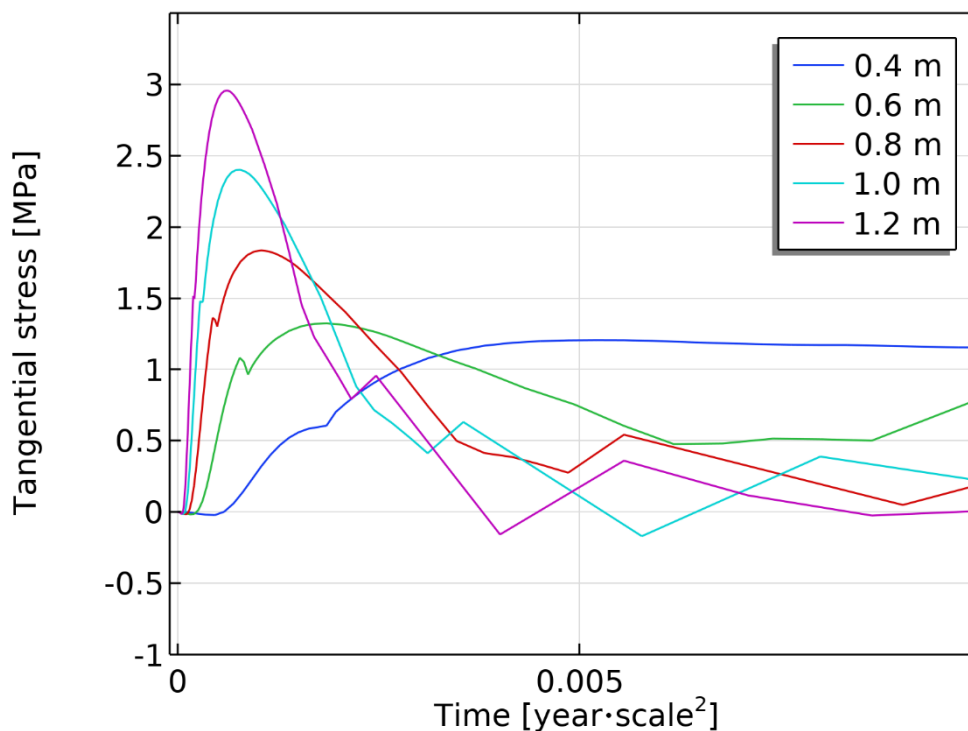


Figure 7.85 Tangential stresses close to the surface assuming time dependent properties

The stresses at the surface in an early stage are insignificant when constant material properties are used, see Figure 7.84. This is not surprising since the heat generation from cement hydration is excluded from this analysis and drying stresses develop on a long-term basis. The small stresses that occur close to the surface is due to external thermal variations and the constraints of the concrete wall.

When time-dependent material properties are assumed the tangential stresses at the surface increase to around 3 MPa (tension) when the wall thickness is 1.2 m, see Figure 7.85. This stress is less than the tensile strength of the concrete (4.5 MPa), but this strength was determined for mature concrete. If the wall thickness is thinner, the surface stresses decrease given equal boundary conditions. The cause of these tangential stresses is the heat generated from the cement hydration, the resulting temperature distribution and the applied boundary conditions in the model. Such results has been shown in previous studies by, e.g., Azenha et al. [32] and Zhang et al. [31].

Stresses in the tangential direction with constant and time-dependent material properties, from 0 to 7 years, are shown in Figure 7.86 and Figure 7.87, respectively. These stresses are evaluated at a normalized distance of 0.05 from the inner surface of the wall thickness.

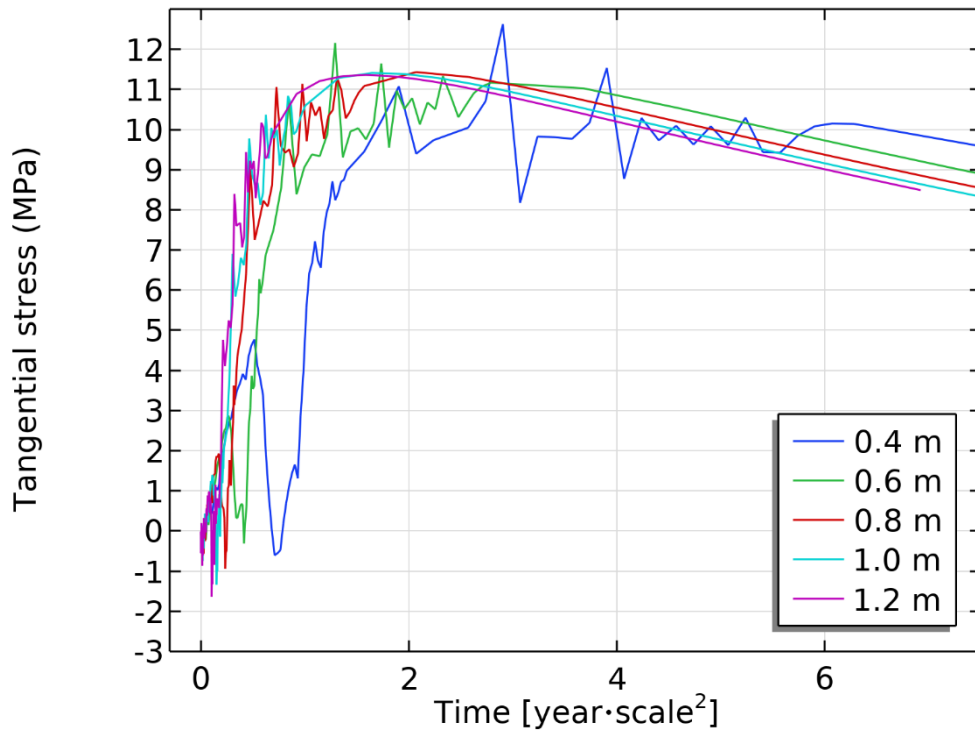


Figure 7.86 Tangential stresses through time with constant material properties

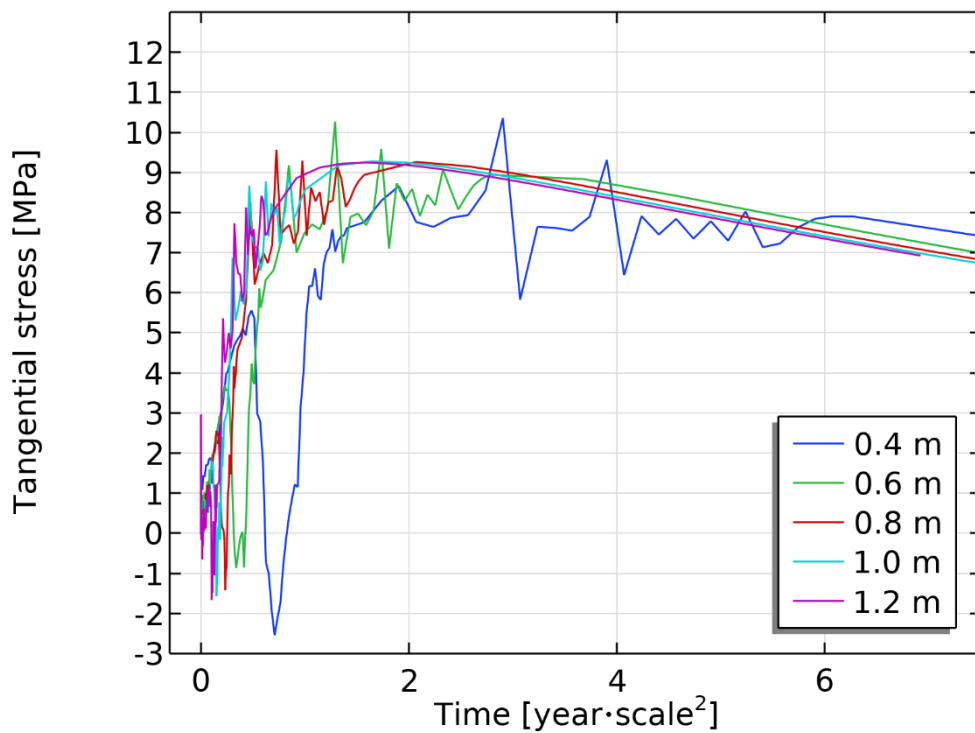


Figure 7.87 Tangential stresses through time with time dependent material properties

The stresses in the tangential direction roughly vary between -1 MPa to 11 MPa when assuming constant material properties, see Figure 7.86. When time dependent material properties are assumed, the stresses roughly vary between -1 MPa to 9 MPa, see Figure 7.87. The decrease in stress, at about 1 year at a wall thickness of 0.4, is caused by a decrease in temperature, see Figure 7.3.

The obtained overall stresses close to the surface of the wall is smaller when time-dependent material properties are used. When analysing the obtained stress evolution at large, the results from the different wall thicknesses overlap each other. However, when analysing the stresses in detail, large differences are obvious.

It is clear that temperature changes in the surroundings add to the stresses caused by drying. These temperature-induced stresses are also dependent on the constraints of the wall. The temperature-induced stresses occur at a much shorter time scale compared to the stresses induced by drying, which is an important result from this analysis.

## 8 Results from other participants

This chapter presents a summary of the participants used models and the results in the workshop VERCORS 2022. These results are presented in a draft report that covers the complete workshop[4].

### 8.1 PARTICIPANTS

Ten teams participated in the workshop and presented their results, these are presented in Table 8.1.

**Table 8.1. Participants in the workshop VERCORS 2022**

Project manager	Organisation	Country
David Bouhjiti	Egis Advanced Solutions	France
Jan Stephan	ÚJV Řež, UJV group	Czech Republic
Petr Havlásek	CTU, University	Czech Republic
Moez Jellouli	ISL Ingénierie	France
Joshua Hogancamp	Sandia National Laboratories	US
Try Meng	IRSN and CEA	France
Jean Michel Torrenti	Université Gustave Eiffel	France
Magnus Åhs, <b>Team 19</b>	Lund university, Vattenfall and Sweco	Sweden
Nicolas Goujard	Ingérop	France
Julien Niepceron	EDF	France

Both industrial companies and universities participated in this benchmark. Some of these teams participated in the earlier organized benchmarks and some entered this workshop without participating before. The team number is not included in the table to make the contributions anonymous, except for this study's contribution to the benchmark, team 19.

## 8.2 MODELS

A short description of the models and codes used by the participants is given in Table 8.2, [4].

**Table 8.2 Models and codes used by the different teams.**

Team	Model	Code
4	Creep: Rheological Burger model – Drying: Mensi’s Model for $RH \geq 40\%$ Global leakage: Darcy’s law for porosity & Poiseuille’s law for cracks	-
6	Linear FE model of the structure Creep: use of the Eurocode EN 1992-2	Abaqus, standard
8	Creep: microprestress-solidification theory for concrete creep Bažant et al. (1997) – Drying: Bažant-Najjar model	OOFEM.org solver
9	3D Model, Creep: analytical formulas – Drying: Granger’s law, Global leakage: Darcy’s law with Van Genuchten’s model for porosity & Poiseuille’s law for cracks	Ansys
13	3D Model, Creep: Bazant’s B3 creep model implemented into Abaqus via a prony series – Drying: Fick’s 2nd Law of Diffusion	Cubit, Abaqus
15	FE model, Creep: use of the BPEL99 code – Drying: analytical formulas, Global leakage: Darcy’s law for porosity & Poiseuille’s law for cracks	SALOME-MECA, Cast3m
17	Analytical biaxial calculation (no use of FEM), delayed strains of concrete decomposed in 4 parts (autogenous shrinkage, basic creep, drying shrinkage, drying creep) using the Eurocode EN 1992-2	
19	Linear FE model, Creep: modelled as a contribution to the strain by using the Eurocode CEN-EN 1992, Leakage: porosity determined by a monitoring campaign on Ringhals - no leakage through cracks included	COMSOL Multiphysics
25	3D Model, Creep: Burger model – Drying: Granger’s law, Global leakage: Darcy’s law for porosity & Poiseuille’s law (Mivelaz approach) for cracks	Code_Aster

### 8.3 RESULTS

The results presented in this section is a sample from the workshop draft report. A more detailed presentation of the results is found in the report.

This benchmark was divided into two phases. The first phase, phase 1, was performed without knowing the results from the measurements and a second phase, phase 2, was performed when knowing the results. This gave the participants an opportunity to improve and calibrate the applied model to better match the measurement results. Some participants used this opportunity, and some did not.

#### 8.3.1 Temperature

The temperature was measured in a number of different positions in the VERCORS mock-up. These measurements were compared with the calculation results of all the teams. In this summary the measurements in two points are shown as an example.

In Figure 8.1, the measured (black solid line) and simulated temperature, phase 2, in point TETA C2 are shown. This point is located in the raft about 0.7 m below the raft's upper surface at a radius of 4.1 m.

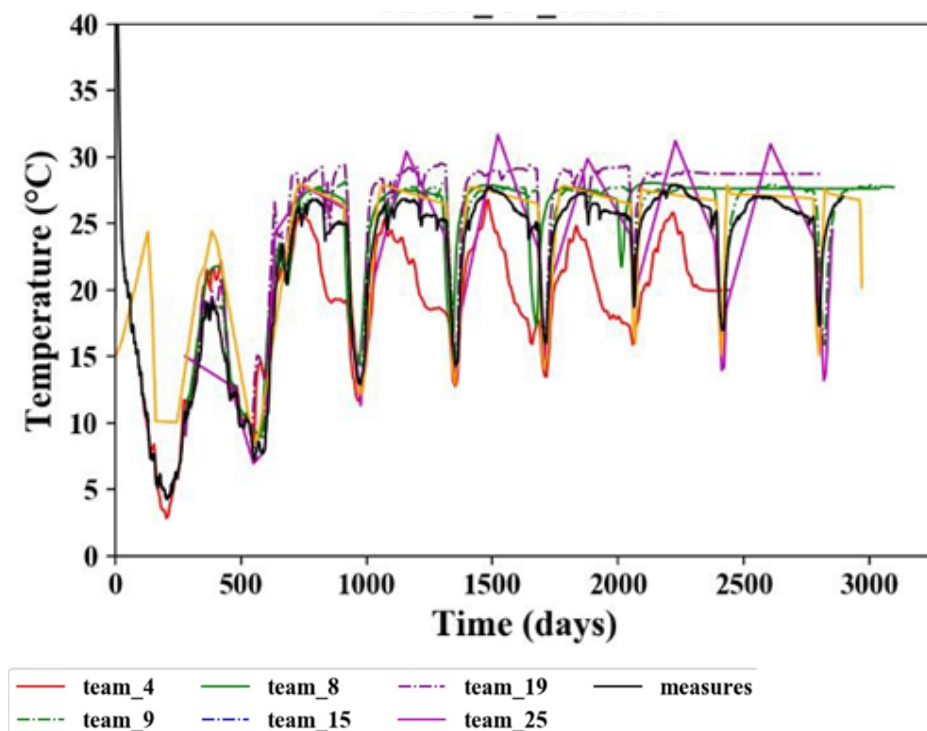


Figure 8.1 Measured temperature (black solid line) and the results from the simulations of the different teams[4].

All the results except one of the different simulations are close to the measurements. The one deviating result is about 7-8 °C lower than the

measurements a long time before each pressure test (team 4). Team 19 predicted the overall highest temperature in this point.

All teams chose to incorporate the decrease in temperature that occurs before the pressure test. And most of the teams used the daily variations in boundary conditions (temperature) distributed by benchmark VERCORS 2022.

### 8.3.2 Moisture profiles

Drying is a key factor in predicting mechanical behaviour of concrete over time. As the moisture content in the reactor wall decreases, it has a direct impact on two phenomena: shrinkage and creep. Therefore, all participating teams were assigned the task of predicting drying profiles across a cross-section of the cylindrical wall.

The predicted moisture content profiles through a cross-section of the cylindrical wall at an elevation of +7.39 m, phase 2, are shown in Figure 8.2. In addition, there is a star that refers to a measurement performed by using a time domain reflectometry, TDR, equipment. The dates represent day 384 (2015-08-12) and 1287 (2018-01-31).

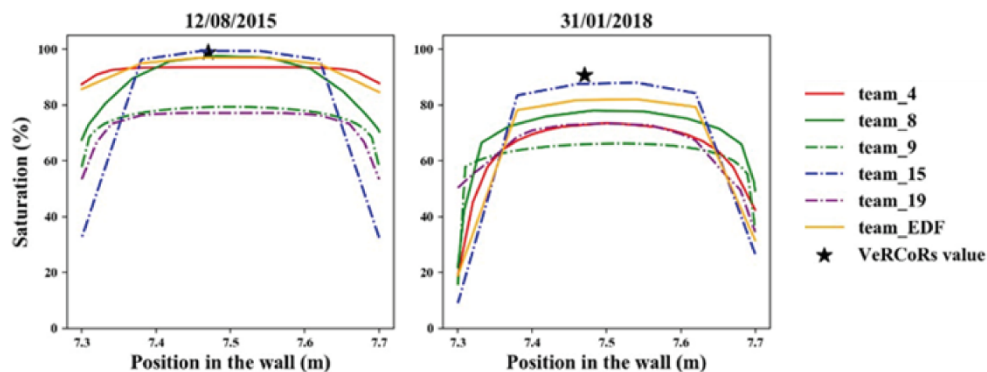


Figure 8.2 Saturation profiles through a cross-section of the cylinder wall at two different times [4].

The predicted moisture content is shown as the degree of saturation. Five of the participants in the workshop evaluated this parameter. All the participants predict drying over time, but the spread is quite large. In the wall centre the highest predicted degree of saturation is about 98% at day 384 and the lowest is 78%. At day 1287 the highest degree of saturation is 85% and the lowest is 65%.

The TDR measurements shows that the degree of saturation is 98% at day 384 and around 90% at day 1287. Team 15 has results that is rather close to the TDR results. However, there is a discussion about the valid and accuracy of TDR measurements. This TDR equipment has been tested in the Flamanville facility to measure moisture content in concrete [34]. The test showed that there are several parameters that need to be addressed and determined, i.e. signal processing, calibration procedure and temperature dependence, before using this equipment in concrete to get valid and reasonable results. TDR was also used in the VERCORS mock-up [35]. TDR was not able to match the requirements and there is still a need

to better assess the real accuracy of this equipment [36, 37]. The measurements of the degree of saturation are therefore not to be considered as reliable.

### 8.3.3 Displacement

The participating teams were asked to calculate the evolution of non thermal radial and vertical displacements at a level of -1, +4 and +9 m. It should be noted that most of the teams sent in total displacements (including thermal contribution). Therefore, the total displacements were selected instead. The results of the total radial displacements, phase 2, are shown in Figure 8.3.

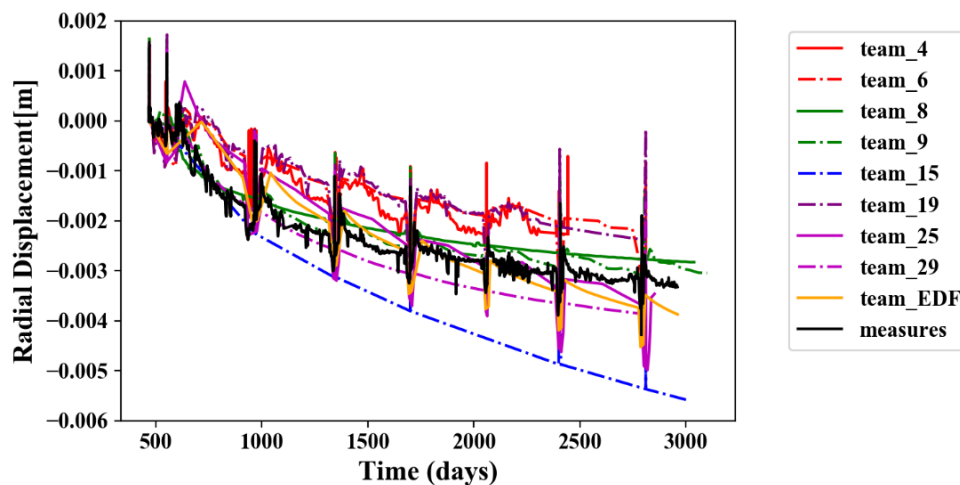


Figure 8.3 Predicted radial displacement at +9 m (mean value of all angles) compared with the measured average measurements by pendula[4].

The measurements indicate a displacement of about 3 mm after 2800 days. The long-term deformations are clearly shown in the measurements, creep. In addition, the measurements show a change of the RC radius during each pressure test. This change is also exhibited by most of the teams. There is a scatter among the different results of about 1 mm, approximately 30%, between all the predictions (apart from team 15) during the last 200 days. In addition, there is a small but notable increase in radius before, during and after the pressure test that may be attributed to the humidity increase and swelling of the RC structure, when the climate system is turned off. In this figure the pre-stressing of the tendons is not included.

### 8.3.4 Strain evolution

All teams presented strain evolutions in the requested points in the RC. The participants contributions and the measured (black solid line) evolution of tangential and vertical non-thermal strains in point H6 are shown in Figure 8.4 and Figure 8.5. Each strain sensor was equipped with a thermal sensor to enable a thermal correction of the strain measurements and to evaluate the non-thermal strains.

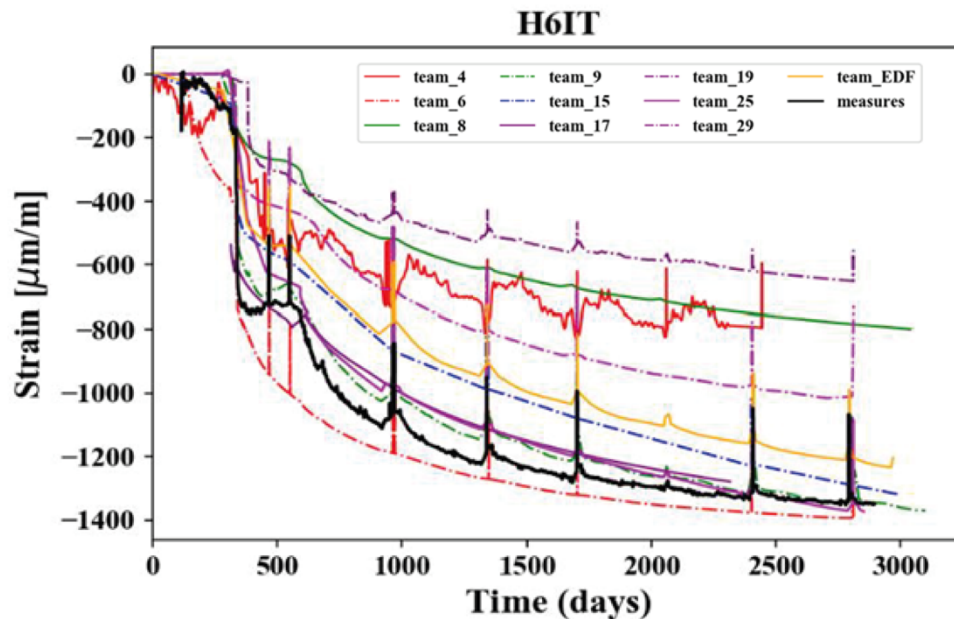


Figure 8.4 Evolution of tangential strains in point H6 [4].

The measurements show that the tangential strain is  $\sim -1300 \mu\text{m/m}$  at the end of the evaluated time. The largest predicted tangential strain is  $-1400 \mu\text{m/m}$  and the smallest tangential strain is  $-600 \mu\text{m/m}$ .

The measurements show that there is a large decrease in radius (negative strains) when the tendons are prestressed. This large decrease in radius is by most participants underestimated and in one case overestimated. There is large scatter in the predicted mechanical response to the prestressing event. It also seems as if the timing of the event is not coherent, some participants start the tensioning at around day 200 but the actual tensioning was supposed to take place at day 384. This could be a misunderstanding of the instructions from the benchmark.

Furthermore, the measurements show a clear mechanical response to the humidity increase before each pressure test. This means that the radius of the RC increases as the humidity increase. This mechanical response is shown by some participants, and some have not included this effect. The magnitude of the humps is in some cases underestimated and, in some cases, very close to the measurements.

In addition, the measurements of the RC show a clear mechanical response to the actual pressure test. Results from the participants show that the magnitude of the predicted tangential strain is either smaller or larger than the measurements.

The rate of strain evolution after the tensioning of the tendons is of about the same order of magnitude. This means that the rate of strain evolution originating from shrinkage and creep is rather coherent between all the groups.

The spread in tangential strains is at the end of the simulation about  $800 \mu\text{m/m}$ . This large scatter is mainly caused by the strains occurring when prestressing the tendons.

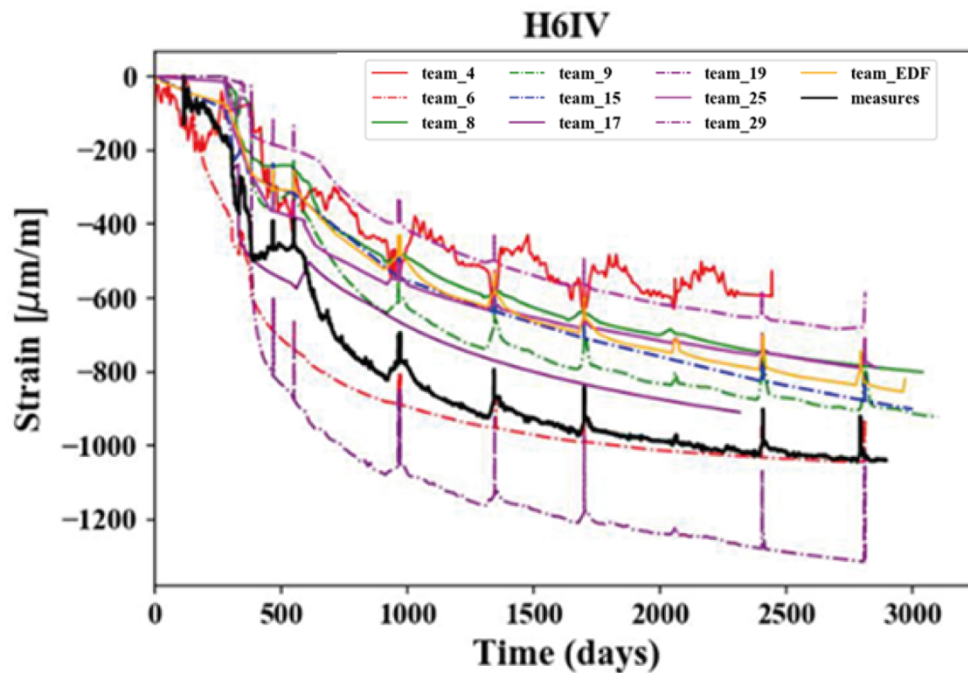


Figure 8.5 Evolution of vertical strains in point H6 [4].

The vertical strains are  $-1000 \mu\text{m/m}$  at day 2800. The largest strain at that time is  $-1300 \mu\text{m/m}$  and the smallest is  $-650 \mu\text{m/m}$ . This gives a spread between all the participants of around  $600 \mu\text{m/m}$ .

The measurements of the vertical strains show the same overall behaviour of the RC as the tangential strains. As the tendons are prestressed the vertical strains becomes large (negative strains) and the height of the RC decreases.

The pressure test increases the height of the RC as the pressure increases and this is clearly shown as peaks in the measurements of the vertical strains. This mechanical response is also shown by the participants predictions.

The height increases as the relative humidity increase before and during each pressure test. This happens because the concrete structure swells as a response to the increasing humidity in the surrounding environment. This behaviour is captured by some participants models but not all.

A more extensive presentation of the results is found in the draft report from VERCORS[4].

### 8.3.5 Leakage

The evolution of the measured and predicted global air leakage is presented in this section. The participants had two options: they could either to provide predictions for the global leakage or break it down into two categories, porous leakage, and local leakage through the cracks in the RC.

The measured and predicted total global leakage provided by six of the participants of the workshop is shown, phase 2, in Figure 8.6, [4].

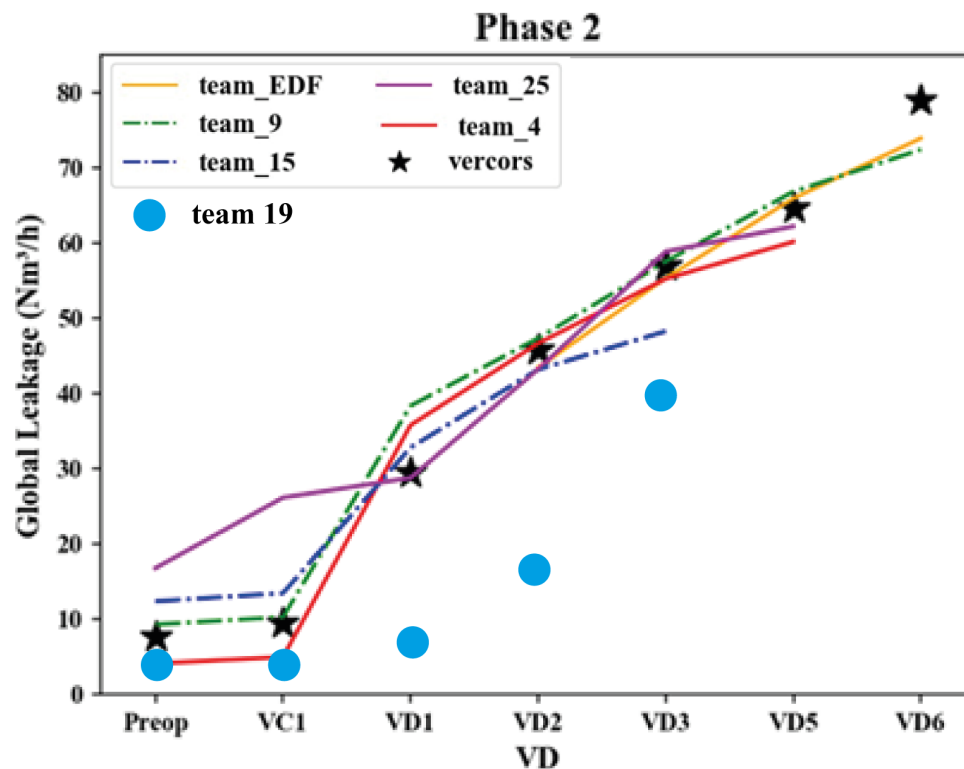


Figure 8.6 Measured and predicted global leakage provided by the participants.

The teams all show an increase of the global leakage. Note that team 19 only considered the porous leakage and did not take into account leakage through cracks (local leakage).

The measured data on leakage reveals a pattern: initially, there is a gradual increase in leakage with time, which subsequently transitions into a more rapid escalation. This shift in leakage behaviour is possibly ascribed to porous leakage. This phenomenon arises from the material's porosity allowing substances to pass through. As the drying continues, a larger fraction of the material's pore system becomes empty. Consequently, this growing void within the pores contributes to the observed increase in porous leakage flow.

Furthermore, the ongoing drying process increases the portion of the material's pore network that is accessible to airflow. This expansion, in turn, amplifies the volume of the material exposed to the moving air. In essence, the increase in porous leakage is intricately linked to the evolving dryness of the material and the resulting changes in its porous structure.

It's worth considering that local leakage through cracks might also contribute to this overall increase in leakage. This could occur if more cracking occurs as time progresses or if existing cracks widen over time.

## 9 General discussion

The discussion presented in this section are derived from the overall goal of this study which was to increase knowledge of the structural response of reactor containment buildings. Another aim was to develop a model that may predict the structural behaviour of the scale model of the French reactor containment, RC, using commonly adopted modelling approaches. In addition, the objectives included developing a leakage model and applying it to the scaled model of the RC. Furthermore, the scale effect of drying was analysed, considering both constant and time-dependent concrete properties.

### 9.1 LONG- AND SHORT-TERM OVERALL BEHAVIOUR

The finite element models, FE models, used in this study effectively demonstrated the general overall long-term behaviour. The major cause of difference between the measurements and the calculation is the uncertainty of the applied models. This uncertainty grows with time. These include differences between actual material properties and modelled material properties. There are also potential discrepancies between measured strains and their actual values, which may occur because of measurement uncertainties. Another factor could be differences in the actual surface temperatures across various parts of the model compared to the temperatures assumed in the model.

These models also capture the general short-term structural behaviour within a reactor containment (RC), caused by temperature fluctuations. When relative humidity changes for a longer period of time, such as the increase of relative humidity occurring before and after a pressure test, the model is able to capture the semi long-term behaviour. However, there remains a noticeable deviation between measurements and calculations, likely attributable to uncertainties in the model. Furthermore, differences may be caused by simplifications in the description of the environmental conditions and the description of the geometry. This was evident when comparing predictions from the FE models against actual measurements.

The analysis showed that the deviation between the measurements and the actual long-term strains was 26% by using the wedge geometry and 31 % by using the complete geometry. However, it is important to emphasise that this difference does not necessarily indicate that the wedge geometry is a more appropriate choice. These two geometries exhibit different discrepancies that may contribute to the deviations. For instance, wedge geometry did not include the hatch, while the complete geometry represented the hatch with a large penetration. Two additional issues with the wedge geometry were the assumptions regarding proper mechanical boundary conditions and the need to adjust the arrangement of the tendons to ensure symmetry relative to the wedge.

The FE models used in this study were also applied in two previous studies, VERCORS 2015 and 2018 [5, 6], which both utilized the wedge geometry.

## 9.2 GEOMETRY

When analysing strains at the mid-height of a cylindrical wall, using a simplified geometry, such as a 45° wedge of the RC, is sufficient. However, it's important to avoid using points near the edges of this limited geometry. If the purpose of the analysis is to examine strains in the dome or at a radius close to zero, it's more suitable to employ the complete geometry. The complete geometry includes all essential aspects of the RC structure, except for the equipment hatch door.

In order to analyse points around the equipment hatch, it is important to include the door that close the hatch in the geometry. In this study there was no information available about the door structure, therefore it was modelled as a large penetration of the cylindrical wall. This means that the strains around the door were affected in the vertical and tangential direction. When analysing a point beside the hatch the tangential strains are less accurate compared to the vertical. Tangential strains are more accurate than vertical, in points above or below the equipment hatch.

## 9.3 TEMPERATURE EFFECTS

The simulations showed that the temperature has a significant impact on the strains and stresses that occur during the service life of an RC. The expansion and contraction caused by temperature are much larger and occur at a higher rate than the volumetric changes due to both shrinkage and creep. Thermal stresses mainly arise when the temperature distribution is non uniform in a cross-section. In reality, temperature changes affect other material properties such as heat conductivity, sorption isotherm, and moisture transport coefficient. However, these effects were not considered in the presented model. It's worth noting that these unaccounted effects are relatively small in magnitude when compared with the thermal expansion and contraction. Benchmark VERCORS 2022 only provided strain measurements where thermal strains were excluded. Therefore, it was not possible to compare the simulated total strains with measurements of the total strains.

## 9.4 RELATIVE HUMIDITY

The sorption isotherm and moisture transport coefficient were evaluated from a generic model and not the data provided by Benchmark VERCORS. This variation of data sources will affect the results. The observed strain increase caused by a temporary increase in relative humidity appear to be smaller than the measurements. This could indicate a need for improvement of the model describing the relationship between swelling, shrinkage, and relative humidity. Additionally, it may be beneficial to calibrate the input parameters associated with this coupling to improve the accuracy of the calculation results.

## 9.5 LEAKAGE

Porous leakage increases with time, which is expected since the drying of the concrete increases the permeability. Cracks may have a substantial contribution to

the total air leakage, especially if through cracks are present in the RC. Superficial cracks that appear near the surface will have a smaller effect on leakage. It's important to note that this study did not consider the impact of leakage through cracks. If the local leakage measurements, as conducted in the VERCORS Benchmark, are accurate, cracks could account for approximately 70% of the total leakage, 39 Nm<sup>3</sup>/h related to 57 Nm<sup>3</sup>/h. Therefore, it's evident that accounting for cracks is essential when calculating total leakage. Moreover, if porous leakage constitutes only 30% of the total leakage, 18 Nm<sup>3</sup>/h out of 57 Nm<sup>3</sup>/h, the model proposed in this study would substantially overestimate porous leakage, which was estimated to be 41 Nm<sup>3</sup>/h.

Many of the teams that participated in the benchmark VERCORS were quite successful in predicting the leakage. However, it is important to consider that the teams were given the opportunity to adjust and calibrate the model to fit the measurements. If these adjustments lack a clear physical basis, the adjusted model should be applied cautiously in other leakage analyses.

## 9.6 SCALE EFFECT OF DRYING

The results of the theoretical study investigating the scale effect of drying suggest that moisture distribution is influenced by the scale. However, to comprehensively understand the long-term effects, additional factors should be taken into consideration. Specifically, factors like the age-dependent variation in material properties and self-desiccation are essential components that should be included in the analysis. The purpose of the study was to investigate the scale effect of drying or aging factor of the 1:3 scale mock up. VERCORS suggested that the aging factor was nine, but the analysis performed in this study show that this is not the case. The shape of the drying profile is dependent on the size of the specimen which has an impact on, for instance stress distribution.

## 9.7 STRESSES/CRACKS

When analysing stresses at an early age of a concrete structure, it is especially important to include heat generation. At early age, a major part of hydration occurs, and heat generated from the hydration causes a temperature increase in the centre of the concrete structure. The non-uniform temperature distribution causes stresses because of a non-uniform volumetric expansion.

Tensile stresses, larger than the tensile strength, occur in points that are located close to the concrete surface, and these stresses might cause surface cracks. These cracks are, as previously mentioned, vital to assess in order to evaluate local leakage during the pressure tests. Cracks that occur also affect the stress distribution.

The pressure tests conducted in the Benchmark VERCORS, especially the final one reaching up to 6 bar, have the potential to intensify any pre-existing cracks, possibly causing additional damage to the RC.

## 9.8 VERCORS MEASUREMENTS

The VERCORS Benchmark has made significant efforts to measure crucial parameters needed for performing long-term analyses, including ambient conditions like air temperature and relative humidity. Detailed information on material properties necessary for the simulations has also been provided. In addition, the mechanical behaviour has been followed with CV sensors and temperature sensors at positions that are of great interest. These measurements are vital to evaluate and verify/validate suggested FE models.

Nevertheless, one vital parameter that should have been assessed is the distribution of relative humidity at specific cross-sections within the reactor containment. These measurements would have increased the opportunity to improve the moisture transfer model and also the coupling between moisture distribution and shrinkage. In addition, it would have made a contribution to possibly improving the creep model.

## 10 Conclusions

Conclusions drawn from this project are as follows:

- The model's accuracy in predicting long-term deformations is approximately 30%. It is important to acknowledge that the quality of the input data to the model directly affects the results. The mean coefficient of variation is of the order of 20% of the predicted creep data in Eurocode 2 [9]. Other uncertainties in material properties also exist like moisture properties and air permeability properties but they are not quantified.
- There are significant discrepancies between the results of the analysis and the measurements. A substantial portion of these discrepancies arises from unsatisfactory predictions of the initial strains corresponding to the stressing of the tendons. However, the modelling of the long-term behaviour of the structure has been more successful. The predicted rate of long-term strains (1/s) aligns reasonably well with the actual measurements.
- Extended analysis of drying has enabled a new approach to utilize the creep coefficient suggested in Eurocode 2. The Eurocode's model is based on experiments with comparatively small specimens. In small specimens, the drying process is faster than that of an RC. In a small specimen, the shrinkage and creep processes occur simultaneously, and the specimen approaches moisture equilibrium much faster than an RC structure. In the analyses presented in this report, the moisture distribution within the structure has been calculated, and the local moisture content of the material has been used as an input to the creep equations. This may explain some of the differences between the measured and calculated results.
- This analysis shows that the presented model underestimated the long-term deformations compared with what was actually observed in many of the analysed points.
- A comprehensive assessment of mechanical conditions in a complete geometry is required before applying them to a sub-model with reduced geometry.
- The performance of an RC is significantly affected by the surrounding temperature. Daily temperature fluctuations and long-term climate changes are important to take into account. This aspect must be considered when making long-term mechanical predictions for an RC. Therefore, it is vital to compare measurements with predictions that include the strains induced by temperature.
- Due to its mass and exposure characteristics, the drying process of the RC is slow. Consequently, the relative humidity of the environment has only a minor impact on its moisture-related behaviour.
- The developed model of leakage tended to overestimate porous leakage. This conclusion is based on the assumption that the local leakage estimation by VERCORS was accurate.
- The evaluated points represent important parts of the behaviour of an RC structure. Table 10.1 shows different physical aspect that may impact the long-term behaviour of the RC. An "s"-character denotes a significant impact upon the behaviour and a "i"-character denotes an insignificant affect of the behaviour.

Table 10.1 The significance of different physical aspects of the long-term behaviour in different parts of the RC.

	Temperature	Humidity	Pressure-test	Creep	Pre-stressing	Local Geometry
Raft	<b>i</b>	<b>i</b>	<b>i</b>	<b>i</b>	<b>i</b>	<b>i</b>
Gusset	<b>S</b>	<b>S</b>	<b>i</b>	<b>i</b>	<b>i</b>	<b>S</b>
Cylindrical part	<b>S</b>	<b>S</b>	<b>S</b>	<b>S</b>	<b>S</b>	<b>i</b>
Equipment hatch	<b>S</b>	<b>S</b>	<b>S</b>	<b>S</b>	<b>S</b>	<b>S</b>
Dome	<b>S</b>	<b>S</b>	<b>S</b>	<b>S</b>	<b>S</b>	<b>i</b>

## 11 Future perspective

This section suggests important areas of interest that the nuclear power industry need to consider in the future in relation to the results of this project.

### 11.1 DESIGN OF NEW REACTOR CONTAINMENTS

The finite element (FE) model developed in this study holds significant potential for use in designing new reactor containments. The key advantage of this model, along with similar types, lies in its versatility. It enables the incorporation of various parameters into the design process that would otherwise be challenging to consider. By performing coupled physical analyses—such as static and time-dependent mechanical analyses—alongside transient processes like temperature and humidity variations, it is possible to gain a better understanding and enhance predictions of long-term structural behaviour.

It's essential to recognize that the accuracy of a model relies, among other factors, on boundary conditions and material properties. These aspects are influenced by time-related factors, such as environmental variations around the structure, aging, and non-linear, time-dependent material behaviour.

When a structure is exposed to outdoor conditions, accurately anticipating the future environmental conditions for the next several decades becomes challenging. Consequently, predicting moisture content, temperature, and temperature-moisture gradients becomes intricate. Both temperature and moisture significantly impact concrete creep, shrinkage, and various degradation mechanisms that may affect the material.

When constructing new RCs, alternative cement types other than standard Portland cement, CEM I, may be used. The quality of these new cements is expected to match that of CEM I. However, there is a lack of knowledge regarding the physical and mechanical properties of these new cements.

While existing knowledge about CEM I's properties is based on decades of research, leveraging past experience allows avoiding starting from scratch. Nevertheless, it will take approximately 0.5 to 1 decade to update the most critical design parameters. When considering the long-term behaviour of concrete, which includes aspects such as creep and shrinkage, it may require more than a decade.

The existing material models in codes and standards can help us to overcome the difficulties. As an initial step, attempting to update the existing models' parameters for the new type of cements can be considered.

### 11.2 SENSITIVITY ANALYSIS

The developed FE model may be used to perform sensitivity analyses to investigate the different parameters' contribution to the long-term behaviour. Such analyses are important for identifying parameters with the greatest impact on structural behaviour. They may also be used to uncover sets of parameter

combinations that collectively contribute more to the structural behaviour than the sum of their individual effects. Furthermore, it is also possible to address the uncertainty associated with each parameter and assess its impact on structural behaviour.

The moisture content of concrete significantly influences its creep and shrinkage. The model presented in this report has the capability to calculate the development of moisture distribution in an RC. Energiforsk conducted a test series at Barsebäck, which, among other measurements, assessed the equilibrium RH within the RC concrete. Barsebäck's RC is situated within a reactor building with a controlled environment. By utilizing Barsebäck's data, it is possible to evaluate the model's ability to predict moisture distribution within Barsebäck's RC. The results will provide insights into the error margins of the model. This analysis can be conducted using data available over the past 40 years, including research findings from the same period.

### **11.3 PRESSURE TEST**

This model can find utility in analysing short-term responses, particularly within the context of regular pressure tests conducted on existing reinforced concrete structures in Sweden. These pressure tests serve as a routine part of structural evaluation, and the model's applicability in this area can provide valuable insights into the structural performance during these assessments.

### **11.4 CORROSION OF STEEL LINERS**

Another suggestion is to address and model the predicting of corrosion in steel liners, presenting an innovative approach to corrosion management, that could potentially extend the lifespan of structures and improve safety. However, it's important to emphasize that exploring these new application areas requires comprehensive research and a thorough validation process to ensure the reliability and accuracy of the model's predictions. Such rigorous testing and validation will be essential for practical implementation and the realization of the full potential in enhancing structural analysis and safety measures.

### **11.5 CREATING A DIGITAL TWIN OF A REACTOR CONTAINMENT**

A digital twin of an RC is a virtual representation of the physical counterpart that mimics both the structure itself and its behaviour. This a digital twin facilitates various types of advanced computational experiments. The focus of this study is based on a digital scale model of a French RC, which may be seen as an initial step towards creating a digital full-scale geometry and material model of a Swedish RC. This digital representation may serve as a foundation for developing a digital twin of a Swedish RC. Such a digital twin may be used to test different scenarios in order to investigate the response of the RC. While this study primarily focused on describing the mechanical behaviour over time, other areas of research may benefit from employing a digital twin. The mechanical behaviour of the RC may be affected by material degradation, such as corrosion of tendons due to inadequate grouting. Analysing this corrosion process through non-destructive testing can

elucidate how corrosion progresses over time. This knowledge enables the possibility to assess how such corrosion might impact the RC mechanical behaviour in the future, a crucial consideration from both maintenance and safety perspectives.

## 12 Acknowledgements

This project was funded by Energiforsk, the research program 'Nuclear power concrete technology'. The project team is grateful for their financial support.

This research project was conducted using the resources of High Performance Computing Center North (HPC2N).

The computations were enabled by resources provided by the Swedish National Infrastructure for Computing (SNIC), partially funded by the Swedish Research Council through grant agreement no. 2018-05973.

The project team thanks Åke Sandgren at SNIC for his assistance with technical and implementation aspects, which was made possible through the application support provided by SNIC.

Some of the computations were enabled by resources provided by LUNARC.

## 13 References

1. Corbin, M., *International Benchmark VeRCoRs 2018 - Overview, synthesis and lessons learnt*. 2018.
2. Masson, B., M. Corbin, and J. Niepceron, *The VeRCoRs program at mid term - Results at experimental level*, in *International Benchmark VeRCoRs 2018: Program & abstract*. 2018: Paris- Saclay.
3. Corbin, M. and M. Garcia, *International Benchmark VeRCoRs 2015 - Overview, synthesis and lessons learnt*. 2015.
4. Poulain, C., et al., *International Benchmark VeRCoRS 2022 Overview, synthesis, and lessons learnt, DRAFT*. 2023, EDF-DIPNN-DT: Lyon.
5. Bernstone, C., et al., *Verifiering av struktur- och fuktmekaniska beräkningsverktyg*. 2017, Energiforsk.
6. Åhs, M., et al., *Reaktorinneslutningars mekaniska långtidsbeteende*. 2019, Energiforsk.
7. Nilsson, L.-O., *Kapitel 17 Fukt och betong*, in *Betonghandbok, Material*. 2021, AB Svensk Byggtjänst: Stockholm.
8. Sutherland, B.P. and O. Maass, *Measurement of the viscosity of gases over a large temperature range*. *Canadian Journal of Research*, 1932. **6**(4): p. 428-443.
9. *Eurocode 2: Design of concrete structures Part 1-1: General rules for Buildings*, in *EN 1992-1-1 Appendix B*. 2004, European committee for standardization: Brussels. p. 225.
10. Neville, A.M., *Properties of Concrete*. 5:th ed. 2011: Pearson Education Limited.
11. Jonasson, J.E., *Modelling of temperature, moisture and stresses in young concrete*, in *Division of structural engineering*. 1994, Luleå university of technology: Luleå. p. 225.
12. Norling Mjörnell, K., *Moisture Conditions in High Performance Concrete. Mathematical Modelling and Measurements*. 1997, Institutionen för byggnadsmaterial, Chalmers tekniska högskola.
13. Åhs, M., *Fuktegenskaper för byggnadsmaterial - en litteraturstudie*. 2012.
14. Hedenblad, G., *The use of mercury intrusion porosimetry or helium porosity to predict the moisture transport properties of hardened cement paste*. *Advanced Cement Based Materials*, 1997. **6**(3): p. 123-129.
15. Fagerlund, G., *Struktur och strukturutveckling*, in *Betonghandbok Material*. 2017, AB Svensk Byggtjänst: Halmstad.
16. Fredlund, P. and L.O. Nilsson, *Gasinträning i reaktorinneslutningar av betong - mätningar och modellering*. 2009.
17. Monlouis-Bonnaire, J.P., J. Verdier, and B. Perrin, *Prediction of the relative permeability to gas flow of cement-based materials*. *Cement and Concrete Research*, 2004. **34**(5): p. 737-744.
18. Burström, P.G., *Byggnadsmaterial Tillverkning, egenskaper och användning*. 4:1 ed. 2021: Studentlitteratur.
19. Eriksson, D., R. Malm, and H. Hansson, *Nugenia Acceppt - Analysis of stress concentrations and crack risk*. 2015, KTH Royal Institute of Technology.
20. Hassanzadeh, M., R. Malm, and M. Åhs, *Reaktorinneslutningars respons vid höga inre tryck och reducerad förspänning*. 2018. p. 63.
21. Charpin, L., et al., *Ageing and air leakage assessment of a nuclear reactor containment mock-up: VERCORS 2nd benchmark*. *Nuclear Engineering and Design*, 2021. **377**: p. 111-136.
22. *COMSOL Multiphysics reference manual Version 6.1*. 2022, Stockholm, Sweden: COMSOL AB.
23. Emborg, M., A. Hösthagen, and W. Cyron, *Kapitel 19 Egenspänningar och sprickor av temperaturrelaterade och krympning*. *Värme- och mognadsutveckling*, in *Betonghandbok - Material*. 2021, Svensk Byggtjänst: Stockholm.

24. Lewis, W., *The evaporation of a liquid into a gas*. International Journal of Heat and Mass Transfer, 1962. **5**(1-2): p. 109-112.
25. Granger, L., J.M. Torrenti, and P. Acker, *Thoughts about drying shrinkage: Scale effects and modelling*. Materials and Structures, 1997. **30**(2): p. 96.
26. Bažant, Z.P. and J.-K. Kim, *Consequences of diffusion theory for shrinkage of concrete*. Materials and Structures, 1991. **24**(5): p. 323-326.
27. Oxfall, M., P. Johansson, and M. Hassanzadeh, *Moisture Profiles in Concrete Walls of a Nuclear Reactor Containment after 30 Years of Operation*, in XXII Nordic Concrete Research Symposium, 2014-08-13. 2014, Norsk Betongforening.
28. Vinkler, M. and J. Vitek, *Drying Concrete: Experimental and Numerical Modeling*. Journal of Materials in Civil Engineering, 2016. **28**: p. 04016070.
29. Samouh, H., E. Rozière, and A. Loukili, *Influence of specimen size and measurements duration on the long-term extrapolation of drying shrinkage*. Construction and Building Materials, 2017. **150**: p. 276-286.
30. Vinkler, M. and J.L. Vitek, *Drying and shrinkage of massive concrete wall segments – 3 years experiment and analytical observations*. Materials and Structures, 2019. **52**(2): p. 29.
31. Zhang, J., J. Wang, and X. Ding, *Calculation of shrinkage stress in concrete structures with impact of internal curing*. Engineering Fracture Mechanics, 2018. **192**: p. 54-76.
32. Azenha, M., et al., *Thermo-hygro-mechanical modelling of self-induced stresses during the service life of RC structures*. Engineering Structures, 2011. **33**(12): p. 3442-3453.
33. Granger, L., *Comportement différé du béton dans les enceintes de centrales nucléaires : analyse et modélisation.*, in Mécanique [physics.med-ph]. 1995, Ecole Nationale des Ponts et Chaussées.
34. Courtois, A., et al. *Water Content Monitoring for Flamanville 3 EPR Prestressed Concrete Containment: an Application for TDR Techniques*. in International Symposium Non-Destructive Testing in Civil Engineering. 2015. Berlin, Germany.
35. Oukhemanou, E., et al. *Vercors Mock-Up: Comprehensive Monitoring System for Reduced Scale Containment Model*. in 3rd conference on Technological Innovations in Nuclear Civil Engineering, Tince-2016. 2016. Paris, France.
36. Courtois, A., F. Taillade, and D. Placko, *Optimization of sensor location and method analyzing for in-situ monitoring of concrete containment structures: a case involving embedded moisture sensors*. Materials and Structures, 2022. **55**(2): p. 77.
37. Courtois, A., F. Taillade, and D. Placko, *Some considerations on the benefit of measuring concrete moisture to predict long term structural behaviour*. Construction and Building Materials, 2020. **265**: p. 120283.

# LONG-TERM MECHANICAL ANALYSIS OF NUCLEAR REACTOR CONTAINMENTS

The main purpose with this project has been to study reactor containments mechanical behaviour with time and to evaluate leakage during performed pressure tests.

The report presents results of a benchmark, Vercors 2022, which Electricité de France organised. A multiphysics mathematical model has been developed applied to predict the long-term mechanical behaviour of a reactor containment. In addition, a leakage model has been developed that estimates the air leakage through a reactor containment when a pressure test is performed. The model is available to both designers and researchers. Many different parameters that give rise to deformations are included in the model like, temperature and moisture variations, pre-stressed tendons and creep according to Eurocode 2.

This analysis shows that the presented model underestimated the long-term deformations evaluated when compared with the actual observations at many of the analysed points. This underestimation applies to all examined structural components such as cylinder wall, gusset, dome, and raft structure.

The leakage model presented in this report is relatively simple yet provides a reasonably good agreement with measurements. It takes into account that air density varies with pressure and that the concrete air permeability increases as it dries.

## A new step in energy research

The research company Energiforsk initiates, coordinates, and conducts energy research and analyses, as well as communicates knowledge in favor of a robust and sustainable energy system. We are a politically neutral limited company that reinvests our profit in more research. Our owners are industry organisations Swedenergy and the Swedish Gas Association, the Swedish TSO Svenska kraftnät, and the gas and energy company Nordion Energi.

